Multiplexed Microresonator Sensors for Optical Fibre Cable Surveillance

Thesis submitted for the degree of PhD

Department of Electronic and Electrical Engineering
University College London
Torrington Place
London WC1E 7JE

by

Rebwar M A Fatah
BSc(Physics), MSc(Solid State Physics)

March 1991

Supervisor: Professor Gareth Parry

ProQuest Number: 10797713

All rights reserved

INFORMATION TO ALL USERS
The quality of this reproduction is dependent upon the quality of the copy submitted.

In the unlikely event that the author did not send a complete manuscript
and there are missing pages, these will be noted. Also, if material had to be removed,
a note will indicate the deletion.

ProQuest 10797713

Published by ProQuest LLC (2018). Copyright of the Dissertation is held by the Author.

All rights reserved.
This work is protected against unauthorized copying under Title 17, United States Code
Microform Edition © ProQuest LLC.

ProQuest LLC.
789 East Eisenhower Parkway
P.O. Box 1346
Ann Arbor, MI 48106 – 1346

Abstract

In this thesis we have developed a multiplexed sensor system suitable for optical fibre cable surveillance. To achieve an optimum multiplexed sensor system three technologies have been merged, silicon processing, lasers and optical fibres, and optical time domain reflectometry (OTDR). We have demonstrated that a silicon based sensor can be combined with a fibre optic cable without the involvement of any electronics for an all optical monitoring system.

A silicon vibrating element produces an optical output that is a function of the measurand. This optical signal can then be converted to a digital bit stream and then processed using digital signal processing techniques. At resonance the device needs just enough optical power in order to over come its losses. The power required to sustain resonance can be less than 10μW. The resonator dimensions are comparable with that of the fibre optic cross section which makes it easy to fit the device into the end of the optical fibre. Silicon is a mature technology resulting in a low unit cost. Silicon as a material has suitable mechanical properties, including low hysteresis and reproducibility. Silicon historically has been well studied and well understood.

Communicating with the sensor head optically has several advantages. The cost of installation is low because redundant fibres are present in installed cables. Optical signals propagating in fibres are immune to EMI.

A two-source fibre optic system has been developed to study the vibration characteristics of silicon and silicon dioxide resonators. The properties of both metal coated silicon and its oxide are studied. It is concluded that the resonator beams are under stress. This is because during fabrication stress is induced in the material due to the thermal mechanical mismatch between silicon and its oxide, also between the metal and the silicon and its oxide.

The pressure and temperature sensitivity of silicon and silicon dioxide resonators is theoretically and experimentally studied. It is found that silicon is more suitable as a pressure sensor and silicon dioxide as a temperature sensor.

A potential of a 'self-excited' system for sensitivity and multiplexing has been demonstrated. In such a system, a single source has been used for activation and detection of the resonant frequency.

An optical fibre system has been proposed for multiplexing resonator sensors. Sensors with the same resonant frequency are differentiated from each other by using long pulse optical time domain reflectometry (LPOTDR). In this system, the signal gives information about the location of the sensor and the effect of the measurand.

To Chnoor and Sheelan

Acknowledgements

I have found it difficult to classify all the friends and colleagues who have contributed to this work. So I should like to stress that the names have not been classified. This is in order not to undervalue anyone's contribution.

The support of Professor Gareth Parry is appreciated. I believe I could not have completed this thesis without him.

Although Dr Shalini Venkatesh left half-way through the project I have not forgotten her. She introduced me to the field to which she has made a considerable contribution.

All the hours I spent with Dr Nigel Stocks in the laboratories and outside is now part of my character. Although he was difficult occasionally, his contribution is not forgotten. He fabricated the silicon dioxide devices. I enjoyed working with him.

All the help of my colleagues in Optical Fibre Systems and Components at UCL, namely, Mahmoud Farhadiroushan, Akis Markatos, Mike Zervas, Rajesh Kadiwar, Tony Kerr who flavoured the work with a good sense of humour. I am grateful to them.

At least closing down Optical Fibre Systems and Components at UCL had one benefit and that was my joining British Telecom Research Laboratories. I have met several individuals from whom I have learnt a great deal. My supervisor Keith Cameron who never hesitated in helping me to finish this PhD. Other individuals Dr Ann Matthews and Miss Laura Barker who were always willing to help, from reading the text to invaluable discussions. All the help of Maurice Cox and Mike Pryke to make what they call incredibly small devices has not been forgotten. The help of David Bird is particularly appreciated. He read all the text and made a considerable contribution. Paul Garner is acknowledged for making comments on chapters one, eight and nine. Dr Peter Cochrane, the head of my division (RT45), is acknowledged for encouraging me to continue working on this project after I joined RT45.

The encouragement of my schoolmate, Dr Shara Amin, is appreciated. He had a considerable interest in section 3.5, universal resonance response, and discussed the potential of that section with me. The support of David Hall is appreciated. He read the final copy of the thesis and made a considerable linguistic contribution.

I should not express my feeling toward Chnoor and Sheelan. I am surprised they are still with me! I hope I can now spend more time with them.

I apologise to those I have not mentioned.

Rebwar Fatah
British Telecom Research Laboratories
Martlesham Heath, Ipswich IP5 7RE
March 1991

CONTENTS

Abstract......3
Acknowledgements......4
Publications by the author relating to this thesis......11
Glossary of variable......14

CHAPTER ONE: Literature Mechanical resonance sensor: A Review...16
1.1. Introduction......16
1.2. Piezoelectric activations......17
1.3. Piezoresistive effect......20
1.4. Electrostatic activation......22
1.5. Electrothermal activation......26
1.6. Optical activation......29
1.6.1. Optical activation using a bulk optic system......29
1.6.2. Optical activation using a fibre optic system......35
1.7. Other methods of activating micromechanical resonators......37
1.7.1. Activation with swept frequency modulations......37
1.7.2. Activation with approximated Dirac-pulses......37
1.7.3. Activation by noise-modulated light......37
1.7.4. Transit activation......38
1.8. Summary and the scope of this project......39
1.9. References......42

CHAPTER TWO: Devices Fabrication: silicon and silicon dioxide.....46
2.1. Introduction......46
2.2. Fabrication techniques......48
2.2.1. Photolithographic patterning......48
2.2.2. High-density doping......49

2.2.3. Anisotropic etching..52
2.2.4. Silicon dioxide devices...53
2.3. Conclusions..53
2.4. References..54

CHAPTER THREE: Theoretical Analysis................................55
3.1. Introduction...55
3.2. Optical fibre system...56
3.3. Mechanisms of optical activation of micromechanical resonators....57
3.4. Resonant modes...67
3.4.1. The resonant frequency of longitudinal vibrations..................67
3.4.2. The resonant frequency of torsional vibrations......................68
3.4.3. The resonant frequency of flexural vibrations 69
3.4.4. Discussion...74
3.5. Universal resonance response...78
3.6. Resonance frequency dependence on metal coatings.................83
3.6.1. Introduction...83
3.6.2. Dependence of resonance frequency on different metal coatings..84
3.6.3. Dependence of fundamental resonance frequency on different metal coatings and metal thickness...................................86
3.7. Fibre optic detection of resonator vibrations..........................89
3.7.1. Introduction...89
3.7.2. Mathematical treatments..90
3.7.3. Coupling coefficient...92
3.7.4. The interferometric signal..98
3.7.5. Conclusions...102
3.8. The intensity distribution within the cavity..........................104
3.9. Overall conclusion..107
3.10. References..109

CHAPTER FOUR: Vibration characteristic of micromechanical resonators.111
4.1. Introduction.....111
4.2. Optical fibre system.....111
4.3. Vibration characteristic.....112
4.4. Optical activation of silicon micromechanical resonators.....121
4.4.1. Introduction.....121
4.4.2. Experiments.....121
4.4.3. Discussion.....126
4.5. Stress measurements of doped silicon using micromechanical resonators.128
4.5.1. Introduction.....128
4.5.2. Theoretical analysis.....128
4.5.3. Devices and experiments.....129
4.5.5. Discussion and conclusions.....130
4.6. Reproducibility of the results for silicon beams.....134
4.7. Optical activation of silicon dioxide micromechanical resonators.....135
7.7.1. Introduction.....135
4.7.2. Dependence of compression stress on thickness-to-width ratio.....140
4.7.3. The neutral equilibrium stress.....140
4.7.4. Discussion and conclusions.....151
4.7.5. Consideration of metal coatings.....152
4.8. Quality-factors of microresonators.....159
4.8.1. Introduction.....159
4.8.2. Theory of the quality-factor of flexural vibrations.....159
4.8.3. Experimental work.....162
4.8.4. Conclusions.....171
4.9. Overall conclusions.....173
4.10. References.....174

CHAPTER FIVE: Electrical activation of micromechanical resonators.....177
5.1. Electrostatic activation of micromechanical resonators....................177
5.1.1. Introduction...177
5.1.2. Device construction..178
5.1.3. Principle of activation...179
5.1.4. Electromechanical analysis...182
5.5. Experimental work...184
5.5.1. Frequency response of resonators..................................184
5.5.2. Dependence of signal amplitude on applied voltage magnitude........186
5.5.3. Comparison between electrical and optical activation..................187
5.6. Discussion and conclusions..189
5.2. Electrothermal activation of resonator sensors............................190
5.2.1. Introduction...190
5.2.2. Theory...191
5.2.3. Experiments...194
4.2.4. Discussion and conclusions..195
5.3. References...197

CHAPTER SIX: Self-excitation of micromechanical resonators.........198
6.1. Introduction...198
6.2. Experimental work...201
6.2.1. Observation of self-excitation..201
6.2.2. Sensitivity measurements and multiplexing self-excited
resonators..204
6.3. Conclusions...205
6.4. References...207

CHAPTER SEVEN: All fibre-optic micromechanical resonator sensor system....................................208
7.1. Introduction..208
7.2.Theoretical analyses..210
7.3. Experimental work...220
7.3.1. Pressure sensitivity of resonance frequency.......................220
7.3.2. Temperature sensitivity of resonance frequency....................226
7.4. Assembly of the sensor head to the systems fibre......................232
7.5. Conclusions...234
7.6. References..235

CHAPTER EIGHT: Multiplexed Microresonator Sensors for Optical Fibre Cable Surveillance..........................236
8.1. Introduction..236
8.2. Systems architecture..237
8.3. Multiplexing of sensors on a single fibre.............................240
8.4. Improvement in LPOTDR system performance..............................241
8.3.1. The sensor...241
8.3.2. The system...242

CHAPTER NINE: Summary, Discussion and Conclusions...........244
9.1. Introduction..244
9.2. The sensor head...245
9.3. The optical fibre system..247
9.4. Electro-optic system..128
9.5. Theoretical work..249
9.6. LPOTDR: A technique for multiplexing resonator sensors..........252
9.7. References..253

Publication and patent applications list:

1. Publication and patent application list related to the PhD project:

1.1. Publications:

1. Stokes N A D, **Fatah R M A** and Venkatesh S: 'Self-excited vibrations of optical microresonators', Electron Lett, Vol 24, 23 June 1988, pp 777-778.
2. **Fatah R M A** , Stokes N A D and Venkatesh S: 'Activation of silicon micromechanical Resonators in Fibre Optic Systems', Proceeding of EFOC '89, Amsterdam, June 1989.
3. **Fatah R M A**, Stokes N A D and Venkatesh S: 'All Fibre-Optic Microresonator Sensor System', Symposium on 'Sensors and Their Applications-S+AIV', University of Kent, 25-27 September 1989.
4. Stokes N A D, **Fatah R M A** and Venkatesh S: 'Self-Excitation in fibre-optic microresonator sensors', Conference on solid-state sensors and actuators (Proceedings of Transducers '89, Montreux, June 1989.
5. **Fatah R M A**: 'Optical Activation of micromechanical resonators: theoretical analysis', Proceeding of BROADBAND '89 FOC/LAN, San Francisco, CA, October 30-November 3, 1989.
6. **Fatah R M A** and Stokes N A D: 'Optical activation of micromechanical resonators: end conditions', Proceeding of 'EOLI 90 Conference: Frontiers in Electro optics', Birmingham, UK, March 1990, pp 118-125.
7. Stokes N A D, **Fatah R M A** and Venkatesh S: 'Self-excitation in fibre-optic microresonator sensors', Sensors and Actuators, A21-A23, 1990, pp 369-372.
8. **Fatah R M A** and Stokes N A D: 'All Fibre-Optic Microresonator Sensor System', New Materials and their applications 1990 (IOP conference series No 111, Norfolk, 1990)
9. **Fatah R M A:** 'Frequency response of optically activated beam microresonators in Fibre Optic Systems', New Materials and their applications 1990 (IOP conference series No 111, Norfolk, 1990).
10. Gafouri-Sheraz H, Cameron K and **Fatah R M A**: 'Achievement of low coupling loss between a 1.5μm wavelength laser and a high NA MCVD-single-mode fibre by conical microlens', Microwave and Optical Technology Letters, Vol 3, No 6, June 1990.

11. **Fatah R M A:** 'Electrostatic activation of micromechanical resonators', Electron Lett, Vol 27, No 2, 1991, pp 166-168.

12. **Fatah R M A**: 'Analysis of pressure sensitivity of microresonators', To be presented to 'Sensors and Their Applications-S+AV', University of Edinburgh 25-27 September 1991.

13. **Fatah R M** A: Detection of Microresonator Vibrations in Fibre Optic Systems, To be presented to 'Sensors and Their Applications-S+AV', University of Edinburgh 25-27 September 1991.

14. **Fatah R M A**: The effect of metal coating upon resonance frequency of silicon dioxide microresonators, To be presented to 'Sensors and Their Applications-S+AV', University of Edinburgh 25-27 September 1991.

15. **Fatah R M A**: Stress Measurements of doped silicon using micromechanical resonators, submitted to 'Applied Physics'

1.2. Patents:

16. **Fatah R M A** et al: 'Optical fibre system: optical fibres in water born yachts', UK patent applications No 8928363.4, 15 December 1989.

17. **Fatah R M A** and Cameron K H: 'Multiplexed microresonator sensors for optical fibre cable surveillance', UK patent application No (not known yet), 1990.

2. Publication and patent application list not related to the PhD project and achieved during the PhD project period:

2.1. Publications:

18. **Fatah R M A**, Cox M K, Bird D M and Cameron K H: Miniature lens positioner: BT R&T memorandum No RT45/034/89, December 1989.

19. **Fatah R M A**, Cox M K, Bird D M and Cameron K H: Miniature angular positioner: BT R&T memorandum No RT45/007/90, January 1990.

20. Bird D M, **Fatah R M A**, Cox M K, Constantine P D, Regnault J C, and Cameron K H: 'Miniature packaged actively mode-locked semiconductor laser with tunable 20ps transform limited pulses', Electron Lett, 26(25), 1990, p 2086.

21. **Fatah R M A**, D M Bird, Cox M K and Cameron K H: 'Subminiature external cavity laser', Proceeding of 'Optical Science and Engineering', The Hague, The Netherlands, 11-15 March 1991.

22. **Fatah R M A**, Bird D M, Cox M K, Pryke M J and Cameron K H: 'MQW packaged external cavity / mode locked laser', 3rd Bangor Communication Symposium, 29-30 May 1991, pp 26-29.

23. Bird D M, Armitage J R, Kashyap R, **Fatah R M A** and Cameron K H: 'Narrow line semiconductor laser using a fibre grating', To be published in Electron Lett.

24. **Fatah R M A**, Bird D M, Cox M K, Pryke M J and Cameron K H: 'Wavelength tunable ring lasers', To be published.

2.2. Patent Applications:

25. **Fatah R M A**, Bird D M, Cox M K and Cameron K H: 'Miniature lens positioner', UK patent application No (not known yet), December 1989.

26. **Fatah R M A**, Bird D M, Cox M K and Cameron K H: 'Miniature angular positioner', UK patent application No 9012324.1, 1, 1 June 1990.

27. **Fatah R M A**, Bird D M, Cox M K and Cameron K H: 'Wavelength tunable polarisation Optical Switch', UK patent application No (not known yet), 1990.

Glossary of variables:

λ:	wavelength of light
λ_i:	end-condition dimensionless parameter
Q:	quality-factor
μ:	thermal diffusion length
δ_{op}:	optical penetration depth
α:	linear thermal expansion coefficient
α_{th}:	thermal diffusively
ρ:	density
ω:	angular frequency
f:	resonant frequency
κ :	thermal conductivity
χ:	absorption coefficient
I:	intensity of laser beam
I:	second moment of area
Φ:	Complex temperature
T:	temperature
v:	velocity
c:	specific heat capacity
ε_{op}:	strain due to optical absorption
σ_{op}:	stress due to optical absorption
E:	Young's modulus
w:	width of the beam
t:	thickness of the beam
L:	length of the beam
G:	torsional modulus
ν:	Possion's ratio
i:	mode number: an integer
n:	refractive index
n:	an integer
m:	an integer (chapter 3): mass (chapter 4)
d:	distance (chapter 3): wafer thickness (chapter 7)
r & t :	reflection & transmission coefficients

w:	beam radius
w_o:	bean waist
D:	total travelling distance
Θ:	effective tilt
k:	$2\pi/\lambda$: propagation constant
C_m:	coupling coefficient
D_N:	normalised distance
Θ_N:	normalised tilt
ΔP:	differential pressure
R:	radius of the sample in which pressure is applied
r:	distance from the centre of the sample in which pressure is applied to any point on it
w_o:	displacement of a circular sample under differential pressure

CHAPTER ONE

Mechanical Resonator Sensors: Activation and Detection Methods of Resonant Elements (A Review)

1.1. Introduction

The effect of resonance as with any other phenomenon is two-fold on human kind: it is either destructive or constructive. Humankind build ships and buildings with structures whose resonant frequencies do not coincide with frequencies of the natural forces such as winds, sea waves and earthquakes. However, we do not avoid resonance all the time; on the contrary, there are occasions when we carefully study and attempt to make the criteria for resonance. In musical instruments, electrical circuits, microwave ovens, and in structure studies resonance is required.

If it is possible to transfer energy from a vibrating (drive) system to a second (driven) system, the latter starts vibrating too. Resonance is a special case of vibration. That is when maximum energy is transferred from the drive system to the driven, i.e. there is a minimum loss of energy in the transformation process, and the amplitude of vibration is maximum. A system at resonance requires enough energy to recover its losses and is at its lowest energy level. Any disturbance to the drive system at resonance will move the system into an unstable state and if the disturbance continues, the system may take another mode of resonance: another minimum energy level or another stable state. Hence, there are several modes (energy states) that keep the system stable. These modes are a function of the system's geometry, structure and the environmental conditions. A vibrating structure not

kept at resonance always tries to go back to its lowest energy state by either decaying the vibration or by going to a resonant state. During these processes the conservation laws of energy and momentum are obeyed by the systems involved.

Here we study miniature mechanical elements. The vibration of these devices can be sustained at their natural mechanical resonance. These resonant structures are referred to in the literature as oscillating elements, vibrating elements, mechanical oscillators, resonators, resonant structures, mechanical resonators, micromechanical resonators and microresonators which imply their capability to be sustained at resonance.

While this review does not cover all the work done in this field, it also does not supersede previous reviews; on the contrary it aims to be complementary. Langdon (1985) [1] and Gast (1985) [2] reviewed resonator sensors which covered aspects of sensors for liquids and gases, force, mass and temperature. The devices they dealt with are large devices (not microresonators). Venkatesh (1989) [3] also gave an account of microresonant sensors focusing on optically activated methods. On the fabrication side, the most comprehensive review covering silicon micromachining techniques was done by Petersen (1982) [4]. Elwenspoek et al (1989) [5] reported the possible methods of activating and detecting microresonators. It is a short but comprehensive report on the research mainly conducted in their institution (University of Twente).

The intention of this review is to show the role of this project along the line of resonator pressure sensors. It describes all the possible methods and systems of activating and detecting resonators, and then shows the need for an all optical fibre system for optical fibre cable surveillance.

1.2. Piezoelectric activations

One of the electromechanical interaction in materials is called piezoelectricity. Crystals like quartz, tourmaline, berlinite, lithium niobate and lithium tantalate, bismuth germanium oxide and bismuth silicium oxide and rochelle salt all exhibit the piezoelectric property. Ceramics of polycrystalline substances based on solid solutions of Pb(Zn, Ti) O_3 with polymers like

polyvinyl chloride (PVC), polyvinyl fluoride (PVF) and difluor polyethylene (PVF_2) also have piezoelectric property [6]. When a crystal is mechanically stressed, charges with opposite signs appear at the two ends of the crystal (Jacques and Pierre Curie 1880). The inverse is also possible (Lippmann 1881), i.e. application of an electric field produces stress in the crystal [6,7]. Consequently, an application of a periodic electric field produces periodic mechanical vibration. Conversely, a periodic mechanical vibration also produces a periodic electric charge in the crystal. In this way a piezoelectric effect can be used for activation and detection of resonators.

Piezoelectric activation of mechanical elements has been achieved using two methods. Firstly a piezoelectric transducer is fabricated in the resonator and secondly the resonator is mounted in contact with a piezoelectric oscillator (Fig 1.1). In this way the energy transfers from the piezoelectric transducer to the resonator. When the frequency of the transducer is equal to that of the resonator, resonance will occur.

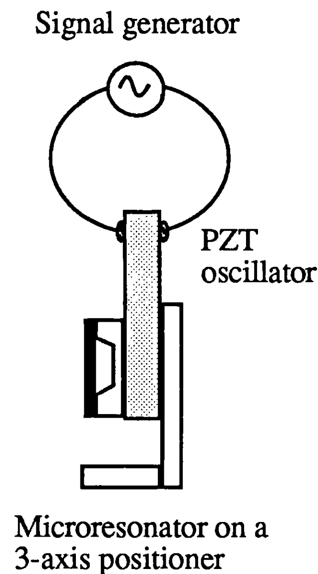

Fig 1.1: Activation of a resonant structure using piezoelectric oscillator. The detection method is not shown.

Smith et al (1985) [8,9] activated a multilayer structure diaphragm of $1mm^2$ and $20\mu m$ thickness. Activation was achieved electrically by the application of a periodic potential difference to a pair of piezoelectric transducers which exerted a periodic force on the

diaphragm. The detection was achieved both electrically and optically. The vibration was detected electrically by use of a pair of piezoelectric transducers (receptors) and optically by use of a pair of fibre optics. The periodic force on the receptors produces a periodic output electrical signal. From one of the fibres a light beam was directed to the surface of the diaphragm. This beam was modulated by the vibration of the diaphragm and collected by the second fibre positioned close to the first one[1]. This device was used as a pressure sensor and the sensitivity was 0.11 Hz Pa^{-1}.

Other applications of piezoelectric materials include balances, one example of which was reported by Mulder (1984) [10]. This balance was used to weigh up to 300mg and had a load-to-sensitivity ratio of 10^6. Two piezoelectric elements were used. One of the elements was used to activate one of the wires and the other element was used to detect the change in the resonant frequency. Hanging a weight on the end of the wires applied a force to the wires; this in turn changed the resonant frequency. Calibrating the resonant frequency with weights made the device suitable as a weighing device.

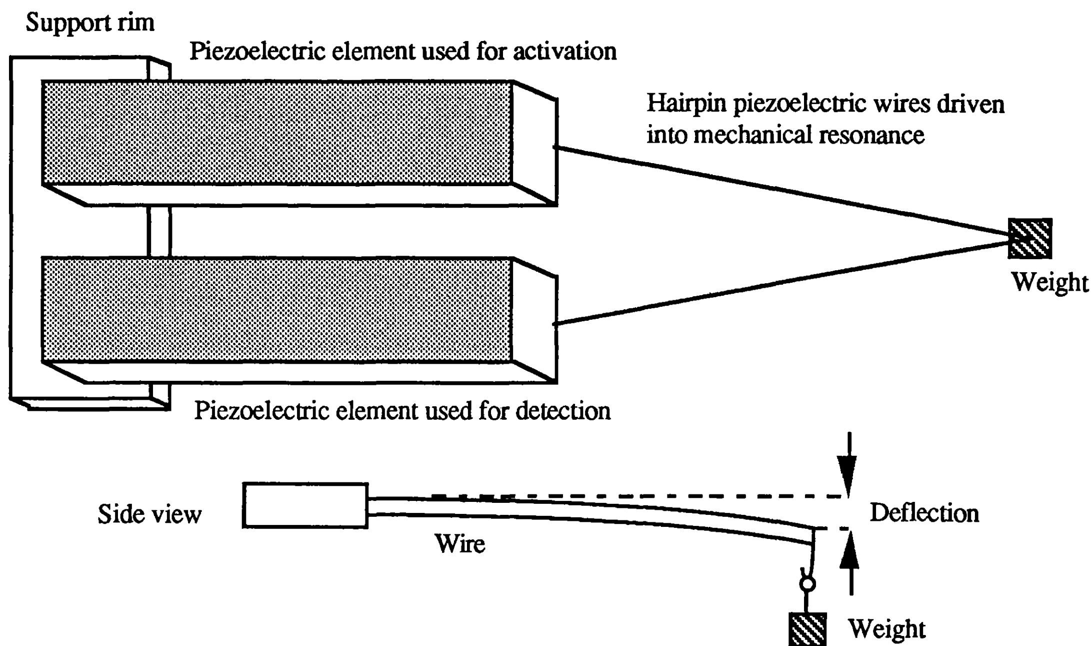

Fig 1.2: Microbalance based on mechanical resonance of a loaded quartz wire. Adapted from Mulder [10].

[1] The detection method will be dealt with in chapter 3, Section 3.7.

1.3. Piezoresistive effect

The piezoresistive effect is used to detect stresses induced in a piezoresistive material. This subject is well reported in the literature [11-15]. Nevertheless, it is still useful to show the principle of detection of resonant elements using the piezoresistive effect. The piezoresistive effect as defined by Tufte and Long [16] is the change in the electrical resistance of a conductor or a semiconductor when it is subjected to an external stress. Hence, a periodic electric signal applied to a piezoresistive conductor produces a periodic stress/strain in it. This method is mainly used for detecting stresses/strains introduced in a semiconductor wafer with a piezoresistive area on it.

Tufte et al (1962) [16] used a silicon diaphragm as a pressure/stress sensor. A strip of low-resistivity material was fabricated by impurity diffusion on a thin (0.6mm) circular (25mm in diameter) high-resistivity single crystal silicon wafer (Fig 1.3). The diaphragm is then placed on a glass tube for pressure applications. The fractional resistance change with pressure is shown in Fig 1.4. It is worth noting that this is a static method of pressure measurement in which the sensing element (diaphragm) was not activated at its natural resonant frequency.

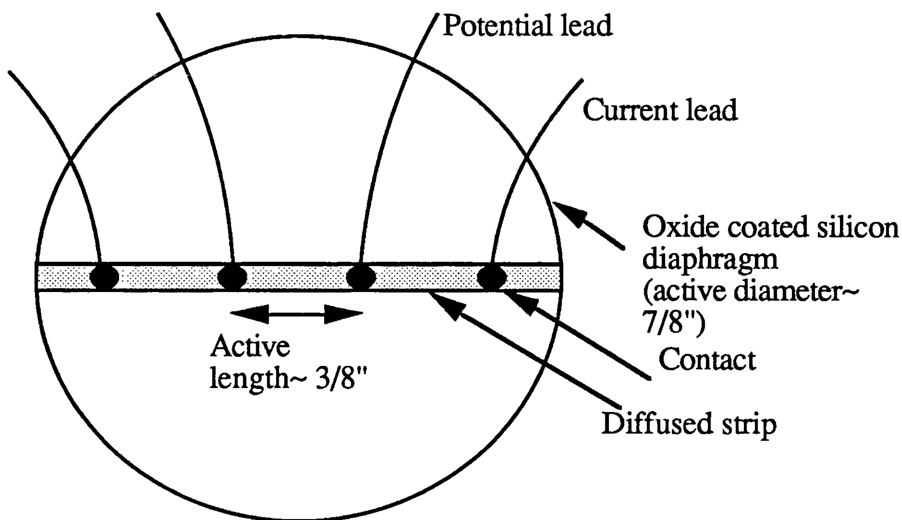

Fig 1.3: A strip of low-resistivity material was fabricated by impurity diffusion on a thin circular high-resistivity single crystal silicon wafer and was used as a pressure sensor. Adapted from Tufte et al (1962) [16].

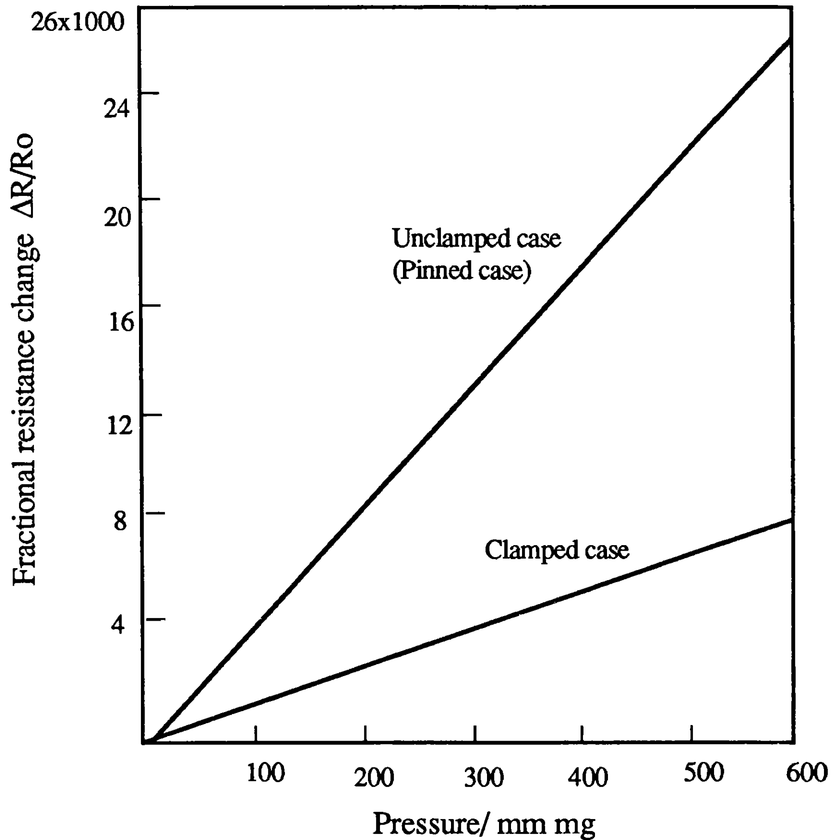

Fig 1.4: The fractional resistance change with pressure for the strip used shown in Fig 1.3. Adapted from Tufte et al (1962) [16]. For end-conditions (clamped and pinned) see pages 68 (Fig 3.7) and 212 (Fig 7.1).

Beneck et al (1985) [17] used a piezoelectric element to activate silicon cantilevers suspended over an etched pit as shown in Fig 1.5. Their length varied between 600μm and 1100μm and they were used as a vibration sensor. The resonant frequency of these devices was in the range of 4.2KHz to 6.4KHz. Other cantilevers with similar geometries were fabricated, each having an extended end mass. They had resonances in the range of 0.87KHz and 1.96KHz with quality-factors[2] of over 100. The resonant frequency of the devices was detected by a piezoresistive material which was mounted in the suspended end of the cantilever. The mechanical vibration produced an electric signal in the piezoresistive material which was monitored.

[2] For more details on quality-factor see section4.8.

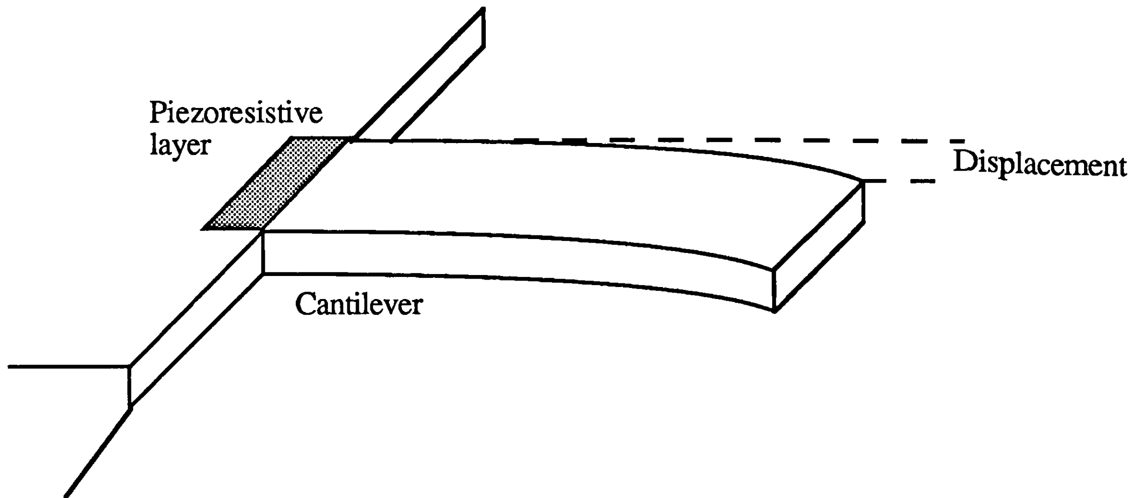

Fig 1.5: Piezoresistive detection of cantilever vibration. Adapted from Beneck et al [17].

1.4. Electrostatic activation of mechanical structures

By application of a voltage across two electrodes, one of which consists of a free-to-move element (resonator), a capacitive effect is utilised between them. Hence, a voltage applied across the electrodes causes the resonator-electrode to be displaced from its initial position towards the fixed electrode. A periodic input signal across the two electrodes causes the resonator to move in an oscillatory fashion following the input signal. There will be a time delay between the input signal and the mechanical oscillation. Resonance will occur whenever the periodic voltage is equal to one of the resonant frequencies of the resonator. This is shown schematically in Fig 1.6.

The first beam structure that was used as a resonant device was activated and detected electrostatically by Nathanson et al (1967) [18] when they introduced the resonant gate transistor (RGT) (Fig 1.7). Typical dimensions of these devices (cantilevers and microbridges) were, for example, 240μm long, 4.0μm thick and beam to substrate separation 10μm. They had resonant frequencies from 1 to 132KHz, quality-factors of up to 500 and temperature coefficients of the resonant frequency of approximately 90 ppm^{o}C. These devices have been extensively studied by Nathanson et al and discussed by Petersen [4] and Newell [19,20].

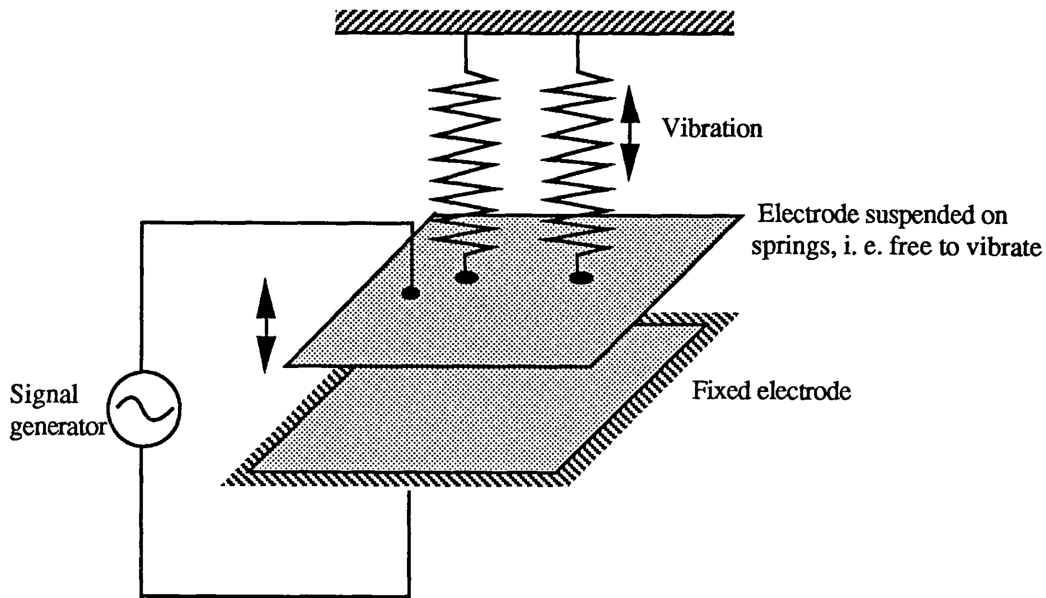

Fig 1.6: The principal of electrostatic activation.

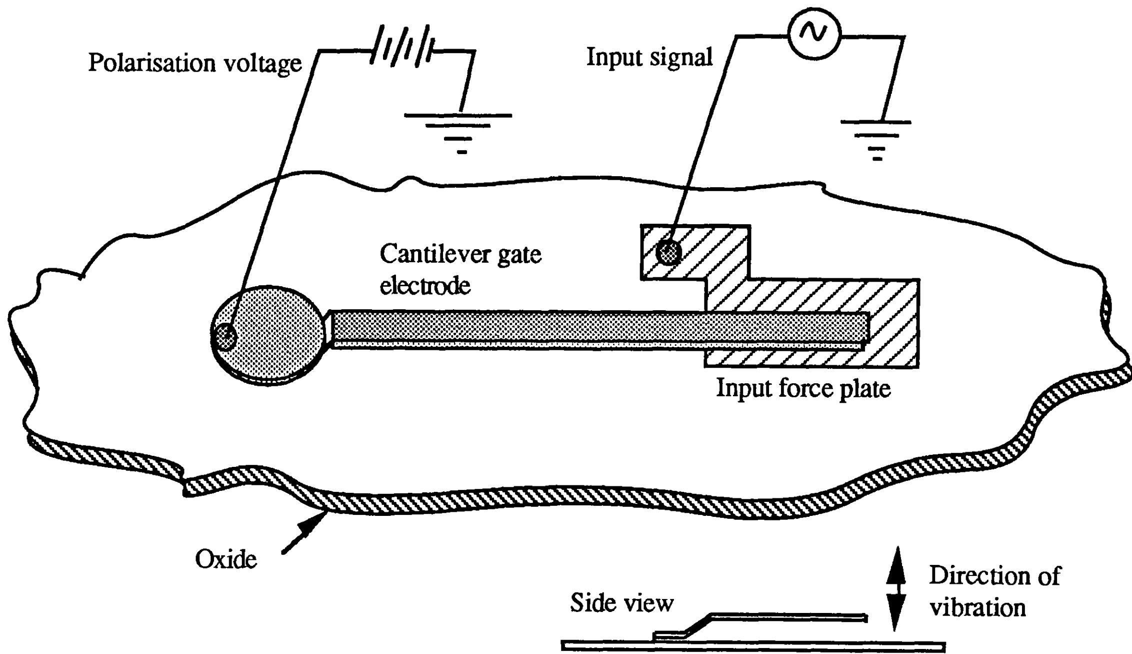

Fig 1.7: Activation method of resonant gate transistors. Not all the connections are shown. Adapted from Nathanson et al [18].

Petersen (1977) [21] used fabricated silicon dioxide cantilevers, with dimensions of 100μm long, 25μm wide and 0.5μm thick, as optical displays. Each individual beam was used in an optical modulator array. The deflection required was obtained by the application of an electrostatic voltage between the top electrode and the buried boron doped layer which acted as an electrode (Fig 1.8). These mechanical devices were sustained at their resonance frequency by the application of a periodic electrostatic force. This idea was used by Petersen and Guarnieri (1979) [22] to measure Young's modulus of thin dielectric films thermally grown or deposited using resonant structures. These were cantilever beams of thin dielectric films driven into mechanical resonant frequency electrostatically and detected optically. The detection was achieved by focusing a laser beam on the resonator and detecting the reflected light which was intensity modulated at the mechanical resonant frequency. The Young's modulus was calculated from the equation of resonance by measuring the dimensions of the device and using a given density. This was the first time that laser beams were involved in detecting resonant frequencies.

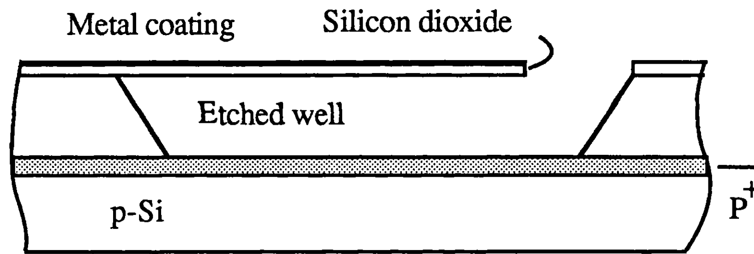

Fig 1.8: Cantilevers of thin films fabricated by Peterson. Adapted from Petersen [21].

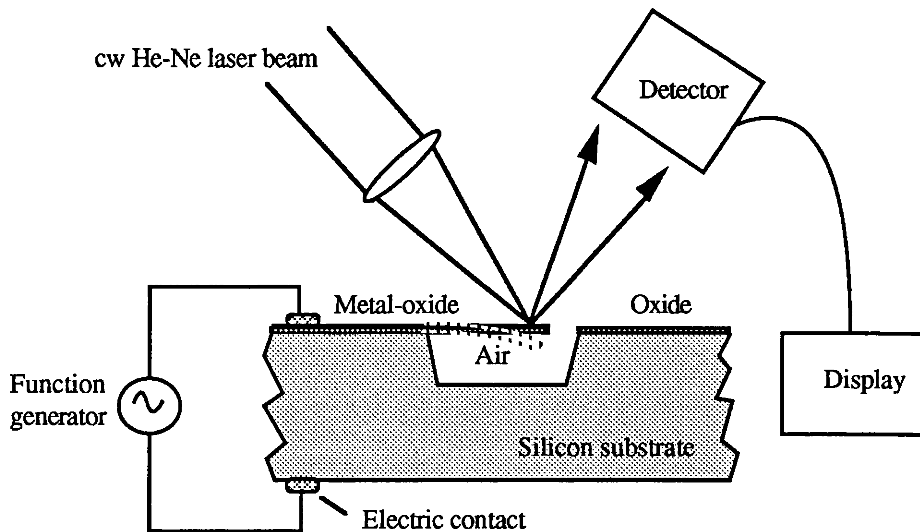

Fig 1.9: Activation and detection of micromechanical cantilever. Adapted from Petersen and Guarnieri [22].

Greenwood (1981, 1984) [23-25] reported a device which was regarded as the first silicon based sensor based on resonant frequency monitoring. The device (Fig 1.10) was fabricated on a single substrate. It consisted of two rectangular plates or flaps each suspended from two sides by V-shaped strips. The flaps were also connected to each other from one side by a springy strip which provided easy transfer of energy from one flap to the other. This device was then mounted at a distance of about 10-20μm on a pattern substrate which provided the necessary electrodes for activation and detection. The device had a fundamental resonant frequency of about 63KHz, a quality-factor of 10 000 in vacuum of 10^{-3} Torr and a pressure sensitivity of 175Hz KPa^{-1}. It did not vibrate in pressures higher than 1 Torr because of air resistance.

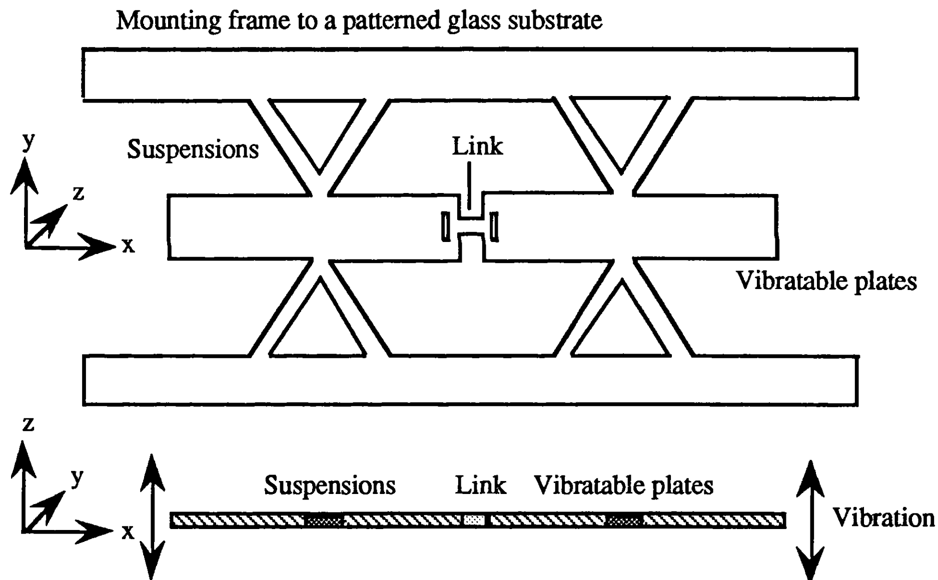

Fig 1.10: STL's resonant sensor. Adapted from Greenwood [23-25].

An example of the utilisation of torsional vibration is a structure made by Petersen (1980) [26] which is a torsional scanning mirror (Fig 1.11). This assembled device provided only torsional rotation. A mirror element with two torsional bars made of single crystal silicon was bonded on to a (glass or silicon) substrate into which a rectangular well had been etched. At the bottom of the well were two electrodes which were powered alternately to deflect the mirror. Transverse oscillations were avoided by providing a ridge in the middle

of the well. Two of these devices, one with a resonant frequency of 2KHz and the other with a resonant frequency of 15 KHz, produced quality-factors of 3 and 15 respectively.

Fatah (1991) [27] activated silicon dioxide and nitride beams using electrostatic activation and used a fibre guided laser beam to detect the mechanical resonance. This will be discussed in detail in chapter 5.

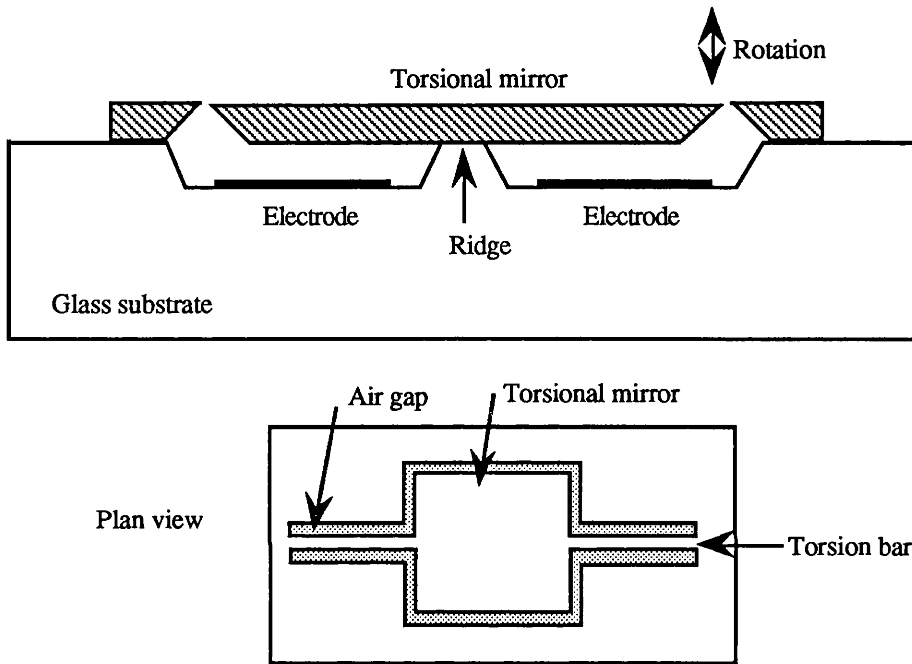

Fig 1.11: Silicon torsional mirror. Adapted from Petersen [26].

1.5. Electrothermal activation

Electrical power can be delivered and partially dissipated in the form of heat in a resonator which may be in the form of a beam, diaphragm or more complicated structure, using some form of resistor (heater). As the resonator heats up, the heating (Joule) effect deflects the resonator from its initial position because part of the electrical energy transfers to heat and introduces a stress in the resonator. As the beam cools down, the stress releases and the beam goes back to its initial position. A periodic electric current input therefore causes the

resonator to be displaced in an oscillatory fashion. Whenever the periodic voltage is equal to one of the natural resonant frequencies of the resonator, resonance will occur. The mechanical oscillation lags the input signal by some phase difference which is due to the inertia of the system. This is the principle of electrothermal activation.

Wilfinger et al (1968) [38] were the first group who activated silicon cantilevers by dissipating heat in its suspended end (Fig 1.12). Resistors diffused in the suspended end dissipated periodic electric power (Joule effect). As a result periodic contraction and expansion in the skin near the surface occurred. When the period of the heat generated is equal to the resonant frequency of the cantilever, resonance occurred. The cantilever of 50 x 30 x 8mm had a resonant frequency of 200KHz and a quality-factor of 250. Other cantilevers with resonant frequencies of 1-2KHz and quality-factors of 4400 were obtained. A device with 3.6KHz and a quality-factor of 1400 was loaded with a 3gm mass to the unloaded end of the cantilever. The frequency reduced to 1.4KHz but the quality-factor was increased to 2500. This was the first time that the Joule effect has been associated with resonance in silicon beams.

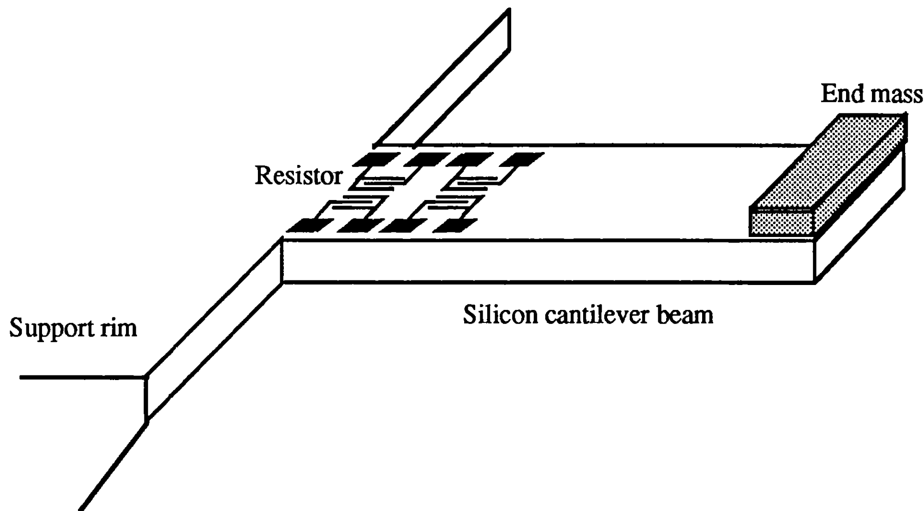

Fig 1.12: Activation of silicon cantilevers by dissipating heat in the suspended end using diffused resistors. Adapted from Wilfinger et al [28]

Lammerink and Wlodarski (Twente University, 1985) [29] fabricated square diaphragms with a thickness of 15μm and sides of 1, 2, 3 and $4mm^2$. They used electro-thermal (Joule) effect for activation by which a periodic voltage was applied to a resistive material in the device. Piezoelectric (Mechano-electrical) transduction was used for reading the vibration. A receptor read the vibration of the device by producing a signal proportional to the amplitude of the vibration. A pressure sensitivity of $0.5Hz\ Pa^{-1}$ was achieved.

Dieulesaint et al (1986) [30] activated sapphire (Al_2O_3) beams (40 x 3 x 3 mm) that were suspended at two points away from the ends to form a free ended beam (Fig 1.13). A 100nm thickness of chromium provided the resistor. A periodic current was applied to the suspension wire. This produced a periodic heating and hence mechanical vibrations. When the electrical frequency was equal to the mechanical resonance of the beam, the resonant condition was met. Because of the size of the device the air resistance was high enough to damp the mechanical resonance; hence vacuum encapsulation was required to achieve the resonant condition. The optical wedge scheme was used for detection of the vibration (Fig1.14). That is to say, the beam of a He-Ne laser was mechanically chopped by the vibration of the beam. The resonant frequency of the device was 20262Hz and the quality-factor 800000. This was the first time that sapphire (Al_2O_3) beams had been activated. It was also the first time that the metal coating of a beam was utilised to provide the Joule effect for activation of a beam.

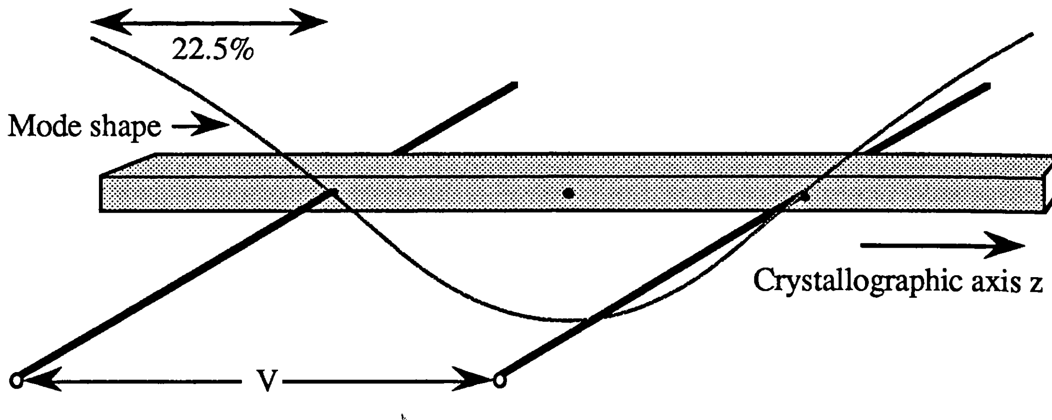

Fig 1.13: Sapphire beam activated, utilising the Joule effect and detected optically. Adapted from Dieulesaint et al [30].

Othman and Brunnschweiler (1987) [31] mounted a U-shaped polysilicon resistor in a cantilever. This resistor dissipated periodic heat in the cantilever and as a result resonance occurred. The device was a single crystal cantilever defined by etching away the substrate. It was 1μm thick, 60μm long and 20μm wide. The beam was covered with 0.4μm thermal silicon dioxide and a U-shaped polysilicon resistor was mounted in the suspended end. Its resonant frequency was 250KHz with quality-factor of 200. This resonator only operated in a vacuum.

Fatah (1989) [32] activated silicon beams electrothermally. This will be discussed in detail in chapter 5.

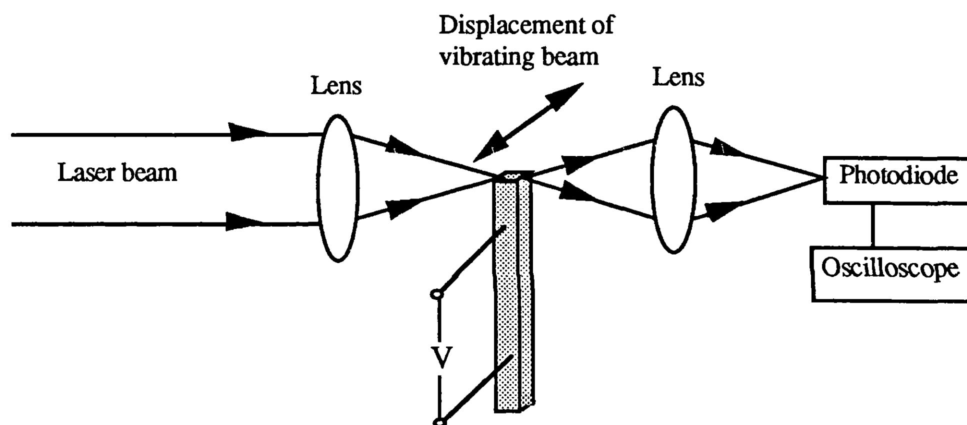

Fig 1.14: Optical detection of vibration of sapphire resonator. Adapted from Dieulesaint et al [30].

1.6. Optical activation

1.6.1. Optical activation using bulk optic systems:

In this section we deal with transferring optical energy into mechanical energy in a resonant structure. The first experimental work on transferring optical modulation to mechanical vibrations was achieved by A G Bell (1880) [33]. The same phenomenon was also observed in 1881 by W Rontgen [34] and J Tyndall [35].

Development of the laser in the early 1960s was a prerequisite for photoacoustic studies of microstructures. Lasers made it possible to accumulate high intensity collimated light beams in areas of less than one mm. With this new source, it was more effective to focus high energy beams on microstructures.

Dieulesaint et al (1981) [36] were the first group who employed this combination of silicon and laser technology together. This group activated silicon discs whose diameters were 4, 6, 9mm and were 10μm thick. To increase the absorption of the optical power they applied black paint to the silicon samples. Their experimental set up is shown in Fig 1.15. They used two different sources for activation (a He-Ne and a LED) with an average modulated output power of 5mW in both cases. The mechanical vibrations were detected using a 2mW laser beam by the knife edge method. Resonant frequencies of 2-7KHz and a quality-factor of about 10 were measured.

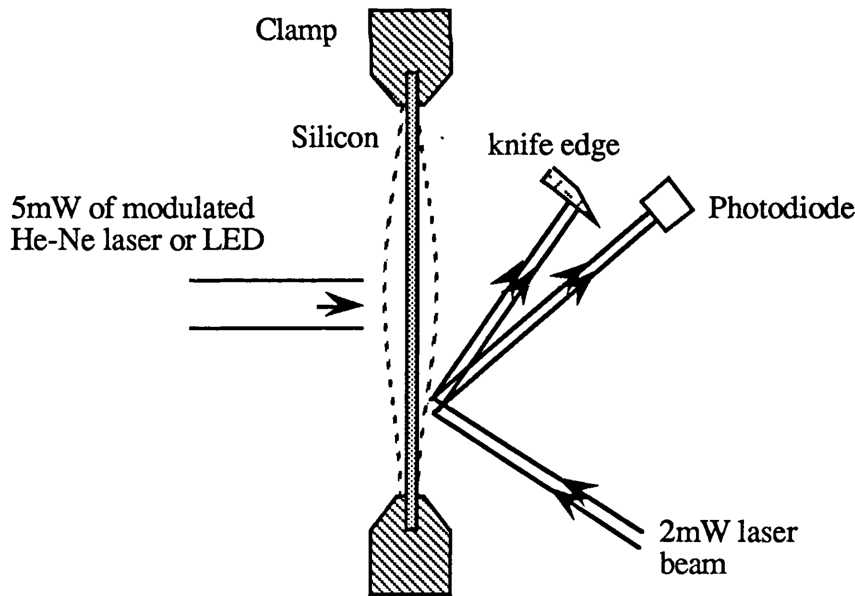

Fig 1.15: Optical activation and detection of silicon discs by Dieulesaint et al [36].

Dieulesaint et al again (1981) [37] optically activated quartz plates (dimensions: 38 x 4.3 x 1 mm), bars (dimensions: 30 x 3 x 3 mm) and discs (radius 15mm and thickness 1.5mm).

These devices had resonant frequencies of 70KHz, 16KHz and 1000KHz, with quality-factors of 30 x 10^3, 90 x 10^3 for the first two resonant frequencies, respectively. In this experiment, they used the piezoelectric effect for detecting the mechanical vibrations. The optical source used for activation was an externally modulated He-Ne laser beam with an average output power of 10mW. It should be noted that the quality-factors were very high despite the experiment having been carried out at atmospheric pressure.

Mallalieu et al (1985) [38] activated a quartz beam which was designed for piezoelectric activation. The beam was utilised as a force sensor which was mounted on a steel cantilever with a slot cut in it to allow the displacement of the beam (Fig 1.16). Steel was used for temperature stability since quartz and steel have close thermal expansion coefficients. The sensor had a resonant frequency of 13.6KHz, quality-factor of 2000 and sensitivity of 1Hz gm^{-1}. This group also gave a theoretical analysis of the optical activations.

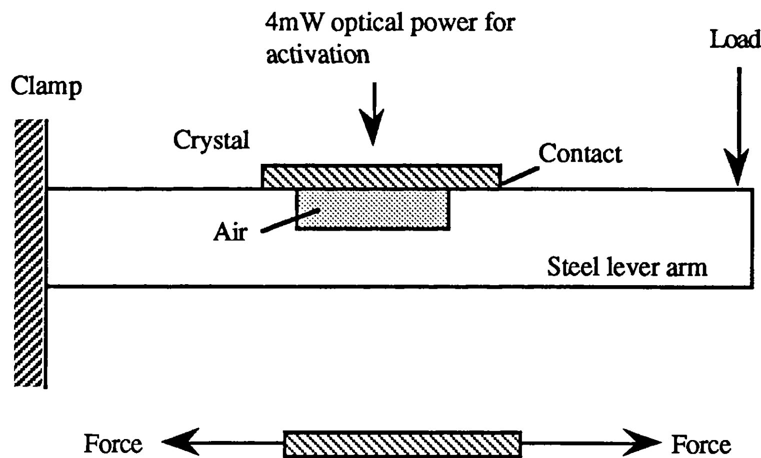

Fig 1.16: Optically activated quartz beam arranged to sense force. Adapted from Mallalieu [38].

It should be pointed out that in 1977, even before Dieulesaint et al [35], Johnson and Ulrich [39] reported optical activation and detection of a fibre optic relay. In Fig 1.17, fibre A was mounted to form a cantilever which was capable of mechanical movement. This

fibre was then aligned with another fibre in such a way that light emitted from A could be launched into fibre B. Two methods were used for activating fibre A. In the first method, an LED was used to periodically heat a metallic coating deposited on one side of fibre A. In the second method, light guided in fibre A itself was used to activate the fibre. The cladding of A was removed by etching and the absorber was coated directly on the core.

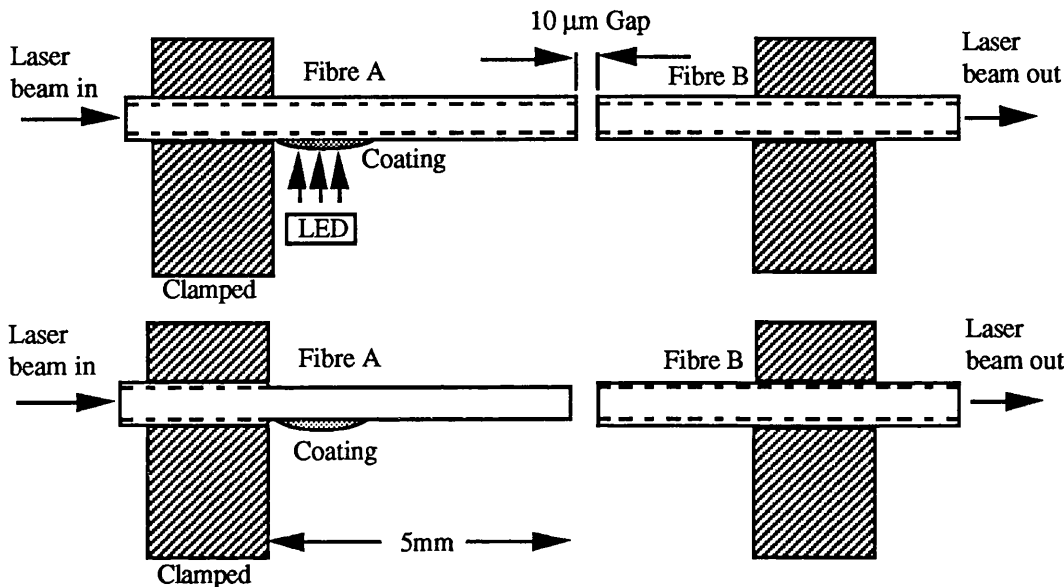

Fig 1.17: Fibre optic relay. Adapted from Johnson and Ulrich [39].

The pressure sensing system of Fig 1.18 was reported by Johnson [40]. The resonant body was 10 x 0.24 x 0.06mm. The activation was achieved by modulating LED2. As a result of the differential thermal expansion between the Pyrex and a 0.2 mm^2 polymer film bonded to the tube's outer wall, the tube starts to vibrate. This causes the vane to chop the beam from LD1 to the photodetector, hence modulating the beam at the mechanical vibration frequency. Varying the pressure inside the tube changes the resonant frequency and the frequency of modulation and hence pressure sensitivity.

All the above devices were millimetre-size devices. The first microresonator (micrometer-size resonator) optically activated and detected was by Venkatesh and Culshaw (1985) [41,42]. These devices were silicon dioxide beams (microbridges) whose dimensions were 80-200µm long, 5µm wide and up to 1µm thick etched on silicon wafers, and sputtered

with gold. Venkatesh and Culshaw used a He-Ne laser beam in a heterodyne interferometric configuration for activation and detection, as shown in Fig 1.19. The small amount of optical power (50μW) used to activate these devices was encouraging for further work. However, the quality-factor of these devices (about 10) was rather disappointing.

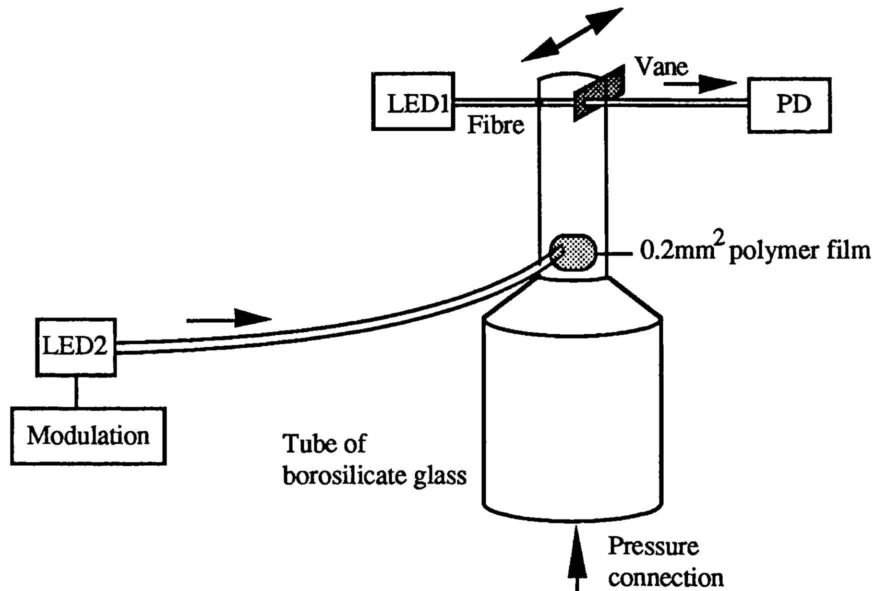

Fig 1.18: Optical actuator pressure sensor. Adapted from Johnson [40].

Thornton et al (1986) [43] etched silicon square diaphragms of sides 760μm and thickness about 4μm and followed by 0.5μm of evaporation deposited aluminium. They measured four modes of resonance using bulk optic system (Fig 1.18): 89, 176, 263, 329KHz. The amplitude of the diaphragm at resonance was 60nm and a quality-factor of 100 was measured. The temperature sensitivity was measured to be about 60Hz $^{o}C^{-1}$. The same group (1987) [44] etched silicon square diaphragms of sides 750μm and thickness about 5μm. These devices were deposited with 0.5μm of evaporation aluminium. The activation was achieved using the bulk optic system of Fig 1.19 at 121KHz. Deflections of 20nm were achieved with a quality-factor of 40. The average optical power used for activation was 1mW. The group showed the pressure sensitivity of these devices (Fig 1.20) to be 0.04% $mbar^{-1}$. This was the second device (after Mallalieu) that had been optically activated and used as a pressure/force sensor.

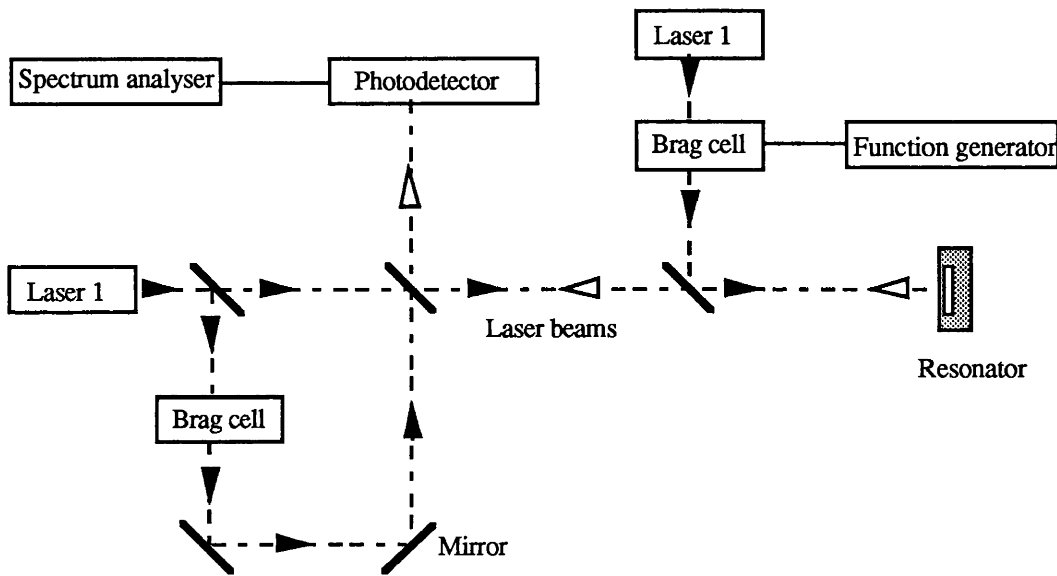

Fig 1.19: Bulk optical resonator system.

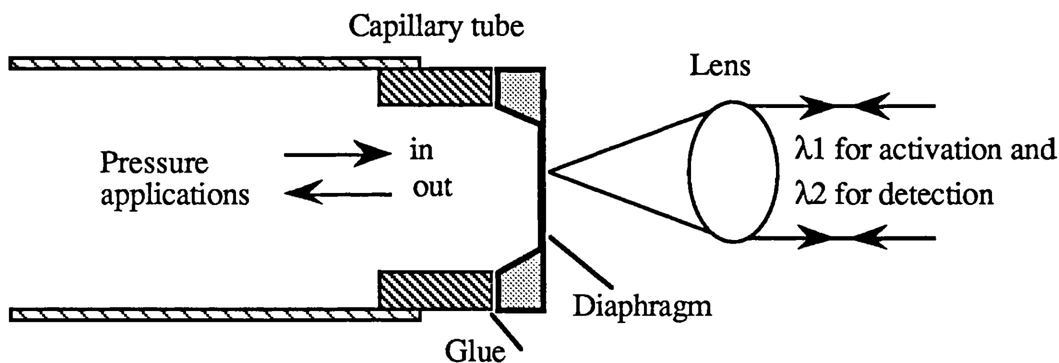

Fig 1.20: Optical activation and detection of silicon diaphragm by the Strathclyde group. With such a system positive or negative pressure can be measured.

The bulk optic system was used on two other occasions for activation and detection microresonators by Strathclyde University. Uttamchandani et al (1987) [45] activated beam

resonators whose dimensions were 130 μm x 5.5μm x 2.5μm and had a resonant frequency of 1389KHz and quality-factor of 300. The temperature and the pressure sensitivity of these devices was 0.64% $^{o}C^{-1}$ and 0.26KHz $mbar^{-1}$ respectively. Thornton et al (1987) [46] reported the pressure (0.027% $mbar^{-1}$) and temperature sensitivity (0.46 % $^{o}C^{-1}$) of silicon beam resonators. This beam was different from the previous in that it was attached to the silicon wafer by means of tapered silicon pillars of 30μm height. The resonant frequency of this device was 566KHz and its quality factor was 400.

1.6.2. Optical activation using fibre optic systems:

In a practical sensor system, a bulk optic system (Fig 1.19) is not desirable. The optical fibre can be used as flexible, low loss media to deliver the light to and from the sensor head (resonator). The technique of using optical fibres for mechanical vibrations was well established in surface acoustic wave detections [47-49]. However, it was not used with mechanical resonators until 1986. It should be pointed out that unguided laser beams were first used by Petersen [7] as mentioned previously.

Andres et al (1986) [50] activated devices similar to those activated electrically and piezoelectrically by Greenwood in 1978 [9,10,11]. The devices were made by the latter's laboratory at STL (Fig 1.10) and they had dimensions of 100 x 125 x 8 μm. They positioned two fibres on the resonator. The first one was carrying the activation laser beam and the second acted as the detection fibre. The resonant frequency of these devices were in the range of 100-200KHz with very high quality-factors (4 x 10^3-18 x 10^3).

In the same year 1986, Venkatesh and Novak [51,52] for the first time guided two beams with two different wavelengths through the same optical fibre for both activation and detection of silicon dioxide resonators. The devices were similar to those activated by Venkatesh and Culshaw [41,42]. This system will be discussed in chapter 3.

Wolfelschneider et al (1987) [53] activated and detected silicon cantilevers with two optical

fibres, one for detection the other for activation. The dimensions of one of these devices are shown in Fig 1.21. The devices had a resonant frequency of about 2KHz and quality-factor of 50.

Fatah et al (1989) [54-57] for the first time used a single optical fibre to activate and detect a variety of geometries of silicon beams (chapter 4). This group also measured [56,57] the pressure and temperature sensitivity of silicon and silicon dioxide beams using a single fibre positioned on the beam for both detection and activation (chapter 7).

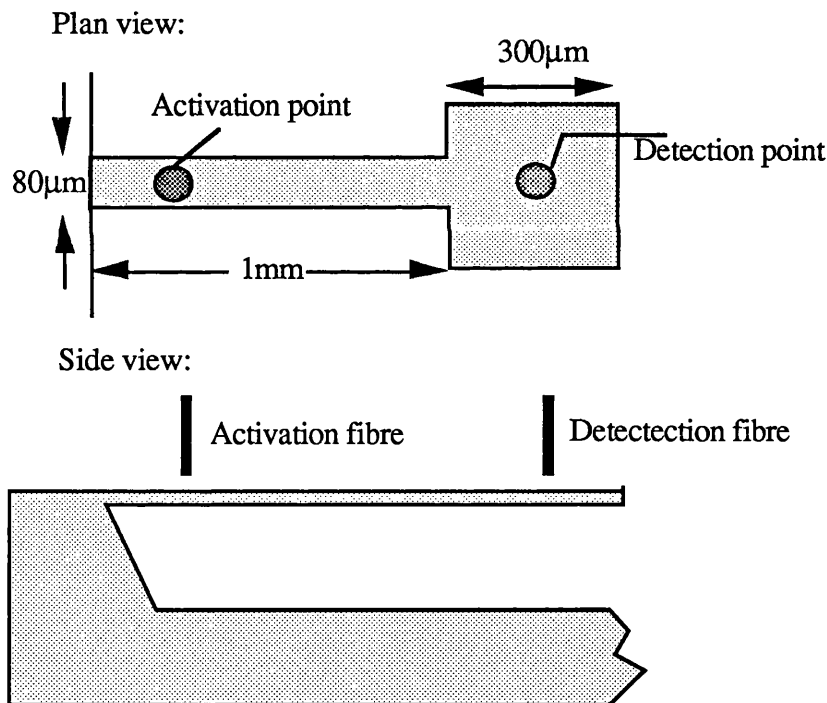

Fig 1.21: Optical activation and detection of cantilevers. Adapted from Wolfelschneider et al [53]

1.7. Other methods of activating micromechanical resonators

We shall consider four types of activation:

1.7.1. Activation with swept frequency modulations:

This technique was used by Hildebrand and Wolfelschneder (from Fraunhofer-Institut) 1988 [58]. They used the devices and the same experimental configuration of Fig 1.21. The activating laser was modulated with a frequency sweep that covered the natural resonant frequencies of the resonator which may be predicted theoretically. Pressure sensitivity of -1.5×10^4 $HzPa^{-1}$was reported. It is interesting to note that the pressure coefficient of the resonant frequency was negative.

1.7.2. Activation with approximated Dirac-pulses:

A short pulse with a power spectrum broad enough to cover the resonant frequency range of the device may be used to activate the resonators. This method was first reported by Hildebrand and Wolfelschneider (1988) [58]. They activated the device of Fig 1.21. A 7μs pulse with sinusoidal shape showed that due to a low pulse power density a high averaging (500) is necessary to obtain a desirable SNR (20).

1.7.3. Activation by noise-modulated light:

Another way of activating microresonators is by noise-modulated light which was first reported by Hildebrand and Wolfelschneider (1988) [58]. In this experiment broadband noise (200KHz) was superimposed on the laser to activate the device of Fig 1.21. As the noise spectrum was absorbed by the resonator beam from the light incident on its surface, the beam only responds to the frequencies equal to its resonant frequency. In other words, the resonator behaves like an optical filter that blocks the rest of the spectrum but not the frequencies at which the resonance occurs. This method also may be used for a

multiplexing scheme since the spectrum of the noise is broad enough to cover the whole frequency spectrum. A commercial signal analyser with a Fourier Transformation capability was used to analyse the detected spectrum.

1.7.4. Transit activation:

The Strathclyde group (1989) [59] used a single source (laser diode) for activation and detection of microresonators. They used a Michelson interferometer as their optical system. The laser pulsed with a duration of 10μs and 5mW peak power which activated the device and then switched to a power of 0.5mW to act as a source for the interferometer which measured the decaying (transient) vibration. Therefore, the same optical source was used for activation and detection. The silicon beam used in this experiment had dimensions of 1.4mm long by 12μm wide and 2μm thick and was coated with 40nm of silver. A personal computer was used to Fourier-transform the recorded time-domain signal to the frequency spectrum. This group used a bulk optic system for their measurements. However a fibre optic version can be used similar to that shown in Fig 1.22.

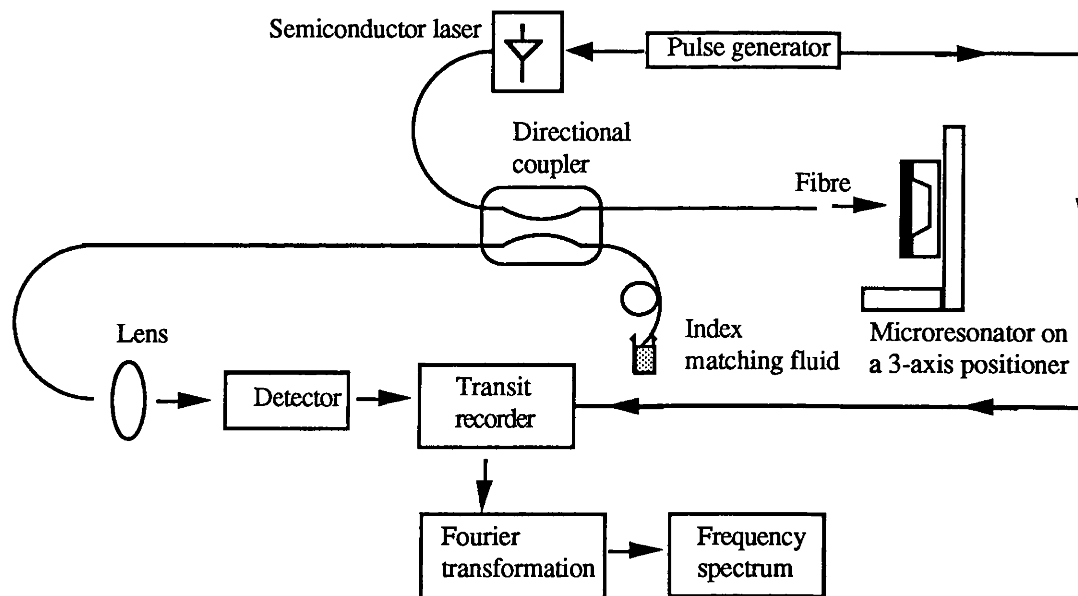

Fig 1.22: Transit activation and detection microresonators in fibre optic systems.

1.8. Summary and the scope of this project

We have reviewed the methods that have been used for activation and detection resonant structures. An optical fibre system is an ideal system for monitoring the parameter in question. However, there are occasions where electrical activations are useful, for example for current or magnetic sensing. We summarise the main points of this chapter in two tables: Table 1.1 and Table 1.2.

Table 1.1: The important events in the history of resonators:

The event	The year and the reference
The piezoelectric effect is discovered	Jacques & Pierre Curie 1880, Lippmann 1881[6,7]
Photoacoustic effect found	Bell 1880[36], Rontgen 1881[34], Tyndall 1881[35]
Development of semiconductor lasers	Nathan et al 1962. Hall et al 1962. Holonyal & Bevacqua 1962.[60]
Development of optical fibres	Goubau & Schwering 1961, Eaglesfield 1962, Kao & Hockham 1966. Kapron et al 1970 [60].
The first device electrostatically activated	Nathanson et al 1967[18]
The first device electrothermally activated	Wilfinger et al 1968[25]
The first device optically activated	Dieulesaint et al 1981[36]
The first microresonator optically activated	Venkatesh & Culshaw 1985[41,42]
The first optical fibre system used to activate and detect microresonators	Venkatesh & Novak 1985[51,52]
The pressure and temperature sensitivity of microresonators measured in fibre optic systems. It is also shown that silicon dioxide resonators are not suitable for pressure sensing, However they can be used for temperature sensing.	Fatah et al 1989 [54-57]

Table 1.2: A summary of the devices driven into mechanical resonance frequency. The resonator dimensions, the method of activation and detection, the year of the event and the reference are shown.

Key: Cantilever (C), SD: square diaphragm (the side is shown), CD: circular diaphragm (the radius is shown), B: microbridge, CS: complicated structure. P: Piezoelectrically, ES: Electrostatically, ET: Electrothermally, BO: bulk optic system. FO: Fibre optic system

Resonator dimensions	Activation (detection) method	Resonant frequency (Q-factor)	Year [Ref]
SD: 1mm^{2}x20μm	P(P & FO)	198KHz (150)	1985[8,9]
C & B: 240x10x4μm	ES(ES)	from 1 to 132KHz (500)	1967[18]
C: 100x25x0.5μm	ET(BO)	40KHz(10)	1977[22]
CS:	ES(ES)	63KHz (10 000 in vacuum)	1978[23-25]
C(Si): 50x30x8mm	ET(P)	200KHz (250)	1968[28]
SD(Si): 1-4mm^{2}x15μm	ET(P)	120KHz	1985[29]
B(sapphire): 40x3x3mm	ET(BO)	20.2KHz (800 000 in vacuum)	1986[30]
C:(Si):60x20x1μm	ET(P)	250KHz (200 in vacuum}	1987[31]
CD(Si): 4,6,9x10μm	BO(BO)	2-7KHz (10)	1981[35]
B(Quartz):250x?x?	BO(BO)	13.6KHz (2000)	1985[38]
SD(Si): 460μm^{2}x4μm	BO(BO)	89KHz 100)	1986[43]
CS(Si): 100x125x8μm	FO(FO)	100-200KHz (4000-18000)	1986[50]

At present conditions on optical cables are generally monitored using additional metal carriers. The move towards cables with no metal bearers indicates the need for an optically based monitoring system. To date the major parameter which has been continuously monitored has been the pressure of joint housings in the cable. These are normally measured using simple contact pressure sensors which at a certain pressure put a loop on to the monitor pair and signal an alarm at the repeater station. A subsequent bridge measurement identifies the sensor which has been triggered. At the present time the terrestrial cables are pressurised to keep moisture and gases out up to 30psi. Although the submarine cables are not pressurised, it has to be ensured that the pressure on the cables is

at about the same level as terrestrial cables (30psi). With increasing use of optical fibres for communications, the need for an all optical fibre pressure sensor becomes inevitable.

This project has two goals: First of all, an all optical fibre system has to be developed. The sensor head has to be optically activated and detected. Secondly, a multiplexing scheme has to be developed to multiplex several sensor heads at the same time. It will be desirable if all the sensor heads have the same resonant frequency. This makes the fabrication simpler. A system like this will be able to continuously monitor pressure and temperature of the optical cables. It is also capable of detecting explosive gases in the cables. Resonator sensor heads are desirable because of the frequency output which is compatible with digital signal processing. Optical fibres are chosen as the medium to communicate with the sensor heads since communications and television broadcasting are moving towards electrical free transmission, i.e. optical cable communications. Therefore, electrical detection will soon not be compatible with the modern optical communication networks and yet monitoring the stress and temperature states of the cables will be necessary. This system will be compatible with the existing optical cables because there are already spare optical fibre cables in the network that can be adapted for sensing purposes.

The desired optical fibre sensor system is shown in Fig 1.23 which consists of a fibre coupler and a sensor head. The same laser is used for activation and detection. The sensor head is a silicon beam resonator which is fabricated on silicon. The possibility of a system like this will be discussed in chapter 6.

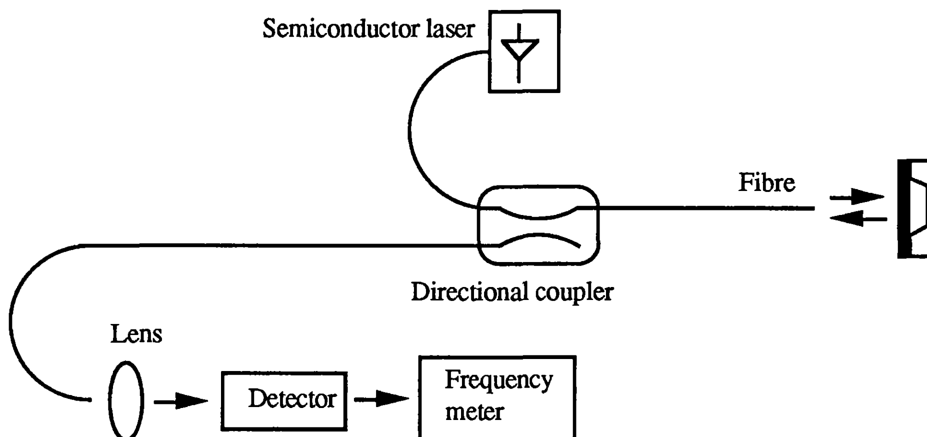

Fig 1.23: The desired optical fibre system.

1.9. References

1 . Langdon R M: 'Resonator Sensor', J Phys E: Sci Instrum, Vol 18, 1985, pp 103-115.

2 . Gast T: 'Sensors with Oscillating Element', J Phys E: Sci Instrum, Vol 18, 1985, pp 783-799.

3 . Venkatesh S: 'Optical microresonator sensor systems', J of the Institute of Electronic and Radio Engineers, Vol 58, No 5, July/August 1988, pp S79-S84.

4 . Petersen K: 'Silicon as a Mechanical Material', Procs of IEEE, Vol 70, No, 5, May 1982, p 420-457.

5. Elwinspoek M, Blom F R, Bouwstra S, Lammerink T S J, van de Pol F C M, Tilmans H A C, Popma J A and Fluitman J H J: 'Transduction mechanisms and their applications in micromechanical devices', Procs IEEE Micro Electro Mechanical Systems. 1989, pp 126-132.

6 . Zelenka J: Piezoelectric resonators and their applications', (Elselvier Science Publishing Co Inc, 1986, pp 20-63).

7 . Narasimhamurty T S: 'Photoelastic and electro-optic properties of crystals', (Plenum Press, New York, 1981, pp 333-344.)

8 . Smiths J G, Tilmans H A C, Hoen K, Mulder H, Vuuren J V and Boom G: 'Resonant diaphragm pressure measurement system with ZnO on Si excitations', Sensors and Actuators Vol 4, 1983, pp 565-571.

9. Smiths J G, Tilmans H A C and Lammerink T S J: 'Pressure dependence of resonant diaphragm', Procs IEEE Conf Transducers 85, Philadelphia, 1985, pp 97-100.

10. Mulder B J: 'Simple piezoelectric microbalance based on a vibrating quartz wire', J of Phys E: Sci Instrum, Vol 17, 1984, pp 119-21.

11 . Smith C S: 'Piezoresistance effect in germanium and silicon', Physics Review, Vol 94, No 1, April 1954, pp 42-49.

12. Herring C: 'Transport properties of many-valley semiconductors', Bell Syst Tech J, Vol 34, March 1955, pp 237290.

13. Pollak M: 'Piezoresistance in heavily doped n-type germanium', Phys Rev, Vol 111, No 3, August 1958, pp 798-802.

14. Geyling F T and Forst J J: 'Semiconductor strain transducers', Bell Syst Tec J, Vol 39, May 1960, pp 705-31.

15. Tufte O N and Long D: 'Recent developments in semiconductor piezoresistive devices', Solid State Electronics, Vol 6, 1963 pp 323-38.

16. Tufte O N, Chapman P W and Long D: 'Silicon diffused-element piezoresistive diaphragm', J Appl Phys, Vol 33, No 11, 1962 , pp 3322-3327.

17. Benecke W, Csepregi L, Heuberger A, Kuhl K and Seidel H: 'A frequency-selective piezoresistive silicon vibration sensor' , Procs Int Conf on solid-state sensors and actuators-Trans UCER 85, Boston, 1985, pp 105-8.

18. Nathanson, H C, Newell, W E, Wickstrom, R A and Davis, J R: 'The resonant gate transistor', IEEE Trans of Electr Devices, Vol ED-14, No 3 march 1967, pp117-133.

19. Newell, W.E: 'Miniaturisation of tuning forks'; Science, Vol. 161, 1968, pp 1320-1326.

20. Newell, W.E: 'Ultrasonics in integrated electronics'; Procs IEEE, Vol. 53, 1965, pp 1305-1309.

21. Petersen K E: 'Micromechanical light modulator array fabricated on silicon', Appl Phys Lett, Vol 31, 1977, pp 521- .

22. Petersen K E and Guarnieri C R : 'Young's modulus measurements of thin films using micromechanics', J. Appl Phys, Vol 50, 1970, pp 6761-6766

23. Greenwood J C: British Patent No 1588669 (Filled 1977, Published 1981).

24. Greenwood J C: 'Resonant silicon sensor at STL' Abstract of Eurosensors, 3rd Conference on Sensor and their Applications, Cambridge, 1984, pp 14-15.

25. Greenwood J C: 'Etched silicon vibrating sensor' J Phys E: Sci Instrum., Vol 17, 1984, pp 650-652.

26. Petersen, K E: 'Silicon torsional scanning mirror', IBM J Res Dev, Vol 24, No 5, Sep 1980, pp 631-636.

27. Fatah R M A: 'Electrostatic activation of micromechanical resonators', Electron Lett, Vol 27, No 2, 1991, pp 166-168.

28. Wilfinger R J, Bardell P H and Chhabra D S: 'The resonator: a frequency selective device utilizing the mechanical resonance of silicon substrate', IBM J Res and Dev, Vo 12, Jan 1968,pp 113-118.

29. Lammerink T S J and Wlodarski W: 'Integrated thermally excited resonant diaphragm presser sensor', Procs IEEE Conf Transducers 85, Philadelphia, 1985, pp 97-100.

30. Dieulesaint E, Royer D and Servajan X: 'Sapphire resonator', Electron Lett, 27 Feb 1986, Vol 22, No 5, pp 266-268.

31. Othman M B and Brunnschweiler A: 'Electrothermally excited silicon beam mechanical resonators,' Electron Lett, 2 July 1987, Vol 23 No 14, pp728-30.

32. Fatah R M A: ' Micromechanical resonator in fibre-optic systems' MPhil thesis, University College London, London, May 1989, pp 177-122.

33. Bell A G: Am J Sci '', Vol 20, 1881, pp 305.

34. Rontgen W C: '', Philos Mag, Vol 11, 1881, pp 308.

35. Tyndall J: '', Proc R Soc, London, Vol 31, 1881, pp 307.

36. Dieulesaint E, Royer D and Bonnefoy C: 'Mechanical excitation of a membrane by an optical beam', Procs of IEEE Ultrasonics Symposium, 1981, pp 3802-805.

37. Dieulesaint E, Royer D and Rakouth H: 'Optical excitation of quartz resonators', Electron Lett, 1982, Vol 18, No 5, pp 382-383.

38. Mallalieu K: 'An analysis of the photothermal drive of a quartz force sensor', Procs SPIE Conf on Fibre-Optics 85, 1985, Vol 522, pp 211-218.

39. Johnson M and Ulrich R: 'Fibre-optic relay', Appl Phys Lett, Vol 31, No 10, Nov 1977, pp 675-676.

40. Johnson M: 'Optical-actuator frequency-coded pressure sensor', Optics Lett, Vol 311, No 9, Sept 1986, pp 587589.

41. Venkatesh S and Culshaw B: 'Optically activated resonator sensors', SPIE Vol 566 Fibre Optic and Laser sensors III, 1985, pp110-112.

42. Venkatesh S and Culshaw B: ' Optically activated vibrations in a micromachined silica structure', Electron Lett, Vol 21, 1985, pp 315-317.

43. Thornton K E B, Uttamchandani D and Culshaw B: 'Temperature dependence of optically excited diaphragms', Electron Lett, 1986, Vol 22, No 23, pp 1232-4.

44. Uttamchandani D, Thornton K E B and Culshaw B: 'Optically excited resonant diaphragms pressure sensor', Electron Lett, 1987, Vol 23, No 4, pp 152-153.

45. Uttamchandani D, Thornton K E B and Culshaw B: 'Optically excited resonant beam pressure sensor', Electron Lett, Vol 23, No 25, 1987, pp 1333-1334.

46. Thornton K E B, Uttamchandani D and Culshaw B: 'Novel optically excited resonant pressure sensor', Electron Lett, 12 May 1988, Vol 24, No 10, pp 573-579.

47. Bowers J E: 'Fibre-optic sensor for surface acoustic waves', Appl Phys Lett, Vol 41, No 3, August 1982, pp 231-233.

48. Bowers J E, Jungerman R L, Khuri-Yakub B T and Kino G S: 'An all fibre-optic sensor for surface acoustic wave measurements', J Lightwave Tech, Vol LT-1, No 2, June 1983, pp 429-435.

49. Monchalin J P: 'Optical detection of ultrasonic', IEEE Trans Ultrasonics, Ferroelectics, and frequency control, Vol UFFVC-33, No 5, September 1986, pp 485-499.

50. Andres M V, Foulds K W H and Tudor M J: 'Optical activation of silicon vibrating sensor', Electron Lett, Vol 21, 1985, pp 1097-1099.

51. Venkatesh S and Novak S: 'Fibre-optic detection of optothermal vibrations', Technical Digest of OFS '86, Tokyo, 1986, pp PD1-2-PD1-5.

52. Venkatesh S and Novak S: ' Micromechanical resonators in fibre-optic systems', Optics Lett, Vol 12, 1987, pp 129-31.

53. Wolfelschneider H, Kist R, Knoll G, Ramakrishnam, Hofflin H: 'Optically exited and interrogated micromechanical silicon cantilever structure', Procs of SPIE, Vol 798 Fibre Optic Sensor II, 1987, pp 61-66.

54. Fatah R M A, Stokes N A D and Venkatesh S: 'Activation of silicon micromechanical resonators in fibre optic systems', Procs of EFCO 89, Amsterdam, June 1989, pp 418-422.

55. Fatah R M A and Stokes N A D: 'Optical activation of silicon micromechanical resonators: end-conditions', Procs of Frontiers in Electro Optics, Birmingham, 1990, pp 118-125

56. Fatah R M A, Stokes, N A D and Venkatesh S : 'All fibre-optic microresonator sensor system', presented in Sensors and Their Applications-S+AIV, University of Kent, 25-27 September 1989.

57. Fatah R M A and Stokes N A D: 'All fibre-optic microresonator sensor system', New Materials and their Applications 1990 (IOP conference series No. 111, Norfolk, 1990).

58. Hildebrand M and Wolfelschneider: 'Micromechanical structure excited by noise-modulated light via optical fibre', Procs of SPIE Conf: Fibre Optic Sensor III, 1988, pp 95-100.

59. Zhang L M, Uttamchandani D and Culshaw B: 'Transit excitation of silicon microresonator', Electron Lett, Vol 25, No 2, 1987, pp 149-150.

60. Adams M J, Steventon A G, Devlin W T J and Henning I D:' Semiconductor lasers for long-wavelength optical-fibre communication systems', (Peter Peregrinus Ltd, 1987).

CHAPTER TWO

Device Fabrication: Silicon and silicon dioxide

2.1. Introduction

This chapter describes the principles involved in the fabrication of silicon devices and silicon dioxide devices and some of the properties of these materials.

Silicon technology has passed through three phases. The first was mass production of integrated circuits. This technology has found applications in everyday electronic equipment from children's toys to space-craft. The second phase was the development of micromechanical devices fabricated on silicon wafers. It was realised that silicon is not just suitable as an electronic material but has suitable properties for mechanical devices. Furthermore, unlike some other materials silicon can be mass produced by chemical etching. Chemical etching made it possible to fabricate three-dimensional devices such as beams, diaphragms, needles, grooves, holes and any combination of these. Although microfabrication of silicon was born from integrated circuit silicon technology, these two technologies soon integrated and led to an integrated micromechanical technology. One of the applications of the latter was integrated sensor technology and micromechanical electrical components such as micromechanical switches and light modulators. The integrated sensor technology improved sensors by fabricating mechanical devices which were sensitive to some parameter in question with all the necessary electronics on the same silicon wafer.

The third phase of silicon technology is optomechanical technology which interacted with laser and optical fibre technology in two ways. Firstly, microdevices were developed using microfabrication which required very little power (μW) to activate. This in turn led to the development of sensor heads with no electronics involved in them. Secondly, microfabrication provided precision mounting for active and passive optical components such as lasers and optical fibres. One example is microgrooves for aligning fibres to the active region of lasers to improve coupling efficiency. Another example is the fabrication of several grooves together to accommodate a fibre array for WDM systems.

Silicon has a diamond crystal structure, i.e. face centre cubic. Silicon can be oxidised when it is exposed to steam and forms a layer of silicon oxide. Silicon dioxide is electrically insulating and has some novel chemical properties. The oxide layer protects areas of the wafer during fabrication of electronic devices. This property of silicon dioxide has been exploited to form three-dimensional devices on silicon wafers simply by etching the silicon underneath and allowing the oxide part to remain intact. Table 2.1 compares properties of silicon to its oxide and stainless steel. It can be noted that silicon has a Young's modulus comparable to that of stainless steel and a higher yield strength. Properties of silicon dioxide will be discussed in some detail in chapter 4.

Table 2.1: Properties of silicon and silicon dioxide compared with stainless steel:

Parameters	Silicon	Silicon dioxide	Stainless steel
Yield Strength ($x10^5$ Ncm^{-2})	7.0	8.4	2.1
Knoop Hardness ($kgmm^{-2}$)	850	820	660
Young's Modulus ($x10^3$ Nm^{-2})	1.9	0.73	2.0
Thermal conductivity($Wcm^{-1}K^{-1}$)	2.3	2.5	7.9
Thermal expansion($10^{-6}K^{-1}$)	2.33	0.55	17.3

2.2 Fabrication techniques

2.2.1 Photolithographic patterning:

Microfabrication of silicon began with transferring copies of a photographically reduced pattern on to a wafer surface. This is called photolithography. The process involves the use of a glass plate or mask on to which a pattern has been printed in metal opaque to ultraviolet radiation. A thin layer of photoresist (which is an organic polymer) is deposited on the surface of the wafer which the devices are to be fabricated on. The mask is kept in contact with the coated surface of the wafer. This process is called surface contact photolithography. The wafer surface is exposed to ultraviolet radiation. The ultraviolet radiation reacts with the exposed areas of the photoresist through the mask. The irradiated wafer is rinsed in a developing solution which removes the more soluble areas. The remaining photoresist is hard-baked and acts as a protecting mask for etching the substrate. To form a three-dimensional structure from a wafer pattern in this way the silicon substrate must be etched in a well-controlled manner. The principal shaping methods which have been explored are high-density doping followed by anisotropic etching; and growth or deposition of another material on to the wafer followed by anisotropic etching.

2.2.2 High-density doping:

High-density doping involves infusing areas of the wafer with a high level of impurity atoms. At high doping levels (about 10^{20} atoms cm^{-3}) the solubility of silicon in certain etch solutions is reduced [1,2]. For example silicon doped with boron (p-type) at concentrations of about $5x10^{19}$ cm^{-3} is insoluble in an ethylene diamine/pyrocatechol/water etch [1,3].

This allows three-dimensional devices such as cantilevers and micro bridges to be fabricated since by using high-doping the etch may be stopped. A common fabrication method involves the definition of the areas to be doped by selective photoresist masking, as is shown in Fig 2.1. Table 2.2 summarises a number of wet silicon etches [4].

It should be pointed out that devices fabricated by this method are under stress. Silicon beams doped with boron are under tensile stress owing to the replacement of the silicon atoms by smaller boron atoms in the lattice structure [5,6]. This will be discussed in some detail in Section 4.5.

2.2.3 Anisotropic etching:

Anisotropic etching can be used to form structures of highly doped silicon, or of another material grown on or deposited on to the silicon surface such as silicon dioxide or silicon nitride.

The principle of anisotropic etching is as follows. In certain etchant solutions the different crystallographic planes of single crystal silicon etch significantly different rates. The positions of some of these planes relative to the cubic crystal structure of the silicon is shown in Fig 2.2.

Anisotropic etchant attacks the silicon in the <100> and <110> directions at considerable etch rates, but attacks in the <111> direction at a rate typically about 50 times slower [15]. The available geometries are generally obtained by etching either (100) or (110) oriented crystals through a masking window.

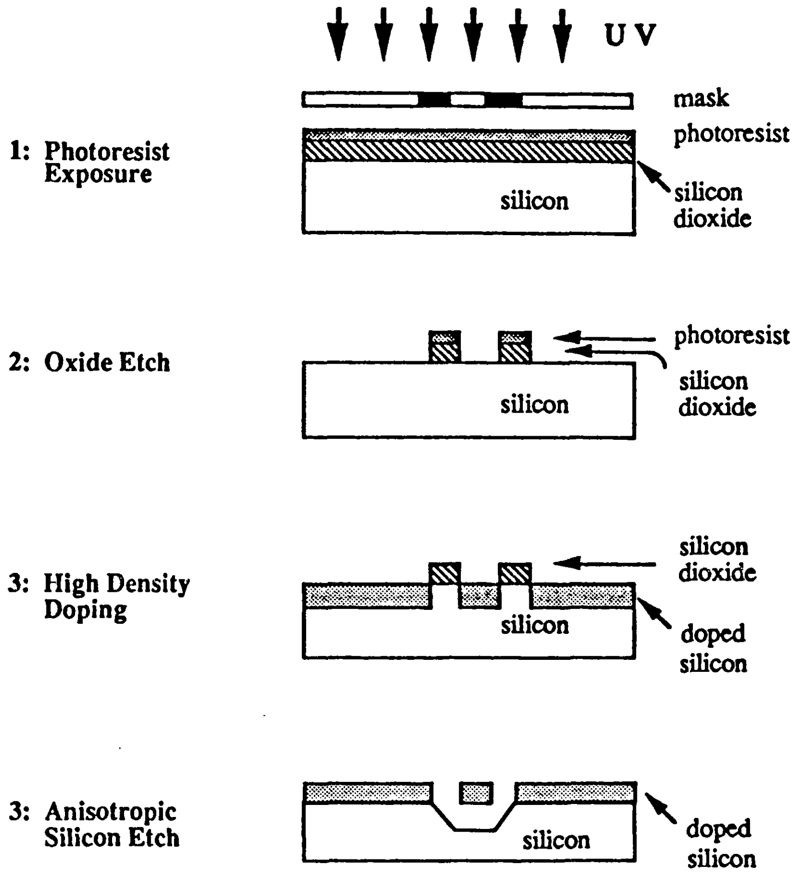

Fig 2.1: Fabrication of silicon structure using photolithography, high-density doping and anisotropic etching.

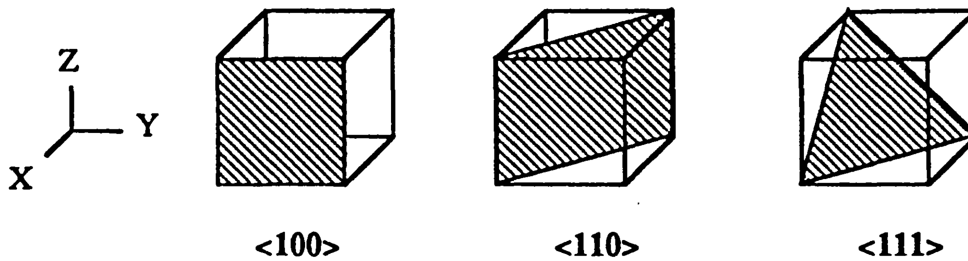

Fig 2.2: Examples of lower index planes.

Table 2.2: A number of wet silicon etches and their properties [4].

Etchant (Diluent)	Typical compo-- sitions	Temp °C	Etch Rate (µm/min)	Anisotropic (100)/(111) Etch rate ratio	Dopant Dependence	Masking films (Etch rate of mask)
HF HNO3 water, CH3COOH)	10ml 30ml 80ml	22	0.7-3.0	1:1	$\leq 10^{17} cm^{-3}$ n or p reduces etch rate by about 150	SiO_2(300Å/min)
	25ml 50ml 25ml	22	40	1:1	no dependence	Si_3N_4
Ethylene diamine Pyrocatecho (water)	750ml 120gm 100ml	115	0.75	35:1	$\geq 17x0^{19} cm^{-3}$ boron reduces etch rate by about 50	SiO_2(2Å/min) Si_3N_4(1Å/min) Au,Cr,Ag,Cu,Ta
	750ml 120gm 240ml	115	1.25	35:1		
KOH (water, isopropyl)	750ml 120gm 100ml	115	0.75	35:1	$\geq 17x10^{19} cm^{-3}$ boron reduces etch rate by about 50	SiO_2(2Å/min) Si_3N_4(1Å/min) Au,Cr,Ag,Cu,Ta
	750ml 120gm 240ml	115	1.25	35:1		
KOH (water, isopropyl)	44gm 100ml	85	1.4	400:1	$\geq 10^{20} cm^{-3}$ boron reduces etch rate by about 20	Si_3N_4 SiO_2(14Å/min)
	50gm 100ml	50	1.0	400:1		
N_2H_4 50gm (water, isopropyl)	100ml 100ml	100	2.0	—	no dependence	SiO_2 Al
NaOh (water)	10gm 100ml	65	0.25-1.0	—	$\geq 17x10^{19} cm^{-3}$ boron reduces etch rate by by about 10	Si_3N_4 SiO_2(7Å/min)

2.2.4 Silicon dioxide devices:

Silicon dioxide beams can be formed from oxidised (100) silicon wafers by a combination of photolithographic patterning and anisotropic etching as shown in Fig 2.3. A silicon dioxide film on silicon wafers can be grown by exposing the wafer at high temperature (900-1200°C) to oxygen. In order to produce undercut oxide beams, the sidewalls of the rectangular etch pit are aligned parallel to the (111) planes of the (100) silicon wafer, so that the (111) planes will define the angular sidewalls of an anisotropic etched cavity. The beam sides are aligned at 45° to this direction so that undercutting of the beam can take place.

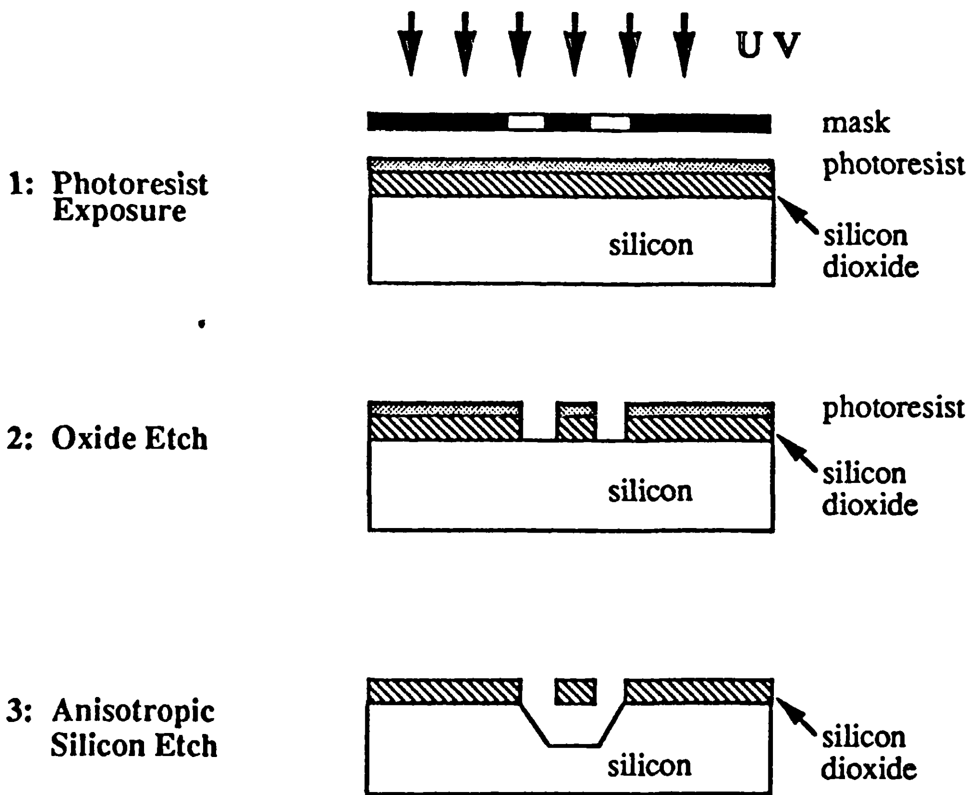

Fig 2.3: Fabrication of silicon dioxide devices.

2.3 Conclusions

A variety of devices have been fabricated using silicon microfabrication technology. This covers a wide range of devices, among them the following:

1 . Mechanical devices such as cantilevers, microbridges, diaphragms and more complicated structures. These devices have application in sensing, accelerometers, modulates and switches [8-10] as described in chapter 1.

2 . Grooves and miniature optical tables have been used for procession alignment of optical fibres to passive and active optical components [4].

3 . Matrices of microlenses have been fabricated on silicon dioxide wafers and found applications in, for example, wave division multiplexing.

Most of these devices have found applications in production.

4.4 References

1 . Greenwood J C: 'Ethylene diamine-catechol-water mixture shows preferential etching of p-n junction', J Electrochem Soc, Vol 116, 1969, pp 1325-1326.

2 . Dalik et al: 'Ellipsometric studies in heavily doped silicon', J Electrochem Soc, Vol 132, 1985, pp 135-141.

3 . Bogh A: 'Ethylene diamine-pyrocatechol-water mixture shows etching anomaly in boron doped silicon', J Electrochem Soc, Vol 118, 1971, pp 401-402.

4 . Petersen K: 'Silicon as a mechanical material', Procs of IEEE, Vol 70, No, 5, May 1982, p 420-457.

5 . Fatah R M A , Stokes N A D and Venkatesh S: 'Activation of silicon micromechanical resonators in fibre optic systems', Procs of EFCO 89, Amsterdam, June 1989, pp 418-422.

6 . Fatah R M A and Stokes N A D: 'Optical activation of silicon micromechanical Resonators: End-conditions', Procs of Frontiers in electro optics, UK, March 1990, pp 118-125.

7 . Buser R A and dr Rooij N F: 'Silicon micromachining and OFC', Procs EFCO/LAN 88, Amsterdam, July 1988, pp 223-226.

8. Gieles A C M and Somers G H J: 'Miniature transducers with a silicon diaphragm', Philips Tech Rev Vol 33, No 1, 1973, pp 14-20.

9 . Clarck K S and Wise K D: 'Pressure sensitivity in anisotropically etched thin-diaphragm pressure sensor', IEEE Trans on Electron Devices, Vol ED26, No 12, Dec 1979.

10. Seidel H and Csepregi L: 'Design optimization for cantilever-type accelerometer', Sensors and Actuators, Vol 6, 1984, pp 81-92.

CHAPTER THREE

Optical Activation and Detection of Micromechanical Resonator Sensors: Theoretical analysis

3.1. Introduction

Micromechanical resonator beams can be used as sensor heads in sensor systems. They measure any parameter that interacts with their resonant frequency such as chemical concentrations, viscosity, density, strain, force, mass flow, acceleration, pressure and temperature. The physical parameters that determine the resonant frequency can be found from the equations of resonance. These parameters are Young's modulus, density, geometry and end-conditions of the beam. Potentially these devices could be used as optical components such as wave guides, modulators, switches and optical filters.

There has been considerable interest in the optical activation and detection of this new class of device. However, there is no current theoretical analysis to identify the mechanisms by which these devices are activated. In this chapter we shall use a one-dimensional analysis to identify the mechanisms of optical activation. The detection system, the effect of the metal coating on the resonant frequency and resonant frequency modes will be analysed.

A resonant structure sustained at resonance produces a stable output for two reasons. Firstly, a resonator at resonance requires enough power to recover its losses which is only

a few nanowatts for the structure described here. Secondly, the resonant frequency is determined by the dimensions and mechanical properties of the beam resonator and not by the activation and detection sources. In this device an optical input is converted into mechanical vibration which is then converted into an optical output again ready to be interfaced with digital signal processing.

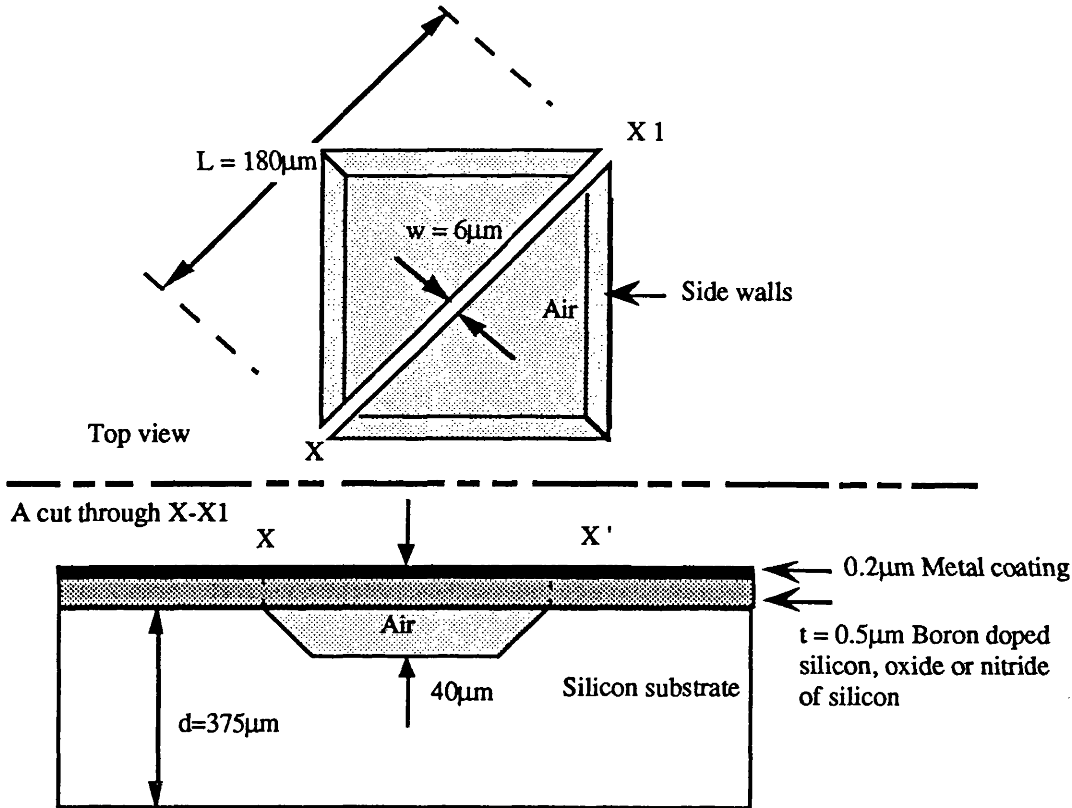

Fig 3.1: Schematic diagram of a microresonator.

3.2. Optical fibre system

The microresonator strips used in this experimental work are typically 0.5μm thick, 5μm wide, and 180μm long. This type of device is shown in Fig 3.1 and has a mass of approximately one nanogram. The all-optical fibre system used for this purpose is shown in Fig 3.2 [1] and the bulk optic system is shown Fig 1.19 [2]. These devices were driven into mechanical resonant vibration by use of an intensity-modulated laser source. The

mechanical vibration was monitored by a cw laser at a different wavelength. Both laser beams were guided through the same monomode optical-fibre network and directed on to the resonator beam surface. At the output the activation wavelength is filtered out so that the detector only sees the detection beam which is carrying the information about the resonator. The resonator beam modulates the cw detection beam. The optical power used for activation was about 200μW, which is the same amount of power used for detection. This is the power delivered to the metal coating of the device and not the amount absorbed in the device.

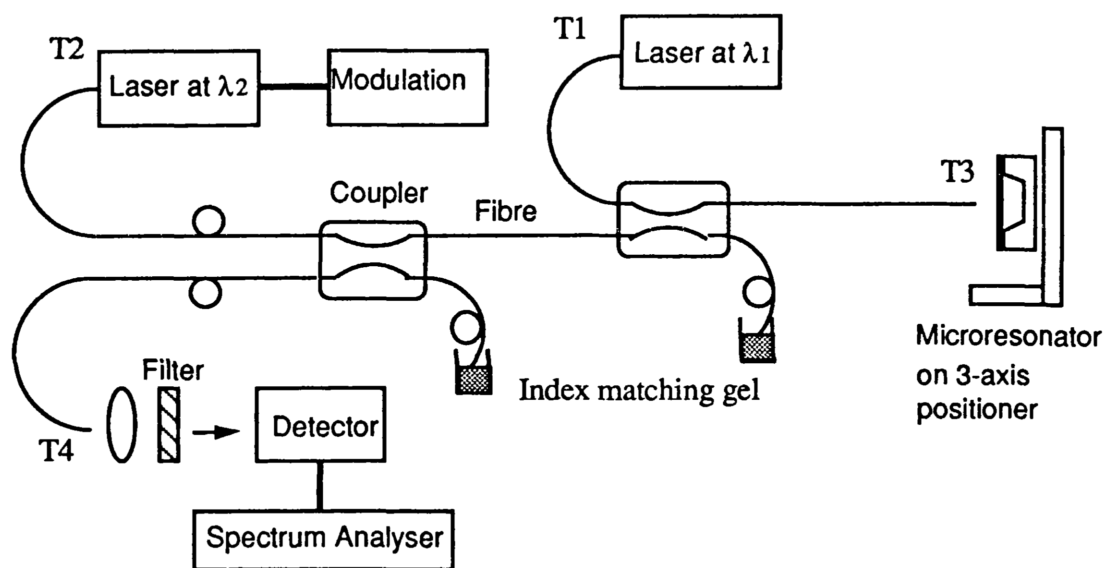

Fig 3.2: Optical fibre system.

3.3. Mechanisms of optical activation of micromechanical resonators

When an intensity modulated optical beam is directed on to the metal coated surface of a resonator strip, some of the optical energy is absorbed, causing localised periodic heating, which can result in periodic expansion and contraction of the structure, leading in turn to flexural vibrations. So optical energy is transformed into mechanical energy via an

intermediate thermal stage as shown in Fig 3.3. Thus, three physical mechanisms are involved in the activation [3]:

Mechanism 1: The absorption of light in the resonator material, which in most cases is by the metal coating, is dictated by its absorption coefficient and the rate at which the laser beam is modulated. The material and geometry of the resonator determine its mechanical resonant frequency and this in turn governs the modulation frequency of the laser. The absorption coefficient χ (m^{-1}) of a metal can be calculated from the optical frequency of the activated laser beam and the imaginary part K of the index of refraction, which is called extinction coefficient or the absorption index.

$$\chi = \frac{4\pi}{\lambda} K \qquad (3.1)$$

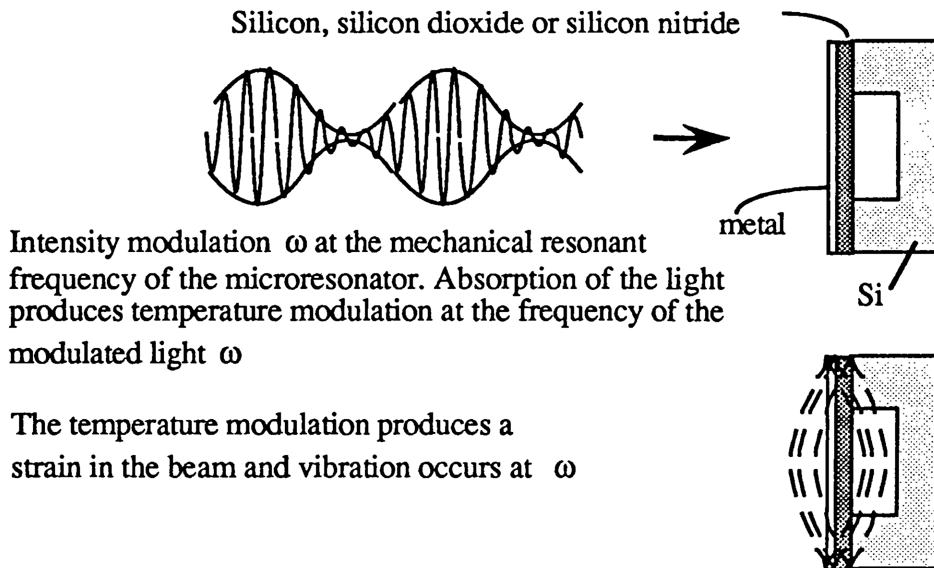

Fig 3.3: The mechanisms of optical activation of micromechanical resonators. Optical energy is transformed into mechanical energy via an intermediate thermal stage.

Where λ is the wavelength of light in the medium. The energy density falls to 1/e of its value after the wave has advanced a distance δ_{op} (the optical penetration depth) where:

$$\delta_{op} = \frac{1}{\chi} = \frac{\lambda}{4\pi K} \qquad (3.2)$$

This quantity is usually a small fraction of the wavelength. For instance, bulk aluminium illuminated with light at a wavelength of 589nm, has an optical penetration depth of approximately 10nm which is under 6% of the wavelength. So, the devices are optically thick, that is, the optical penetration depth δ_{op} is much smaller than the thickness of the metal.

Mechanism 2: The generation and propagation of thermal waves, which occurs as a result of the light absorbed in Mechanism 1. This is limited by its resonant frequency and-the properties of the resonator material(s). These waves penetrate only in the range of the thermal diffusion length of the resonator material(s). The thermal diffusion length is given by:

$$\mu = \left(\frac{2\kappa}{\rho\omega c}\right)^{\frac{1}{2}} \qquad (3.3)$$

where κ is the thermal conductivity, c is the specific heat capacity and ρ is the density.

Consider Fig 3.4 which shows that the thickness of the micromechanical resonators, usually up to a few μm, is within the thermal diffusion length, at their resonant frequency range which is typically 100kHz. At this frequency, the thermal diffusion lengths for silicon dioxide, silicon, aluminium and gold are 0.65, 17, 17 and 19.5μm, respectively. So beam resonators made of these materials, with a typical thickness of about 1μm, are assumed to be thermally thin.

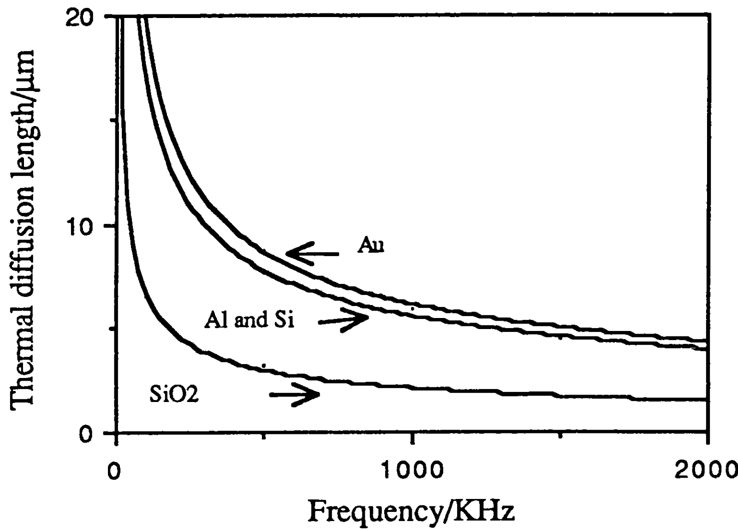

Fig 3.4: The thermal diffusion length for common micromechanical resonator materials, silicon, silicon dioxide, aluminium and gold, as a function of the resonant frequency. It should be noted that the thermal diffusion length of silicon dioxide is multiplied by 0.1.

Since the beam is thermally thin the temperature across the beam thickness is taken to be uniform. The only temperature gradient present is along the length of the resonator beam and not across its thickness. If the activation beam is in the middle of the beam, we get the same temperature gradient in both of its halves (Fig 3.5).

Mechanism 3: The generation and propagation of elastic waves as a result of the temperature increase from Mechanisms 1 and 2 is dominated by the material structure and the geometry of the beam resonator.

Let us assume a sinusoidal intensity modulated monochromatic light source incident on the metal surface with intensity:

$$I = \frac{1}{2} I_o (1 + \cos \omega t) \qquad (3.4)$$

where I_o is the incident light flux (W m^{-2}) and ω is the angular frequency modulation at which the light beam is modulated.

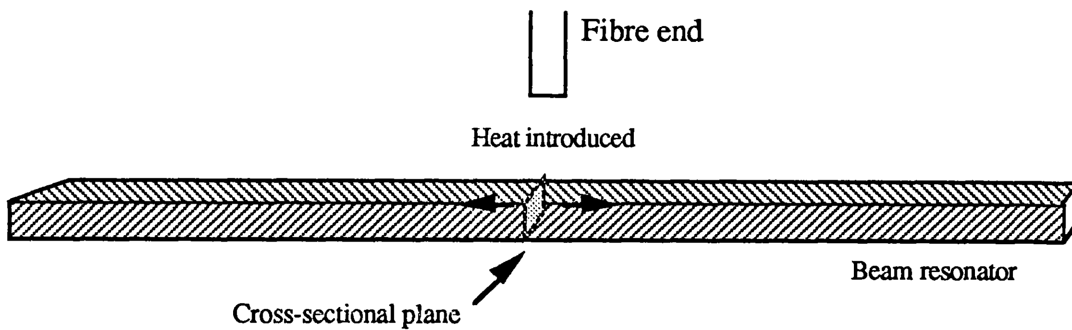

Fig 3.5: The heat introduced to the middle of the resonator via the optical power distributes towards the ends of the resonator.

The one-dimensional heat-flow equation for the complex temperature Φ distribution along the beam can be written in the form [4]:

$$\frac{\partial^2 \Phi}{\partial x^2} - \frac{1}{\alpha_{th}} \frac{\partial \Phi}{\partial t} = 0 \qquad (3.5)$$

where the thermal diffusivity of the beam α_{th} is given by:

$$\alpha_{th} = \frac{\kappa}{\rho c} \qquad (3.6)$$

Equation 3.5 has a complex solution. The real-part represents the time-dependent component of the temperature field along the beam relative to the ambient temperature. So the temperature along both halves of the beam resonator can be written as [5]:

$$T(x,t) = \text{Re}[\,T(x,t)\,] + \Phi_a \qquad (3.7)$$

where "Re" denotes the "real part" and Φ_a is the ambient temperature. The time-dependent temperature along both halves is given by [4]:

$$T(x,t) = \frac{\mu I_o}{4\kappa} e^{-\frac{x}{\mu}} \left[\cos\left(\omega t - \frac{x}{\mu}\right) + \sin\left(\omega t - \frac{x}{\mu}\right) \right] \qquad (3.8)$$

We may describe the propagation of the temperature along the beam as a thermal wave, and we may note the following points:

i) The temperature of the thermal wave decreases exponentially in the medium, with a rate dictated by the thermal diffusion length μ.

ii) The phase velocity of the propagation of the thermal wave which is given by:

$$v = \omega\mu = \left[\frac{2\kappa\omega}{\rho c}\right]^{\frac{1}{2}} \qquad (3.9)$$

is highly dispersive, since it is proportional to the square root of the modulation frequency.

The expansion δx in the beam along its length is given by:

$$\delta x = \alpha \int_0^\infty T(x,t)\,dx \qquad (3.10)$$

where α is the coefficient of linear expansion, and leads to the result:

$$\delta x = \frac{\alpha I_o}{2\omega\rho c} \sin(\omega t) \qquad (3.11)$$

It should be noted that the expansion of the resonator is in quadrature with the input optical power, which we have observed experimentally.

Equation (3.11) represents the expansion of the beam off resonance. However, the beam expansion is maximised when the optical frequency of the modulation ω_{op} is equal to one of the 'natural' frequencies ω_{mech} of the strip, as resonance occurs, that is:

$$\omega_{op} = \omega_{mech} = \omega = 2\pi f_o \qquad (3.12)$$

where f_o is the mechanical resonant frequency. This is because at resonance, there is a gain factor which is equal to the quality-factor of the resonator. So the displacement equation should be multiplied by the quality-factor Q of the resonator to get the amplitude of the expansion at resonance X, thus:

$$X = Q\,\delta x = \Delta L \sin(\omega t) \qquad (3.13)$$

We note that so far we have been calculating the displacement of the beam along its length, i.e. its expansion. Therefore, the expansion and contraction of the resonator beam takes a sinusoidal shape given by (3.13) and its amplitude ΔL is given by:

$$\Delta L = \frac{\Omega Q I_o}{2\omega} \qquad (3.14)$$

where Ω characteristic of the material property measured in m^3 s W^{-1} is given by:

$$\Omega = \frac{\alpha}{\rho c} \qquad (3.15)$$

The geometry of the beam manifests itself in the above equations through the resonant frequency. Typical values of Ω for common resonator materials are in Table 3.1.

Table 3.1: Typical values of Ω for common resonator materials

Materials	Ω/m^3 s W^{-1}
silicon	13.2×10^{-13}
silicon dioxide	2.5×10^{-13}
aluminium	98.6×10^{-13}
gold	55.9×10^{-13}
chromium	28.9×10^{-13}

It can be concluded from the table that aluminium coated devices have the highest amplitude of vibrations since the linear expansivity of aluminium (24×10^{-6} $^oC^{-1}$) is higher than that of gold (14×10^{-6} $^oC^{-1}$) and chromium (8.5×10^{-6} $^oC^{-1}$). Silicon beams also have a higher amplitude of resonance than silicon dioxide. This is a result of silicon having a linear expansivity of (2.4×10^{-6} $^oC^{-1}$) whereas silicon dioxide is a good thermal insulator with a linear expansivity of (0.4×10^{-6} $^oC^{-1}$).

However, silicon dioxide is still a reliable material for microresonators but ideally it has to be used as a composite structure probably with silicon and/or a metal. Because silicon dioxide is a good thermal insulator, it establishes a higher temperature gradient along the

beam, and temperature gradient is the origin of the optical activation. A good thermal conductor such as aluminium has a temperature rise of about 1°C for each milliwatt of optical power absorbed, whereas the corresponding temperature rise for silicon dioxide is 190 °C [6]. This high temperature gradient suggests that even thicker devices than those characterised here can be activated.

We can calculate the absorbed light from the incident beam by assuming that only 5% of the incident light is absorbed in the metal coating. The incident optical power is typically about 200μW and the area over which light absorption occurs is approximately equal to the cross-sectional area of a typical optical fibre core. So 10μW of optical power is absorbed over a cross-sectional area of the beam i.e. wt = $3\mu m^2$, where w (6μm) and t (0.5μm) are the width and the thickness of the beam resonator. This gives a value for the light intensity of about 3.3×10^6 Wm^{-2}. It should be noted that here we have assumed that the light is absorbed in the middle of the resonator and propagates along the suspended ends of the beam (Fig 3.5). Therefore any temperature gradient across the thickness of the beam or across its width has been neglected assuming that the beam is as wide as the beam spot and is thermally thin as discussed above. The optical power absorbed in the resonator beam induces stress/strain in it. The strain ε_{op} and stress σ_{op} respectively can be defined as:

$$\varepsilon_{op} = \frac{\Delta L}{L} \qquad (3.16)$$

$$\sigma_{op} = \varepsilon_{op} E \qquad (3.17)$$

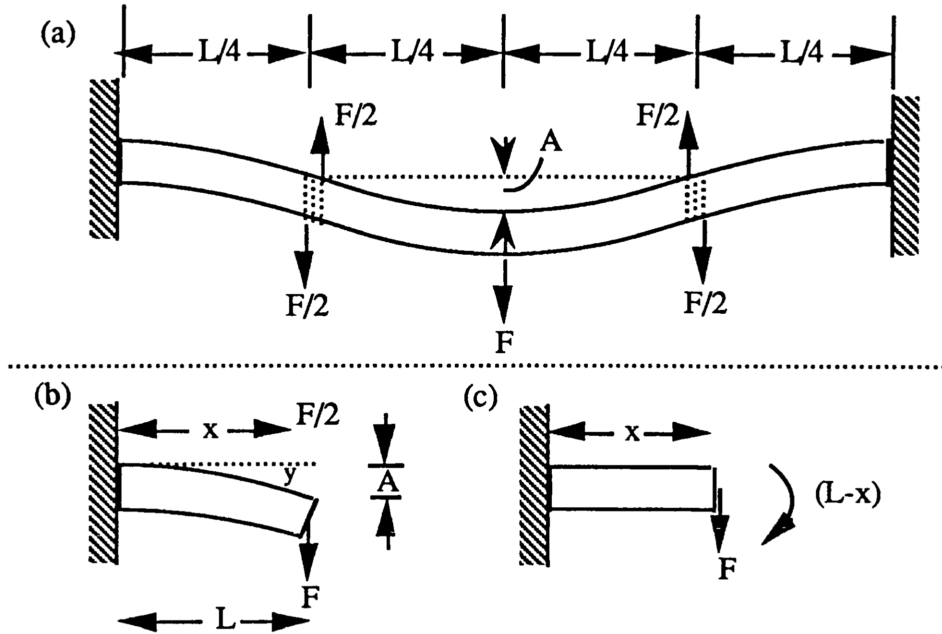

Fig 3.6: The beam (a) can be regarded as four-quarter-length beams each like that shown in Figs b and c loaded at one end and held horizontally at the other. The points of inflexion occur half-way between the ends and the centre. Fig b shows the deformation of a cantilever by an end load [7].

The bending force of a beam with both ends clamped (section 5) is given by [7]:

$$F = 192\frac{A\,(E\,I)}{L^3} \qquad (3.18)$$

where A is the amplitude of the deflection. So the bending force depends on the beam's flexural rigidity EI, where I is the second moment of area and E is Young's modulus, and also depends on the length of the beam L. Therefore the bending force of the beam is inversely proportional to the cube of the length and directly proportional to the flexural rigidity of the beam.

Considering the geometry of the device of Fig 3.1 and assuming that the amplitude of resonance is about 50nm [2,8,9], the bending force is 2×10^{-8} N which results in stress of the order 6.6×10^3 Nm^{-2} in the beam. This value of stress is close to the value (5.1×10^3 Nm^{-2}) that can be obtained from (3.14) to (3.17).

3.4. Resonant modes

There are various resonance modes that can be activated. Activation of a mode depends on the geometry, the drive and place of activation. Some modes are straightforward such as transverse vibrations, others such as torsional modes may be more complicated. Once a certain mode of resonance is activated, it is then a matter of increasing the drive frequency to activate the higher modes. A given geometry can be designed to give a certain mode of resonance. Here we should distinguish between resonant modes such as torsional modes and modes in higher modes. The latter implies harmonics of the fundamental resonance while the former implies the resonant type. In theory, any beam can be activated in three modes of resonance, namely:

3.4.1. The resonant frequency of longitudinal vibrations
3.4.2. The resonant frequency of torsional vibrations
3.4.3. The resonant frequency of flexural vibrations

These modes are shown in Fig 3.7 and will be discussed below:

3.4.1. The resonant frequency of longitudinal vibrations:

The cross-section of the beam remains plain and the particles of the cross-section move only in the axial direction of the beam. In Fig 3.7, the length of the longitudinal waves is large in comparison with the cross-sectional dimensions of the bar. In these cases the effect of lateral displacement upon the longitudinal motions can be neglected. The resonant frequency of longitudinal vibration for a beam with one end clamped is given by [10]:

$$f_i=\frac{i}{2L}\sqrt{\frac{E}{\rho}} \qquad (3.19)$$

where i=1, 2, 3, etc gives the resonance mode number.

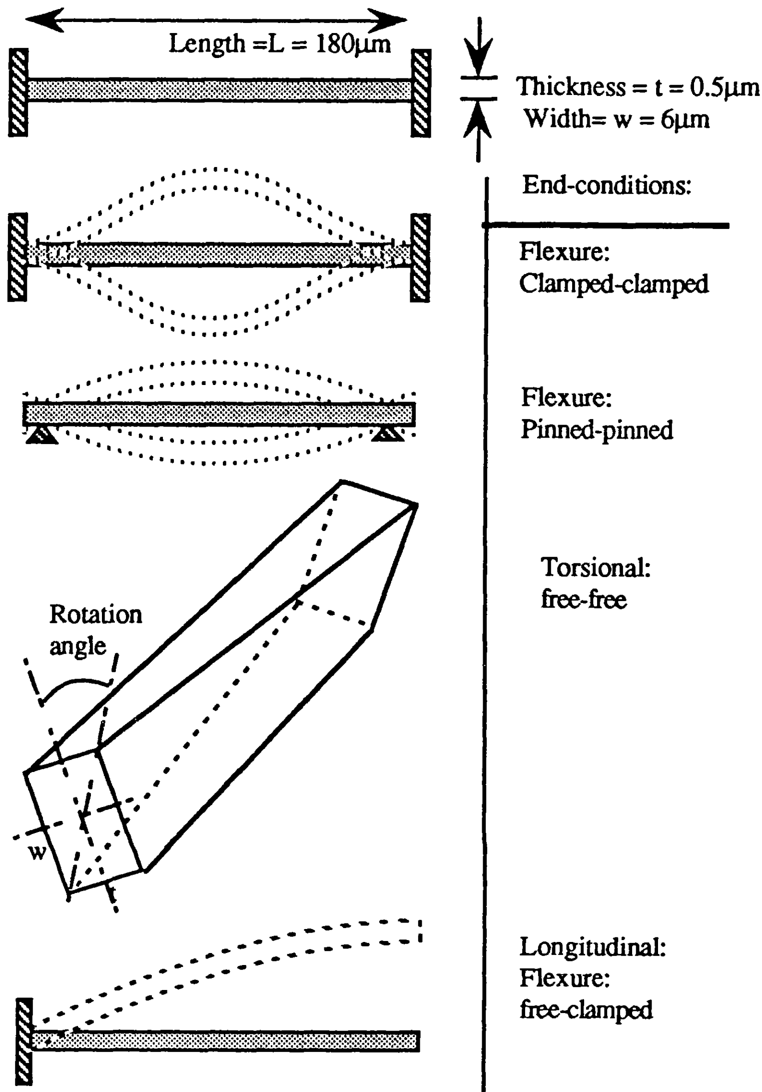

Fig 3.7: Various modes of resonance.

3.4.2. The resonant frequency of torsional vibrations:

Torsional vibration is the twisting of a beam about its own axis. This vibration is usually coupled to the flexural vibrations. For a beam with rectangular cross section the torsional resonance is given by [10]:

$$f_i = \frac{i}{2L}\sqrt{\frac{CG}{\rho I_p}} \qquad (3.20.a)$$

I_p is the polar moment of area and for a rectangular cross-section is given by:

$$I_p = \frac{1}{12(t^3 w + w^3 t)} \qquad (3.20.b)$$

where G is the torsional modulus, t and w are the width and the thickness of the beam, and

$$C = \frac{e\, w^3 t^3}{w^2 + t^2} \qquad (3.20.c)$$

where the shape factor e is determined by the ratio w/t as follows:

w/t:	1	2	4	8	∞
e:	0.281	0.286	0.299	0.312	1/3

Therefore the approximate torsional resonant frequency for the case considered can be given by:

$$f_i \approx \frac{i}{2\pi L} \frac{t}{w} \sqrt{\frac{6E}{1+v}} \sqrt{\frac{E}{\rho}} \qquad (3.20.d)$$

where v is Poisson's ratio.

3.4.3. The resonant frequency of flexural vibrations:

This mode will concern us so we shall study it in some detail.

i) Resonant equation:

The resonant frequencies f_i of flexural vibrations of a homogeneous prismatic beam are given by [10]:

$$f_i = \frac{\lambda_i^2}{2\pi L^2}\left[\frac{EI}{m}\right]^{\frac{1}{2}} \qquad (3.21)$$

where λ_i is a dimensionless parameter which is a function of the boundary conditions applied to the beam, and i is an integer. L and t are the length and the thickness of the beam respectively and m is the mass density of the beam. Resistance of a beam to bending depends upon its flexural rigidity EI, where I is the second moment of inertia and E is Young's modulus. So one of the factors that determine the resonant frequency of microresonators is the end-conditions. Using the appropriate values of I (= $wt^3/12$) and m (= ρtw) in (3.21) we have:

$$f_i = \frac{\lambda_i^2}{4\sqrt{3}\,\pi}\left[\frac{t}{L^2}\right]\left[\frac{E}{\rho}\right]^{\frac{1}{2}} \qquad (3.22)$$

where t, w and ρ are the thickness, the width and the density of the beam. According to (3.22) the resonant frequencies of a beam are determined by three factors. The first of these is the end-conditions, the second is the geometry of the device and the last is the material properties. The resonant frequency does not depend upon the width of the beam. The dependence of the resonant frequency upon the length and the thickness in a three dimensional plot is shown in Fig 3.8 in which clamped end-conditions are assumed.

ii) Resonant mode shape:

When an elastic beam deflects transverse to its own axis y under a force, the overall lattice spacing of the convex side lengthens and the overall lattice spacing on the concave side shortens in proportion to the distance from the neutral surface, as shown in Fig 3.9. The neutral surface which retains its original length passes through the centroid of the cross-section of the beam unless stress is applied axially; therefore the atoms on the convex side

will be under tension. By contrast those on the concave side will be under compression while those on the neutral surface do not experience any stress [7,11]. This is assuming that the deflection of the centre of the beam is small compared with its thickness. Thus the stress on the atomic structure alters between tension and compression as the beam vibrates. The condition is more complicated if the deflection of the centre of the beam is large compared to the beam's thickness.

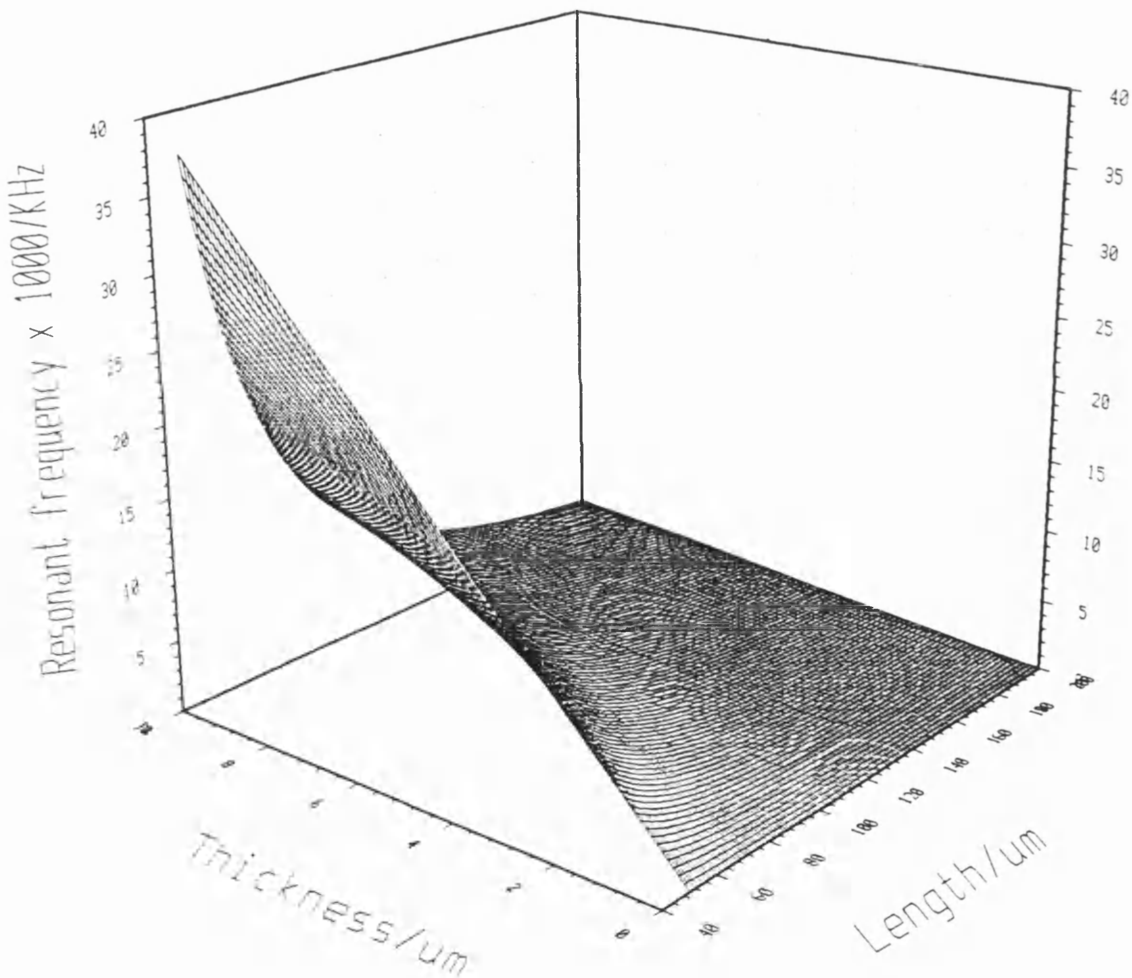

Fig 3.8: The dependence of the resonant frequency upon the length, thickness and the mode number for geometry of the device shown in Fig 3.1.

In the above analysis the effect of the end-conditions has been ignored. However, the end-conditions affect the mode shape and hence the stress states of the beam. The relevant end-conditions in this context are that both ends are either clamped or pinned. The mathematical formulae for these cases is as follows [7,11]:

i) For clamped end-conditions λ_i, the expression for the end-conditions applied and the mode shape are given by:

$$\begin{aligned} \lambda_i &= (i+\frac{1}{2})\pi \\ y &= \frac{\partial y}{\partial x} = 0 \\ y_i &= \cosh(\frac{\lambda_i x}{L}) - \cos(\frac{\lambda_i x}{L}) - \sigma_i \left(\sinh(\frac{\lambda_i x}{L}) - \sin(\frac{\lambda_i x}{L}) \right) \end{aligned} \tag{3.23}$$

where σ_i is a constant with a value of approximately unity.

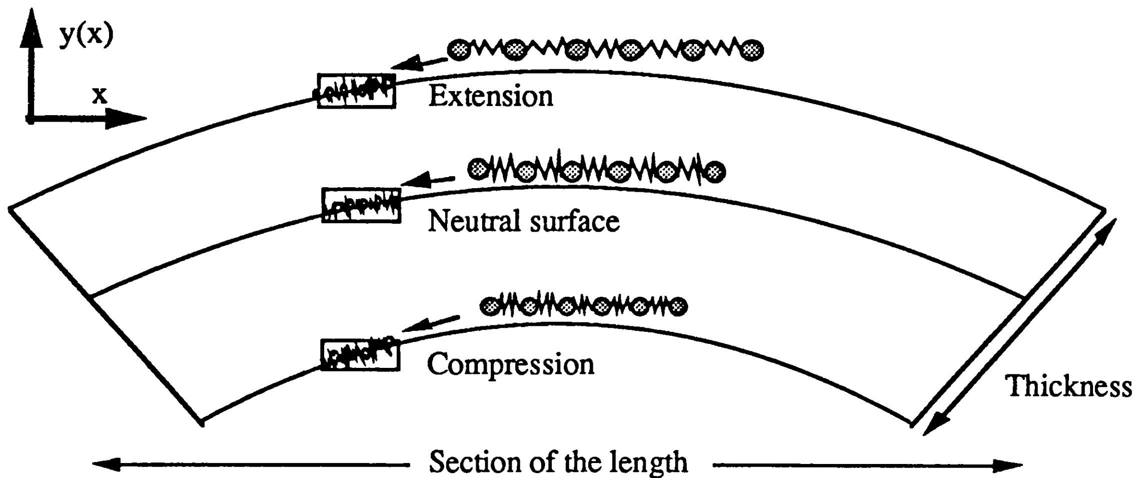

Fig 3.9: The central part of an elastic beam transverse to its own axis.

ii) For pinned end-conditions:

$$\lambda_i = i\pi$$
$$y = \frac{\partial^2 y}{\partial x^2} = 0 \qquad (3.24)$$
$$y_i = \sin(\frac{i\pi x}{L})$$

The fundamental mode shape for each case is shown in Fig 3.10(a) and 3.10(b), respectively. In the clamped end-conditions the tensile and compression stress can be produced in the same side of the beam, while in the pinned end-conditions only one type of stress can exist in each side. The clamped end-condition has always been assumed in designing and modelling these devices since it is suitable for built-in beams. Fig 3.11 shows the mechanical displacement field associated with the deflection of a clamped beam.

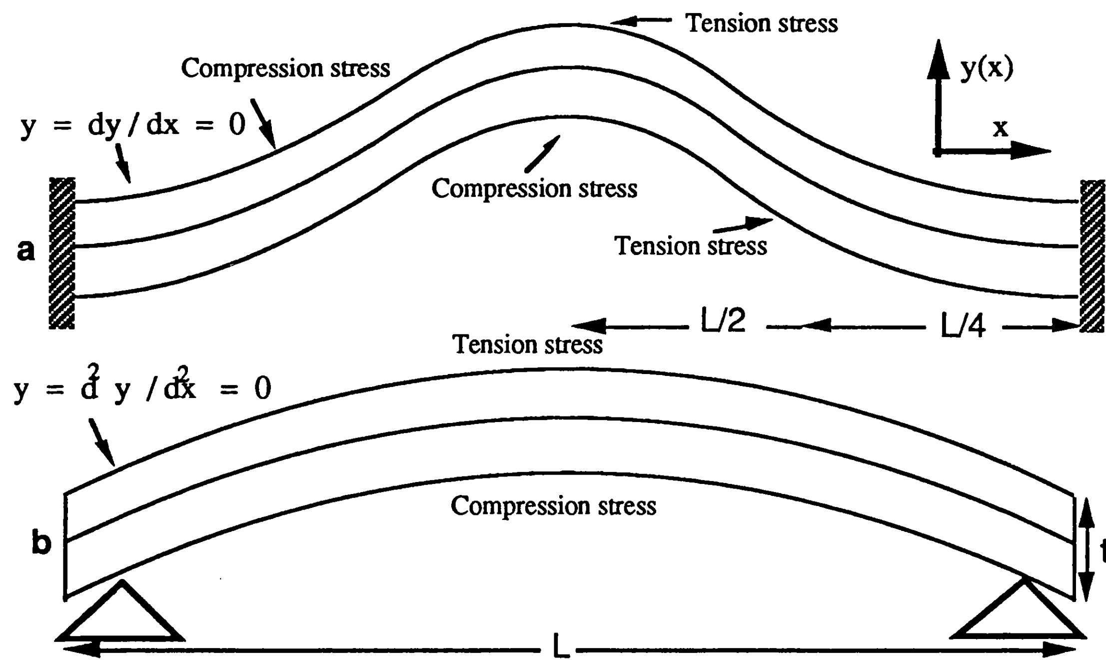

Fig 3.10: A beam with two end conditions: (a) clamped and (b) pinned.

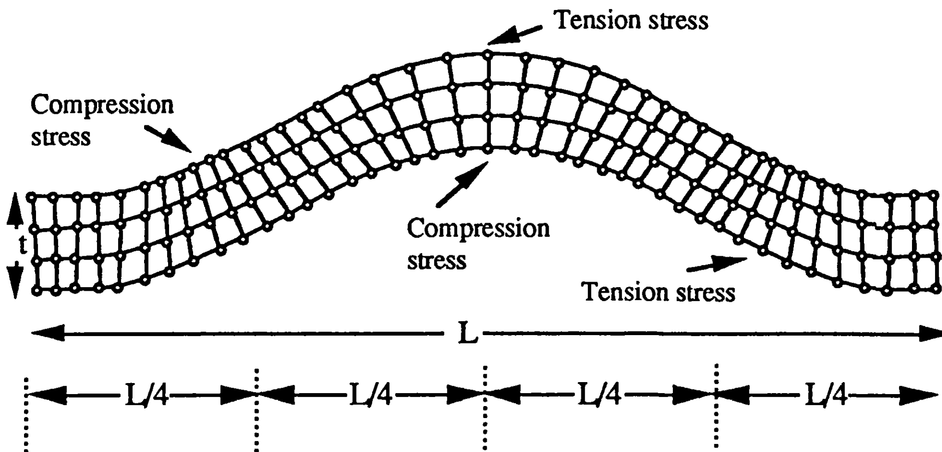

Fig 3.11: A clamped end beam considered as a four-layer thick atom (see Fig 3.6).

3.4.4. Discussion:

The question remains how a certain mode of resonance, for instance torsional, can be activated. Piezoelectrically controlling the resonant mode is rather simple: it has been discussed by Zelenka [12] and can be achieved by arranging the electrodes on the beam. Fig 3.12 is an attempt to establish two principles, firstly that the wider beams are more likely to be activated with torsional modes than the narrow ones; and secondly that the paddle beams are more likely to be activated with torsional modes than the simple beams.

It is simpler to control the modes of vibration electrostatically than optically. For example, the design of Fig 3.13 gives torsional vibrations of a simple beam and Fig 3.14 those for a 'paddle' beam [13]. The difficulty with optical activation arises from the fact that the activation depends on distribution of heat in the beam and not on an attraction force like electrostatic activation.

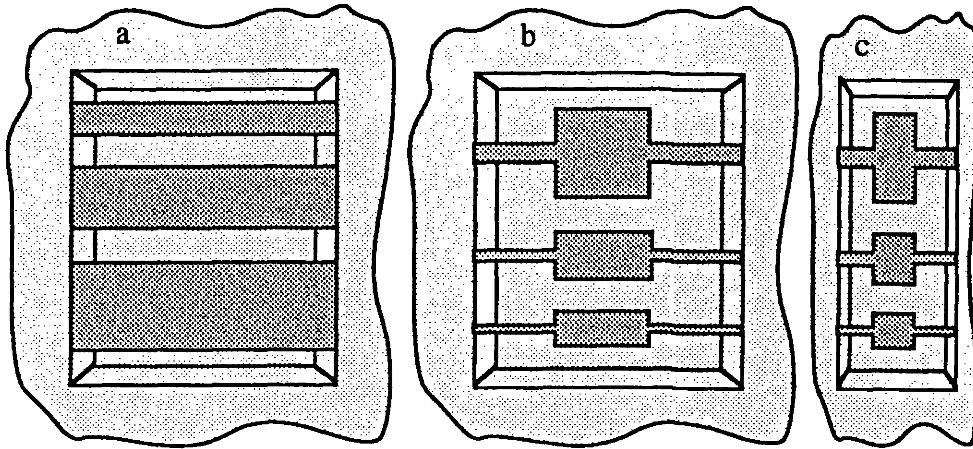

Fig 3.12: Three sets of devices are shown. It is more likely to activate devices shown in (c) to torsional vibration while it is more likely to activate the devices shown in (a) to transverse vibration.

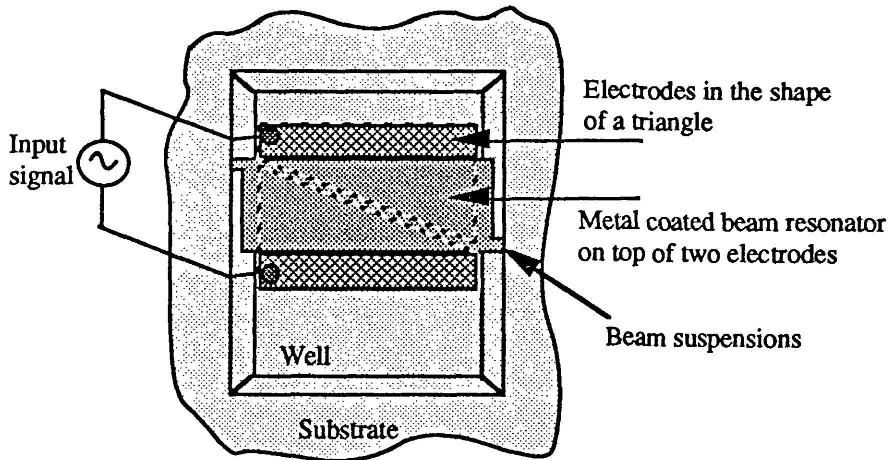

Fig 3.13: Introducing torsional vibration to a beam resonator.

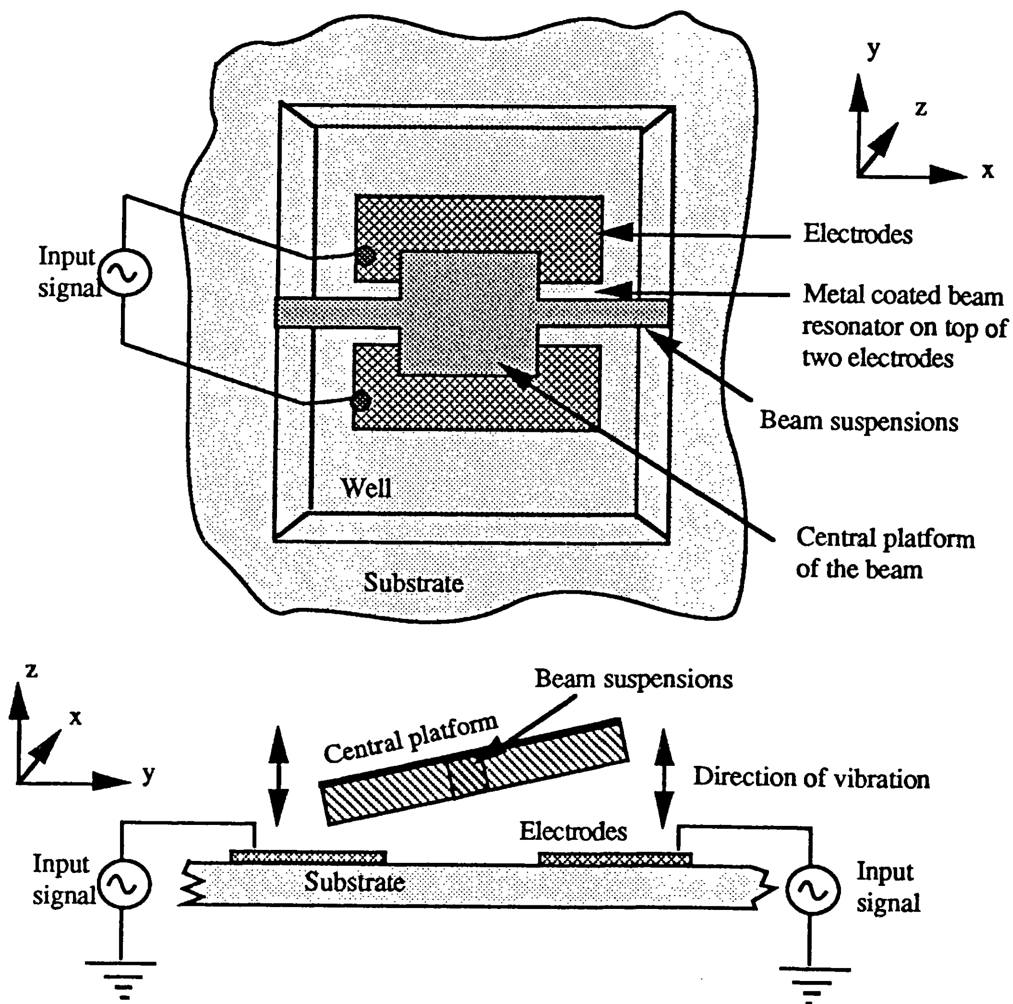

Fig 3.14: Introducing torsional vibration to a paddle beam resonator [13].

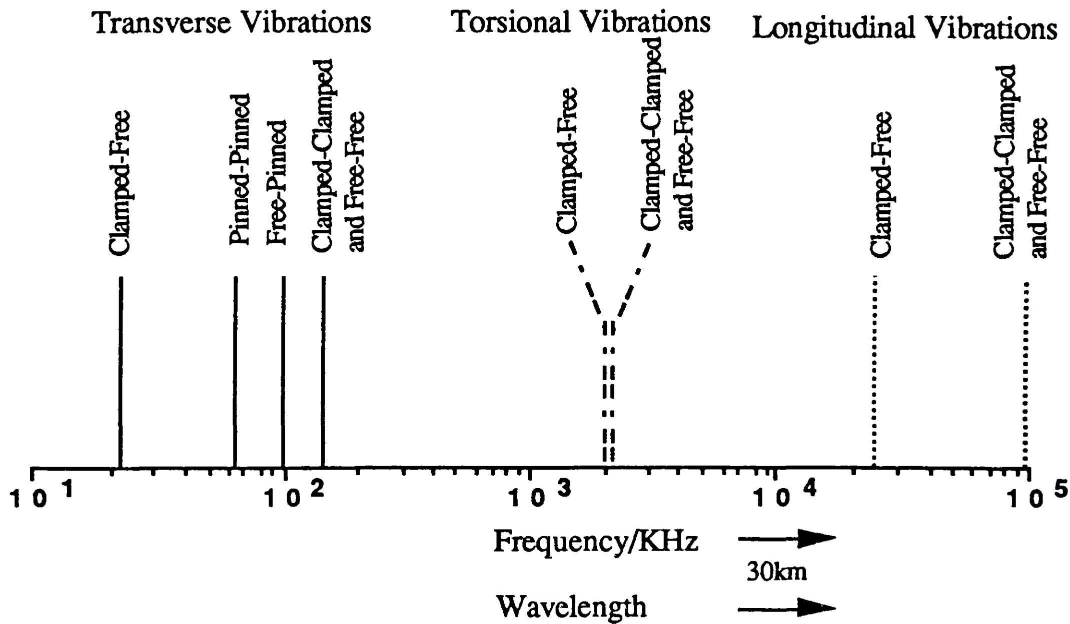

Fig 3.15: The fundamental resonant frequency spectrum of a silicon beam of Fig.3.7.

Nonetheless, any mode of vibration can be activated since the modes are all part of the same frequency spectrum but the only difference between them is that they are separate from each other in the spectrum. So to obtain a mode of vibration the input modulation (optical or electrical) should be equal to the natural frequency of the required resonance mode. However, an appropriate design is needed to enhance the required mode which may be predicted theoretically from the resonant equation. Fig 3.15 shows the resonant frequency of a silicon resonator with dimensions shown in Fig 3.7. It can be deduced that the longitudinal vibration is the highest mechanical resonance.

3.5. Universal resonance response

In this section we discover a universal relationship between the resonant frequency and the ratio of Young's modulus to the density of the materials [14]. Considering (19), for given geometries and end conditions, the resonant frequency only depends on the material property, i.e. (E/ρ). Now if we consider a wide range of materials and plot the resonant frequency against (E/ρ) values, we discover a simple relationship. Fig 3.16 and Fig 3.17 show the dependence of the resonant frequency upon the material properties, namely (E/ρ) value. Fig 3.16 consists of elements whilst Fig 3.17 is of compounds and alloys. It is assumed that the beams have dimensions of 180μm long and 0.5μm thick, and clamped end-conditions are assumed. Some of the elements with their resonant frequency values are shown in the periodic table in Fig 3.18.

Accepting that Fig 3.19 is a universal frequency response we can plot the resonant modes against (E/ρ) values and we have Fig 3.20. Remembering that each mode corresponds to a value of i in (3.22), i.e. 1, 2, 3, 4, and 5.

Three points may be deduced from the graphs:

i) All the resonator materials obey a simple equation which can be given by:

$$f_i = \text{constant}\left(\frac{E}{\rho}\right)^{\frac{1}{2}} \qquad (3.25)$$

The constant is given in (3.22) and can be found from the slope of the line in each of the figures (Figs 3.17, 3.18 and 3.20).

ii) The graph can be used as a master curve to compare and correct the existing or forthcoming experimental (E/ρ) data.

iii) Keeping the geometry constant, it is possible to control the resonant frequency by changing the material. For example silicon beams have higher resonant frequencies than silicon dioxide.

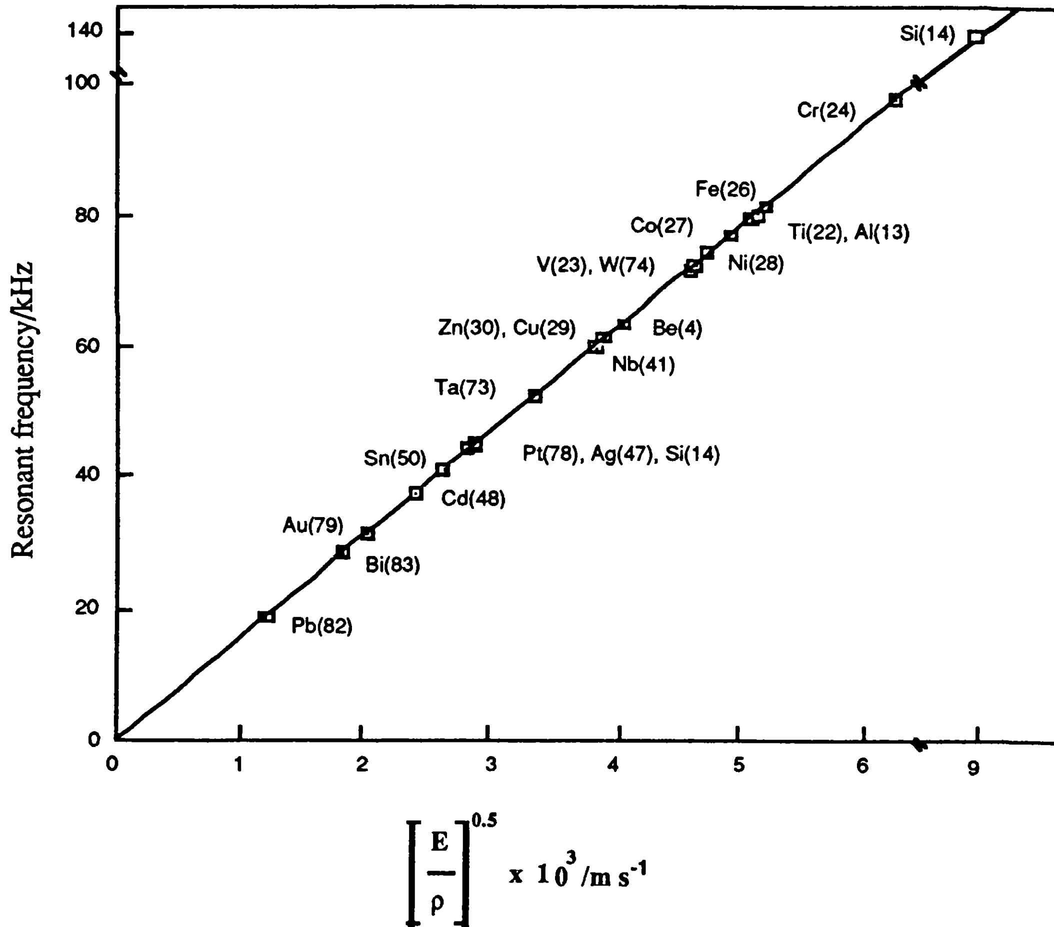

Fig 3.16: The relationship between material properties and resonant frequencies of some of the elements. It is assumed that the beams have dimensions of 180μm long and 0.5μm thick, and clamped end-conditions are assumed.

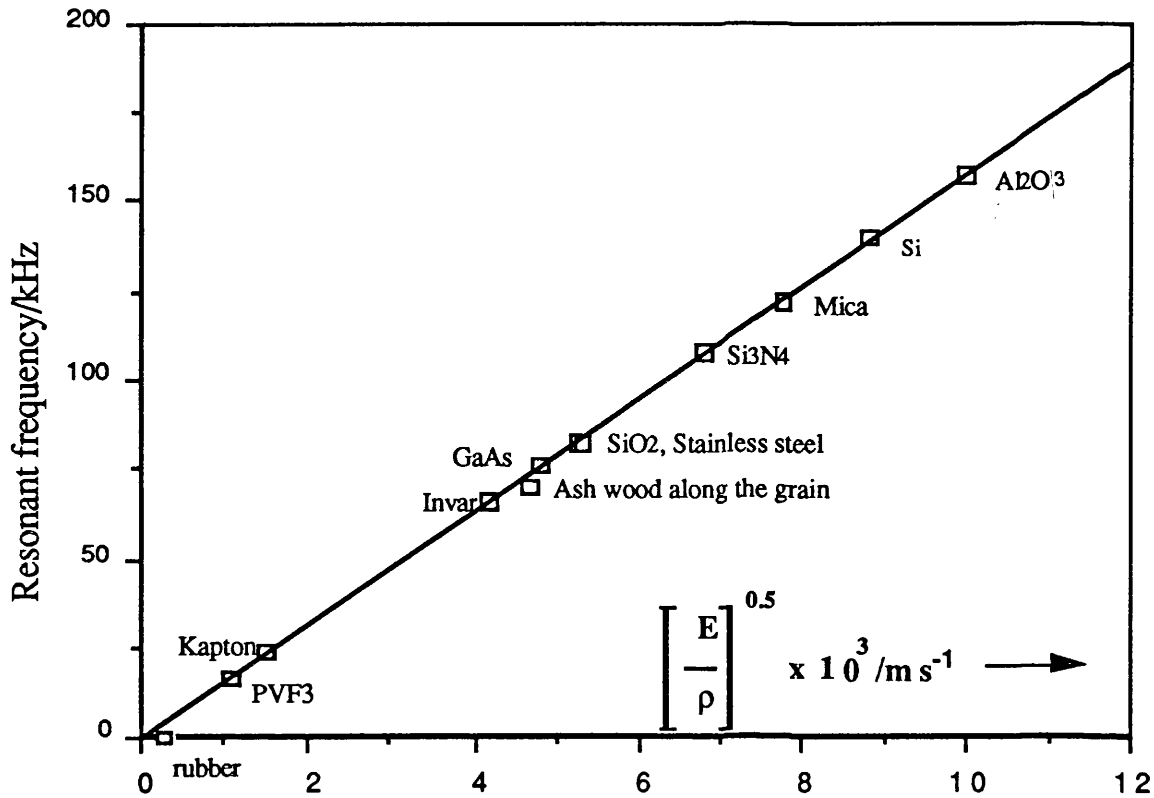

Fig 3.17: The relationship between material properties and resonant frequencies for some alloys and compounds. It is assumed that the beams have dimensions of 180μm long and 0.5μm thick, and clamped end-conditions are assumed.

IIA	IVA	VA	VIA	VIIA	VIII	VIII	VIII	IB	IIB	IIIB	IVB	VB
Be(4) **63.58**												
Mg(12) **79.85**										Al(13) **80.37**	Si(14) **142.2**	
	Ti(22) **79.76**	V(23) **72.07**	Cr(24) **98.07**		Fe(26) **81.59**	Co(27) **76.91**	Ni(28) **74.51**	Cu(29) **60.02**	Zn(30) **61.37**			
		Nb(41) **55.06**						Ag(47) **44.19**	Cd(48) **37.82**		Sn(50) **41.21**	
		Ta(73) **52.55**	W(74) **72.81**				Pt(78) **44.06**	Au(79) **31.67**			Pb(82) **18.76**	Bi(83) **28.4**

Fig 3.18: The elements of Fig 3.16 are shown in the periodic tables of elements with their atomic numbers (in parentheses) and their resonant frequencies in KHz **(in bold)**.

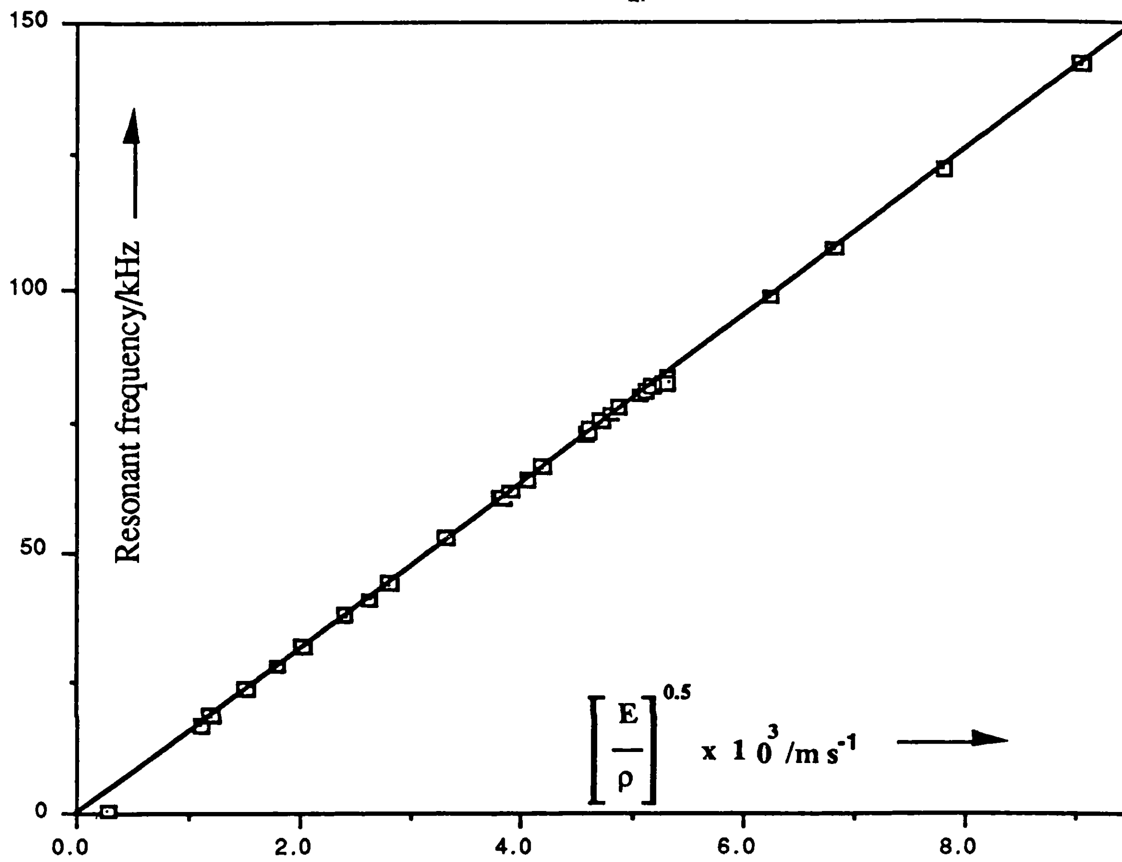

Fig 3.19: The universal resonant frequency response: the same as that of Fig 3.17 and Fig 3.18 but here all the materials of those figures are included. All the values are given in Table 3.2.

Table 3.2: Young's modulus, density and the fundamental resonant frequency of all the materials given in Fig 3.20. It is assumed that the resonator has dimensions of 180μm long and 0.5μm thick, and clamped end-conditions are assumed.

Material (Atomic No.)	Young's modulus, E 10^{10} Pa	Density, ρ 10^3 kg m^{-3}	$(E/\rho)^{0.5}$ 10^3 m s^{-1}	Resonant frequency, i=1 KHz
SiO_2	7	2.2	5.6	143
Si_3N_4	15	3.1	6.9	107
Al_2O_3	330	3.9	32.6	157
Be(4)	3.0	1.8	4.1	63.6
Mg(12)	4.4	1.7	5.1	79.9
Al(13)	7.0	2.7	5.1	80.4
Si(14)	19	2.3	9.1	142.2
Ti(22)	11.6	4.5	5.1	79.8
V(23)	12.8	6.1	4.6	72.8
Cr(24)	2.5	7.2	1.9	98.1
Fe(26)	21.1	7.9	5.2	82.0
Co(27)	21.0	8.8	4.9	76.9
Ni(28)	2.0	8.9	1.5	74.5
Cu(29)	13.0	8.9	3.8	60.0
Zn(30)	10.8	7.1	3.9	61.4
Nb(41)	10.5	8.6	3.5	55.1
Ag(47)	8.3	10.5	2.7	44.2
Cd(48)	5.0	8.6	2.4	37.8
Sn(50)	5.0	7.3	2.6	41.2
Ta(73)	18.6	16.7	3.3	52.6
W(74)	41.2	19.3	4.6	72.8
Pt(78)	16.8	21.5	2.8	44.1
Au(79)	7.8	19.3	2.0	31.7
Pb(82)	1.6	11.3	1.4	18.8
Bi(83)	3.2	9.8	1.8	28.4

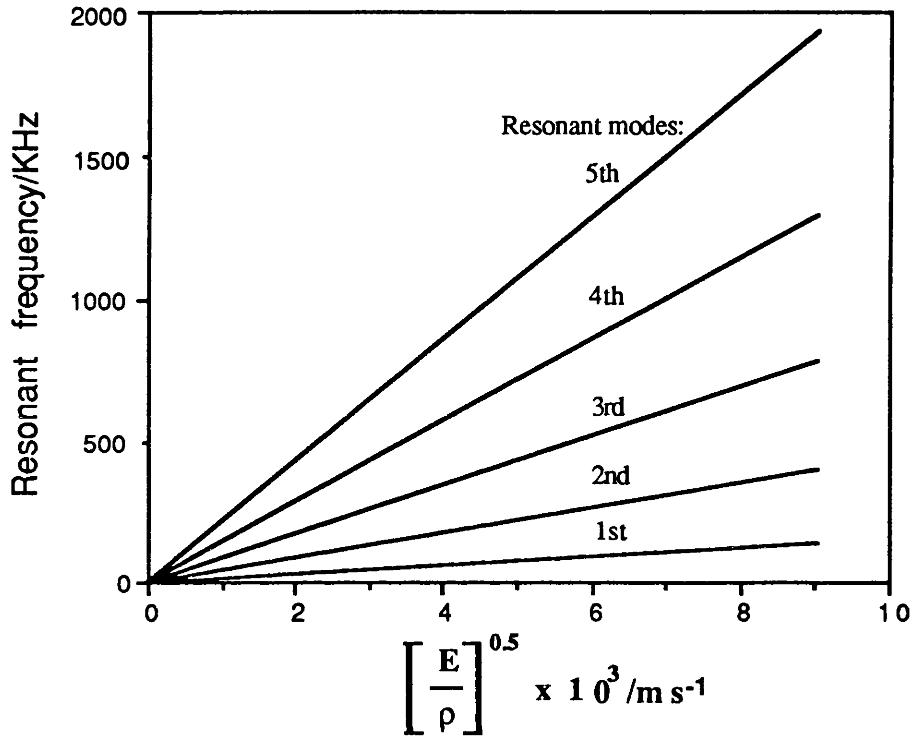

Fig 3.20: The first five universal resonant frequency modes.

3.6. Resonant frequency dependence on metal coatings

3.6.1. Introduction:

Resonators made of silicon, silicon dioxide and silicon nitride are coated with a thin metal layer. The metal coating is an essential part of the device independent of the method of activation and detection. In optical activation, it provides the light-absorbing surface for opto-thermal conversion, which allows the beam to be set into vibration. In electrothermal activation, it provides the necessary resistor which transfers the current into mechanical vibration via an intermediate heating effect. In electrostatic activation, the metal coating

forms one of the electrodes of the capacitor. Moreover, this coating is important for the optical detection system, increasing the level of the detected optical signal. The metal coating changes the resonant frequency of the beam, and according to [10] the equivalent value for EI is given by:

$$EI_{equiv.} = \frac{w\, t_p^3 t_m E_p E_m}{12(t_m E_m + t_p E_p)} \left[4 + 6\frac{t_m}{t_p} + 4\left(\frac{t_m}{t_p}\right)^2 + \frac{E_m}{E_p}\left(\frac{t_m}{t_p}\right)^3 + \frac{E_p}{E_m}\frac{t_p}{t_m} \right] \quad (3.26)$$

where w is the width of the beam, subscript m denotes the principal material and subscript p denotes the metal coating.

3.6.2. Dependence of resonant frequency on different metal coatings:

The effect of the common metal coatings on the resonant frequency modes are shown in Fig 3.21, Fig 3.22 and Fig 3.23 for silicon, silicon dioxide, and silicon nitride resonators respectively. In these figures, the beam is assumed to have dimensions of 180μm long and 0.5μm thick, and to be coated with 0.2μm of metal. Two points can be summarised from these figures:

i) Aluminium is the only metal coating that increases the resonant frequency of the resonators while silver, chromium and gold all reduce the resonant frequency.

ii) The higher the resonant mode the greater the effect of the metal coating.

Here it should be pointed out that it is an experimental observation that aluminium beams or aluminium coated beams may have higher resonant frequencies than those predicted because aluminium oxidises at room temperature to form aluminium oxide (Al_2O_3), and the latter has a higher (E/ρ) value as shown in Table 3.2.

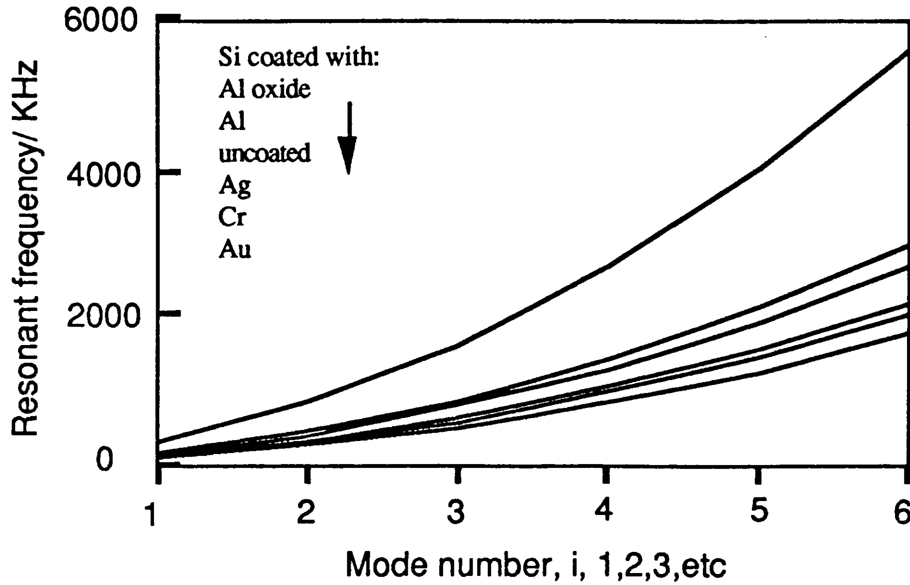

Fig 3.21: The dependence of the resonant frequency of a silicon beam on different metal coatings. The beam is assumed to have dimensions of 180μm long and 0.5μm thick, and to be coated with 0.2μm of metal.

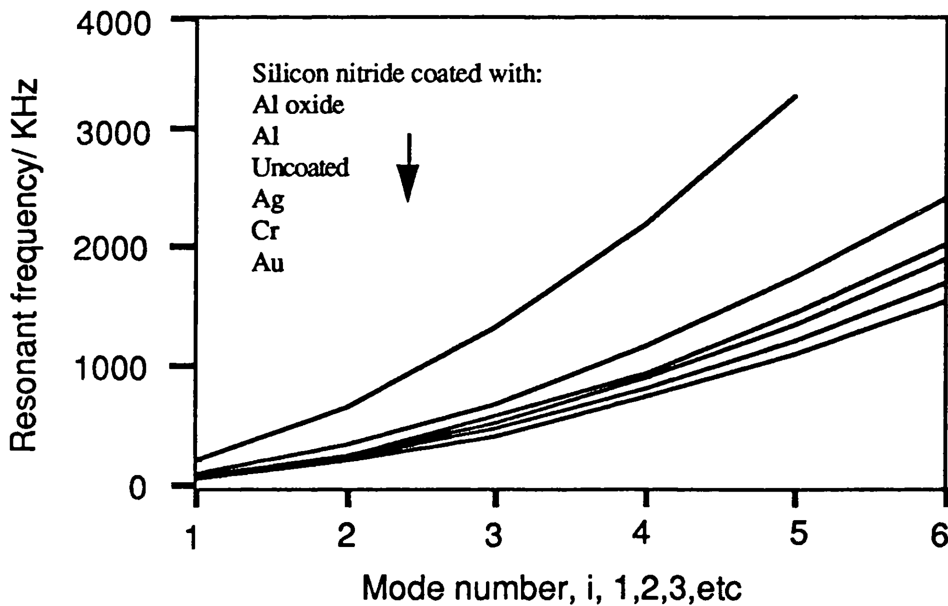

Fig 3.22: The dependence of the resonant frequency of a silicon nitride beam on different metal coatings. The beam is assumed to have dimensions of 180μm long and 0.5μm thick, and to be coated with 0.2μm of metal.

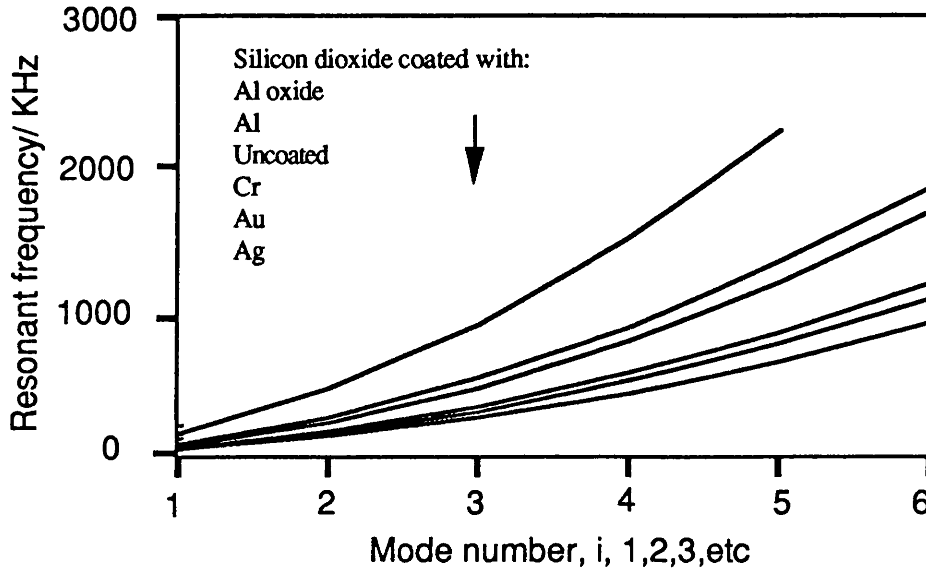

Fig 3.23: The dependence of the resonant frequency of a silicon dioxide beam on different metal coatings. The beam is assumed to have dimensions of 180μm long and 0.5μm thick, and to be coated with 0.2μm of metal.

3.6.3. Dependence of fundamental resonant frequency on different metal coatings and metal thicknesses:

Fig 3.24, Fig 3.25, Fig 3.26 and Fig 3.27 show the effect of different metal coatings on different resonator thicknesses at the fundamental resonant frequency. The resonator is considered to be silicon and to have dimensions of 180μm long and 0.5μm thick. It can be noted that aluminium is different from the rest in that it increases the resonant frequency.

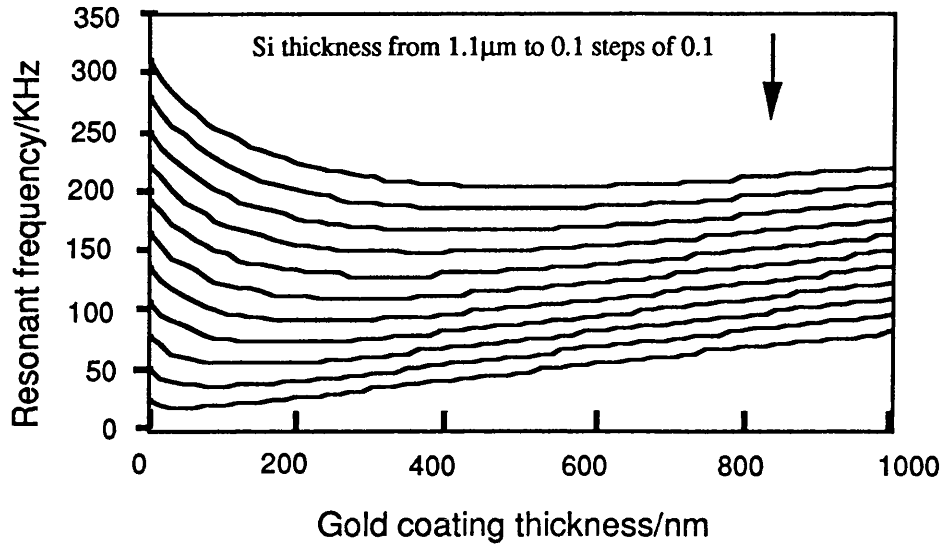

Fig 3.24: The dependence of the fundamental resonant frequency of a silicon beam on gold coating for different resonator thicknesses. The beam is assumed to have dimensions of 180μm long and 0.5μm thick.

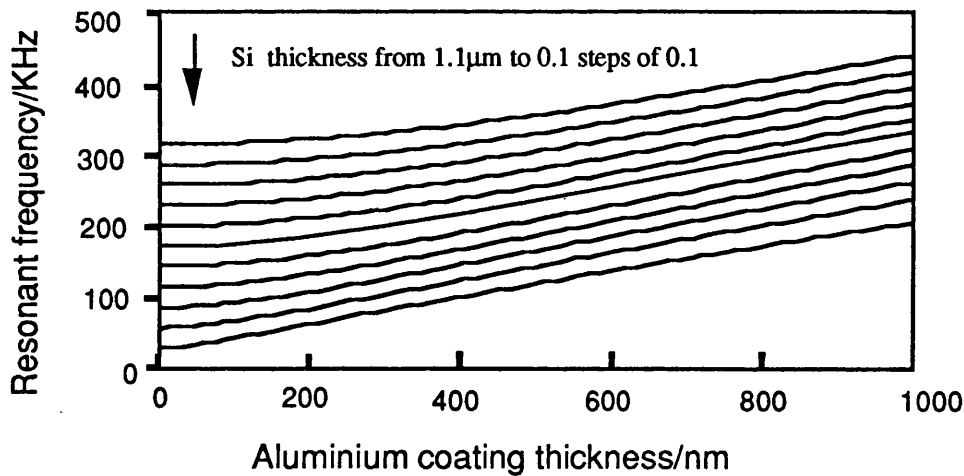

Fig 3.25: The dependence of the fundamental resonant frequency of a silicon beam on aluminium coating for different resonator thicknesses. The beam is assumed to have dimensions of 180μm long and 0.5μm thick.

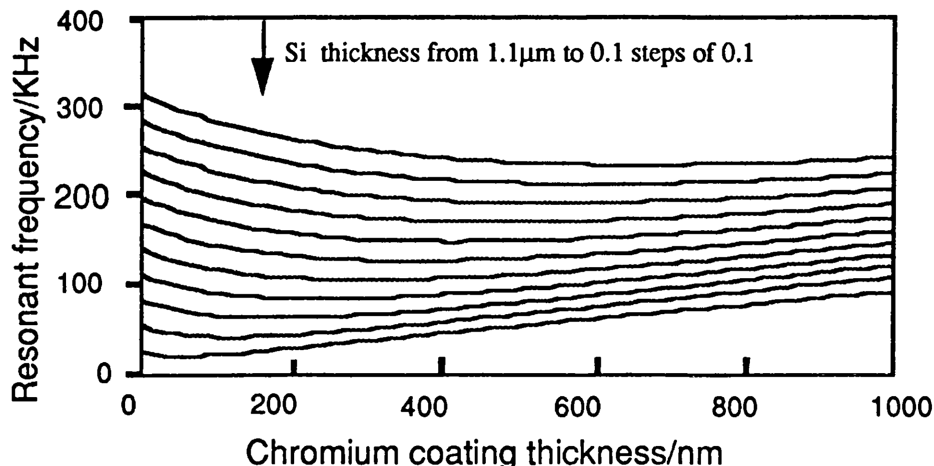

Fig 3.26: The dependence of the fundamental resonant frequency of a silicon beam on chromium coating for different resonator thicknesses. The beam is assumed to have dimensions of 180μm long and 0.5μm thick.

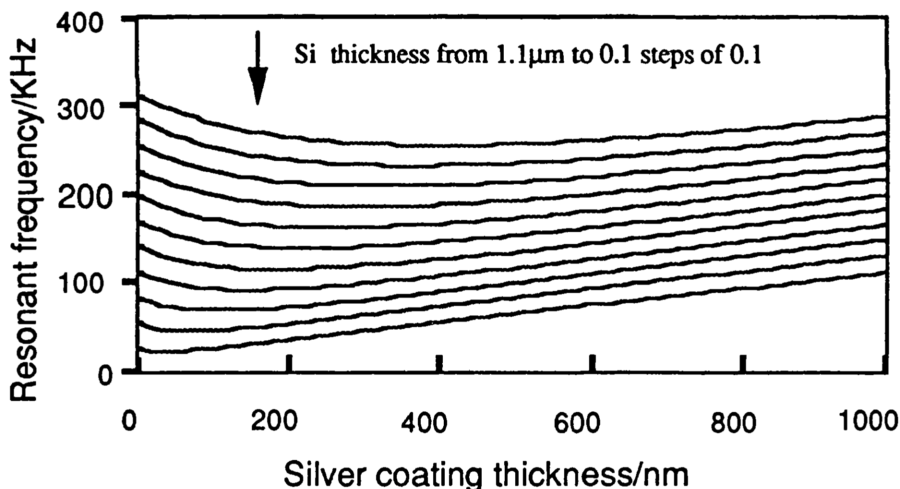

Fig 3.27: The dependence of the fundamental resonant frequency of a silicon beam on silver coating for different resonator thicknesses. The beam is assumed to have dimensions of 180μm long and 0.5μm thick.

In conclusion, the effect of four metal coatings on the resonant frequency were studied and it was found that aluminium is different in behaviour from the rest (silver, gold and chromium).

3.7. Fibre optic detection of resonator vibrations

3.7.1. Introduction:

The vibration of the resonator was sensed optically using a fibre optic coupler as shown in Fig 3.28. The detection scheme is that described by Andres et al [15]. The laser beam was guided into the fibre coupler from terminal T1 to the resonator surface at T2. This beam was reflected, firstly from the internal fibre surface at T2 and secondly via multi-reflection within the cavity formed between the fibre end and the resonator surface. These two reflected signals interfered and were detected in the detector at T3. As the resonator vibrated the cavity length between the fibre end and the resonator surface changed, altering the interfered signal from maximum to minimum and vice versa. Hence, the mechanical vibration of the resonator modulated the intensity of the laser beam which was incident on its surface and then monitored by the detector.

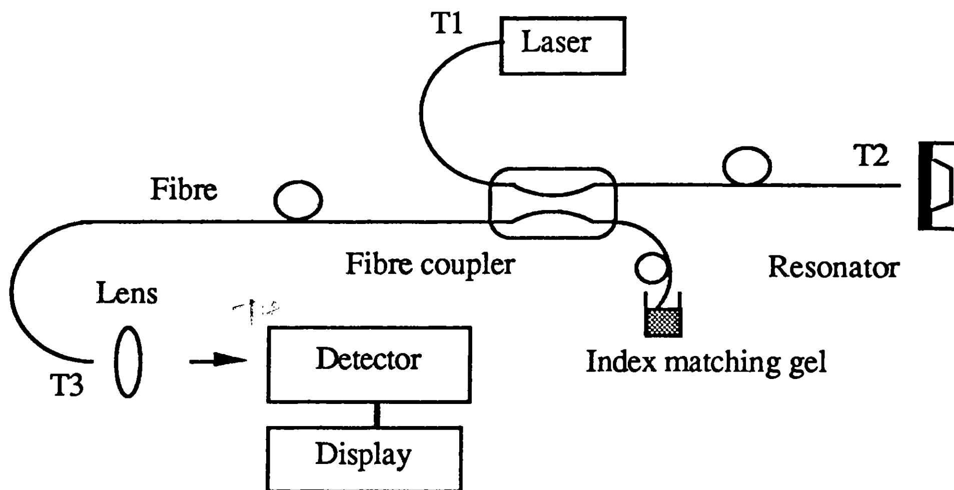

Fig 3.28: The fibre optic detection of resonator vibration.

3.7.2. Mathematical treatment:

Light emitted from the fibre is incident on a resonator surface and couples back to the fibre via multi-reflections in the cavity between them. The resonator surface is metal coated. Although we have shown in Fig 3.29 that the incident light is not normal to the resonator surface but at some angle, we assume normal incidence in this analysis. The reflected signal from the internal fibre surface is given by:

$$S_i = r_i \exp(-\Phi j) \qquad (3.27)$$

where r_i is the internal reflection coefficient of fibre /air interface, and Φ is some phase angle which can be set to zero for ease of calculation. The reflected signal from the sensor is coupled back to the fibre going through a multi-reflection in the cavity between the fibre and the resonator. The m reflective signal can be given by:

$$\begin{aligned} S_1 &= C_1 t_i | r_s | t_e \exp(-j\Phi_1) \\ S_2 &= C_2 t_i | r_s |^2 t_e \exp(-j\Phi_2) \\ &\vdots \\ S_m &= C_2 t_i | r_s |^m t_e \exp(-j\Phi_m) \end{aligned} \qquad (3.28)$$

where t_i and t_e are the transition coefficient of the fibre/air and air/fibre interfaces: r_s is the reflection coefficient of the sensor: Φ_m and C_m are the phase delays and the coupling coefficients associated with the mth reflected beam. Φ_m can be approximated by:

$$\phi_m = m\phi_1 = m k \Delta = m\left(\frac{2\pi}{\lambda}\right)\Delta \qquad (3.29)$$

where Δ is the path difference between the reflected beam from internal fibre and that of the first reflection from the beam and is given by :

$$\Delta = 2 n_i d \qquad (3.30)$$

where n_i is refractive index of air with a value of a unity.

Summing all the terms of (3.28) we have:

$$S_m = \sum_{m}^{\infty} r_i |r_s| t_e \langle |r_s| r_e \rangle^{m-1} |C_m| e^{-j\phi_m} \qquad (3.31)$$

where m is the number of reflections in the cavity. The successive contribution to the interferometric signal S detected at the detector T3 can be given by [15]:

$$S = r_i + \sum_{m}^{\infty} r_i |r_s| t_e \langle |r_s| r_e \rangle^{m-1} |C_m| \exp(^{-j\phi_m}) \qquad (3.32)$$

The condition for constructive and destructive, i.e. bright and dark fringes, in the detector is:

$$2\, n_i\, d = \begin{cases} \left(n + \frac{1}{2}\right)\lambda \text{ Bright} \\ \left(n + \frac{1}{4}\right)\lambda \text{ Dark} \end{cases} \qquad (3.33)$$

where n_i is the refractive index of air with a value of unity, n (= 1, 2, 3, etc) is an integer.

The intensity I is given by :

$$I = S\, S^* \qquad (3.34)$$

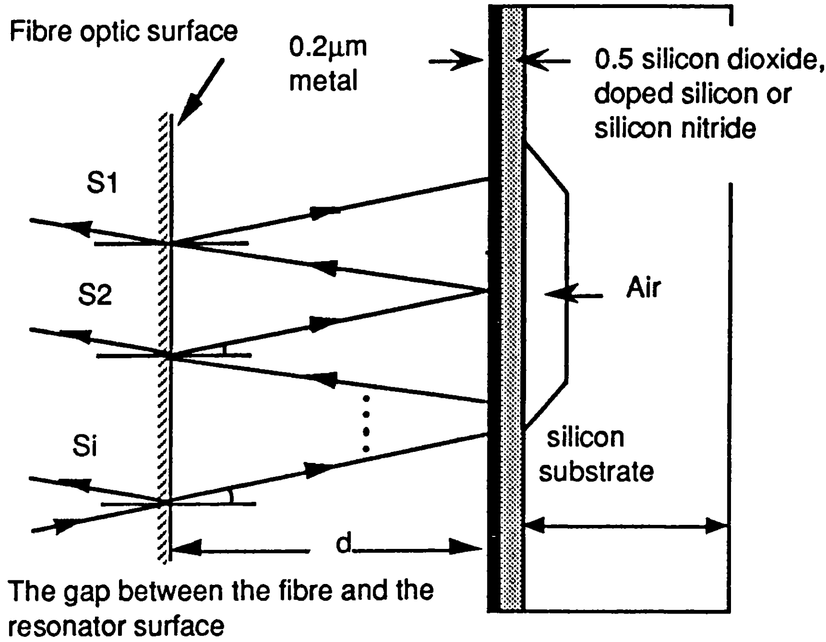

Fig 3.29: The fibre resonator interferometer. The angle of incidence has been ignored in this analysis.

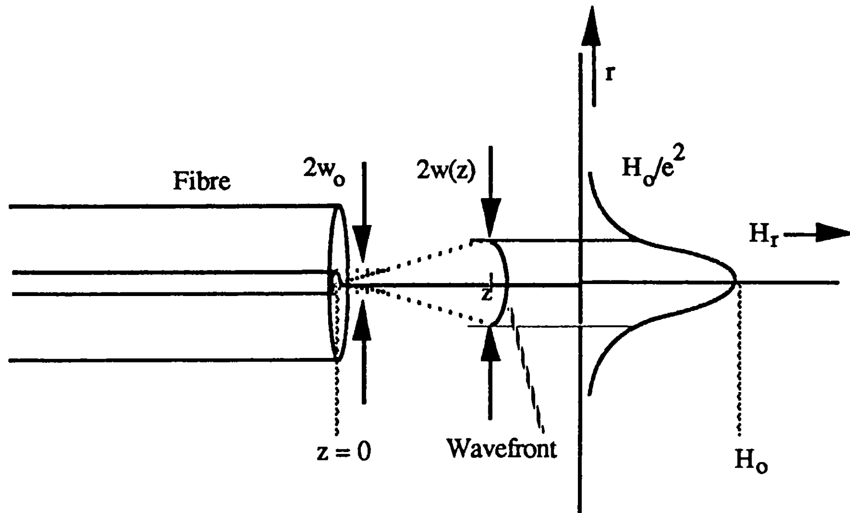

Fig 3.30: A Gaussian approximation for the field distribution of the fundamental mode of a step-index fibre.

3.7.3 Coupling coefficient:

A Gaussian approximation may be considered to calculate coupling efficiency, i.e. an expression for C_m. This is the simplest physical beam that satisfies Maxwell's equations. A Gaussian approximation for the field distribution of the fundamental mode of a step-index optical fibre (Fig 3.30) provides an expression for C_m [15,16].

Let us assume linear polarisation with the electric field orientated into the x-direction, perpendicular to the direction of propagation (z):

$$E_x(r,z) = E_o(z)\exp\left[\frac{-r^2}{w^2(z)}\right] \quad [Vm^{-1}]$$
$$H(r,z) = H_o(z)\exp\left[\frac{-2r^2}{w^2(z)}\right] \quad [Vm^{-2}] \qquad (3.35)$$

where: z is the distance from the beam waist into the direction of propagation: $E_0(z)$ is the electric field on the z-axis which depends on z: $H_0(z)$ is the power density (irradiance) on the z-axis which depends on z: r is radial distance from the z-axis: w(z) is the radius; r is the distance from the z-axis where the power density is down to $1/e^2$ of maximum. At this point, the electric field is down to 1/e of its maximum.

The beam radius w(z) is defined by the $1/e^2$ at any distance z by:

$$w(z) = \frac{\lambda z}{\pi w_o} \quad \text{[for large z]} \qquad (3.36)$$

w_0 is the radius of the beam waist at the point of the $1/e^2$ of the power density H.

The situation is similar to that of splice losses analysed by Marcuse [16] and can be simplified with reference to Fig 3.29 . If we consider that the surface of the resonator is parallel to the fibre end plane then the following picture can be visualised: The light emitted from the fibre is incident on the resonator surface where a fraction is absorbed and a

fraction of it is reflected back to the fibre. The first reflected beam travels a distance 2d and couples back to the fibre end. The second reflected beam travels 4d and then couples back to the fibre and so on. Every time the beam is incident on the resonator a fraction of it will be absorbed. Now the situation is as that analysed by Marcuse with one exception: that the off-set does not arise here providing that the sensor surface is wider than the cross-section of the fibre core. However, Andres et al [15] in a rather unclear analysis considered the off-set of the fibre with respect to the resonator and showed that the off-set does not affect the results of the analysis.

The two factors that affect the coupling efficiency between the resonator and the fibre is the separation between them and the angle of tilt of the resonator surface with respect to the fibre.

(i) The coupling coefficient due to separation: Modifying the formula given by Marcuse, we have the coupling coefficient as a function of separation given by [16]:

$$C_s = \frac{1}{1 + \left(\frac{D}{k\,w}\right)^2} \qquad (3.37)$$

where the total travelling distance is D =2md. The free space propagation constant is k = 2 π/ λ. The optimum width parameter of the Gaussian field w_0 for step-index fibre is given by [16]:

$$w = a\left(\sqrt{\frac{2}{V}} + \frac{0.23}{V^{\frac{3}{2}}} + \frac{18.01}{V^6}\right) \qquad (3.38)$$

where a (= 4.5μm) is the core radius of the fibre and V is a constant with a value of 2.4.

(ii) The coupling coefficient dependence on tilt angle. Modifying the formula given by Marcuse, we have the coupling coefficient due to separation given by [16]:

$$C_t = \exp\left[-\left(\frac{k\,w\,\Theta}{4}\right)^2\right] \qquad (3.39)$$

where the effective tilt angle is $\Theta = 2m\theta$.

Fig 3.31 shows the effect of separation between the fibre and the sensor. Here, the tilt angle and the wavelength are considered to be zero and 1.3μm respectively.

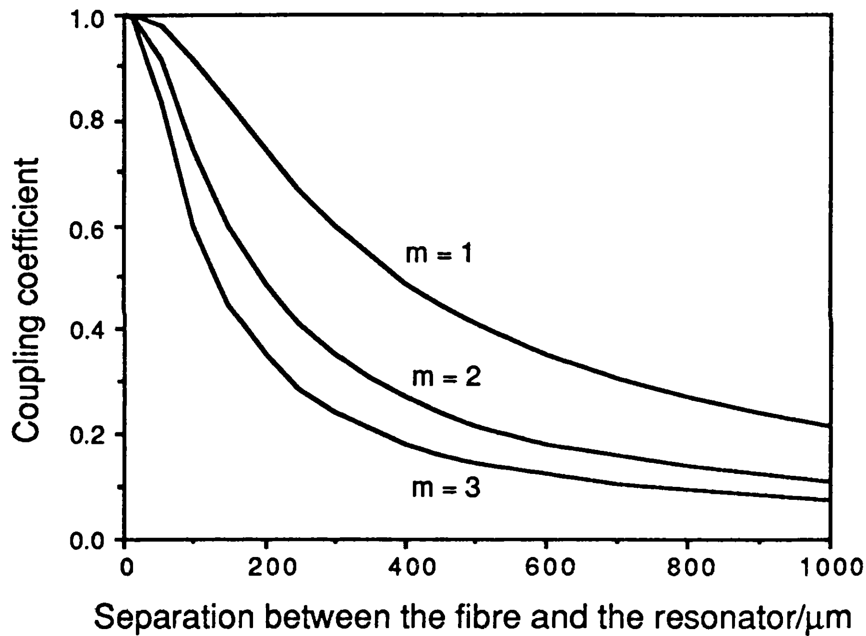

Fig 3.31: Coupling coefficient dependence on separation for the first three reflected beams. The angle of tilt is set to zero and the wavelength to 1.3μm.

The overall expression for coupling coefficient C_m which takes separation and tilt into account can be given by:

$$|C_m|^2 = \frac{1}{1+\left(\frac{D}{k\,w}\right)^2} \exp\left[-\left(\frac{k\,w\,\Theta}{4}\right)^2\right] \qquad (3.40)$$

It may be noted that (3.40) is the same formula given by Andres et al [15] without taking the effect of off-set into account. The normalised distance and tilt are respectively given by:

$$D_N = \frac{D}{k\,w} \qquad \Theta_N = \left(\frac{k\,w\,\Theta}{4}\right) \qquad (3.41)$$

Fig 3.32 shows the coupling coefficient as a function of separation between the fibre and the resonator surface for four wavelengths. The coupling is more efficient with shorter wavelengths. This is because we have chosen the same fibre parameter. So for shorter wavelengths it may be multimode.

Fig 3.33 shows the coupling coefficient dependence for three values of tilt angle and Fig 3.34 shows the dependence of the tilt angel for different values of separations. It is clear that the coupling coefficient depends on tilt more than separation.

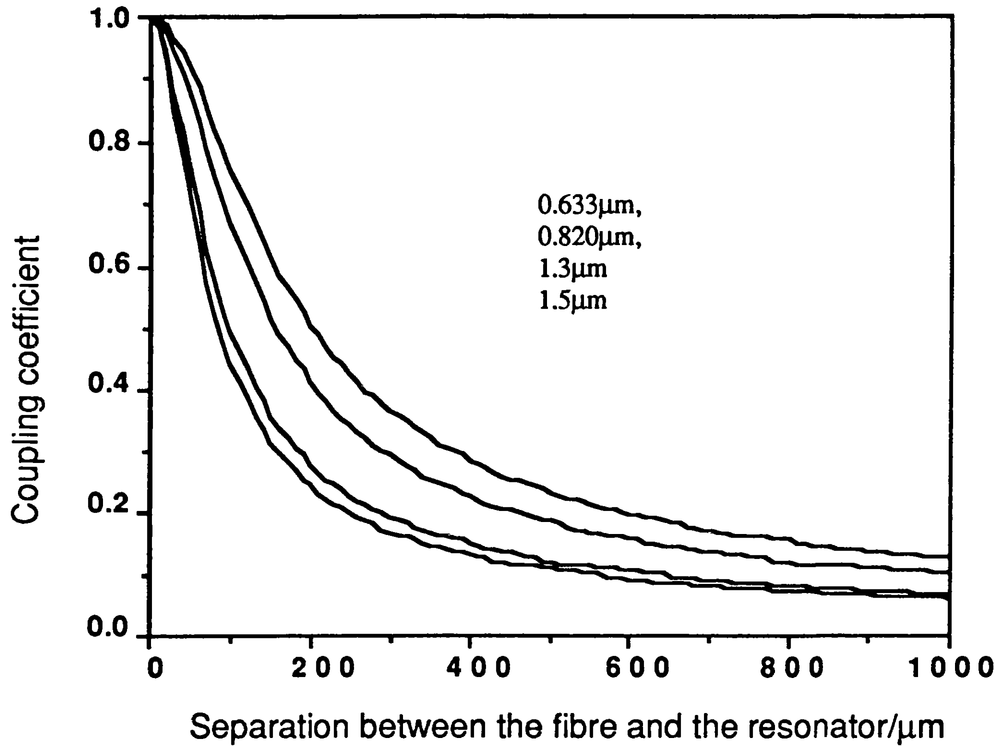

Fig 3.32: Coupling coefficient C1 dependent on separation for four different wavelengths 0.633, 0.820, 1.3 and 1.5μm. The angle of tilt is set to zero.

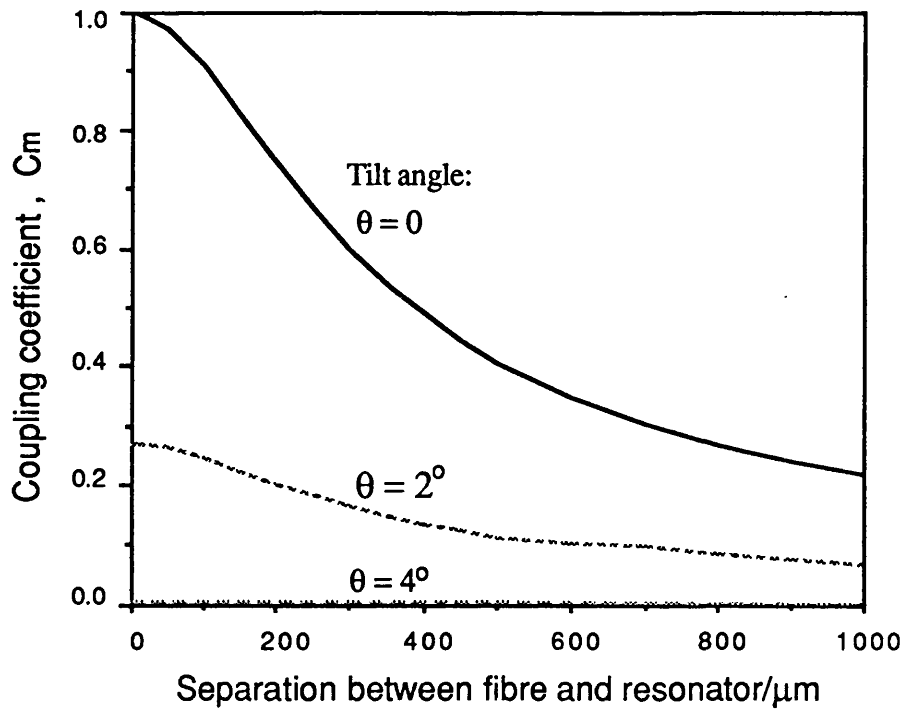

Fig 3.33: Coupling coefficient as a function of separation between the fibre and the resonator surface for three tilt angles.

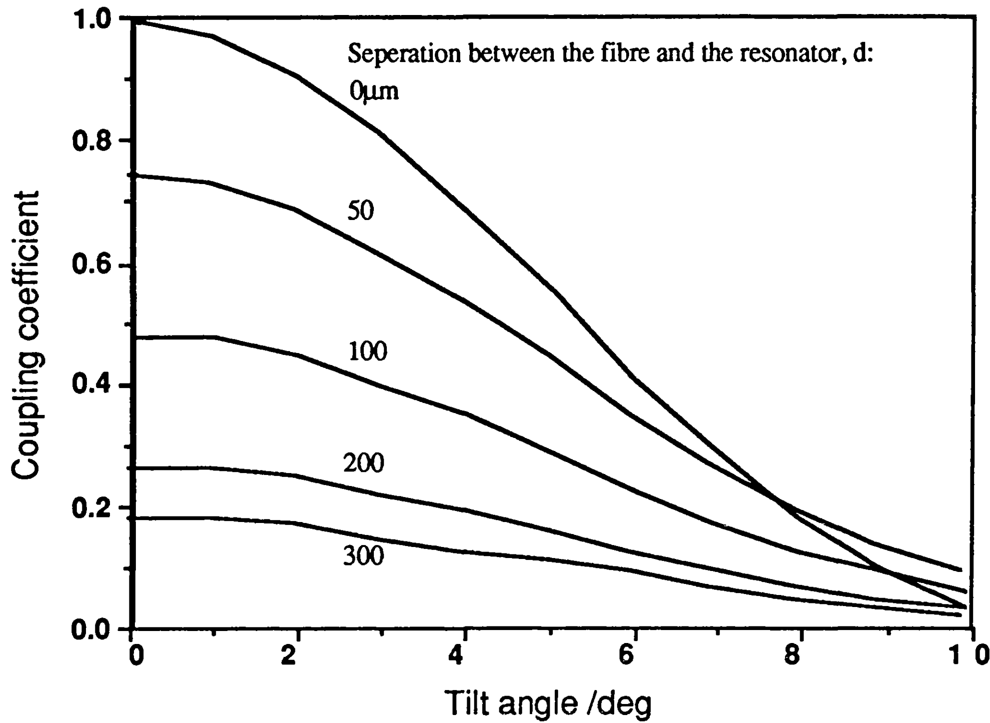

Fig 3.34: The dependence of the tilt angle for different values of separations.

3.7.4. The interferometric signal:

Next we discuss the intensity of the resultant signal of the interferometer which is given by (3.34). There are several ways of improving the intensity of the interferometric signal in the optical fibre detection configurations.

1) Increasing reflectivity of the resonator increases the signal. However, the activation of the resonator should not be forgotten since it is determined by the absorption of light in the resonator. Nonetheless, in our case only a few μW is required for activation so the absorption is not critical. Fig 3.35 shows the dependence of the intensity of the signal on the separation for different values of resonator surface reflectivity at 1.5μm wavelength. Fig 3.36 shows the fringes at 1.5μm for 90% resonator reflectivity.

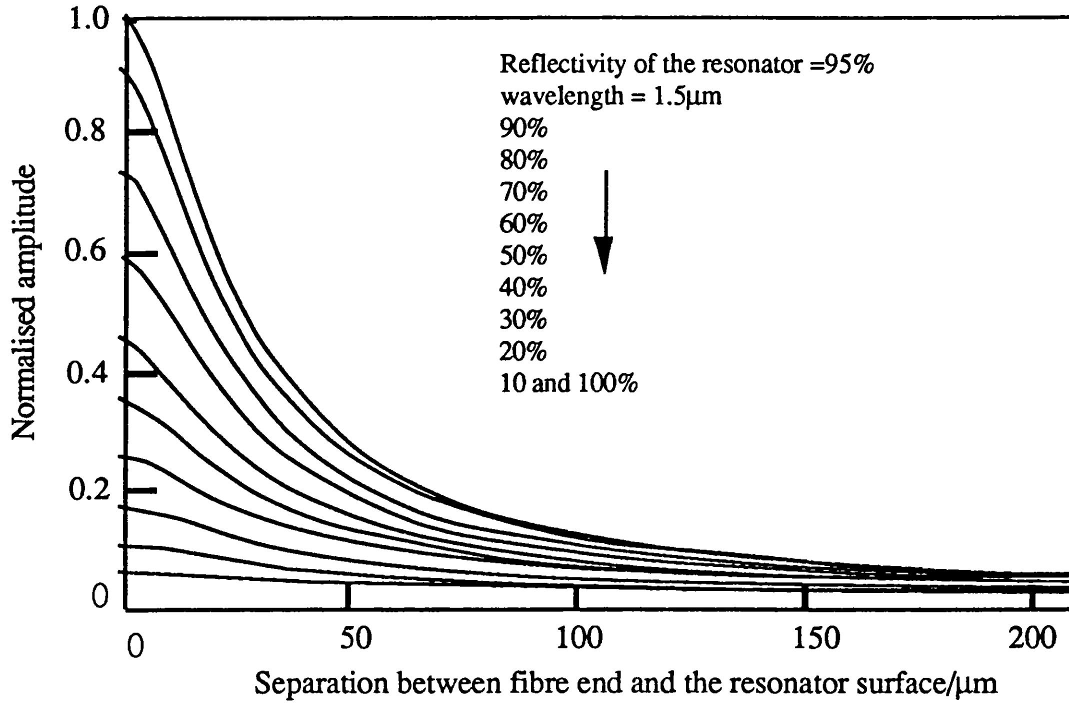

Fig 3.35: The intensity of the interferometric signals as a function of the resonator surface reflectivity.

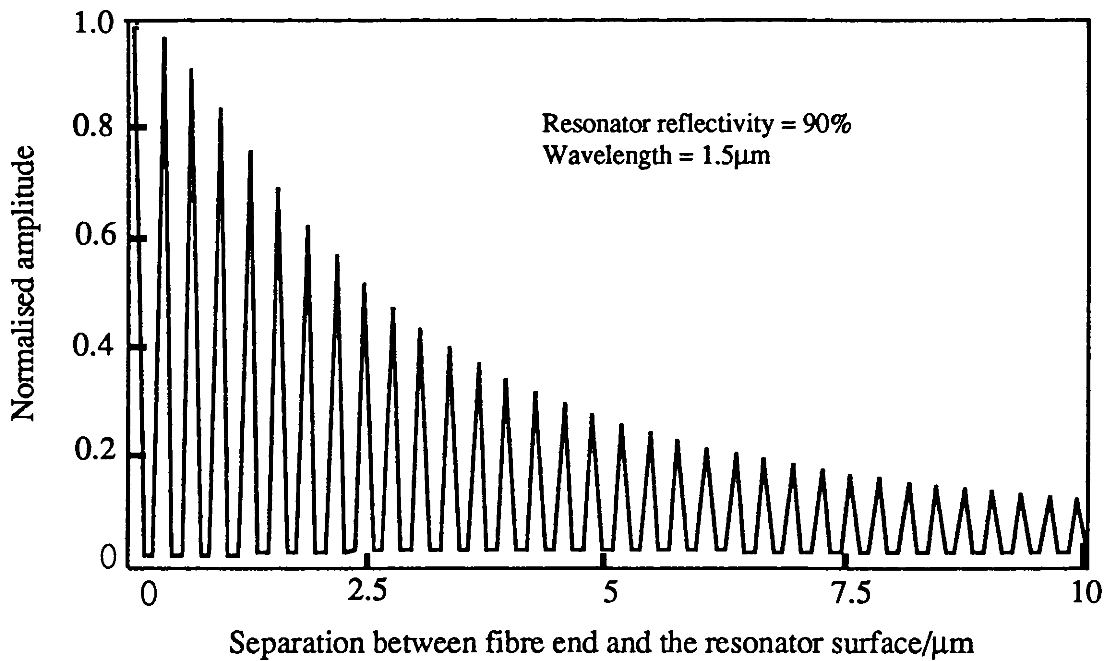

Fig 3.36: The detected fringes of the interferometer for 1.5μm wavelength.

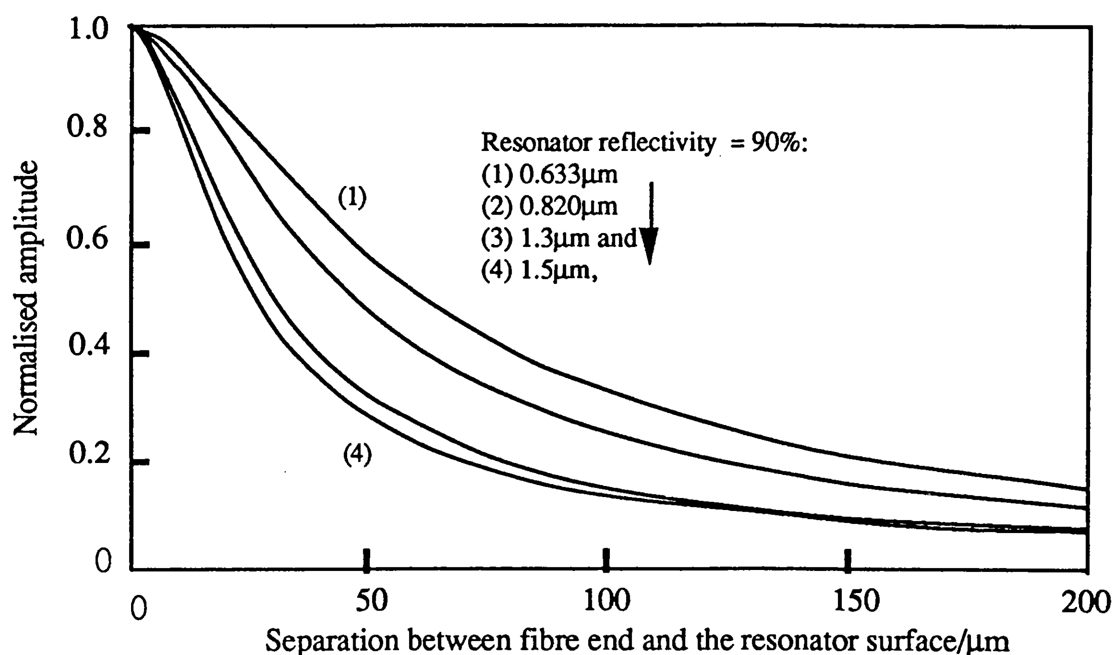

Fig 3.37: The intensity of the interferometric signals as a function of separation for four wavelengths: 0.633μm, 0.820μm, 1.3μm and 1.5μm.

2) To get constructive interference half a wavelength path difference is required and to get destructive interference only a quarter of a wavelength is required. It may be concluded that the shorter wavelength gives a greater depth of modulation. This is because the same parameters (of equation 3.38) have been considered for all the wavelengths which implies that the shorter wavelengths may be multi-moded in the fibre. The dependence of the signal on the wavelength is shown in Fig 3.37.

3) Increasing the reflectivity of the fibre end increases the modulation depth of the interferometer. Fig 3.38 shows the intensity of the interferometric signals as a function of the fibre-end surface reflectivity. The reflectivity of the resonator is taken to be 95% and the wavelength 1.5μm. Fig 3.39 shows the amplitude of the resultant fringes for two fibre surface reflectivities: 3.5% and 80%.

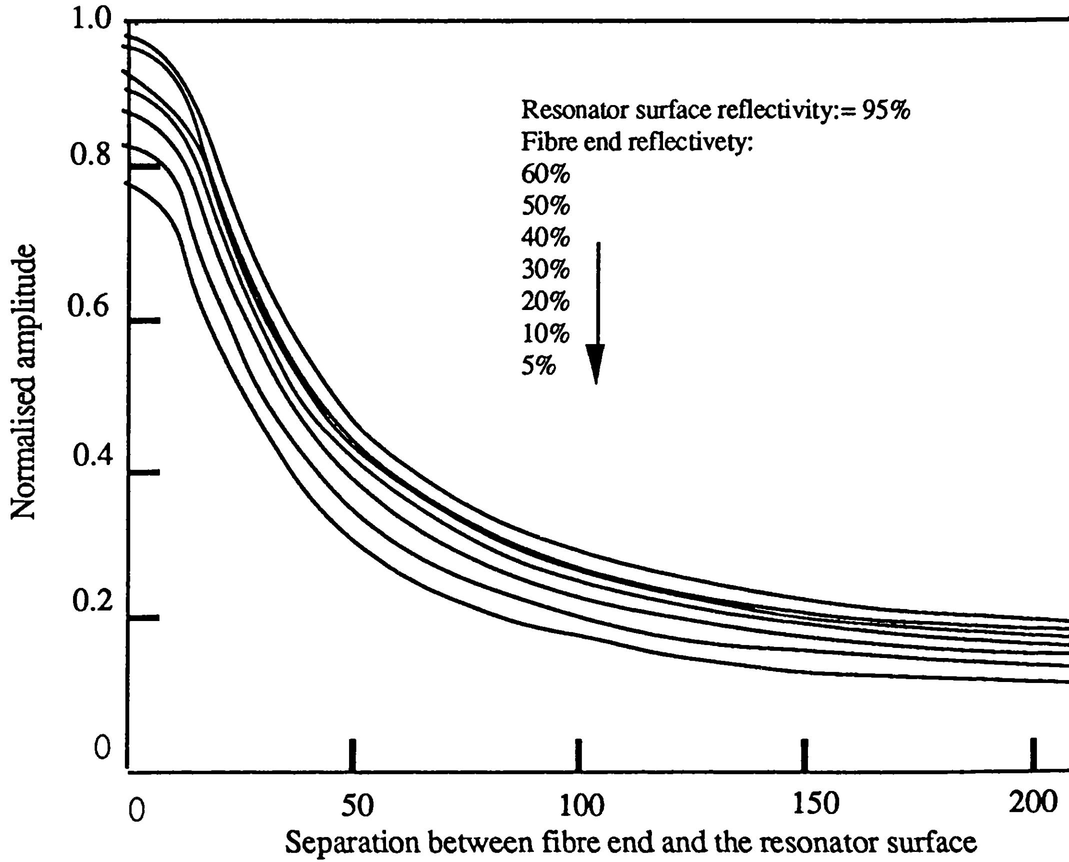

Fig 3.38: The intensity of the interferometric signals as a function of the fibre-end surface reflectivity. The reflectivity of the resonator is taken to be 95% and the wavelength 1.5μm.

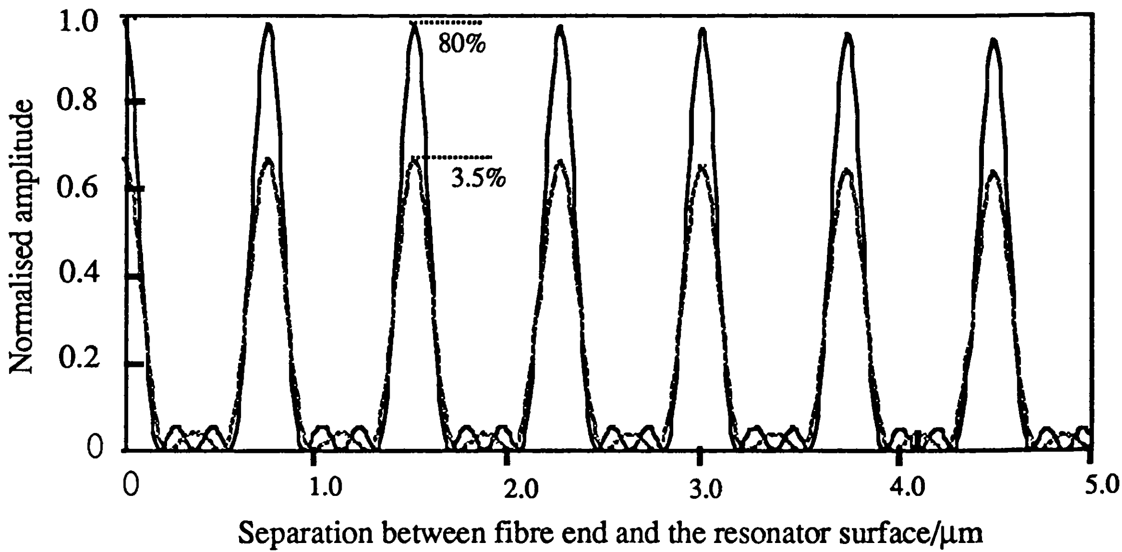

Fig 3.39: The amplitude of two resultant fringes for two fibre reflectivity: 3.5% and 80%. The wavelength is considered to be 1.5μm and the resonator reflectivity 95%.

The effect of the tilt on the intensity depends on the length of the cavity, i.e. the value of d. If the resonator is tilted where the value of d satisfies (3.33.a), i.e. where constructive interference occurs in the detector, the intensity decreases with changing tilt angle, as shown in Fig 3.40. By contrast, if the resonator is tilted where the value of d satisfies (3.33.b), i.e. where a destructive interference occurs in the detector, the intensity changes (increases or decreases) with changing tilt angle. The latter curve is shown in Fig 3.41 by itself. In this case, the intensity may increase despite increasing the tilt angle. This is because the resonator is in a position where the interference is destructive (dark fringes), and any change in the position of the resonator will bring it closer towards a position where the interference is constructive (bright fringes). Remembering that the distance between a bright and a dark fringe is only a quarter of a wavelength. However, the change in the intensity for 6° tilt is less than 20% of the intensity of a bright fringe (Fig 3.40). This does not invalidate the detection scheme since what we discuss here is for the steady surfaces, the fibre end and the resonator surface. In the analysis, nevertheless, the vibration of the resonator surface with amplitude of about 100nm is ignored. So the resonator sends out a signal wherever it is since it covers just under a quarter wavelength of light at 633nm. Besides, for sensing-applications the information about the measured parameter is encoded in the resonant frequency and not in the amplitude.

3.7.5. Conclusions:

We have analysed optical detection of vibrating surfaces using optical fibres. The main points to be concluded are as follows:

1) The interferometric output was determined by the relative amplitudes and phase of the two reflected beams and hence was independent of the length of optical fibre and consequently was unaffected by the environmental parameters [15].

2) The intensity of the signal can be improved by two methods: increasing the reflectivity of both surfaces, the resonator and the fibre end, and decreasing the wavelength used for detection.

3) The two parameters affecting the coupling coefficient are the separation between the fibre and the resonator and the tilt angle between them.

4) Using this technique the sensor can be detected remotely and it is immune to EMI.

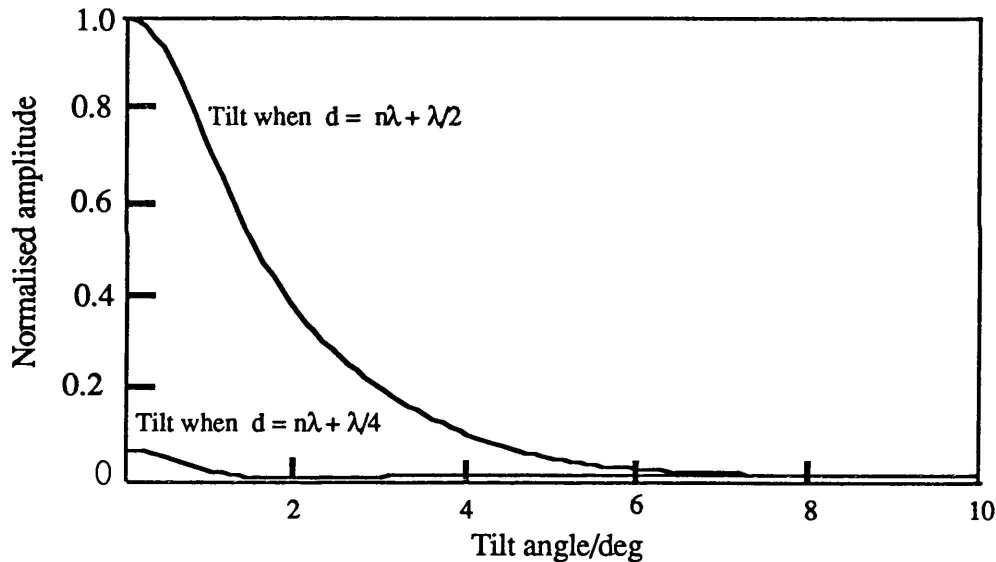

Fig 3.40: The intensity of the interferometric signals as a function of the tilt angle of the resonator. Two cases are shown: while the resonator is at a point where d is equal to ($m\lambda+\lambda/4$) and while it is equal to ($m\lambda+\lambda/2$) away from the fibre.The wavelength is taken to be 1.5μm.

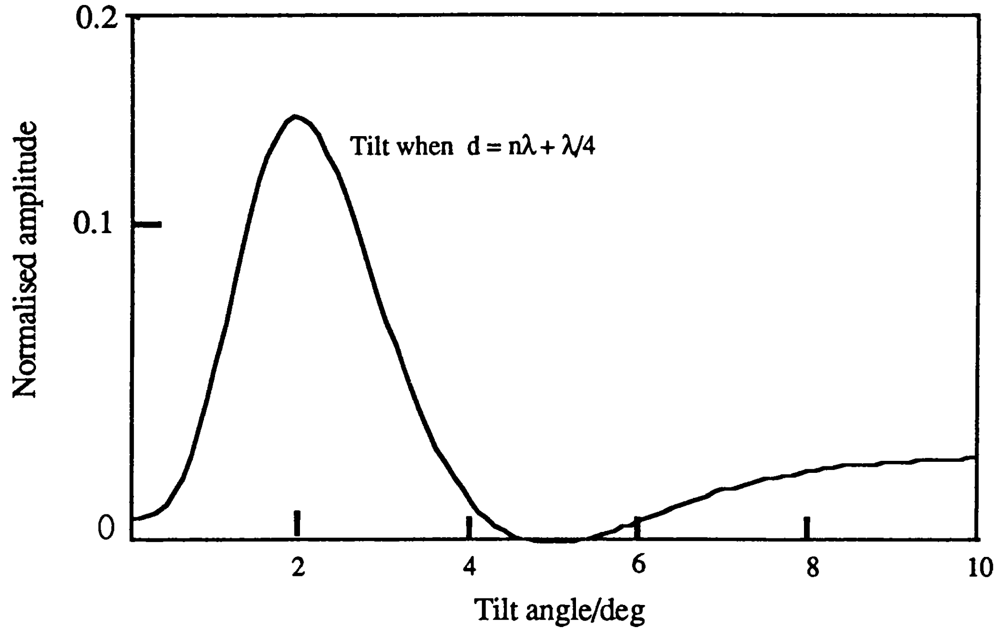

Fig 3.41: The intensity of the interferometric signal as a function of the tilt angle of the resonator while the resonator is at a point where the fibre-resonator separation is equal to $(m\lambda+\lambda/4)$. This is a magnification of Fig 3.40. Both figures are on the same scale. The wavelength is taken to be 1.5μm.

3.8. The intensity distribution within the cavity

Now, we calculate the light intensity distribution within the cavity between the fibre end and the resonator surface. A Fabry-Perot interferometer is set up between the end of the fibre positioned at the resonator surface and the surface itself, the air gap between them forming the etalon, Fig 3.29. The incident light transmitted from the fibre end falls on the resonator surface. A multiple reflection in the etalon builds up an intensity distribution of light. The fibre/air interface has a 4% Fresnel reflection and the metalisation layer on the beam/air interface has a reflection efficiency of 90% at a wavelength of 633nm. If the amplitude of the transmittance T and reflectance R of the fibre and the metal coating are denoted respectively by the subscripts f and b, then:

$T_f = 0.96,\ R_f = 0.04,\ T_b = 0.10 \text{ and } R_b = 0.90$ (3.42)

With reference to Fig 24, a modified Airy formula for this condition can be derived and the intensity distribution in the etalon, I, is given by:

$$I = \frac{I_o T_f T_b}{(1-\sqrt{R_b R_f})^2}\left[1+\frac{4\sqrt{R_b R_f}}{(1-\sqrt{R_b R_f})^2}\sin^2\left(\frac{\Delta}{2}\right)\right]^{-1} \qquad (3.43)$$

where I_o is the intensity of the incident beam and Δ is given by:

$$\Delta = \frac{2\pi}{\lambda} 2\, d\, n \cos\gamma \qquad (3.44)$$

where d is the separation between the fibre and the resonator surface, and n is the refractive index of air. The distribution of the intensity within the etalon, expressed by (3.43), gives about 25% depth of modulation as shown in Fig 3.42 when the angle of incident γ is zero and I_o is unity.

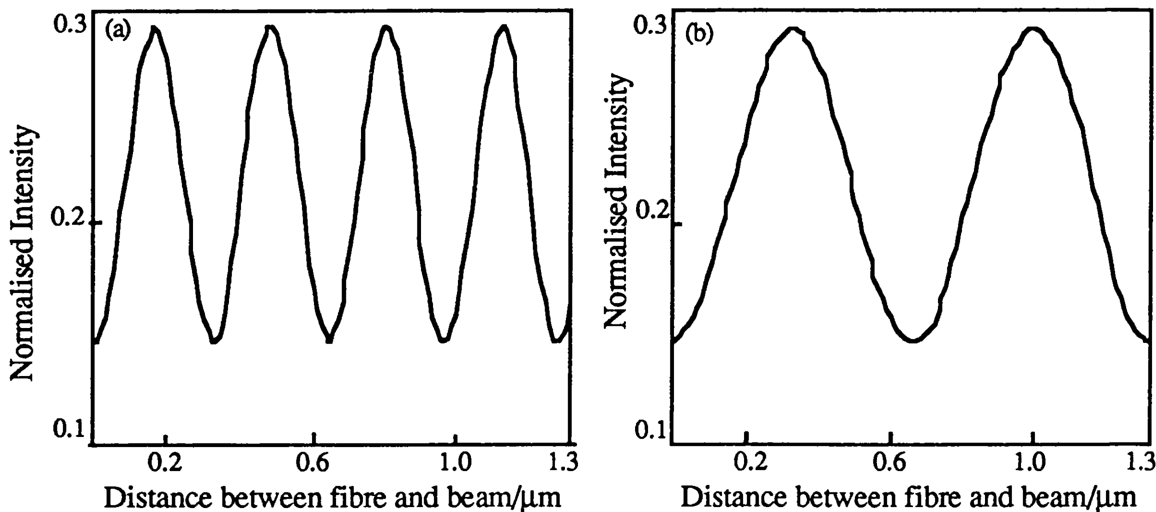

Fig 3.42: Plots showing the distribution of the light intensity in the etalon: (a) for 0.633µm wavelength and (b) for 1.3µm wavelength .

In the case of 'self-excitation' [17,18] only a cw laser beam is needed, without any external drive either optical or electrical, to drive the resonator beam into its natural resonant frequency.

The reflected signal from the resonator can be monitored either in the frequency-domain on a spectrum analyser or in the time-domain on an oscilloscope. In the frequency-domain a peak can be detected at the frequency at which the beam resonator is vibrating, Fig 3.43. In the time-domain a phase difference of $\pi/2$ can be detected between the input electric signal and the reflected optical signal from the resonator surface, Fig 3.44.

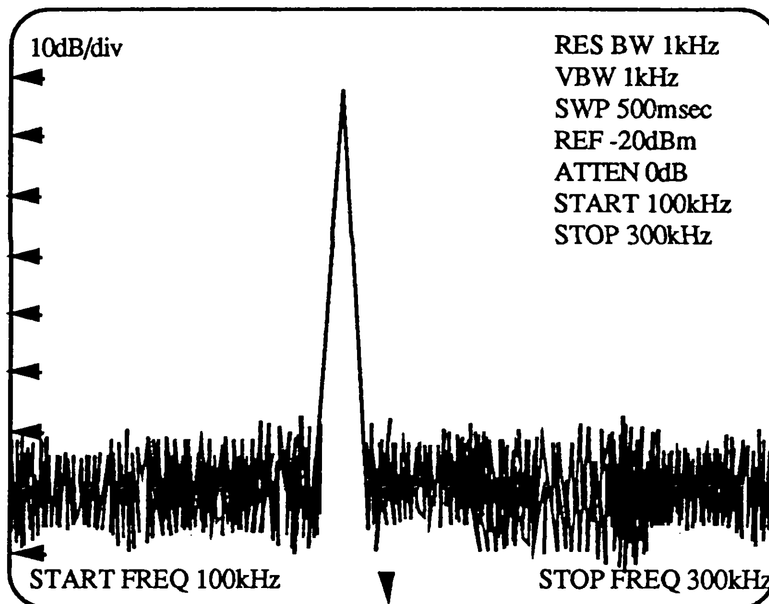

Fig 3.43: The spectrum analyser display of the resonant peak from a resonator surface.

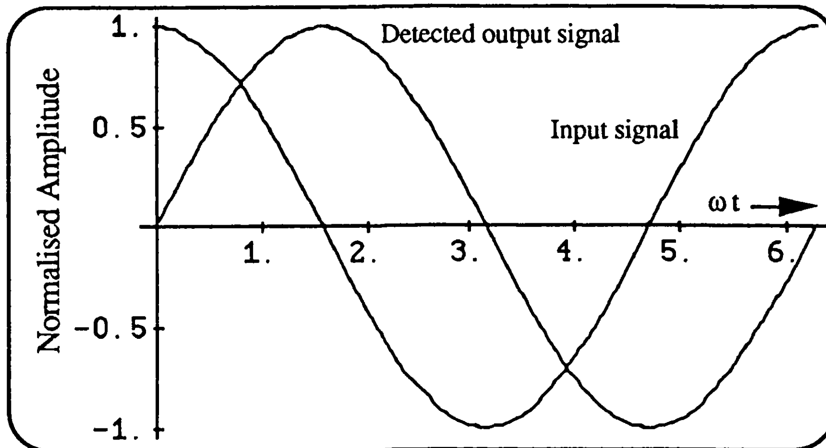

Fig 3.44: An oscilloscope display shows the phase difference between the electrical input and the optical output.

3.9. Overall Conclusion

We have studied the following topics regarding optical activation and detection of micromechanical resonators:

1. The mechanisms of optical activation and detection of micromechanical resonators have been studied, which enables us to improve their systems and device aspects.

2. The frequency behaviour of different modes (e.g. torsional) and methods for enhancing a particular mode have been studied.

3. A universal relationship has been shown between the resonant frequency and mechanical properties of resonators which enables us to consider other materials as resonators and understand the mechanical behaviour of a vast number of materials from a simple mathematical relationship.

4 . The effect of four metal coatings on the resonant frequency have been studied and it has been found that aluminium is different in behaviour from the rest (silver, gold and chromium).

5 . The intensity distribution in the cavity has been studied which is important for the study of self-excitation in which no modulation force is used to drive the resonator. The device is activated utilising the interferometric set-up in the cavity between the fibre and its metal coated surface.

3.10. References

1. Fatah R M A, Stokes N A D and Venkatesh S: 'Activation of silicon micromechanical resonators in fibre optic systems', Procs of EFCO 89, Amsterdam, June 1989, pp 418-422.

2. Venkatesh S and Culshaw B: 'Optically activated vibrations in a micromachined silica structure', Electron Lett, Vol 21, 1985, pp 315-317.

3. Rosencwaig A: 'Thermal wave microscopy with photoacoustics', J App Phys, Vol 51, No 4, April 1980, pp 2210-2211.

4. Ash E A, Neuman V and Petts C R, 'Photo-displacement imaging', Electron Lett, Vol 17, No 10, 1981, pp 337-338.

5. Rosencwaig A and Gersho A: 'Theory of the photoacoustic effect with solids', J Appl Phys, Vol 47, No 1, January 1976, pp 64-69.

6. Opsal J, Rosencwaig A and Willenborg D: 'Thermal-wave detection and thin-film thickness measurements with laser beam deflection', Appl Optics, Vol 22, No 20, 15 October 1983, pp 3169-3176.

7. Cottell A H: 'The mechanical properties of matter', (John Wiley & Sons, Inc,1964, p 129)

8. Uttamchandani D, Thornton K E B and Culshaw B: 'Optically excited resonant beam pressure sensor', Electron Lett, Vol 23, No 25, 1987, pp 1333-1334.

9. Thornton K E B, Uttamchandani D and Culshaw B: 'Novel optically excited resonant pressure sensor', Electron Lett, 12 May 1988, Vol 24, No 10, pp 573-579.

10. Blevins R D: 'Formulas For natural frequency and mode Shape' (Van Nostrand Reinhold Company, New York, 1979).

11. Timoshenko, S, Young, D H and Weaver W: 'Vibration problems in engineering' 4th edition, 1974, pp 454-5.

12. Zelenka J: Piezoelectric resonators and their applications', (Elselvier Science publishing Co Inc, 1986), pp 20-63.

13. Petersen, K E: 'Silicon Torsional Scanning Mirror', IBM J Res Development, Vol 24, No 5, Sep 1980, pp 631-636.

14. Fatah R M A: 'Frequency response of resonant beam sensors', New Materials and their applications 1990 (IOP conference series No. 111, Norfolk, 1990)

15. Andres V, Tudor M J and Foulds K W H: 'Analysis of an interferometric optical fibre detection technique applied to silicon vibrating sensor', Electron Lett, 1987, Vol 23, pp 774-775.

16. Marcuse D: 'Loss analysis of single-mode fibre splices', The Bell System Tech J, Vol 56, No 5, 1977, pp 703-718.

17. Stokes N A D, Fatah R M A and Venkatesh S: 'Self-Excited Vibrations of Optical Microresonators', Electron Let, Vol.13, 1988, pp 777-778.

18. Stokes N A D, Fatah R M A and Venkatesh S: 'Self-Excitation in Fibre-optic Microresonator Sensors', Sensors and Actuators, A21-A23, 1990, pp 369-372.

CHAPTER FOUR

Optical Activation and Detection of Micromechanical Resonators: vibration characteristic

4.1. Introduction

In the three previous chapters we introduced the necessary background that enables us to represent the vibration behaviour of micromechanical devices. In this chapter, five sections will be presented. Firstly, we discuss the optical fibre systems used to conduct this work. Secondly and thirdly the experimental results of activating silicon and silicon dioxide will be presented respectively. Fourthly, the dependence of the quality-factors of these devices on different parameters will be discussed. Finally, the discussion and concluding section will follow.

4.2. Optical fibre systems

These devices were driven into mechanical resonant vibration using an intensity-modulated laser source. The mechanical vibration was monitored by a cw laser at a different wavelength.

Two identical directional fused biconical couplers were spliced together. The two laser beams were mixed together in the directional couplers and guided on to the resonator surface. After cleaving, the fibre end of terminal T2 (Fig 3.2) was held within a few microns of the surface of the resonator under study. The fibre was held in position by

means of a piezoelectrically controlled manipulator which had display facilities to measure the movement in three axes: x, y, and z. Both laser beams, each with a different wavelength ($\lambda 1$ and $\lambda 2$), were mixed in the couplers and were incident to the resonator surface. A fraction of this light was absorbed in the surface of the resonator, while the rest was reflected. A fraction of the reflected light was coupled back to the fibre. The fibre guided the reflected light to the detector at terminal T3. Here, an optical filter, filters the activation light and allows the detection light to be detected. In this way the detector only senses the detection laser beam. If the resonator is vibrating, the detection beam will be modulated at the mechanical resonance. The amplified output of the detector was connected to a spectrum analyser (HP: 8568B) and an oscilloscope. In this way we were enable to monitor the vibration spectrum in both time- and frequency-domain.

The modulation drive to the activation laser emitting at $\lambda 2$ was a microprocessor-controlled synthesiser/function generator (HP: 3325A) which can be programmed to sweep a sinusoidal wave over a preselected range of frequencies up to 99 seconds.

4.3. Vibration characteristic

To find a resonant spectrum of a device, the activation laser was modulated over the expected spectrum range which was usually from 0Hz to about 3MHz and the detection laser was on in order to detect the vibration. Normally in this range the device had more than one resonance peak. The first one is assumed to be the fundamental and the rest were higher modes. Fig 4.1 is an example of a fundamental resonant frequency response of a resonator which was 371KHz. It was possible to record more than one resonance on the spectrum analyser display at the same time by holding the trace at its maximum. Fig 4.2 shows the response between 80 and 120KHz of a resonator. In the latter case both traces are superimposed. At each frequency the trace holds its maximum value while the modulation frequency of the activation is swept across the range in question. Fig 4.3 shows the time-domain response of the device examined in Fig 4.2. It can be shown that the electrical modulation of the activation source leads the resonator response by $\pi/2$.

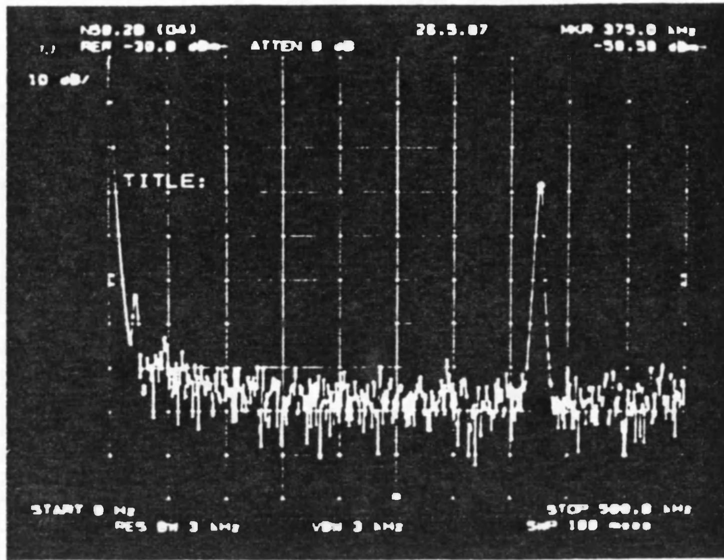

Fig 4.1: The spectrum of reflected signal from a microresonator vibrating at a resonant frequency of 371KHz. The frequency range is from 0 to 500KHz and the amplitude is 10dB/division.

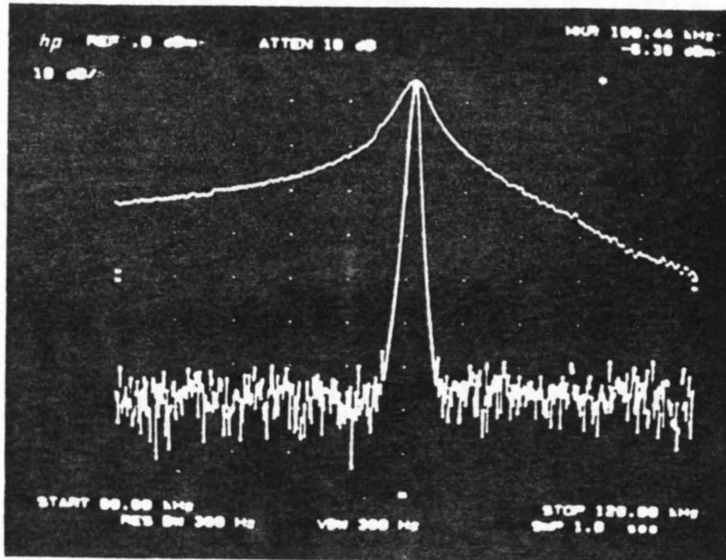

Fig 4.2: The spectrum of reflected signal from a microresonator vibrating at a resonant frequency of 101KHz. The frequency range is from 80 to 120KHz and the amplitude is 10dB/division.

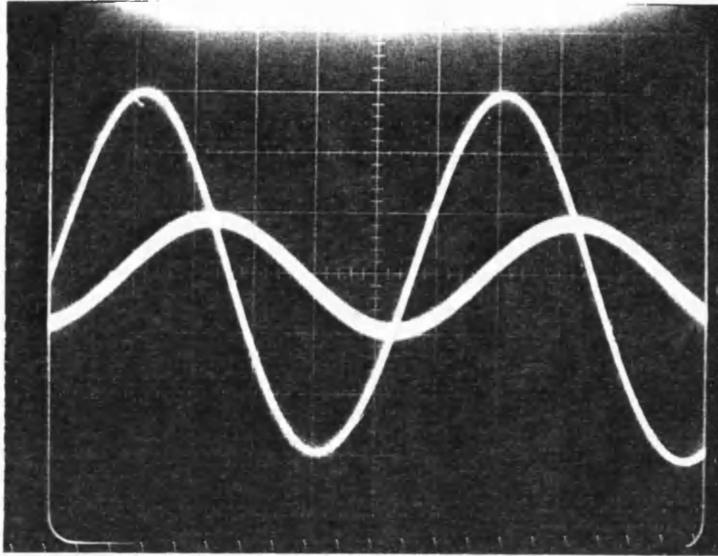

Fig 4.3: The time-domain response of the device examined in Fig 4.2. The drive modulation is also shown.

These devices were activated with a relatively low power. The devices can be sustained at resonance using only 10μW for activation. Fig 4.4 shows the amplitude of resonance against the detection power while Fig 4.5 shows the amplitude against the activation optical power. In each case the signal was measured to an accuracy of ±1dB on the spectrum analyser. The accuracy of the power measured is ±10μW. The spectrum analyser noise floor is -95dBm±5dBm.

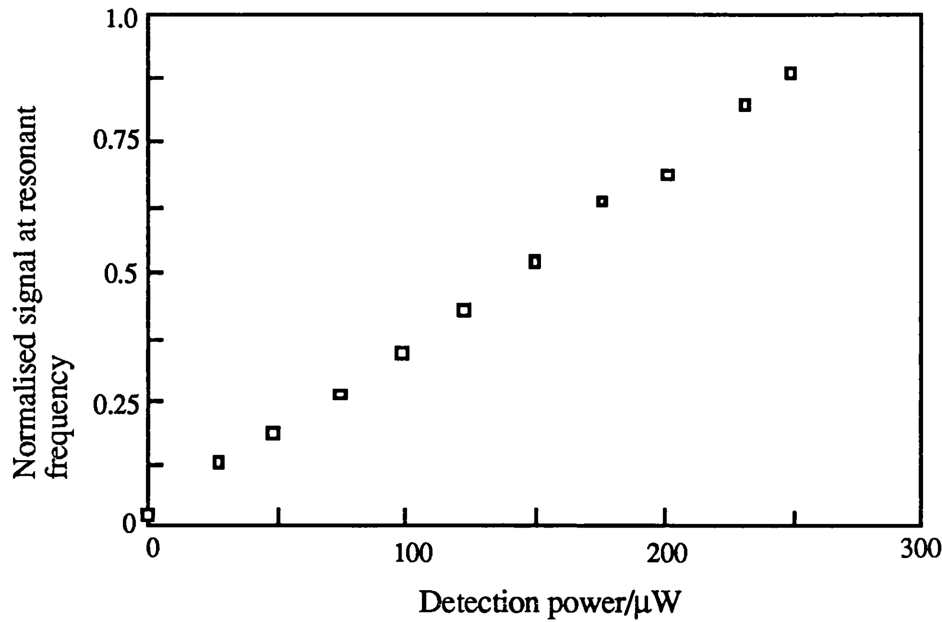

Fig 4.4: Amplitude of received signal at frequency of resonance plotted against incident power used for detection .

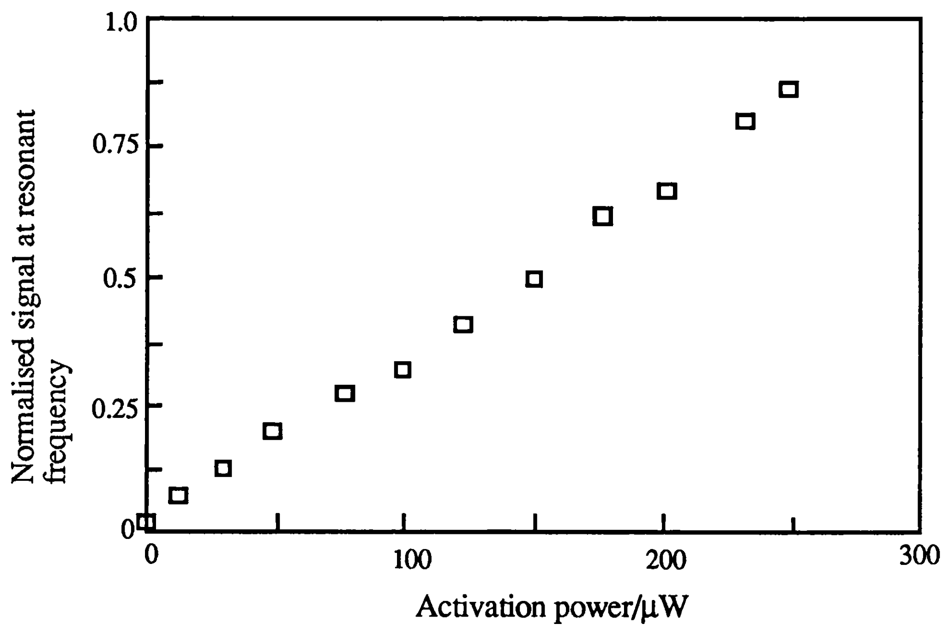

Fig 4.5: Amplitude of received signal at frequency of resonance plotted against incident power used for activation.

Different geometries have been activated, some of them will be discussed in the following:

1 . Paddle beams: The resonant frequencies of the silicon beam of Fig 4.6.a were 111, 269, 347 and 574KHz with quality-factors of 78, 75, 75 and 125 respectively. The dimensions were L=184μm, w= 2, L_w=31, L_p=12 and thickness of 0.5μm. It was sputter-coated with 60nm of gold. A scanning electron micrograph of a paddle beam is shown in Fig 4.7. The resonant frequencies of the silicon beam of Fig 4.6.b were 199 and 581 with quality-factors of 33 and 53. The dimensions were L=170μm, w= 2, L_p=20, w_p=7 and thickness of 0.5μm. It was evaporation-coated with 200nm of aluminium.

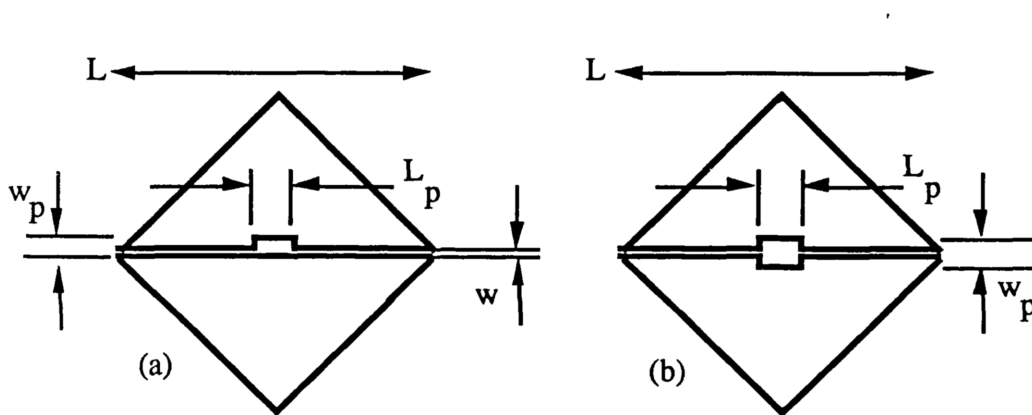

Fig 4.6: A plan view of two paddle beams.

2 . Dual stemmed beams: These beams have a rectangular central platform suspended with a dual stem. The resonant frequency of the silicon beam of Fig 4.8 was 199KHz with a quality-factor of 23. The dimensions were L=170μm, w=2μm, L_p=11μm and a thickness of 0.5μm. It was evaporation-coated with 200nm of aluminium. A scanning electron micrograph of a dual stemmed beam is shown in Fig 4.9.

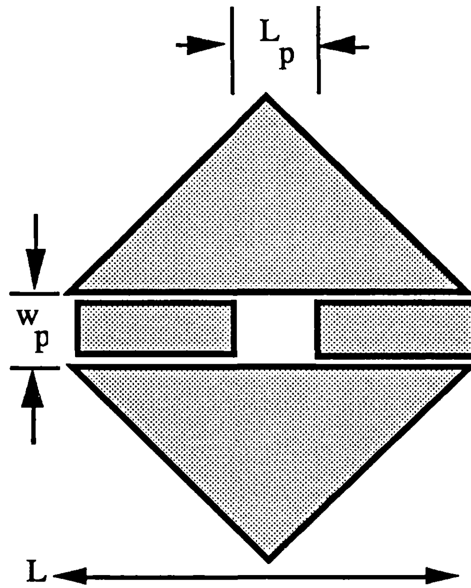

Fig 4.8: A plan view of a dual stemmed beam.

3. Multiple beams: In this structure five simple beams share the same suspensions (Fig 4.10). It may be possible then to couple a vibration from one beam to another via their supports. The fundamental resonant frequencies of these silicon beams were 379, 255, 169, 291 and 284 with quality-factors of 38, 23, 15, 25 and 26. Their dimensions were L=185μm, L_c= 195, w= 7 and they were 0.5μm thick. They were evaporation-coated with 200nm of aluminium. A scanning electron micrograph of a multiple beams is shown in Fig 4.11.

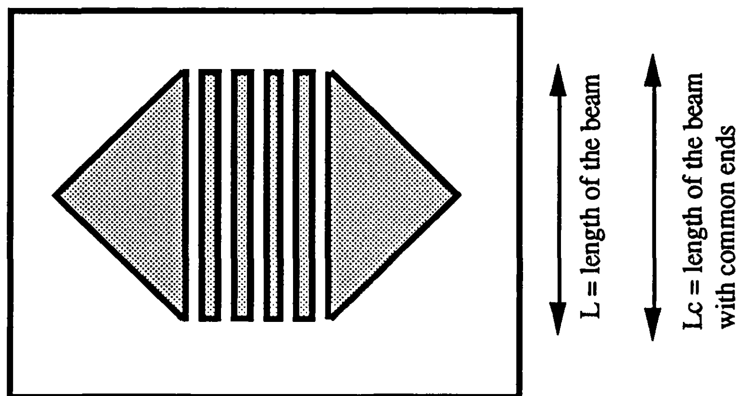

Fig 4.10: A plan view of a multiple beams device.

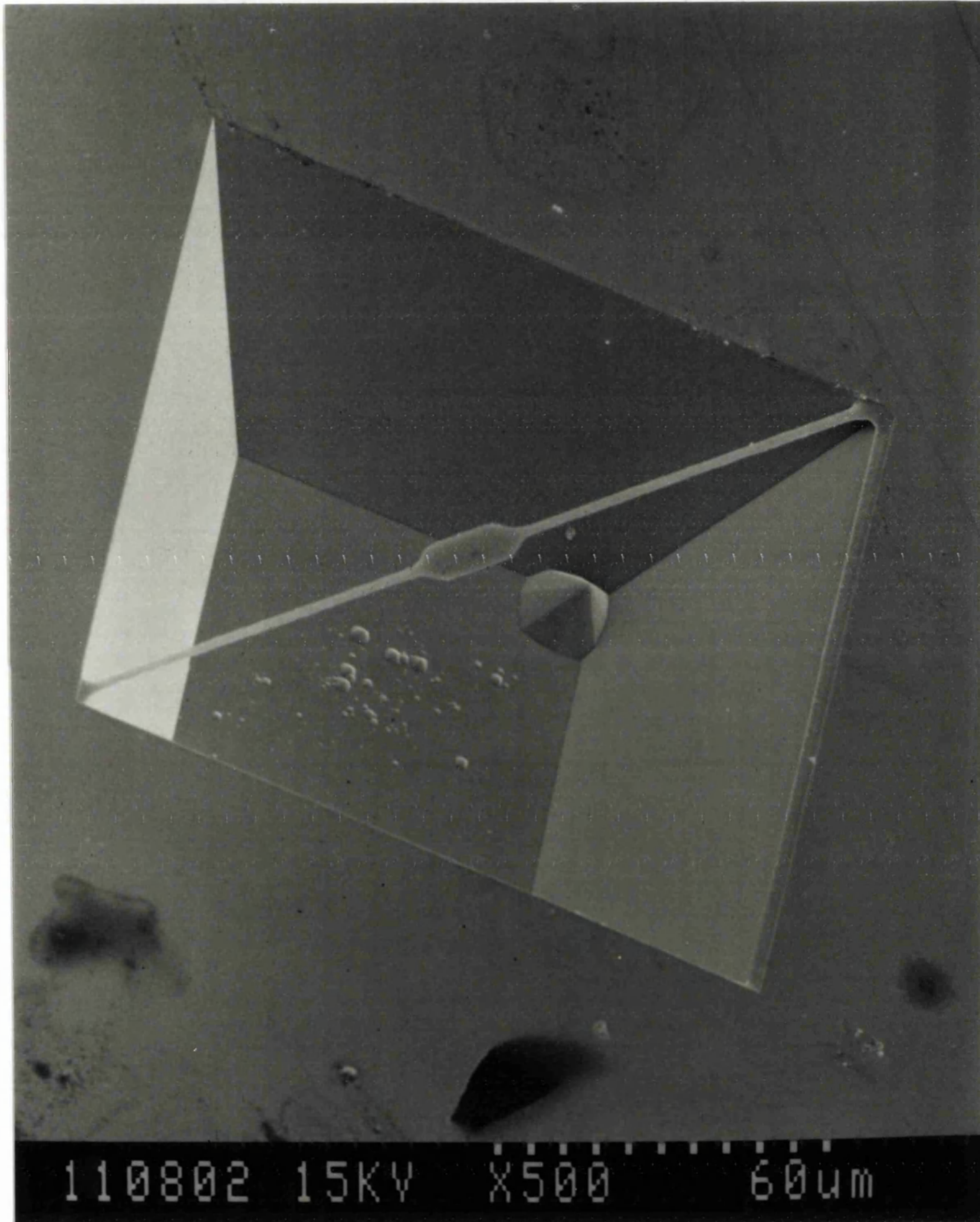

Fig 4.7: A scanning electron micrograph of a paddle beam.

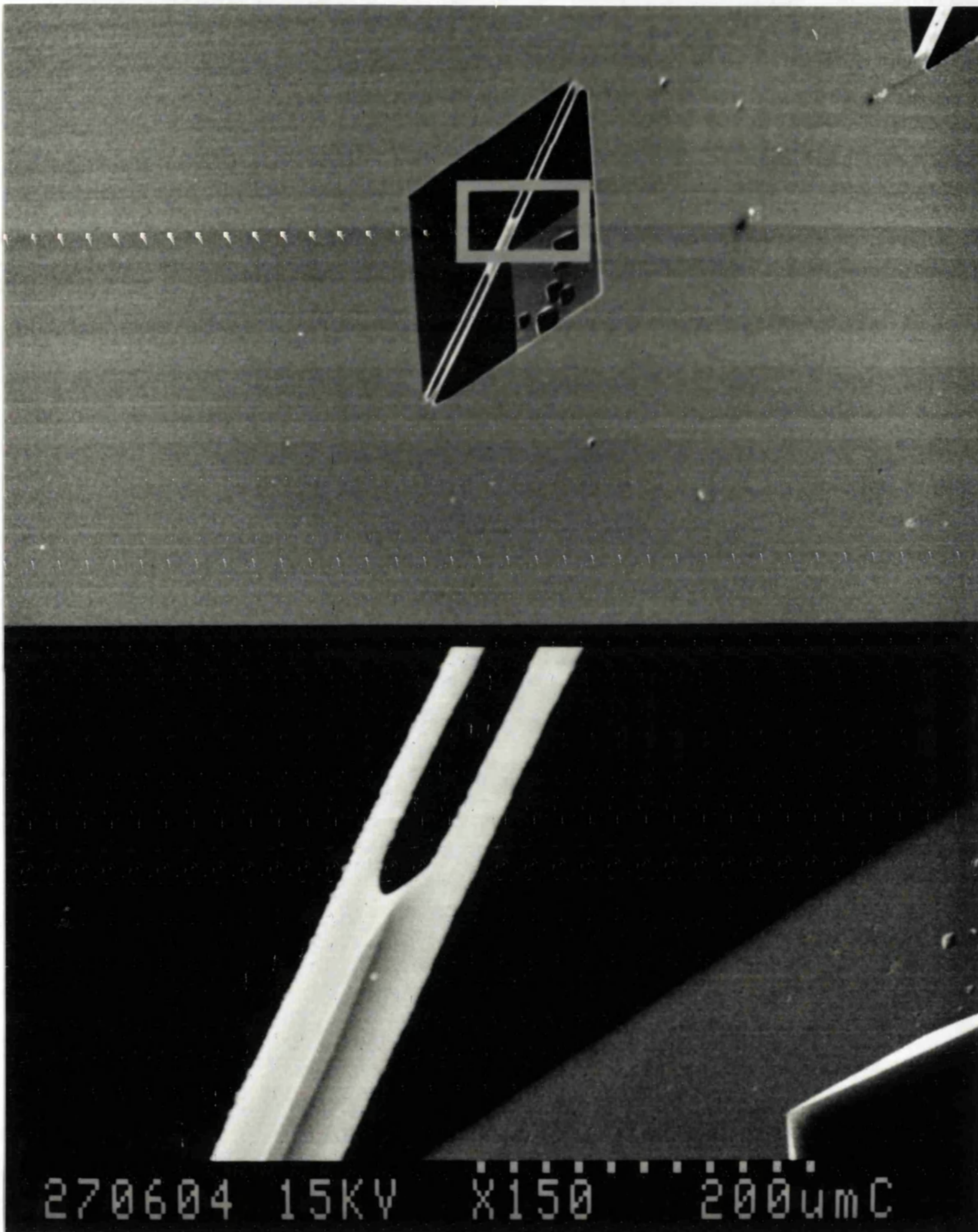

Fig 4.9: A scanning electron micrograph of a dual stemmed beam.

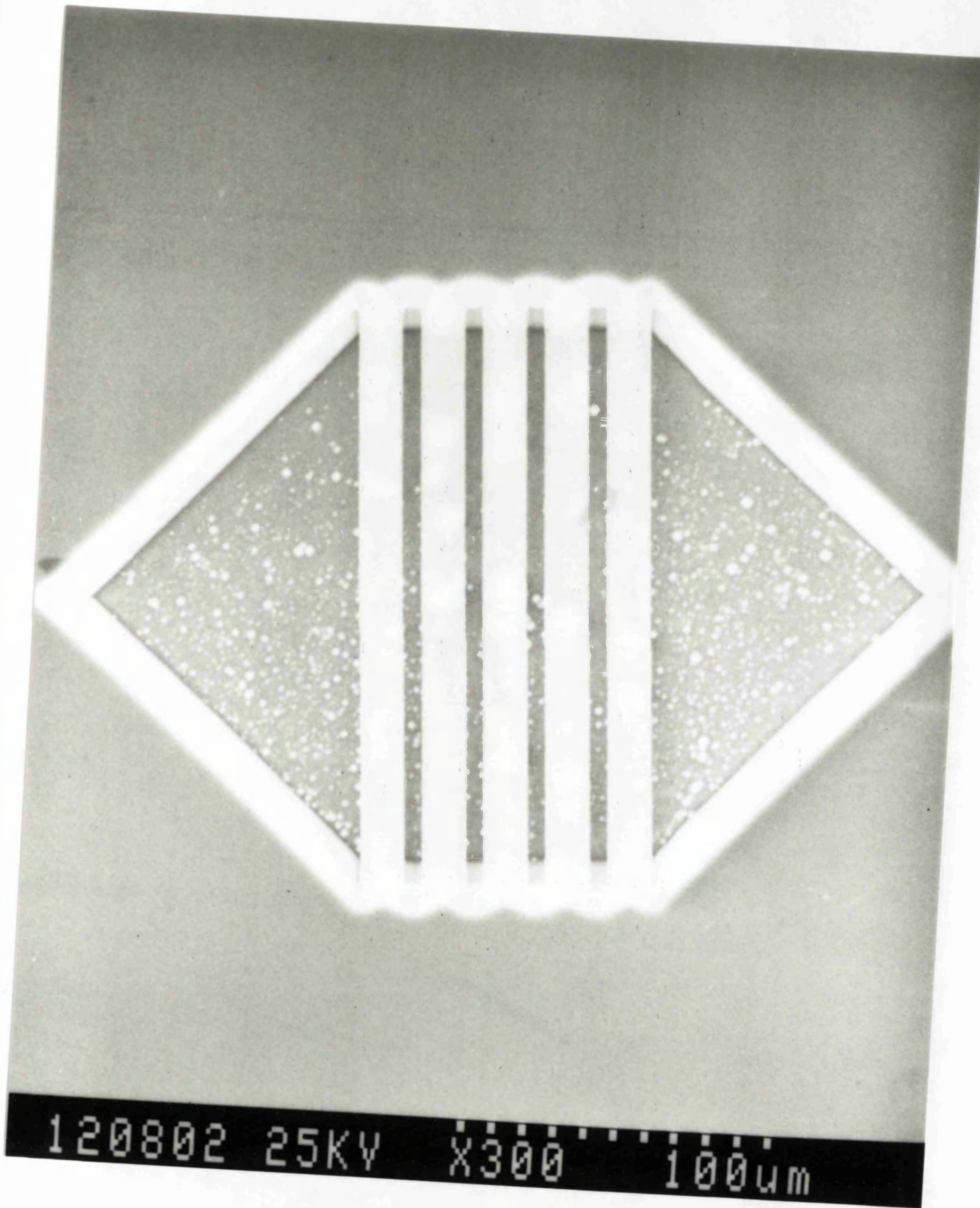

Fig 4.11: A scanning electron micrograph of a multiple beam.

4.4. Optical Activation of Silicon Micromechanical Resonators

4.4.1. Introduction:

The fundamental resonant frequency of silicon microresonators is of principle concern to workers [1-10] in this field for the following reasons. Firstly, the fundamental frequency has the highest amplitude of resonance which is desirable for signal processing. Secondly, for simple strips it has not been possible to activate more than two modes. In the 50 silicon devices that we have characterised, only three are activated into more than two modes, and these have not been simple strips. The experimental results suggest that more complicated shapes of silicon [10-12] or simple strips of oxide or nitride of silicon [13-15] can be activated to more than one mode. Thirdly, the fundamental resonant frequency is well understood quantitatively; mathematical formulas are readily available to quantify effects of stresses and strains upon the fundamental resonant frequency. Lastly, and most importantly, in sensing applications only one resonant frequency is required to interact with the parameter in question [1-7]. Nevertheless, the advantage of the higher modes over the fundamental one is the quality-factor which is related to the mode number. This parameter is required for the precision of the device when used as a sensor; the higher the quality-factor the smaller the change in the measurand that can be measured.

There has also been interest in studying higher resonance modes [11-15], but except for a few cases [11-13], no attempt has been made to find a mathematical formula to model the equation governing the resonance of these devices. The end-condition gives information about the fabrication process and the mode shape of the device which in turn gives information about the state of the atomic stress, the effect of axial stress on the beam and to some extent the geometry of the device.

4.4.2. Experiments:

The devices studied in this section are in the form of simple beams with wider central areas, referred to as wings, coming out from their centres. The first type of beam, shown in Fig

4.12.a, is an asymmetric winged-beam which is 0.5μm thick. The second, shown in Fig 4.12.b, is a symmetric winged beam which is 1μm thick. Fig 4.13 shows a scanning electron micrograph of one of these devices. They were evaporation-coated with 200nm of aluminium.

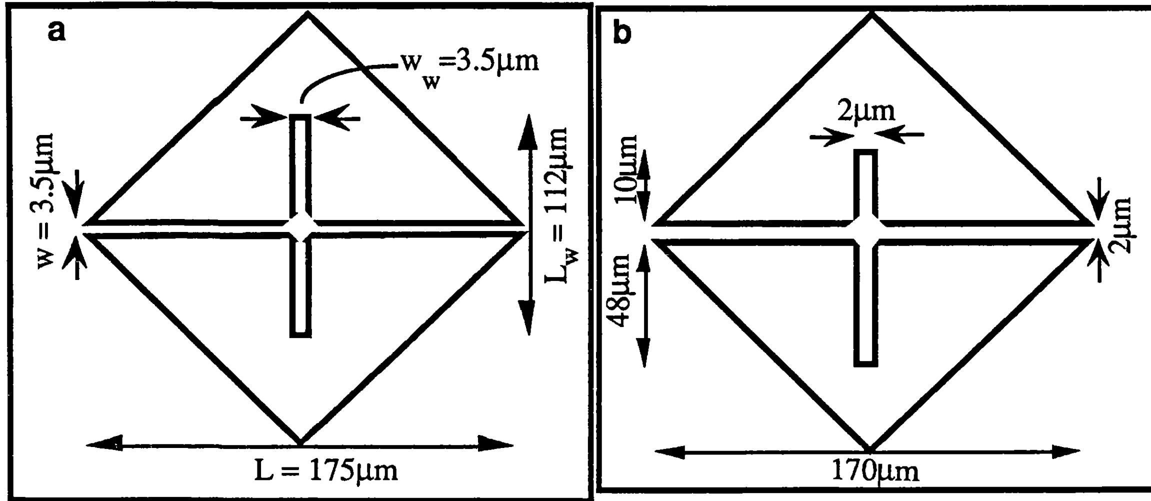

Fig 4.12: A plan view of non-symmetric (a) and symmetric (b) winged beams.

The experimental results for both devices are summarised in Fig 4.14.a and 4.14.b. The experimentally measured resonant frequencies and predicted resonant frequencies are plotted against the mode numbers. The predicted resonant frequencies are calculated from (3.21) and the following points are considered:

i) We have not taken the effect of the wider central area of the wings on the resonant frequency into account; thus the experimentally measured resonant frequencies are expected to be lower than those predicted. The correction factor may be estimated by assuming this additional mass to be in the centre of the beam, in which case the fundamental natural frequency is given by [16]:

$$f_1' = f_1 \left[\frac{2.7\,M}{M_b} + 1 \right]^{-\frac{1}{2}} \qquad (4.1)$$

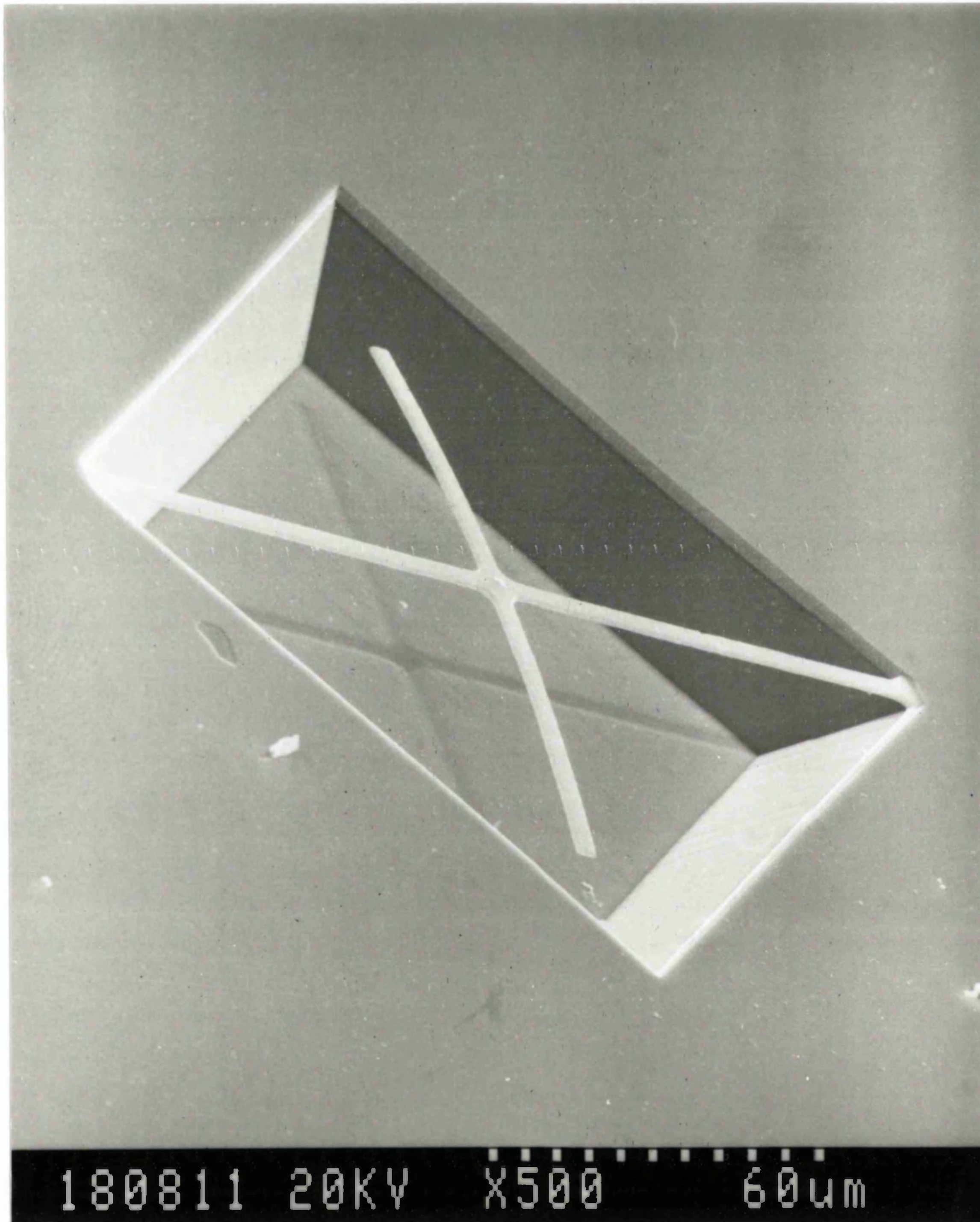

Fig 4.13: A scanning electron micrograph of one of the devices.

where M and M_b are respectively the mass of the central area and the mass of the beam exclusive of the central area, and f_1 is the fundamental natural frequency predicted from (3.21) using the clamped end-condition. For the beam of Fig 4.12(a) and (b), this gives predicted fundamental resonances of about 0.7 and 0.6 of their fundamental resonant frequencies, respectively. The experimentally measured resonant frequency is thus higher than that predicted.

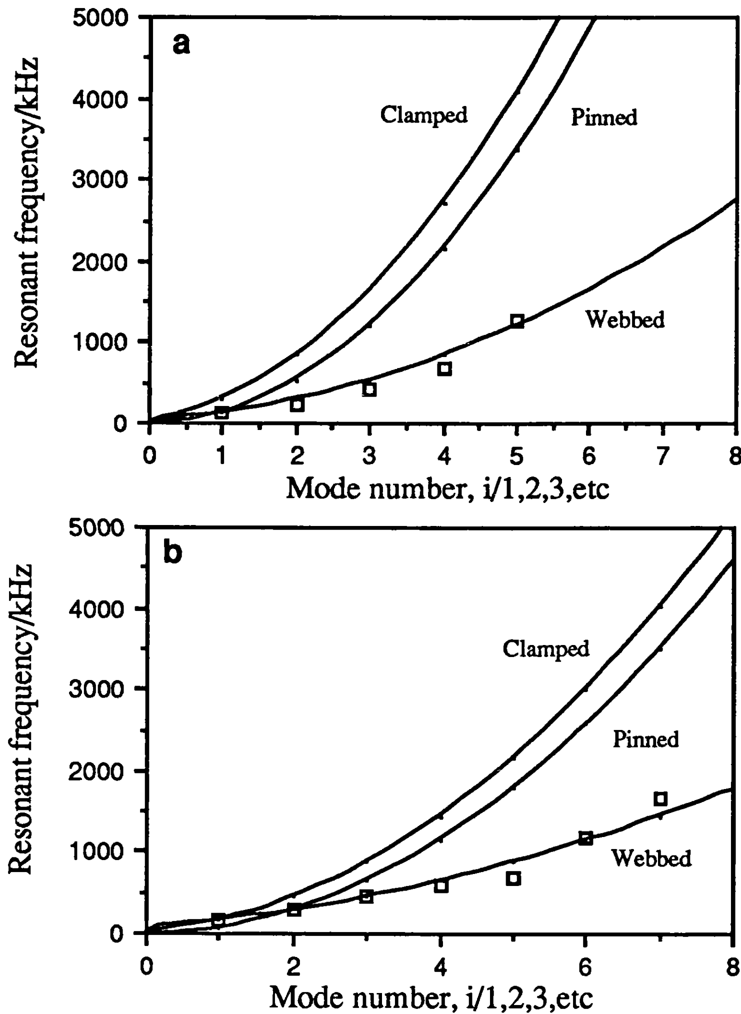

Fig 4.14: Resonant frequency vs mode number for a symmetrical winged beam (a) and non-symmetrical winged beam (b), the devices of Fig 4.12.a and b respectively. The points are experimentally measured values.

ii) A tensile stress introduced to the silicon beam due to boron doping which increases the resonant frequency [11,12,17] has not been accounted for. Overall, the experimental values of the resonant frequencies are higher than those predicted.

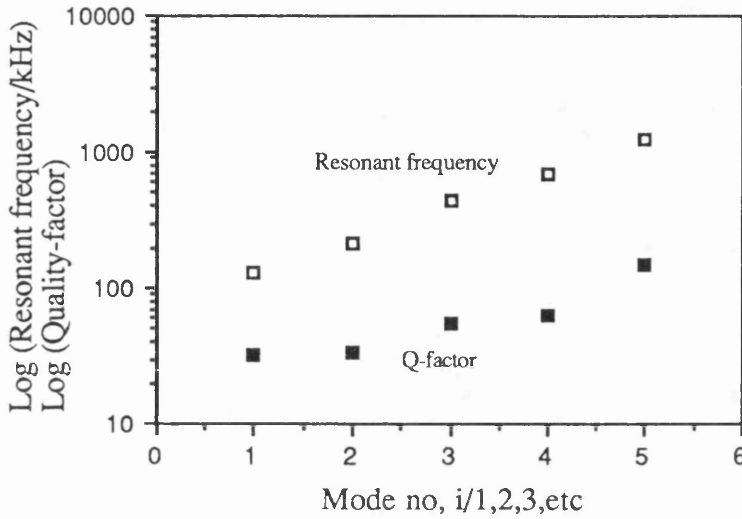

Fig 4.15: The experimental relationship between the resonant frequency, quality-factor and the mode numbers of the device of Fig 4.12.b.

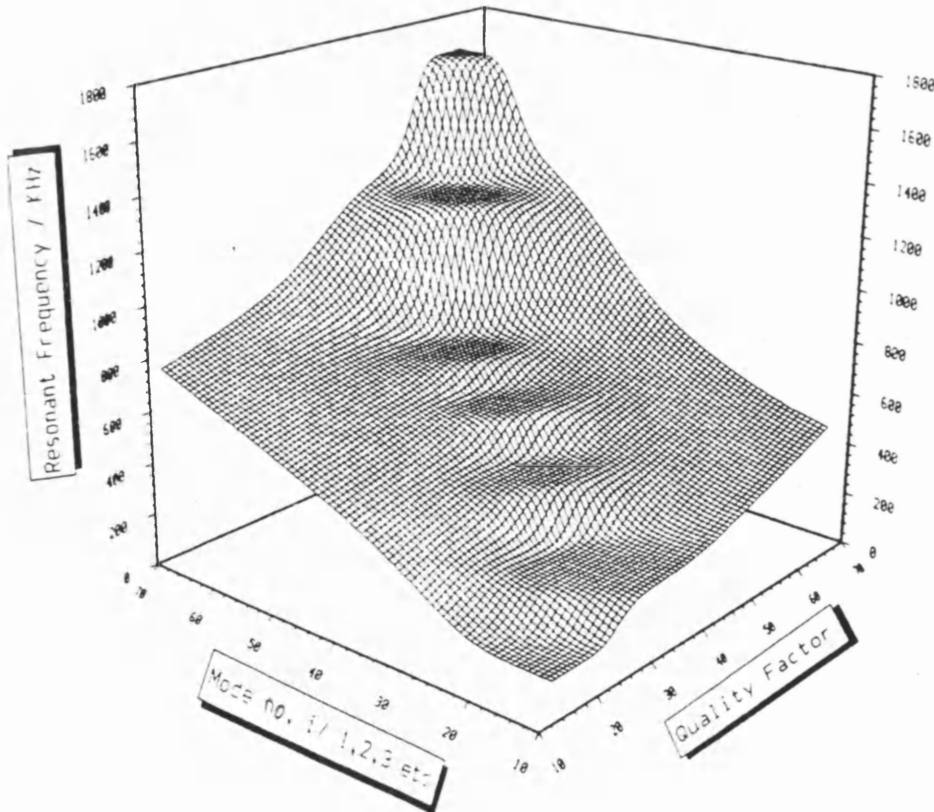

Fig 4.16: A three dimensional plot based on the experimental data shows the relationship between the quality-factor, the resonant frequency and the mode numbers for the device of Fig 4.12.a.

The quality-factor[1] of these devices was also measured and Fig 4.15 shows the experimental relationship between the quality-factor and the resonant frequency of the device of Fig 4.12.b. The experimental dependence of the quality-factor on the resonant frequency and mode number for the device of Fig 4.12.a is shown in Fig 4.16.

4.4.3. Discussion:

In both cases the devices did not obey either of the commonly assumed (conventional) end-conditions, namely pinned and clamped end-conditons[2] . Instead they obeyed a new end condition referred to as 'webbed'. In this case the beam takes end conditions which correspond to a value of λ_i that can be expressed in the form of:

$$\lambda_i = \left(1 + \frac{i}{2}\right)\pi \qquad (4.2)$$

Substituting this value of λ_i in (3.21) we get the equation characterising the resonant frequencies of these devices. Here the integer i has been redefined. When i is an even integer, i.e. i = 0,2,4,etc, λ_i gives a pinned end-condition, and when i is an odd integer, i.e. i = 1, 3, 5, etc, λ_i gives a clamped end-condition.

The new dimensionless parameter λ_i incorporates both end-conditions, clamped and pinned. During the silicon etch stage of the fabrication process, the silicon is undercut at the ends because of the finite etch rate of the (111) silicon planes. This leads to ill-defined strip ends which may be considered to be clamped at their limits but also constrained over about 5μm at both ends by silicon webs. These two effective lengths correspond to the new end conditions (Fig 4.17).

It should be noted that the resonant frequencies of any torsional modes would be proportional to their mode numbers[3] , and do not fit the experimental results.

[1] For quality-factor measurements see section 4.8
[2] See section 3.4.3.
[3] See section 3.4.2.

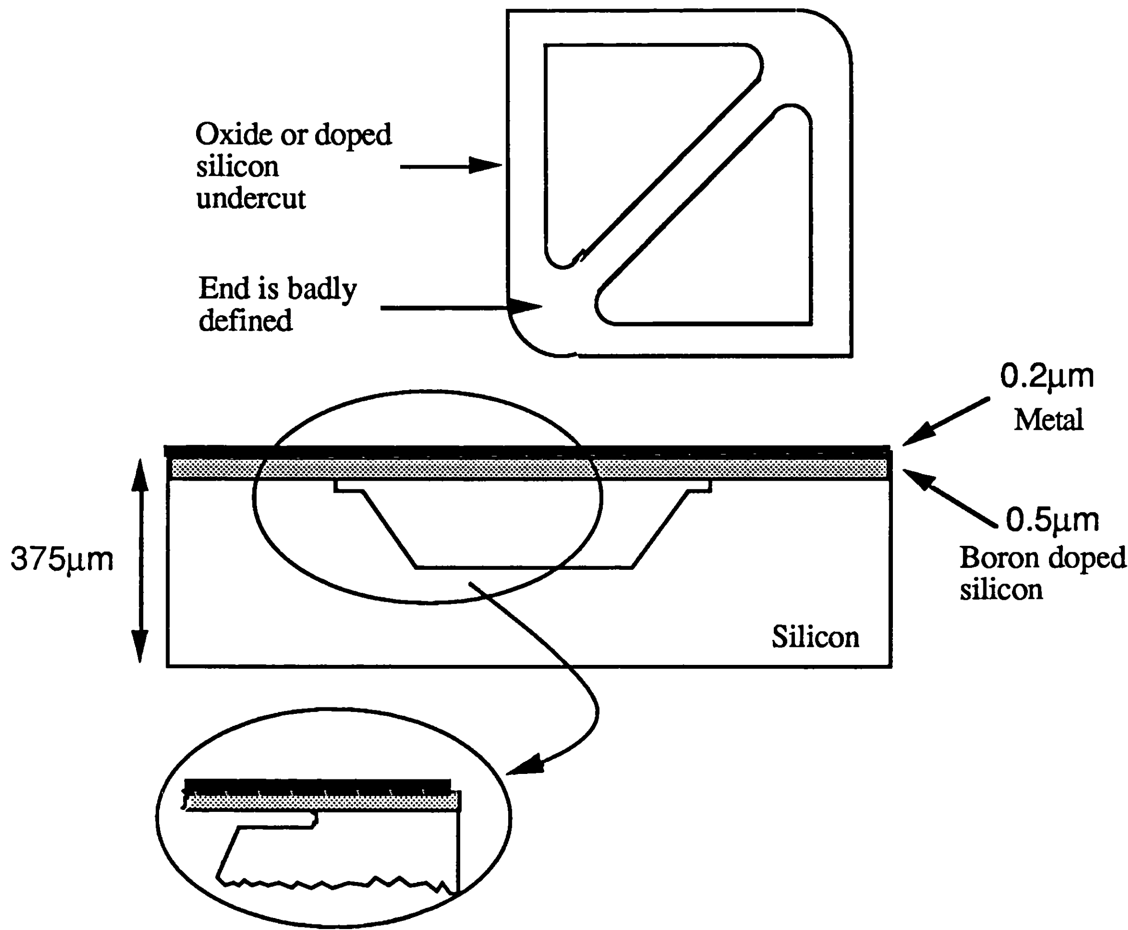

Fig 4.17: Ill-defined resonator ends which may be considered to be clamped at their limits but also constrained over about 5μm at both ends by silicon webs. These two effective lengths correspond to the new end-conditions.

In summary, we have identified the effect of the fabrication on the microresonators which includes a modification of the end-conditions. This may be justified by considering that the resonator beam is undercut beyond the strip itself. The new end-conditions require a new mathematical formula (4.2) which modifies the simple equation for the natural frequencies of flexural vibrations of beams.

4.5. Stress Measurements of Doped Silicon Using Micromechanical Resonators

4.5.1. Introduction:

Boron is commonly used to dope silicon in order to act as an etchant stopper during the anisotropic etching technique. Chemical etching effectively stops in silicon samples doped with more than 4×10^{19} cm^{-3}, i.e. about 0.01% of boron [17]. Using these doping levels, silicon samples can be shaped into simple beams, diaphragms or more complicated devices [17]. Peterson is the first to explain the etch-stop mechanism in terms of B-Si bonds. These bonds are so strong that they stop chemical etching (chemical machining). He was also the first to indicate that the smaller boron atoms replacing the silicon atoms in the lattice structure put the crystal under stress. The mismatch between the atomic radii of single crystal silicon and boron introduces undesirable localised stress in the doped region which changes the properties of silicon.

To date no one has yet quantified these stresses despite the importance of silicon in today's technology. Here, we use a non-destructive method to quantify these stress levels.

The resonant frequency of the single crystal silicon has been calculated and compared with the measured resonant frequency which is the resonant frequency of the silicon after doping and metal coating, i.e. after introducing the stresses. This method has been utilised to quantify the stresses due to boron doping and metal coating. In this technique physical contact was not made with the device. The device is activated and detected optically.

4.5.2. Theoretical analysis:

The resonant frequencies f_i of flexural vibrations of a homogeneous prismatic beam are given by (3.21) and the effect of the metal coating is given by (3.26).

The shift in resonant frequency f_F for a beam of rectangular cross-section subjected to a tensile stress, σ, can be calculated from [18][4] :

$$\left(\frac{f_F}{f_o}\right) = \pm \frac{0.147 L^2 \sigma}{E t^2} \qquad (4.3)$$

where f_o is the resonant frequency of the relaxed beam; L and t are the length and the thickness of the beam, respectively; E is the Young's Modulus. The positive and negative signs are applied to the applications of tensile and compressive stress respectively.

To measure the tensile strength σ_t of an elastic solid, a beam of the solid can be pulled by a tensile stress σ and when the solid reaches a value of tensile strength the atomic bonding joining two neighbouring atomic planes breaks. So the tensile *strength* is the maximum tensile *stress* that the solid can stand before it breaks. Cottrell [19] estimates the tensile strength of a solid by:

$$\sigma_t \approx \frac{E}{10} \qquad (4.4)$$

For silicon with Young's modulus of 19 x 10^{10} Nm^{-2} this value is 19 x 10^9 Nm^{-2}. Petersen's (1982) value for tensile strength of silicon is 6.9 x 10^8 Nm^{-2}.

4.5.3. Devices and Experiments:

Micromechanical resonators, in the form of strips of boron doped silicon, have been fabricated using anisotropic etching techniques, and coated with a thin layer of metal. Two types of end suspensions were designed. Fig 4.18 shows a 'simple' strip beam and Fig 4.19 shows typical 'modified anchor point' strips. The dimensions of these devices are 180µm long, 3.5µm wide and 1µm thick, and they were coated with 200nm evaporated aluminium.

[4] For deals see chapter 7. Here we assumed the end-conditions are clamped.

The typical experimental values of resonant frequencies of both devices were 443KHz which is accurate to within 1%. The typical measured quality-factors were 66 and 56 for simple strips and modified anchor point strips respectively. Thus, these devices show higher resonant frequencies than those calculated from (3.21).

4.5.5. Discussion and conclusions:

The experiment confirmed that the two end structures considered have no effect on the resonant frequency. The calculated resonant frequency from (1) for single crystal silicon is about 286KHz, and taking the metal coating into account the equivalent figure is 294KHz. Therefore the measured value of the resonant frequency (443KHz) is 149KHz higher than that predicted which is equivalent to 150%. A number of factors affect the resonant frequency.

1 . Silicon beams doped with boron are under tensile stress owing to the replacement of the silicon atoms by smaller boron atoms in the lattice structure. The boron atoms, at these levels of concentrations, are an average 20-25 Å apart which is near the solid solubility limit [17]. The solid solubility for boron substitutions introduced into the silicon lattice is 5×10^{19} cm^{-3}. Moreover, at higher concentrations (above 5×10^{19} cm^{-3}) the boron atoms enter interstitial sites. This in turn introduces further tensile stress in the beam resonator which significantly increases the resonant frequency [11,12].

2 . Equation (3.26) predicts that the resonant frequency of the beams increases by 8KHz with 200nm of aluminium coating. However the metal coating may have other effects on the resonant frequency which will be discussed in chapter 7.

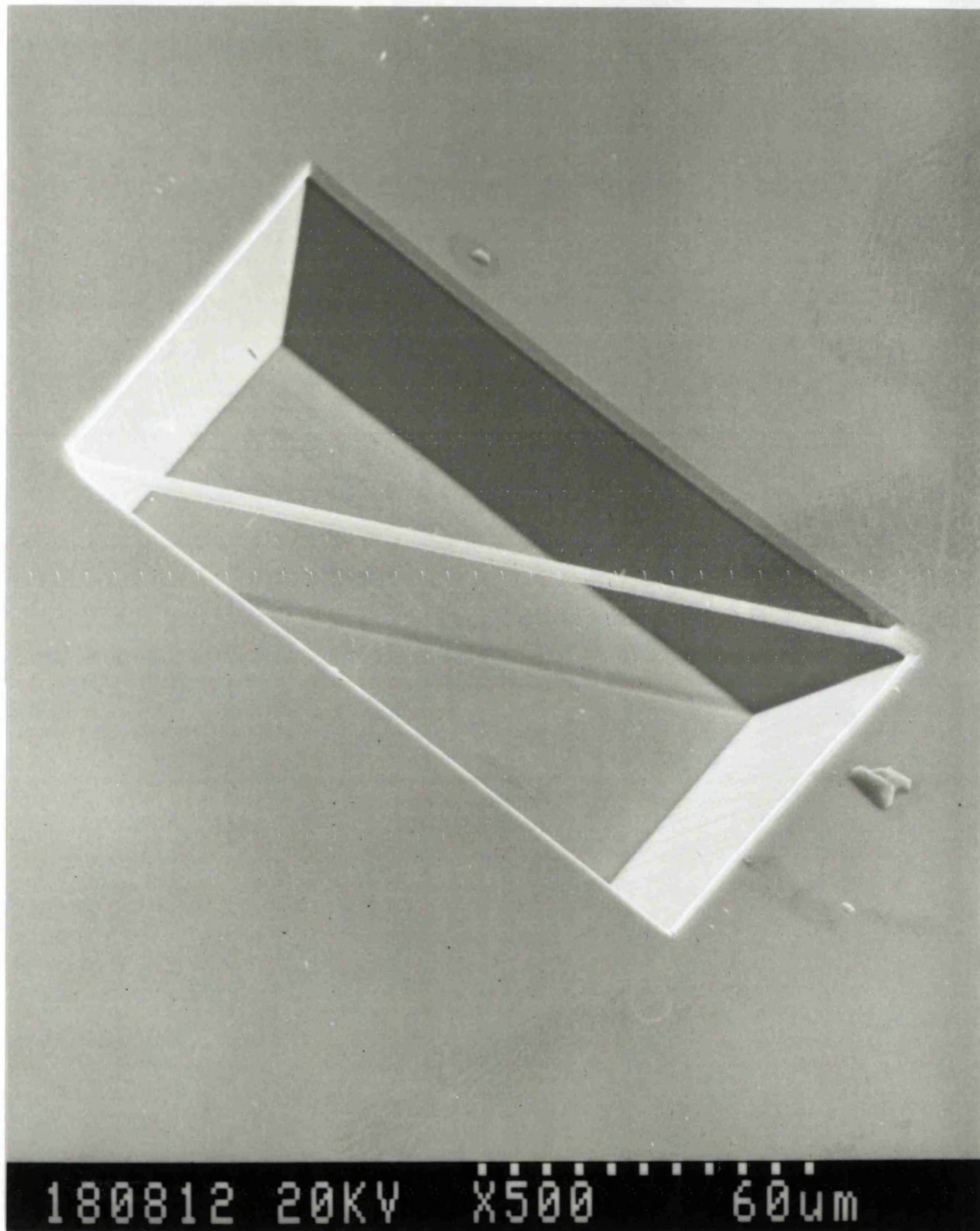

Fig 4.18: Scanning electron micrograph of a simple beam.

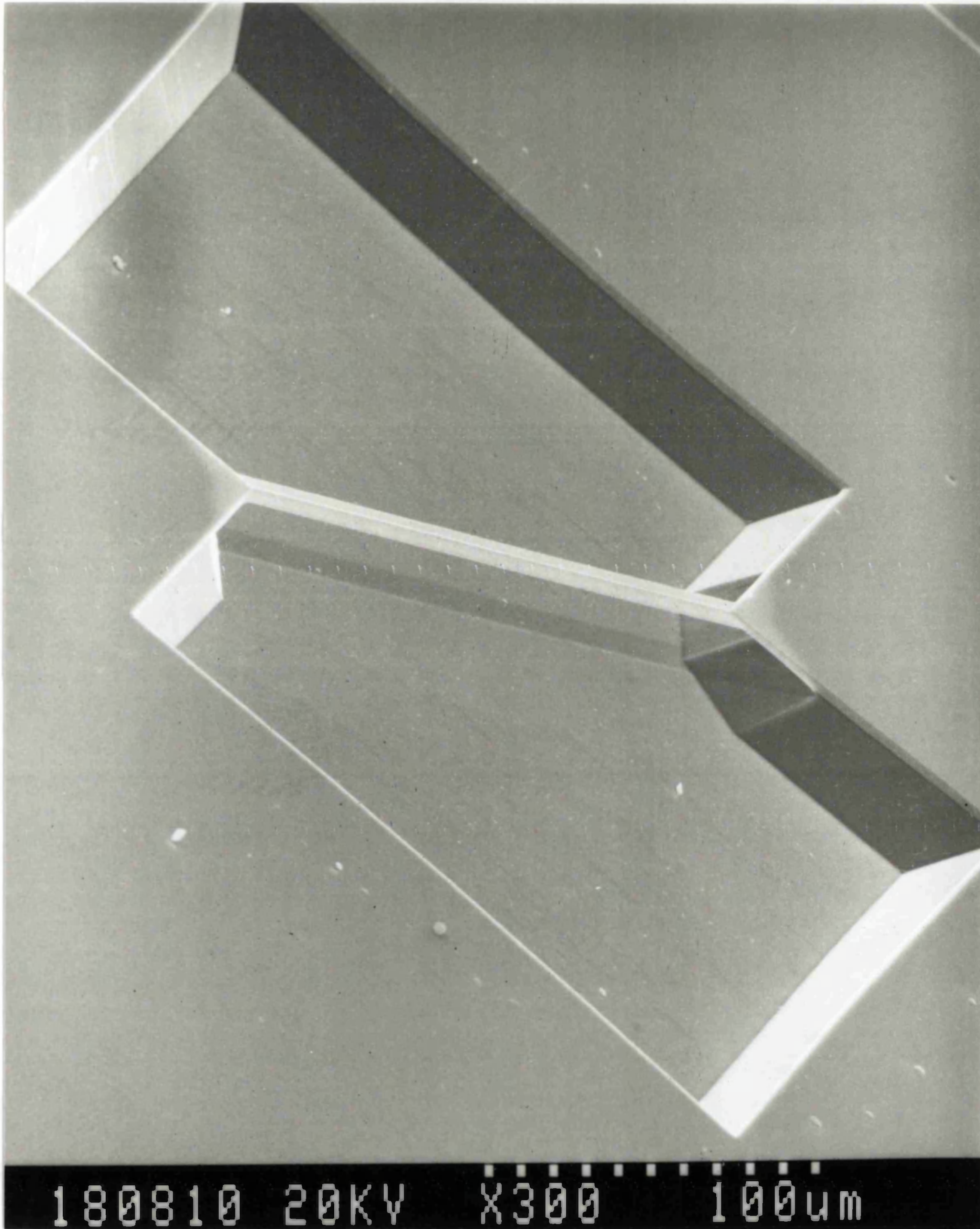

Fig 4.19: Scanning electron micrograph of a modified anchor point.

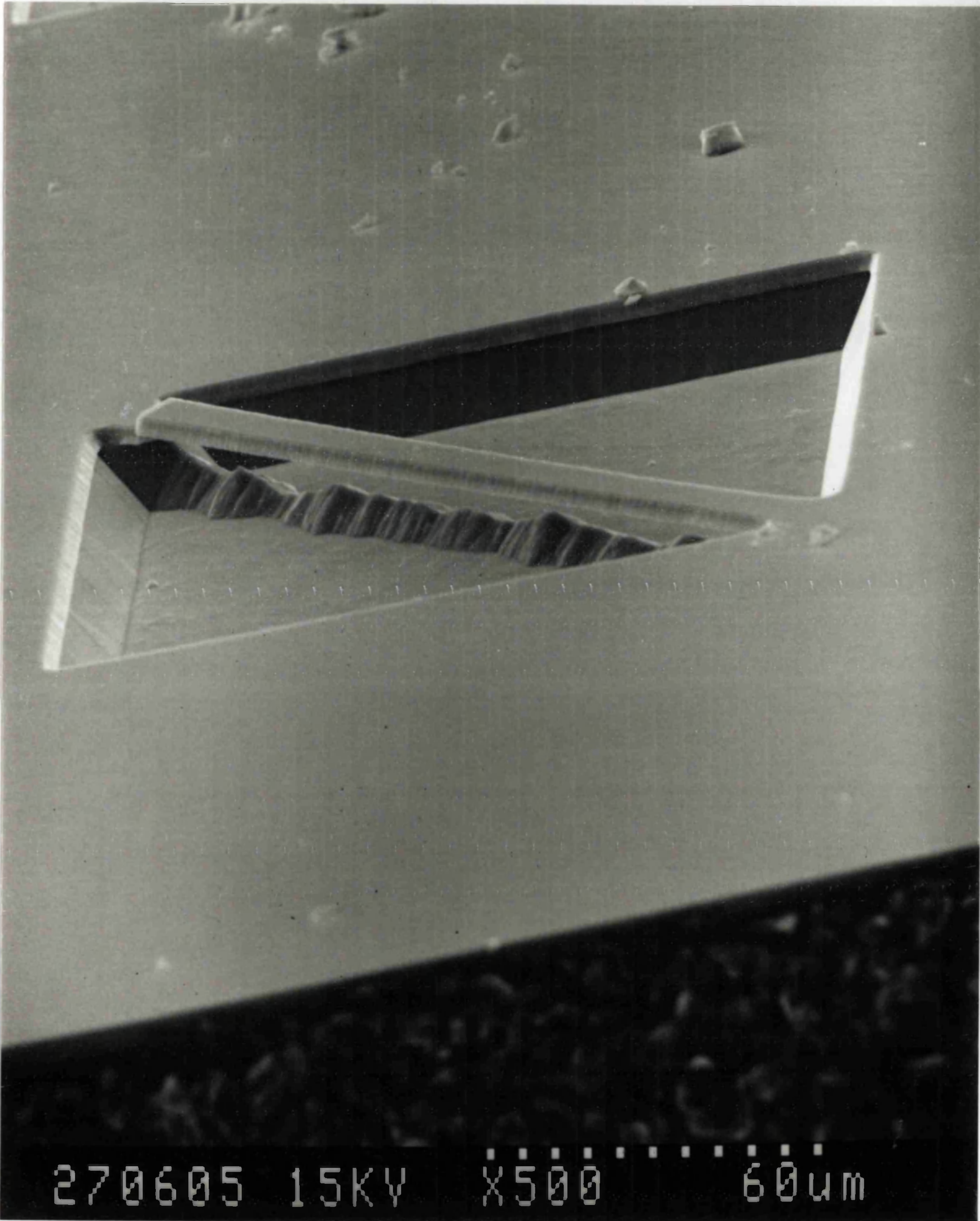

Fig 4.20: Mechanical breakdown of a silicon beam under the tensile stress.

3 . The optical power used for detection increases the temperature of the beam. This in turn offsets the resonant frequency since a stress due to the power absorption will be induced in the beam. If the thermal stress σ_θ is given by

$$\sigma_\theta = E \alpha T \qquad (4.5)$$

where α is the linear expansion coefficient and T is the temperature rise of the beam. Substituting (4.5) in (4.3) shows that this effect gives rise to less than 1% change in the resonant frequency for the dimensions shown here.

The effect of the first mechanism therefore is higher than the rest so we assume that the only mechanism responsible for changing the resonant frequency of silicon beams is due to boron doping.

The doping therefore increases the fundamental natural frequency of the resonator beams by about 150%. This is equivalent to inducing a tensile stress of 601 x 10^6 Nm^{-2}. However, this tensile stress is still well below the theoretical prediction of the tensile strength of silicon. Furthermore, dislocations and defects that may be produced during fabrication and processing the wafer can lead to fracture well below the theoretical value of the tensile strength. Fig 4.20 shows a mechanical breakdown of a silicon strip under the tensile stress.

In summary, we have identified that boron doping in silicon introduces tensile stress in silicon wafers. This stress modifies the simple equation for the natural frequencies of flexural vibrations of beams. Nevertheless, it should be pointed out that the effect is different for different device geometries as can be noticed from (3). This equation shows that the shifted resonant frequency depends upon the length and thickness of the beam resonator.

4.6. Reproducibility of the results for silicon beams

The following beams have the same geometry but different width which does not affect the resonant frequency (chapter 3), and they are evaporated with 200nm of aluminium. Two different dimensions similar to that shown in Fig 3.1 were studied. The first group shown in Table 1 had dimensions of 175μm long, 1μm thick and their widths were as shown below. The second group, shown in Table 2, had dimensions of 170μm long, 0.5μm thick and the width of each of them was 4μm. Each group came from the same wafer, so they experienced the same fabrication conditions.

Table 4.1:

Width/μm	Resonant frequency/KHz	Quality-factor
2	426	47
4	443	66
4	443	56
10	443	67
12	450	80
14	420	54

Table 4.2:

Resonant frequency/KHz	Quality-factor
362	50
342	88
317	47
318	33
348	42
321	51

Therefore, the reproducibility of the results is within 5-10%.

Some inaccuracy in calculating the resonant frequencies occurs owing to the mis-shaping of the resonator. Uneven processing introduces inaccuracies into the calculated frequencies. Slow sideways etching of the silicon creates a trapezoidal beam cross-section which has a lower second moment of area than an equivalent rectangular cross-section, decreasing the resonant frequency.

4.7. Optical Activation of Silicon Dioxide Micromechanical Devices

4.7.1. Introduction:

When silicon is thermally oxidised, the resulting silicon dioxide is in a state of compression, hence when a silicon dioxide beam is defined by etching the silicon beneath an oxide strip deflects it either upward or downward. This compression is a combination of intrinsic stress and thermal stress. The intrinsic stress is attributed to the 120% molar volume expansion resulting from the conversion of silicon to its oxide [20]. The thermal stress is induced when the wafer, oxidised at around $1000^{o}C$, is cooled to room temperature. When the beam is undercut and allowed to deflect, nearly all the stress is relieved.

Two properties of thermally grown silicon dioxide on silicon can be pointed out. Firstly, the abrupt change in material properties from silicon to its thermally grown oxide and the nature of the interface between these two materials. Secondly, silicon dioxide has a similar structure to fused silica. Fig 4.20 shows the structure of amorphous silica which is distinguishable from crystalline quartz by having a more open structure: only 43% of its space is occupied [21]. As a consequence of the open structure of silicon dioxide a wide variety of impurities diffuse through it. These impurities may effect the behaviour of the beam.

Several authors have reported stress measurements of oxide/silicon interface which may be summarised as follows:

1. The stress in 2000Å -20 000Å silicon dioxide films grown on silicon was first measured by Jaccodine & Schlegel (1966) [22]. The radius of curvature of a 'balloon' and a 'beam' were measured. In the balloon method, the oxide is used as a balloon and the radius of curvature is measured in the inflated state. The oxide from one side of a 2mm thick silicon beam was removed; as a result the beam bent under the stress between the oxide and the silicon. The stress was measured from the curvature of the bending beam. Their work had two conclusions. Firstly, for oxidations carried out at 1200°C the compression stress is 3.1×10^{9} dynes cm^{-2}. Secondly, no orientation dependence of strain was found for the (111) and (100) samples.

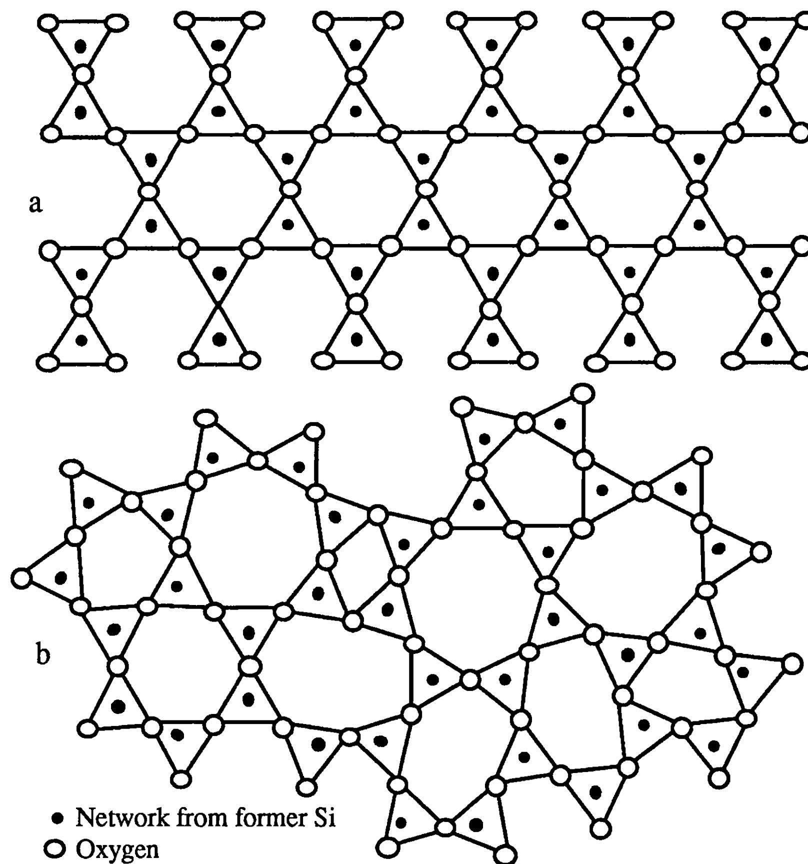

Fig 4.21: The structure of (a) amorphous and (b) fused silica.

2. The oxide from one face of the silicon sample has been removed by Whelan et al (1967) [23] (Fig 4.22) and the resultant bending of the silicon measured by x-ray diffraction to measure these stresses. They found that, for an oxide thickness of about 1µm, the stress is independent of the silicon orientation and its magnitude in the silicon is about 9×10^7 dynes cm^{-2} and in the oxide is about 4×10^9 dynes cm^{-2}. A similar method was used by Alexandrova et al (1988) [24] but they used Newton's rings produced by an interferometer between the curved substrate and the reference with a known curvature. They found that curvature depends on the thickness (12-70nm) of the oxide and the oxidation condition; in general a curvature of 1-2.5 µm was measured for samples of approximately $800mm^2$.

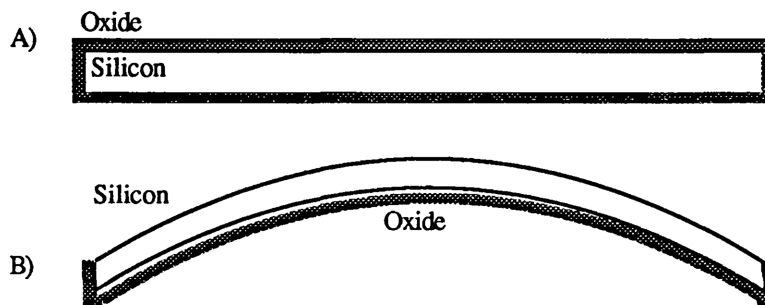

Fig 4.22: Measurement of stresses induced in silicon and its thermally grown oxide used in [23]. A radial cross-section is shown.

3. The bending of unsupported windows (diaphragms) (Fig 4.23) and beams (cantilevers and microbridges) of silicon oxide utilised to obtain relationships between the thickness and width of the windows. Using this method the stable limit thickness/width for diaphragms and beams were obtained by Wilson et al (1972) [25] and by Jully & Muller (1980) [26].

4. Lin and Pugacz-Muraszkiewicz (1972) [27] fabricated silicon dioxide beams (cantilevers and microbridges). The stress in these beams was relieved after undercutting and as a result the beams deflected. The stress induced in the beams was measured by measurement of the deflection. It was of the order of 3×10^9 dynes cm^{-2} in the oxide beam. It was also found that for an oxide thickness below 1µm all the compressive stress is relieved after undercutting of the microbridge. This result is significant for our measurements since we are dealing with an oxide thickness not greater than 1µm.

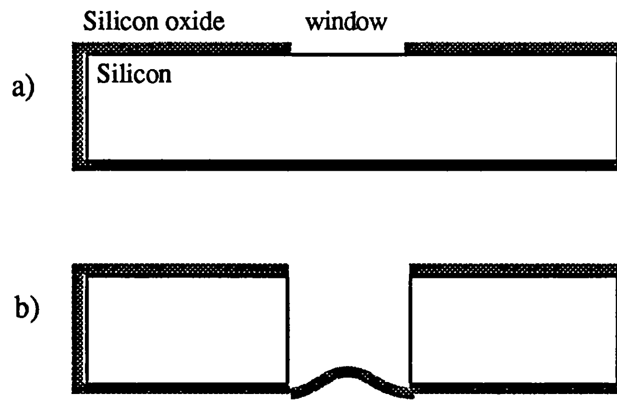

Fig 4.23: Measurement of stresses induced in silicon and its thermally grown oxide used in [25]. A cross-section is shown.

5. Conru (1976) [28] used the gate region of a field-effect transistor (FET) as a thin oxide sample for measuring the stress induced in the silicon/oxide interface After etching the silicon, the oxide in the gate region deflected to release the compression stress and then an SEM was used to measure the deflected oxide film. With this method stresses in the range of 1.5 - 5.1 x 10^{10} dynes cm^{-2} were measured in the oxide of 500-700 Å.

6. With reference to Fig 2.24, the silicon was removed from beneath an oxide film. A relationship, for oxide layers up to 300Å, was found by Pugacz-Muraszkiewicz [29] between the stress and the ratio of the depth of deflection of the oxide to the wavelength of the corrugated oxide (Fig 4.25).

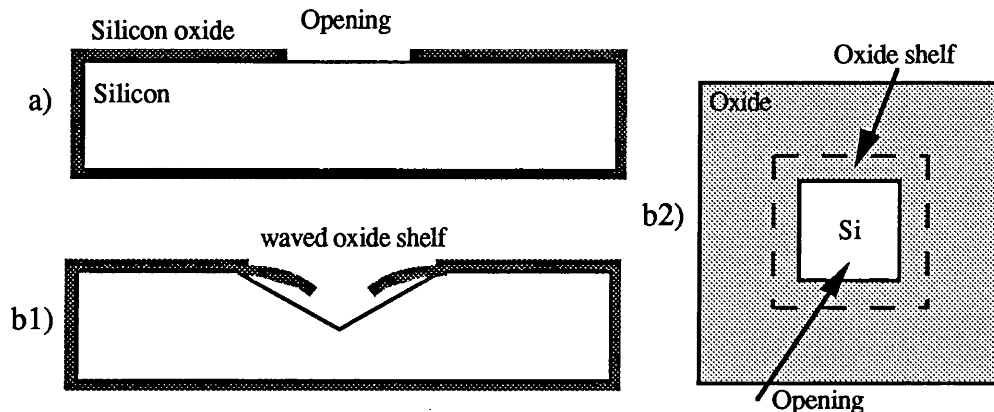

Fig 4.24: The oxide shelf method to calculate compression stress in the oxide grown on silicon. Pugacz-Muraszkiewicz [29].

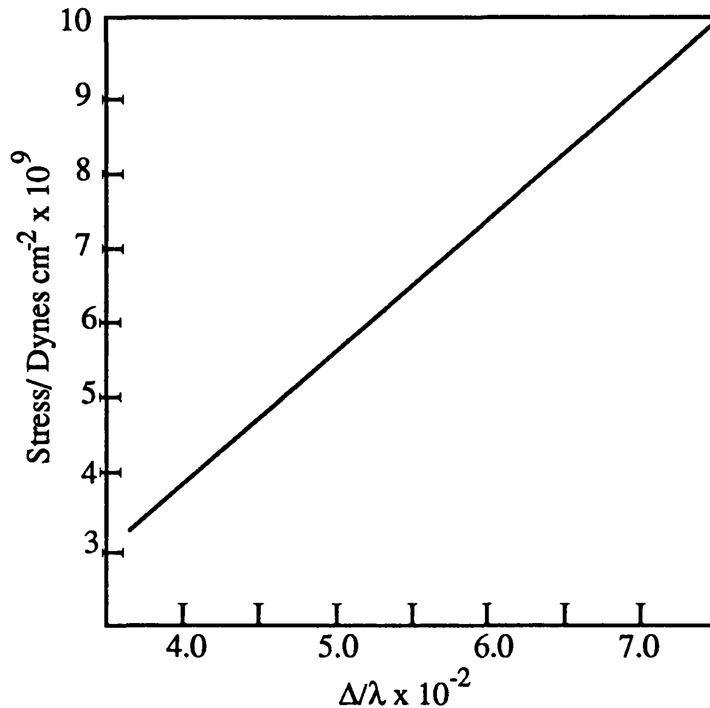

Fig 4.25: The relationship between the stress and the sinusoidal undulations of the oxide shelf. After Pugacz-Muraszkiewicz [29].

The stress measurements in the above methods depend on the measured displacement of the oxide films. The stress has been quantified to be in the order of 3×10^{10} dynes cm^{-2}. However, a complementary technique is to activate the oxide elements (beams or diaphragms) etched on the silicon wafer. This activation can be achieved by sustaining the oxide element at its mechanical resonant frequency which encodes the mechanical state of the beam. By comparing measured and calculated values of the resonant frequencies, the remaining compression stress in the oxide element can be accurately measured. When the oxide element is deflected under compression stress, it is not implied that it is in its plastic regime and unsuitable as a mechanical device. However, this deflection has advantages and disadvantages when the device is used as a sensor (chapter 7).

Using this method the effect of the different metal coatings on the oxide beams can also be studied since the resonant frequency of the beam shifts with varying metal thickness.

4.7.2. Dependence of compression stress on thickness-to-width ratio:

It has been shown that the stable limit of the built-in compression depends upon the ratio of the thickness to the width of the silicon dioxide film. The ratio for unsupported rectangular oxide films (diaphragm) [25] is given by (4.6) and that for cantilevers [26] is given by (4.7).

$$0.52\sqrt{\Delta\alpha\,\Delta T} < \frac{t}{w} < 1.2\sqrt{\Delta\alpha\,\Delta T} \qquad (4.6)$$

$$0.4\sqrt{\Delta\alpha\,\Delta T} < \frac{t}{w} \qquad (4.7)$$

where t, w, $\Delta\alpha$ ($\Delta\alpha_{Si}$ - $\Delta\alpha_{SiO2}$) and ΔT are respectively the thickness, the width, the difference in thermal expansion coefficient of silicon and its oxide and the difference between fabrication temperature of the oxidation and room temperature. Below that limit the cantilevers are not suitable as mechanical devices. Fig 4.26 shows the boundaries found for diaphragms by Wilmsen et al and that found for cantilevers by Jolly-Muller. The points represent microbridges of silicon dioxide thermally grown on silicon that were successfully fabricated and activated by ourselves. These devices were also deflected upwards or downwards (see chapter 7). Nevertheless, activations to their natural resonant frequencies were still achieved. Hence, the beams must still be in the elastic regime.

4.7.3. The neutral equilibrium stress:

Following the analyses done by Cottrell [19], it is possible to calculate the ultimate compression stress induced in silicon oxide beams grown on silicon. Suppose a compressive force is applied to the centre area of an end-facet and acts along the inertial centre of the beam as shown in Fig 4.27. The magnitude of this force is given by [19]:

$$F = \frac{n\pi^2 EI}{L^2} \qquad (4.7)$$

where I is the second moment of area which for a rectangular beam is given by $wt^3/12$. n is verified by the end-conditions and has the following values:

i) Both ends pinned, Fig 4.27.a, n = 1.
ii) Both ends clamped, Fig 4.27.b, n = 4.
iii) One end pinned and one end free to move, cantilever with pinned end, Fig 4.27.c, n= 1/4

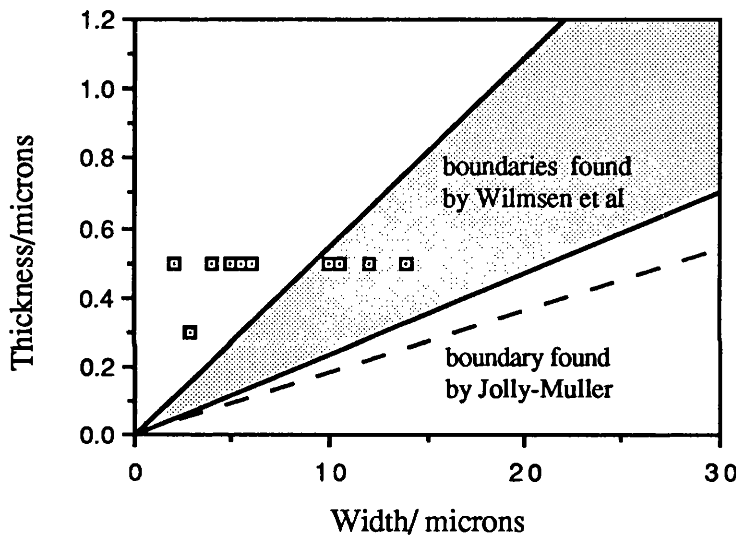

Fig 4.26: The thickness vs width of the successful silicon dioxide structures on silicon. The Jolly-Muller boundary [25] for cantilevers and the Wilmsen et al [26] boundaries for diaphragms are shown. The points represent microbridges of silicon dioxide thermally grown on silicon that has been successfully fabricated and activated by ourselves.

Beams with different end-conditions take different patterns, known as modes. These modes are the minimum energy state that can be taken by the beam. The same argument is true for the resonant frequency modes as discussed in chapter 3. However the modes due to compression stress are 'static' modes while those for resonant frequencies are 'dynamic'. The stress induced due to this force is given by:

$$\sigma = \frac{n\,\pi^2\,E}{12}\left(\frac{t}{L}\right)^2 \qquad (4.8)$$

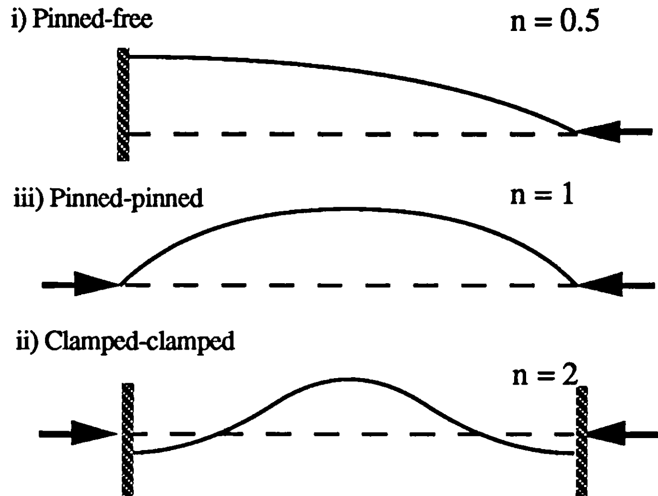

Fig 4.27: The compression stress induced by applications of force, presented by the arrows, in three beams.

This is the neutral equilibrium stress; the buckling and the elastic stress are balanced. For end stresses smaller than this the restoring stress predominates and the beam can go back to its initially straight form; this is stable equilibrium. For larger stresses, the beam deflects and severely distorts and may break. The stress which gives rise to the destruction of the beam is known as buckling stress. However, in the literature, the expression 'buckling force or stress' has been misused. It has been used just for deflection of the beam. For instance, the neutral stress induced is about $1.8MNm^{-2}$ for a beam with dimensions of 180µm long and 0.5µm thick. Therefore, any stress under this value will be in the stable equilibrium region, and the beam can return to its straight form.

If the microresonator beam however is under a higher stress than that given in (4.9), the appropriate explanation is as follows. Firstly films have higher Younge's modulus than bulk materials and secondly the beam may take higher (static) modes. These modes are as follows:

i) For pinned end-conditions, $n = (i+1)^2$

ii) For clamped end-conditions, $n = (i)^2$ (4.9)

where i is the (static) mode number. As the amount of stored energy is increased in the beam, a point of instability can occur and a new deletion pattern (mode) can appear which requires less energy [25]. It can be understood in terms of quantisation of the energy levels required by the beam. The beam does not take any value of energy; there are forbidden gaps between the energy levels. The allowed energy levels are those given above. The first three modes for these two end-conditions are shown in Fig 4.27. By substituting the appropriate value of n in (4.9) the stress for a particular mode can be found. Fig 4.28 shows the predicted values of neutral stress for a silicon dioxide resonator with end-conditions. Therefore, if the beam did not fail during the transit from one static mode to another, it is allowed to take the higher modes. The failure to do so during this transit period depends partly on the end-conditions and the geometry and partly on the way the force is applied. It is understood that the higher the mode shape the higher the buckling stress. The neutral stress for a beam which is 180μm long and 0.5μm thick is 4.5×10^5 Nm^{-2}. In practice, the beam hardly takes higher modes since any physical marks such as dislocations and cracks in the beam propagate and failure is inevitable. A few examples of deflected silicon dioxide beams under compression stress are shown in Fig 4.29. Obviously most often the physical mark is microscopic and cannot be seen.

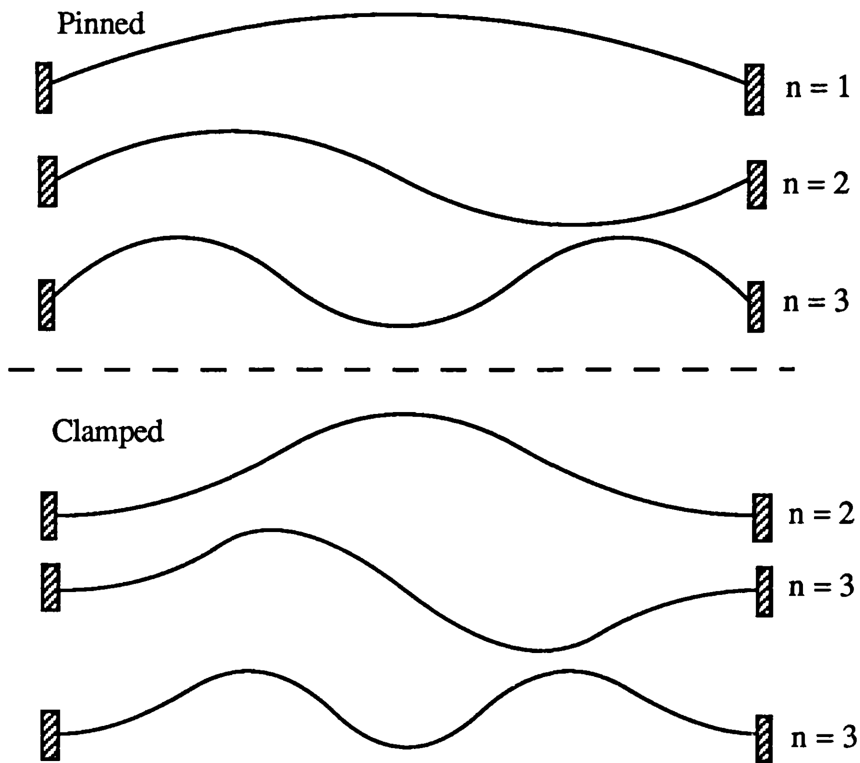

Fig 4.27: The static modes that a beam may take under a compression stress applied axially (Fig 4.18).

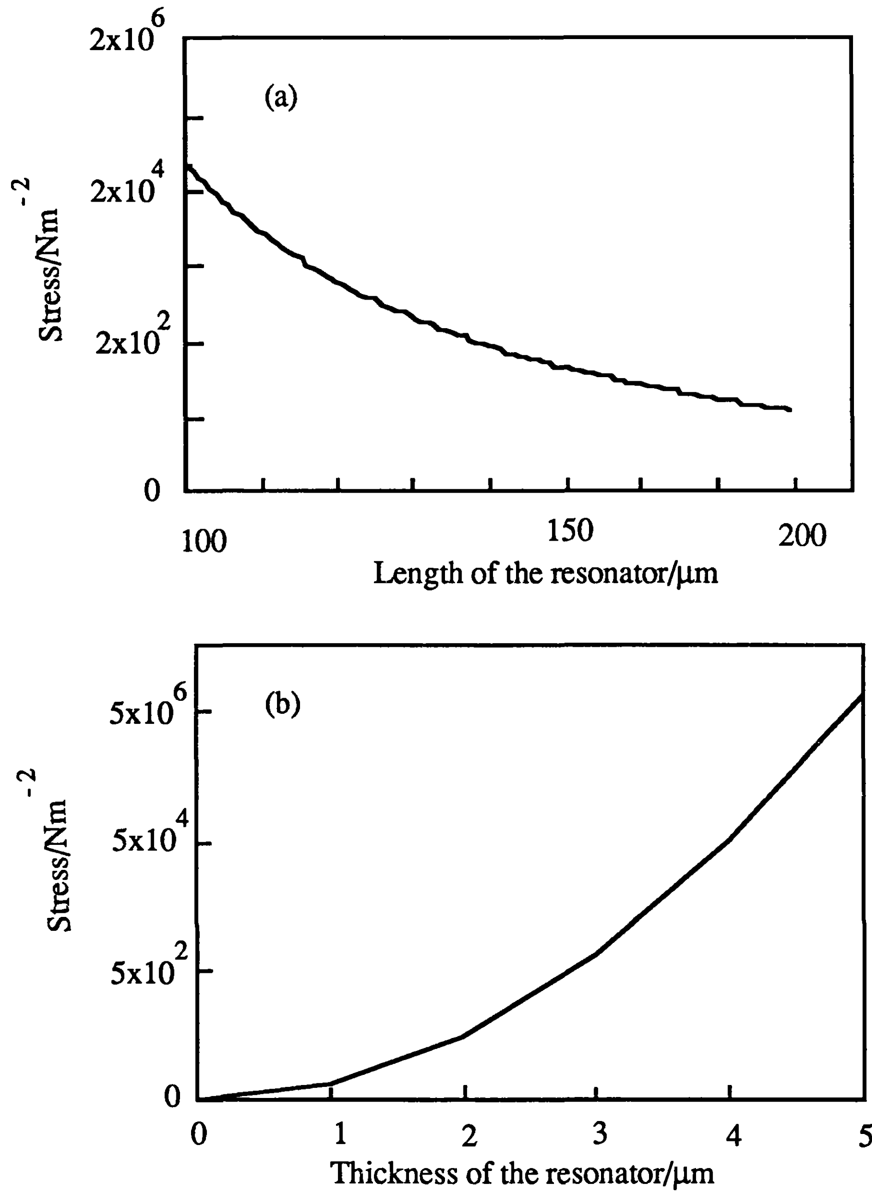

Fig 4.28: The predicted values of neutral stress for a silicon dioxide resonator with clamped end-conditions vs length (a) and thickness (b) of the resonator. In (a) it is assumed that the beam length is 180µm and in (b) it is assumed that the beam thickness is 0.5µm.

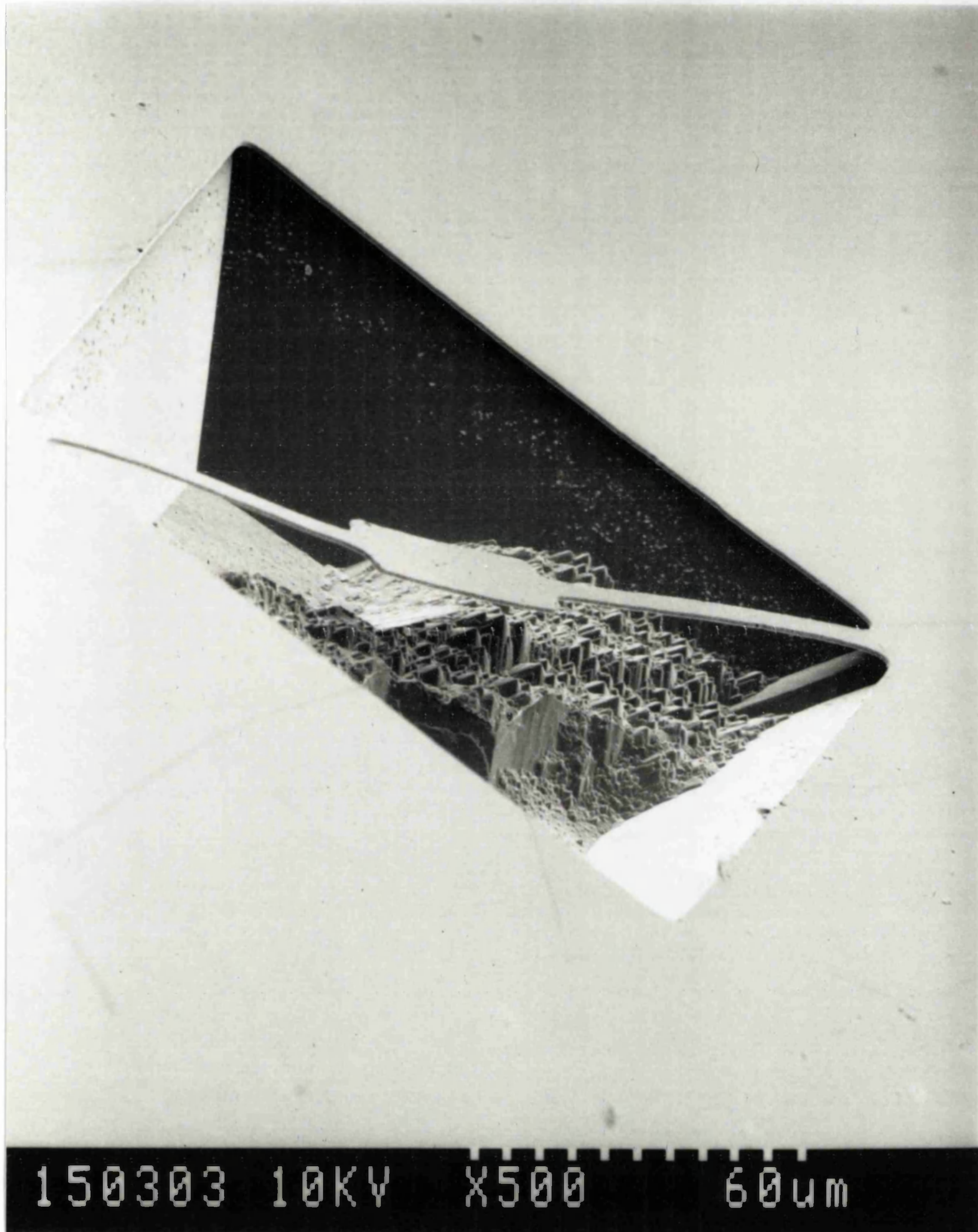

Fig 4.29(a): A silicon dioxide paddle beam deflected downwards under compression stress. Compare this figure with the silicon beam of Fig 4.7 to Fig 4.13, Fig 4.18 and Fig 4.19.

Fig 4.29(b): A silicon dioxide paddle beam deflected upwards under compression stress. Compare this figure with the silicon beam of Fig 4.7 to Fig 4.13, Fig 4.18 and Fig 4.19.

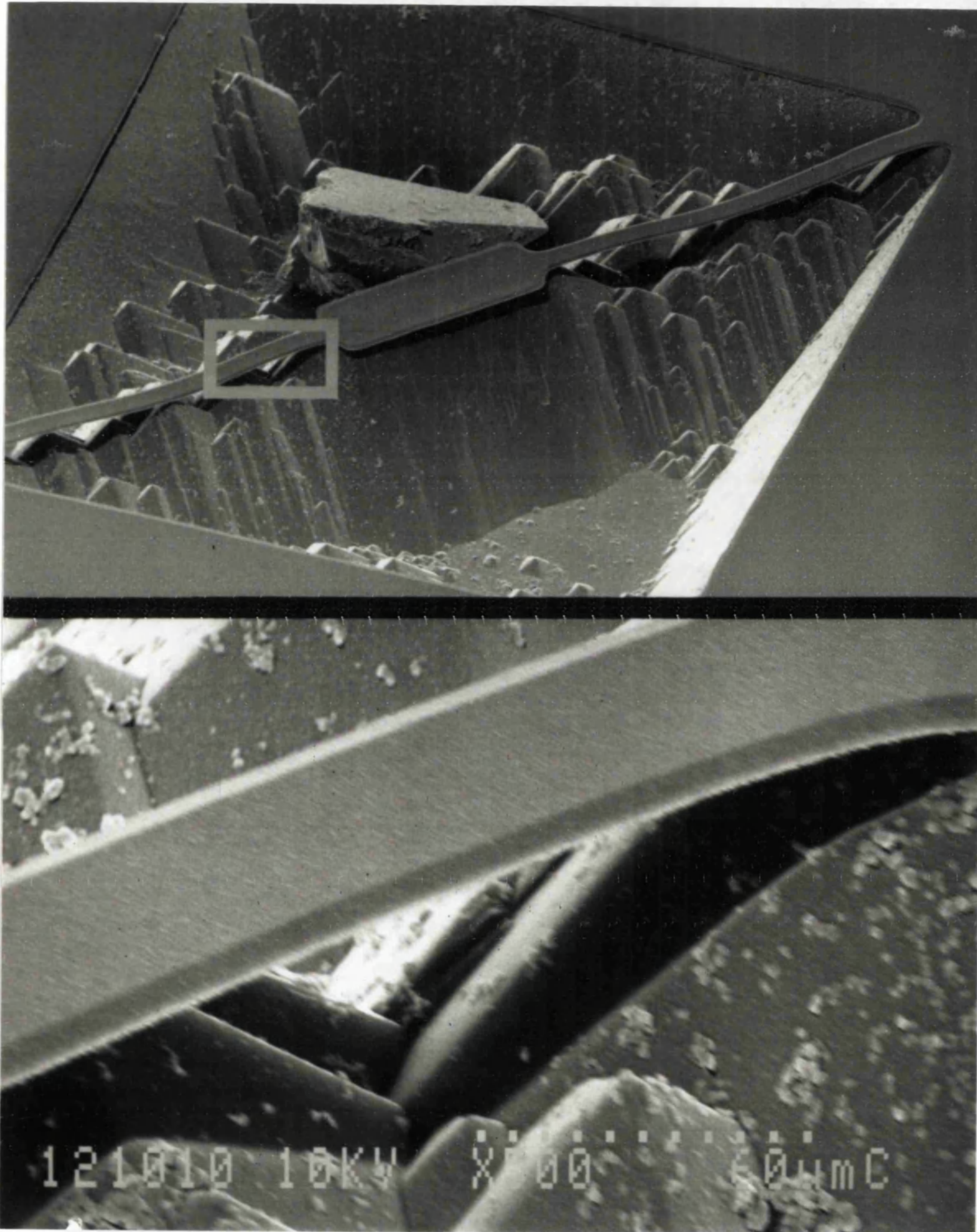

Fig 4.29(c): A silicon dioxide paddle beam has higher mode of deflection under compression stress. Compare this figure with the silicon beam of Fig 4.7 to Fig 4.13, Fig 4.18 and Fig 4.19.

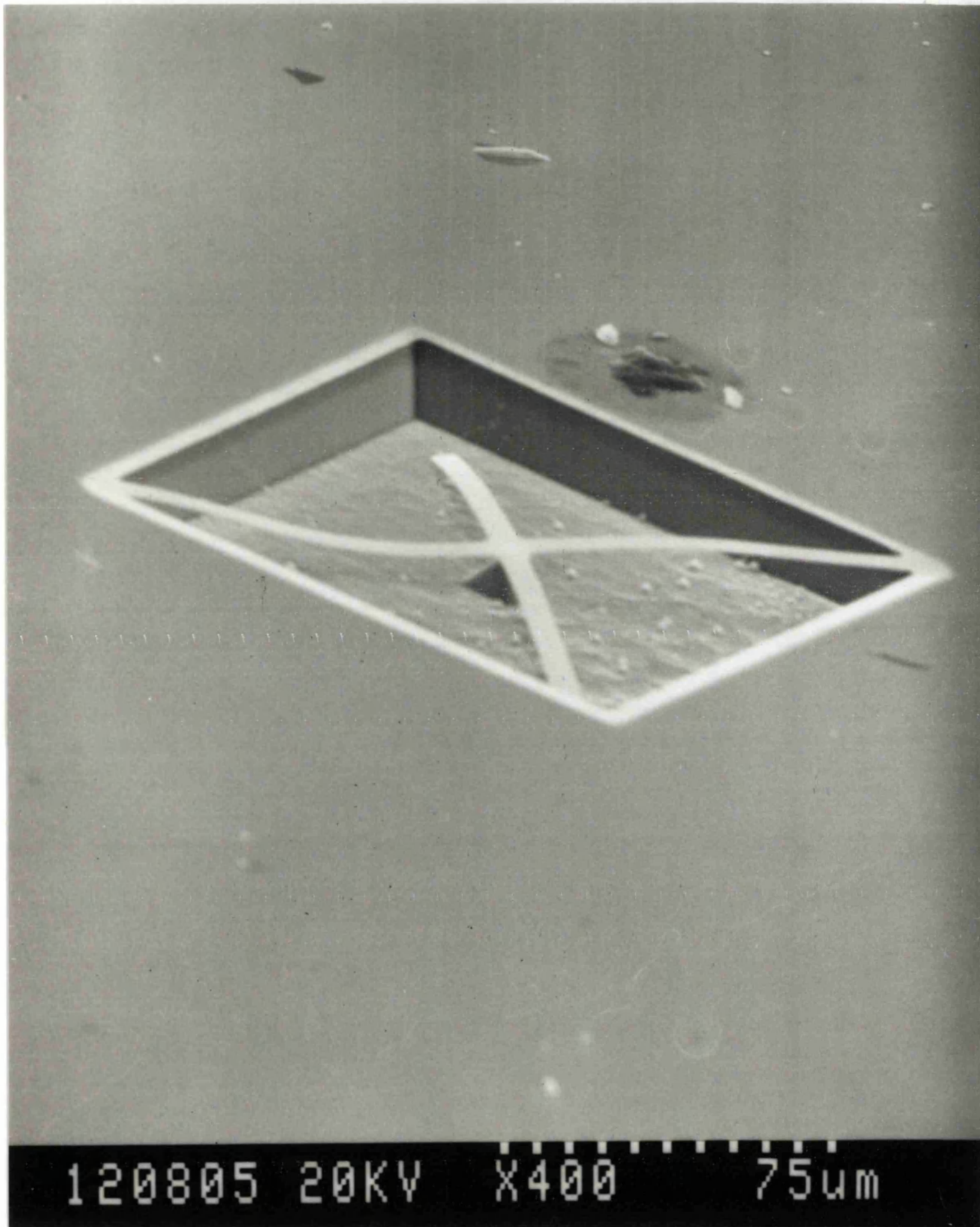

Fig 4.29(d): A silicon dioxide winged beam distorted under compression stress. Compare this figure with the silicon beam of Fig 4.7 to Fig 4.13, Fig 4.18 and Fig 4.19.

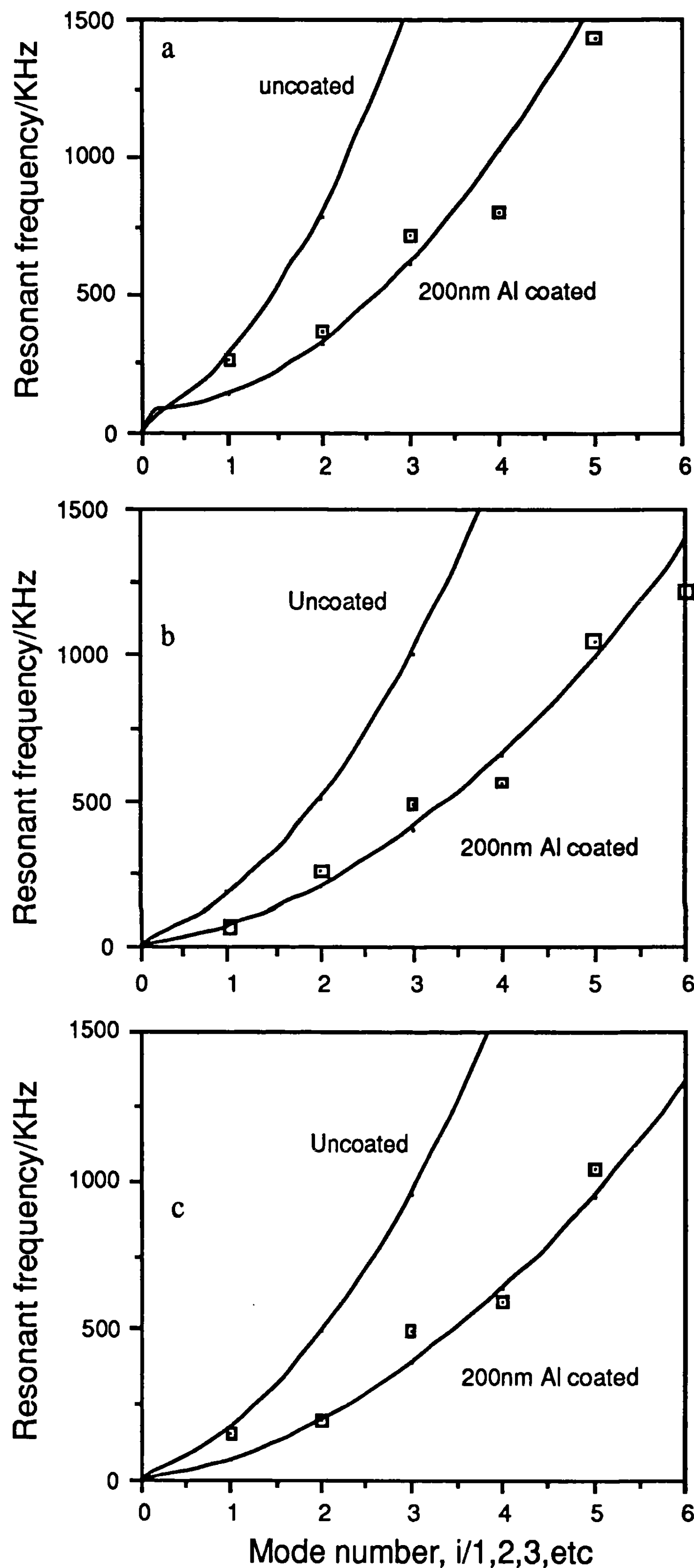

Fig 4.30: The resonant frequency vs mode numbers for simple beams with dimensions of 0.5μm thick and 4μm wide and they have different lengths: (a) 185μm, (b) 230μm and (c) 235μm long. The solid curves present the theoretical values and the points the experimental values. The beams are coated with 200nm of aluminuim.

4.7.4. Discussion and Conclusions:

Figs 4.30 (a, b, c) show the experimental and theoretical results obtained for a three beam resonator with different lengths and the same thickness, width and metal coatings. The experimental results are in good agreement with the predicted results if we consider the criteria of the measurements. There are several parameters effecting the accuracy of the resonant frequency measurements.

1. Inaccuracy of the measurement arises from the measurement of the beam thickness since only ±10% accuracy can be achieved from the SEM measurements.

2. The reproducibility of the resonant frequency is about ±5% since this parameter depends on the environmental parameters such as pressure, temperature and humidity.

3. Most of the inaccuracy arises from the metal coatings which produce compression stress in the beam, and this reduces the resonant frequency as we shall see in the next section. Furthermore, one should be aware of the fact that aluminium also oxidises at room temperature and produces its oxide which has a much higher Young's modulus than aluminium (see Table 3.2). Fig 4.31 shows the predicted values for aluminium and its oxide.

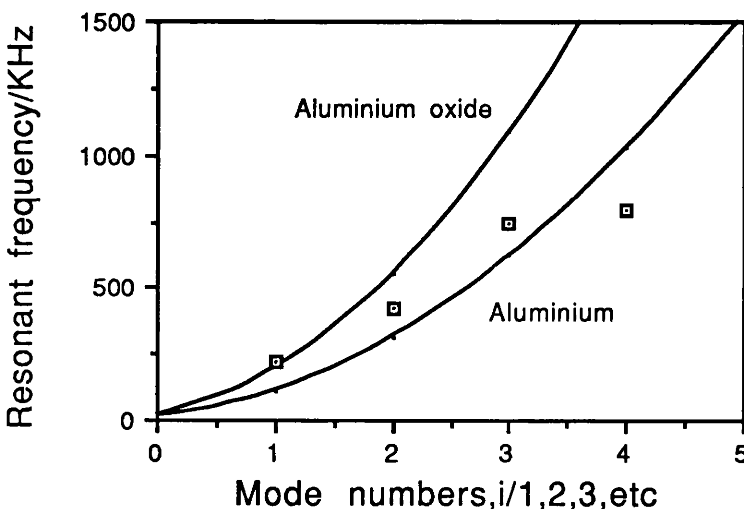

Fig 4.31: The resonant frequency vs the resonant modes for a paddle beam. The theoretical curves for both aluminium and its oxide is shown.

A typical series of results taken for the simple beams of dimensions 185μm long, 5.5μm wide and 0.5μm thick are tabulated below. Each set of resonances was observed at a particular strip position. The quality-factor of each resonance is shown in brackets. All the resonant frequencies are in KHz.

a) 262 (27), 363 (31), 806 (30)
b) 263 (29), 726 (47), 1420 (59), 1608 (70)
c) 367 (38)
d) 258 (-), 371 (38), 1429 (72)
e) 262 (32), 720 (36)
f) 257 (13), 354 (35), 807 (64), 1441 (51)
g) 255 (21), 363 (26), 724 (49)

Although the oxide beams are deflected upwards or downwards under the effect of the thermal property mismatch between the silicon and its oxide but the beams can still be driven into the mechanical resonant frequency. This implies that the beams are still in their elastic regime and are suitable as mechanical devices.

4.7.5. Considerations of metal coatings:

A silicon oxide beam is under compression stress after it is metal coated. This is because of the mismatch between the thermal expansion of the metal (which for gold is $1.4 \times 10^{-5}\,K^{-1}$ and for aluminium $2.4 \times 10^{-5}\,K^{-1}$) and that of the oxide (which is $0.04 \times 10^{-5}\,K^{-1}$). During the metal coating process the temperature of the metal is high, approximately 400°C. This in turn increases the temperature of the oxide film. The evaporation temperature is higher than that of the sputtered process, so evaporation coated beams are expected to have a higher induced tension. However, because the metal expands more than the oxide, when the wafer cools down to room temperature the metal will be under tension. This in turn puts the oxide under compression stress. In short, at room temperature the metal is under

thermally-induced tension, but this keeps the oxide under compression. A decrease in the thickness of the metal will reduce both the tension and the compression stress in the beam.

After the silicon dioxide beam is undercut, not all the stress is relieved in the beam resonator. We relate the decrease in the resonant frequency to the compression stress induced in the beam. This is because the metal coating puts the beam under compression; consequently the resonant frequency decreases. The experimental data of Fig 4.32 and Fig 4.33 suggest that with an increase in the metal coating thickness more compression stress is introduced into the beam since the resonant frequency decreases. Furthermore, increasing the metal coating puts the beam under more compression stress.

The higher the resonant mode the higher the induced stress. The beam experiences more stress if it is activated at a higher mode. The coefficient of the stress induced is -0.1nm KHz^{-1} and -0.4nm KHz^{-1} for the first and the second resonant frequency modes respectively. This can be understood in a similar way to static modes. In the higher modes the beam exerts more stress in the boundaries. The shift in the resonant frequency can be related to the stress induced in the beam as given by (4.3).

The final point that should be emphasised is the effect of the metal coating on the heat conduction. A thin metal coating has a low heat conductivity, so the heat concentrates in the activated region of the beam. The temperature gradient in the case of a thin metal coating may be higher than that of a thicker metal coating. This affects the values of the quality-factor and the resonant frequency. If all the metal coating is at the same temperature, the metal coating expands more than if a point is heated in the middle of the beam. The greater expansion of the metal implies that the beam is under a higher compression.

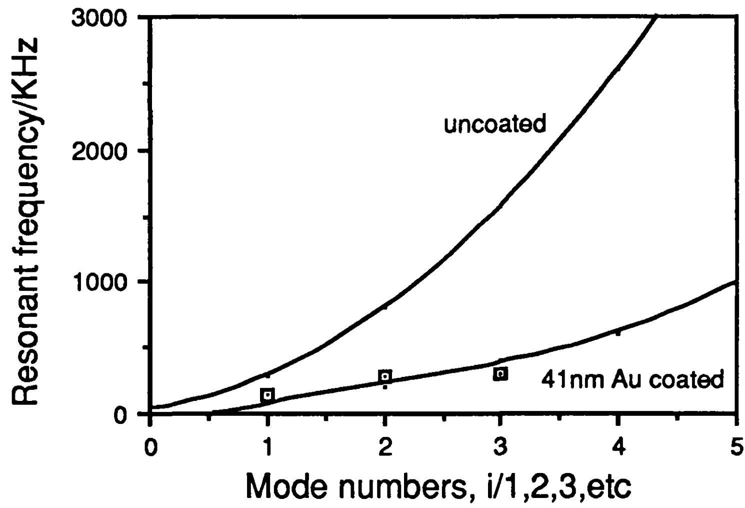
Resonant frequency/KHz
3000
2000
1000
0
uncoated
41nm Au coated
0
1
2
3
4
5
Mode numbers, i/1,2,3,etc

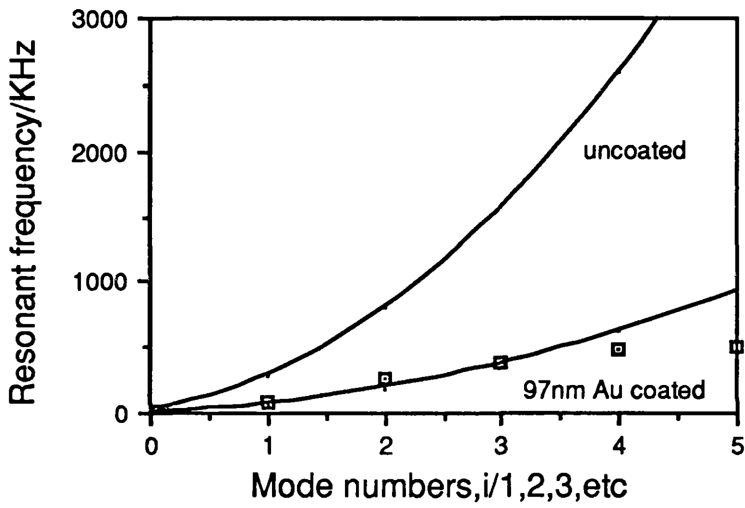
Resonant frequency/KHz
3000
2000
1000
0
uncoated
97nm Au coated
0
1
2
3
4
5
Mode numbers,i/1,2,3,etc

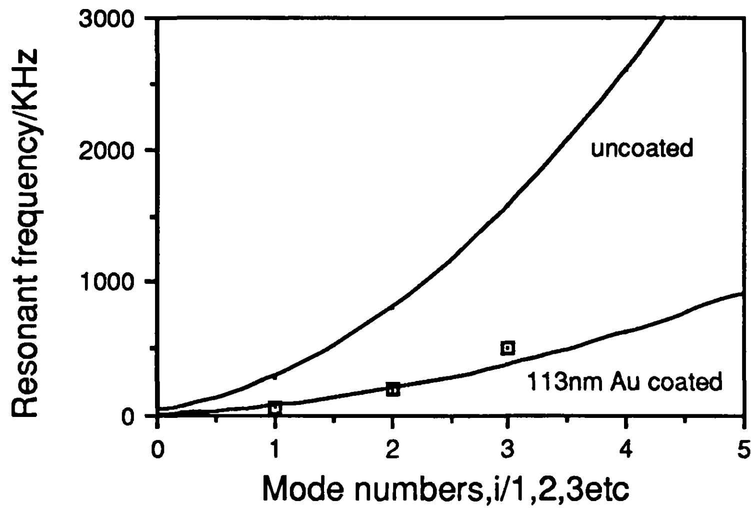
Resonant frequency/KHz
3000
2000
1000
0
uncoated
113nm Au coated
0
1
2
3
4
5
Mode numbers,i/1,2,3etc

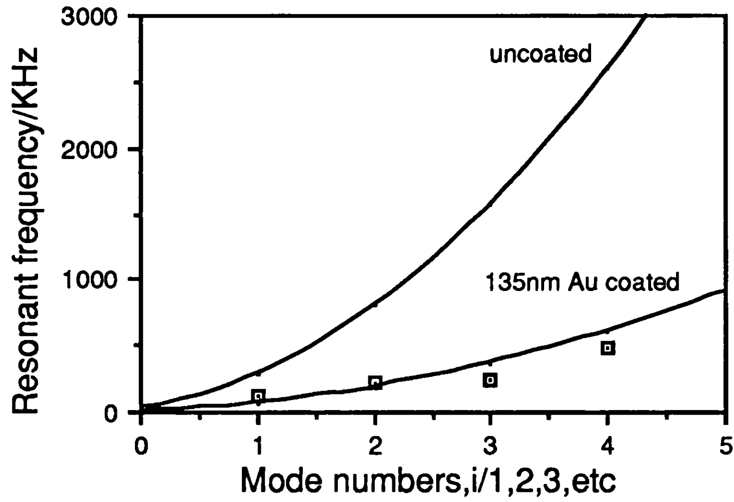
uncoated
135nm Au coated
Resonant frequency/KHz
Mode numbers,i/1,2,3,etc
3000
2000
1000
0
0
1
2
3
4
5

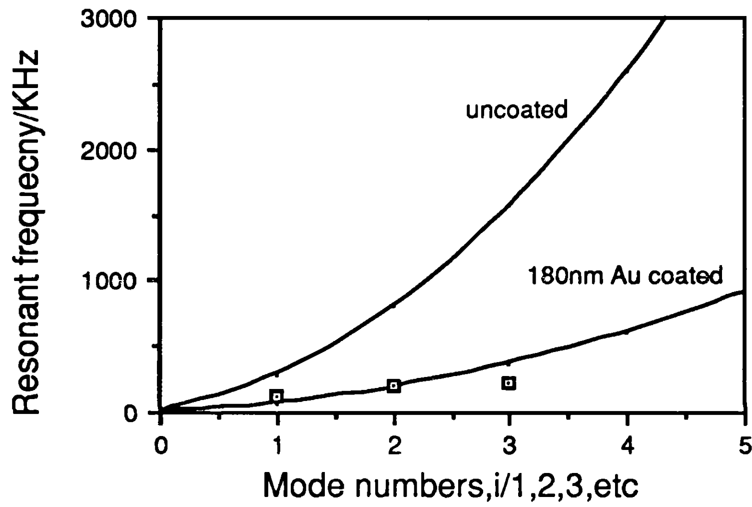
uncoated
180nm Au coated
Resonant frequecny/KHz
Mode numbers,i/1,2,3,etc
3000
2000
1000
0
0
1
2
3
4
5

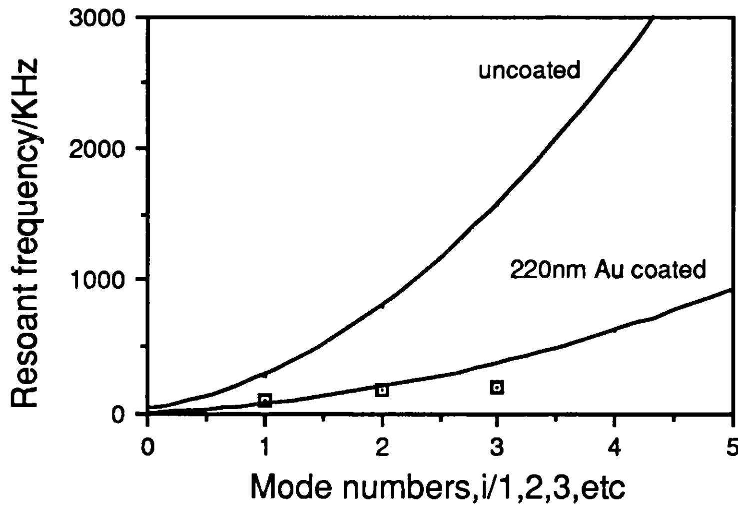
uncoated
220nm Au coated
Resonant frequency/KHz
Mode numbers,i/1,2,3,etc
3000
2000
1000
0
0
1
2
3
4
5

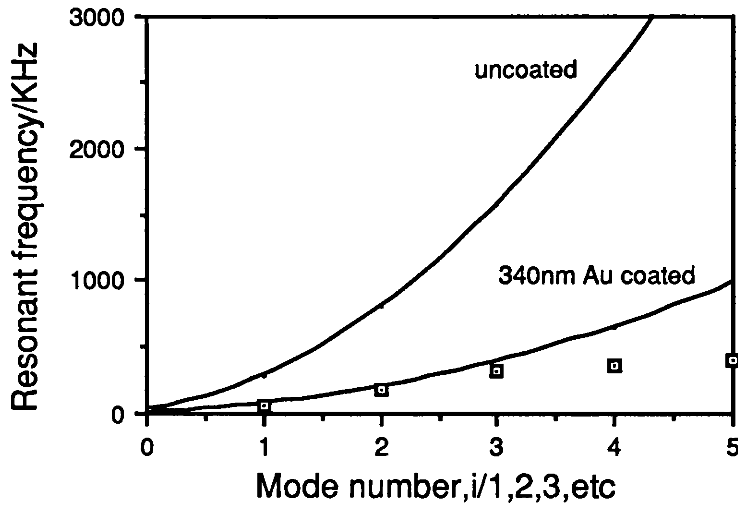

Fig 4.32: The resonant frequency vs mode numbers for a paddle beam (Fig 4.6.b) with dimensions L=184μm, w=4μm L_p=130μm, w_p= 12μm wide and 0.5μm thick. The measurements were repeated for different thicknesses of gold coating: 41, 97, 113, 135, 180, 220, and 340nm.

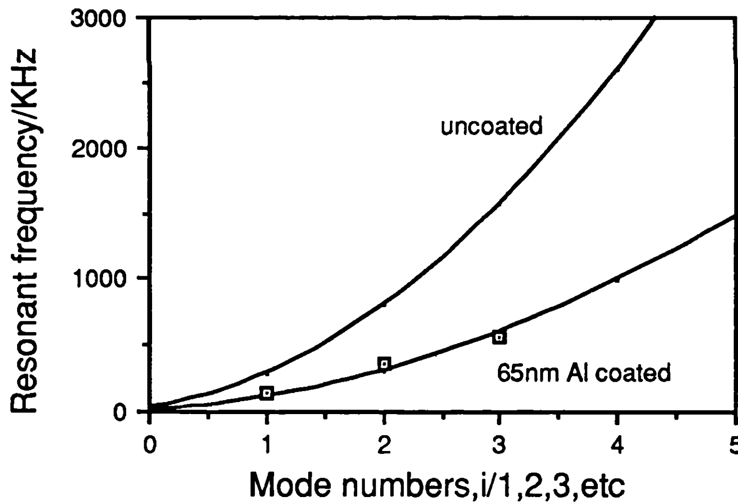

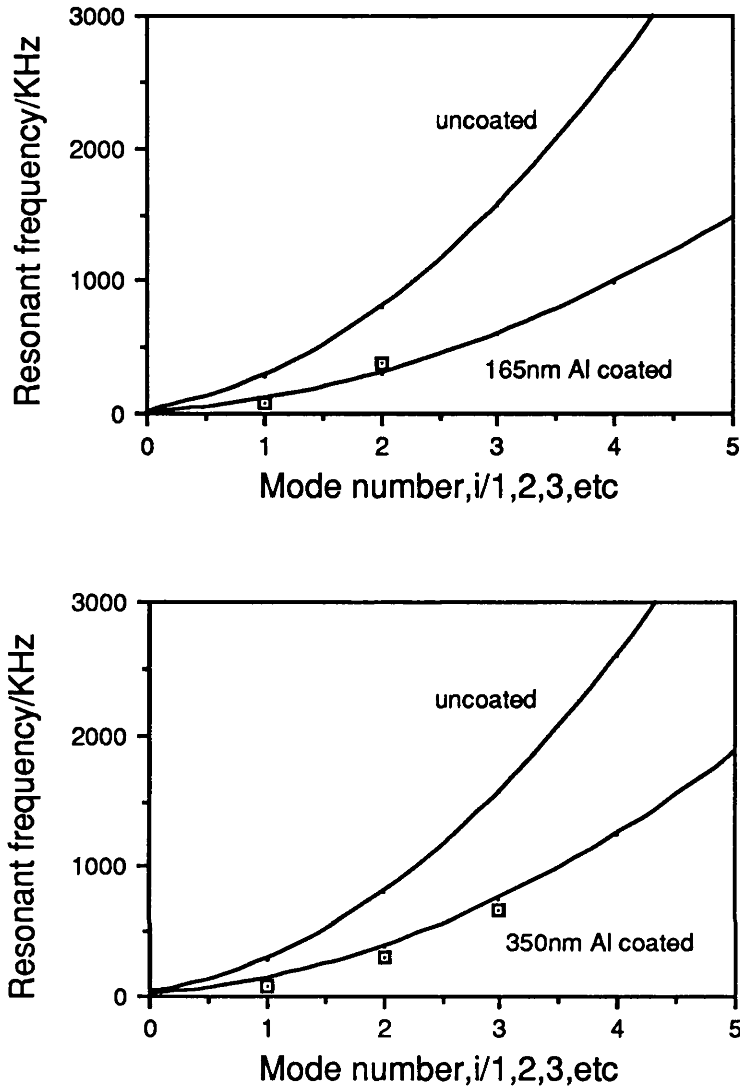

Fig 4.33: The resonant frequency vs mode numbers for a paddle beam (Fig 4.6.b) with dimensions L=184μm, w=4μm L_p=130μm, w_p=12μm wide and 0.5μm thick. Different thicknesses of aluminum coating have been studied (from top to buttom): 65, 97 and 350nm.

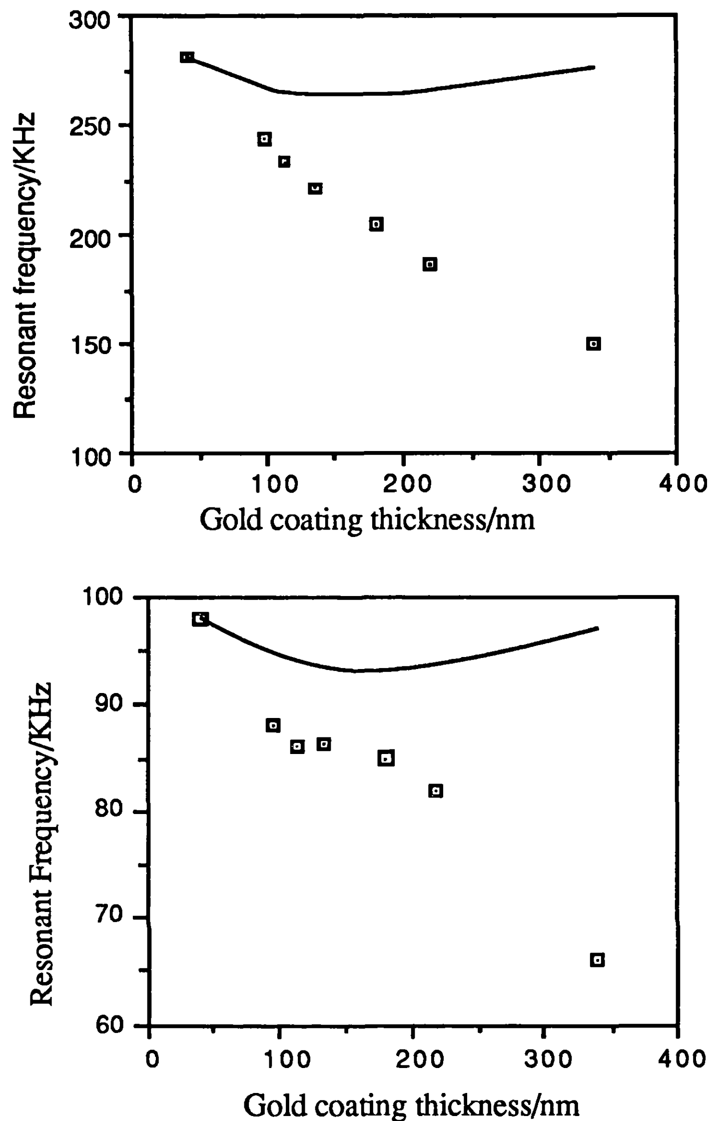

Fig 4.34: Resonant frequency vs gold coating thickness plotted for the first (a) and the second (b) resonant modes. This summarises the results of Fig 4.32. The lines represent the predicted values from (3.21) and (3.26).

We may conclude that the silicon dioxide beam relaxes after undercutting. This results in a deflection of the beam upwards or downwards. After metal coating the thermal expansion mismatch between the metal and the silicon dioxide beam puts the beam under some compression stress and the value of this stress depends upon the relative thicknesses of both materials.

4.8. Quality-factors of microresonators

4.8.1. Introduction:

The quality-factor of a micromechanical resonator is the parameter that determines the precision of the device as a sensor. The parameters that determine the quality-factor are the reflecting boundaries, the geometry, material properties, the state of the stress and damping of the structure. The stress can either be externally induced from the temperature or differential pressure changes or internally induced due to thermal mismatch between the materials of the resonator beam or doping. For example boron doped silicon experiences tensile stress as we have seen. Furthermore, the way the device is fabricated and activated/detected also affects the quality-factor.

The relationship between resonant frequency modes and the quality-factor has been studied for different beam resonator materials. These materials are boron doped silicon, silicon dioxide, deposited or thermally grown, and silicon nitride. The different geometry of these devices has also been studied.

4.8.2. Theory of quality-factor of flexural vibrations:

A resonant frequency can be defined by three factors: the amplitude, the bandwidth and the value of the resonant peak. The amplitude should be high enough to be signal processed. The frequency and the bandwidth can be related together in a parameter called the quality-factor which defines the sharpness of the resonant peak. The quality-factor measures the energy dissipation in the system. Therefore, the sharper the resonant peak the less energy dissipated in the system. A resonant system at resonance needs enough energy to cover its losses.

The quality-factor gives two features to a microresonator as a sensor. The sharper the resonant peak the more accurate the measurement and the smaller the change in the measured parameter that can be resolved. Fig (4.35) shows these two features of the

quality-factor. For sensing applications it is desirable to have high quality-factor devices. The quality-factor at a resonant frequency f_i is defined as:

$$Q = \frac{f_i}{\Delta f} \qquad (4.9)$$

where Δf is the bandwidth of the resonant peak at its half amplitude A, Fig (4.35). If Δf vanishes the quality-factor goes to infinity which indicates an ideal lossless system. The resonant frequency f_i of flexural vibration of a homogeneous prismatic beam is given by (3.21).

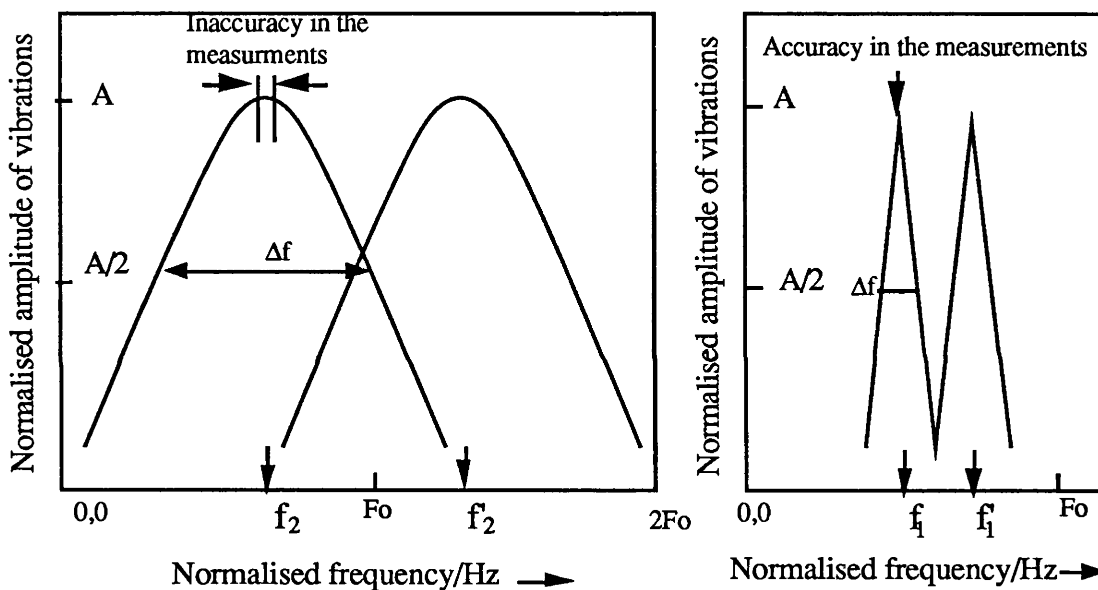

Fig 4.35: The high quality-factor resonant frequency f_1 measures a finer change, from f_1 to f_1', and more accurately than the low quality-factor one.

Newell [30] predicted the quality-factor of cantilevers. His model was based upon the assumption that the viscous drag force is the dominant mechanism. In short, air damping increases as the ratio of the length to the thickness of the resonator. Newman's model is not verified by experimental results although it may give some qualitative information about the quality-factor. However, Newell's model and experimental observation can be related to give a more general formula:

$$Q = \Gamma \lambda_i^2 \frac{(E\rho)^{\frac{1}{2}} w}{\eta} \left(\frac{t}{L}\right)^2 \qquad (4.10)$$

where λ_i is the resonant mode (section 3.4); E and ρ are the Young's modulus and density of the beam; w, t and L are the width , thickness and the length of the resonator; η is the viscosity of air (= $18.2 \times 10^{-6} kg\, m^{-1} s^{-1}$ at 20°C); Γ is a constant verified by the fabrication and experimental criteria. It is a rather complex constant; it is different for different geometries and materials. In (4.10), the first two terms of the right hand side are adopted from experimental observations and the rest from Newman's expression. The first term, λ_i, expresses the end-conditions and the resonant mode number (see section 3.4.3). The quality-factor depends on the end-condition and hence the resonant mode. Therefore to find the quality-factor the end-conditions have to be defined or found from the experimental observations. For a silicon resonator with dimensions of 180μm long by 4μm wide and 0.5μm thick the quality-factor is about 78 if Γ is unity and clamped end-conditions are considered. However, Γ for the dimensions used in this work is less than unity.

The quality-factor for micromechanical resonators is determined by two sets of factors: firstly, intrinsic factors such as the geometry of the resonator, the material properties, the end-conditions and the internal stresses; and secondly extrinsic factors, such as the way they are fabricated, the viscous air damping and to some extent the way they are activated and detected. We shall verify experimentally the dependence of the quality-factor upon these two sets of parameters.

4.8.3. Experimental work:

The effect of the two factors mentioned, namely intrinsic and extrinsic factors, will be studied experimentally.

i) Intrinsic factors:

Four intrinsic factors affect the quality-factor of a resonator.

i.a) End boundaries:

A simple model (Fig 4.36) of a standing wave resonator is analysed by Newell [31]. The essential features are the end-conditions and the acoustic medium characterised by the length L and the propagation constant.

A reflection of unity from the boundaries is ideal for a high quality-factor. There have not been any quantitative calculations on optimised end-conditions. However, qualitatively it can be predicted that the quality-factor of the two end-conditions of Fig 4.36. Fig 4.36.a should have a higher quality-factor since more energy can be reflected into the resonator system. In Fig 4.36.a, the 'sine' components of an atom colliding with the boundary with a force magnitude F do not contribute to the reflected energy to the resonator. Furthermore, the cosine magnitudes also meet again and make another collision and so on. In Fig 4.36.b, if there is no loss except that which arises from the collision with a boundary then the reflected wave has only one component. Resonators of the design of Fig 4.36.b had a quality factor of under a hundred. However quality-factors of a few hundreds were found for resonators designed as in Fig 4.36.a.

i.b) Resonant mode:

Any resonant structure resonates at a number of frequencies known as resonant modes. These modes are related via λ_i where i is the resonant mode, e.g. 1, 2, 3, etc. Therefore, λ_i expresses the end-conditions and the resonant mode at the same time. Equation (4.10)

λ_i expresses the end-conditions and the resonant mode at the same time. Equation (4.10) shows that the quality-factor increases with increase in the resonant mode. Figs (4.37) , (4.38) and (4.39) show the relationship between the resonant mode numbers and the quality-factors for silicon, deposited and thermally grown silicon dioxide and deposited silicon nitride, respectively. The Γ values of 0.25 for the silicon and 0.16 silicon dioxide and 0.1 for deposited silicon nitride are considered.

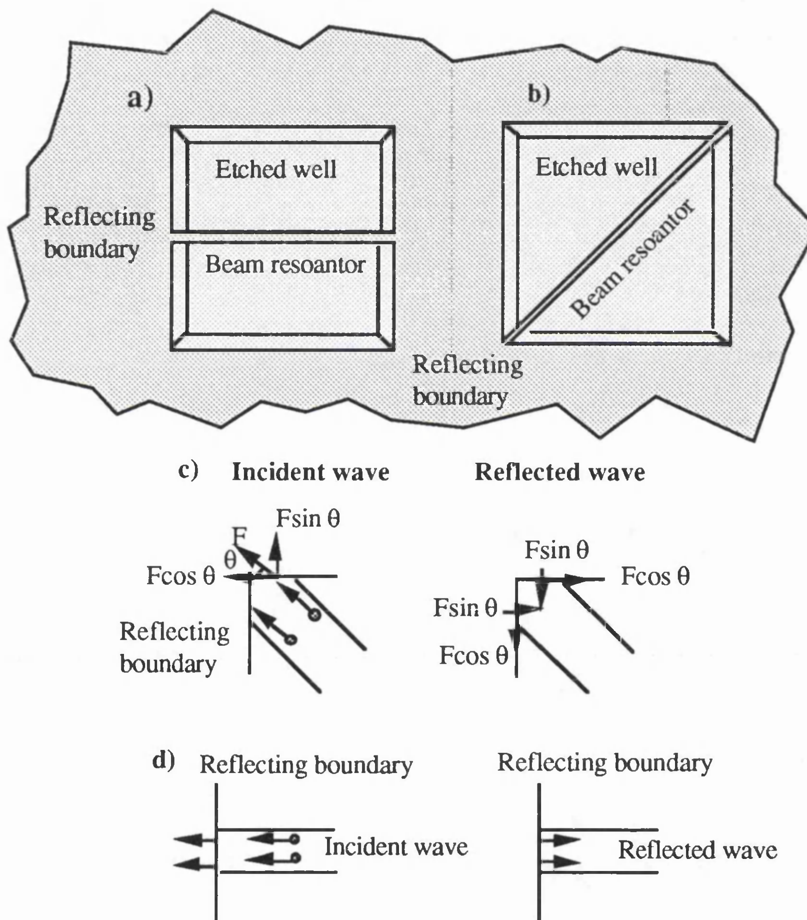

Fig 4.36: The effect of the reflecting end boundaries on the quality-factor of a beam resonator.

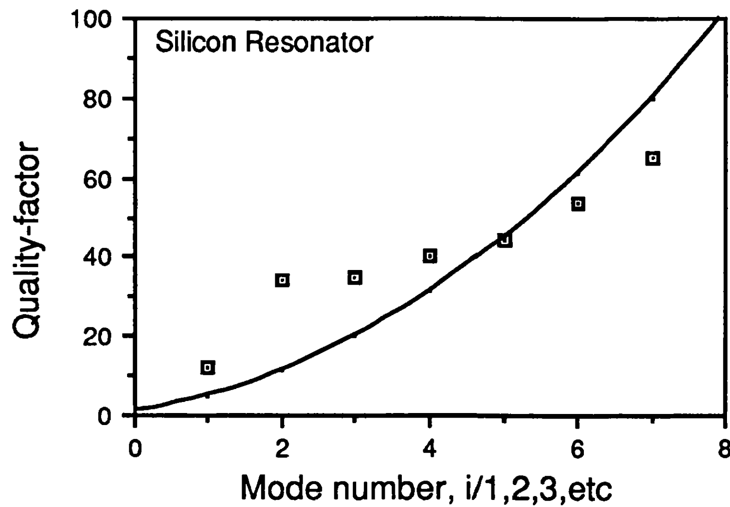

Fig 4.37: The dependence of the quality-factor upon the resonant mode for a silicon resonator of Fig 4.12.b which has Γ of 0.25.

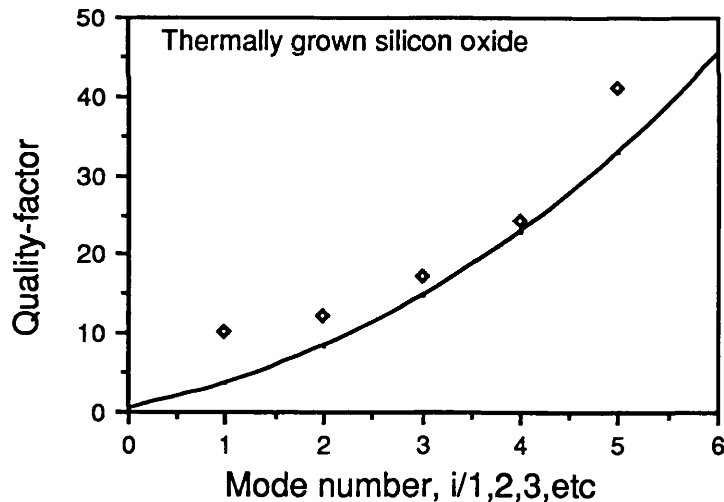

Fig 4.38: The dependence of the quality-factor upon the resonant mode for a thermally grown silicon dioxide resonator which has Γ of 0.16. The resonator is a paddle beam (Fig 4.6) with dimensions of L=175μm, w=12μm, L_p=38μm, w_p=12μm and 0.5μm thick. It is spatter-coated with 65nm of gold.

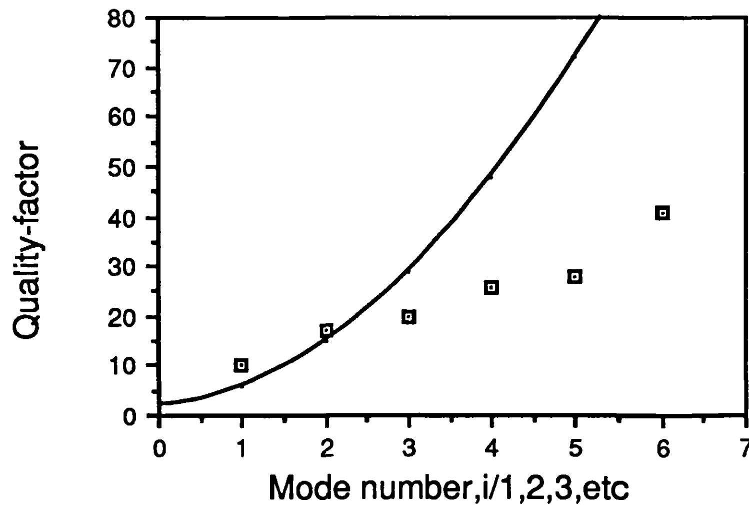

Fig 4.39: The dependence of the quality-factor upon the resonant mode for a silicon nitride resonator which has Γ of 0.10. The device is a simple beam which is 200μm long, 20μm wide, 0.2μm thick evaporation-coated with 20nm of chromium.[5]

i.c) Internal stresses:

It is worth remembering that a compression stress introduces damping in the structure which in turn decreases the quality-factor. Fig 4.40 shows the effect of the thickness of the metal coating on a silicon dioxide resonator.

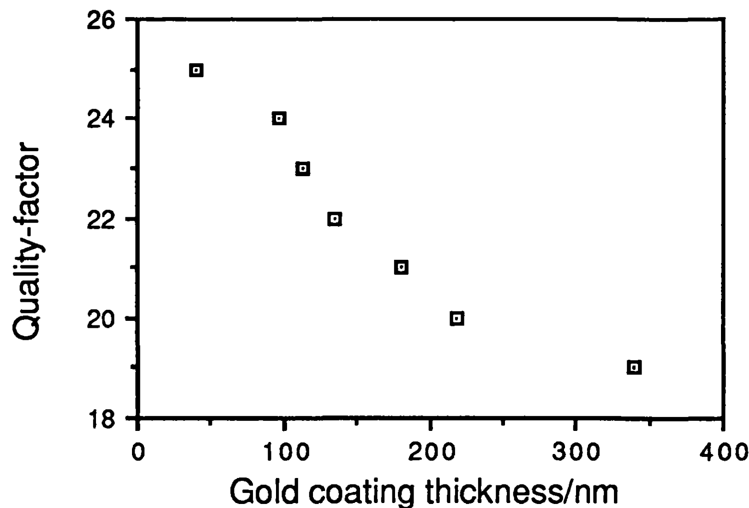

Fig 4.40: The dependence of the quality-factor of a silicon dioxide resonator upon gold coating. The device is characterised in Fig 4.32.

[5] This device is electrostatically activated, see chapter 5.

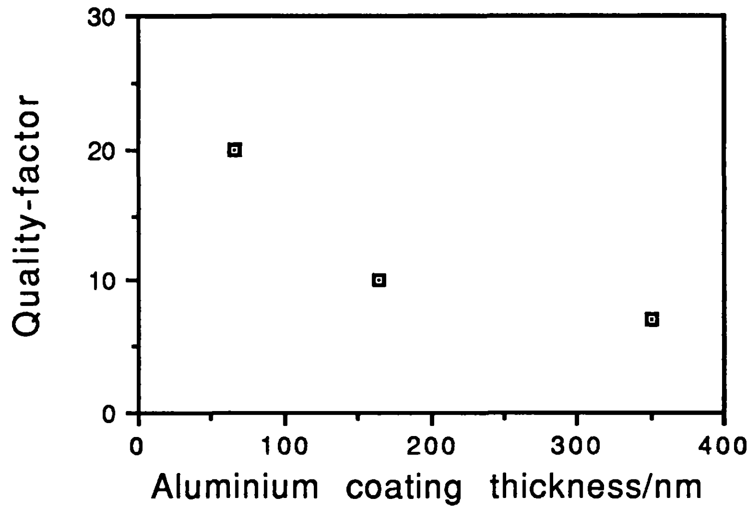

Fig 4.41: The dependence of the quality-factor of a silicon dioxide resonator upon aluminium coating. The device is characterised in Fig 4.33.

i.d) Property of materials:

The typical quality-factors of three different materials have been summarised as follows:

Table 4.1:

Parameters/Materials	Boron doped Si	Deposited Si_3N_4	Deposited SiO_2	Thermally Grown SiO_2
Dimensions/μm (Lengthxwidthxthickness)	170x8x0.5	175x5x0.5	175x6x0.5	175x4x0.5
Resonant frequency/kHz	320	290	220	200
Quality-factor:				
Experimental:	50	30	27	15
Γ	1	1	1	1

The resonant frequencies are the first detectable mode experimentally and may not correspond to the theoretically predicted values. It can be concluded that silicon beams have a higher quality-factor than silicon dioxide. There may be two reasons for this. Firstly

thermally grown or spattered silicon dioxide has a structure similar to that of fused silica which has an open structure that attracts impurities (Fig 4.20). Each impurity produces a scattering cross-section which introduces further losses to the structure. Secondly, the compression stress also reduces the quality-factor.

i.e) Geometry:

From (4.10) it is predicted that the quality-factor is proportional to the width of the resonator. Fig 4.42 and Fig 4.43 show the measured and predicted values of quality-factor dependent upon the width of the resonator which do not show any indication of this proportionality. The explanation of this may be that the compression stress in the beam (due to both metal coating and the silicon dioxide) is proportional to the width of the beam. As the width increases, the stress also increases which in turn introduces more damping in the resonator.

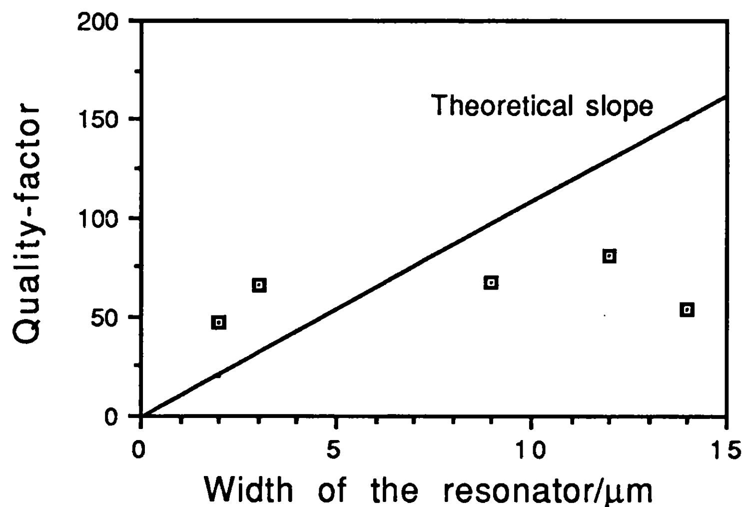

Fig 4.42: The dependence of the quality-factor of silicon resonators upon the width.

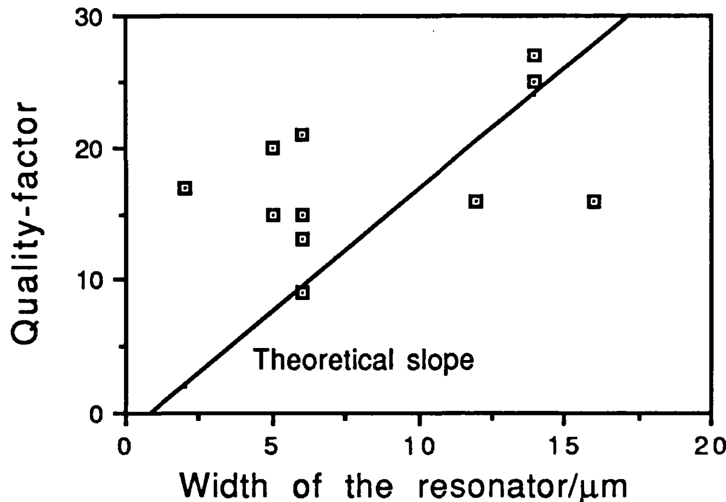

Fig 4.43: The dependence of the quality-factor of silicon dioxide resonators upon the width.

It has been reported that apertured beams increase the quality-factors of the resonators [32]. These beams are in the shape of simple beams with holes (Fig 4.44). The dimensions of the beam were 170μm long, 8 μm wide, 0.5μm thick and each hole was 5μm^2. An attempt was made to activate apertured beams but no drastic change in the quality-factor was observed. Two resonance frequencies were observed, 321 and 722 with quality-factors of 51 and 72 respectively.

ii) Extrinsic factors:

ii.a) Temperature:

External parameters such as temperature affect the resonant frequency which in turn changes the quality-factor. Fig (4.45) shows the dependence of the quality-factor on temperature[6]. As the temperature increases, the metal expands more than the silicon which puts the beam under stress. The quality-factor depends upon the temperature of the environment. This does not just arise from the change of the material properties and the stress state of the beam but it also arises from the temperature dependence of the air viscosity as shown in Fig 4.46 [33].

[6] For effect of the temperature on the resonant frequency see chapter 7.

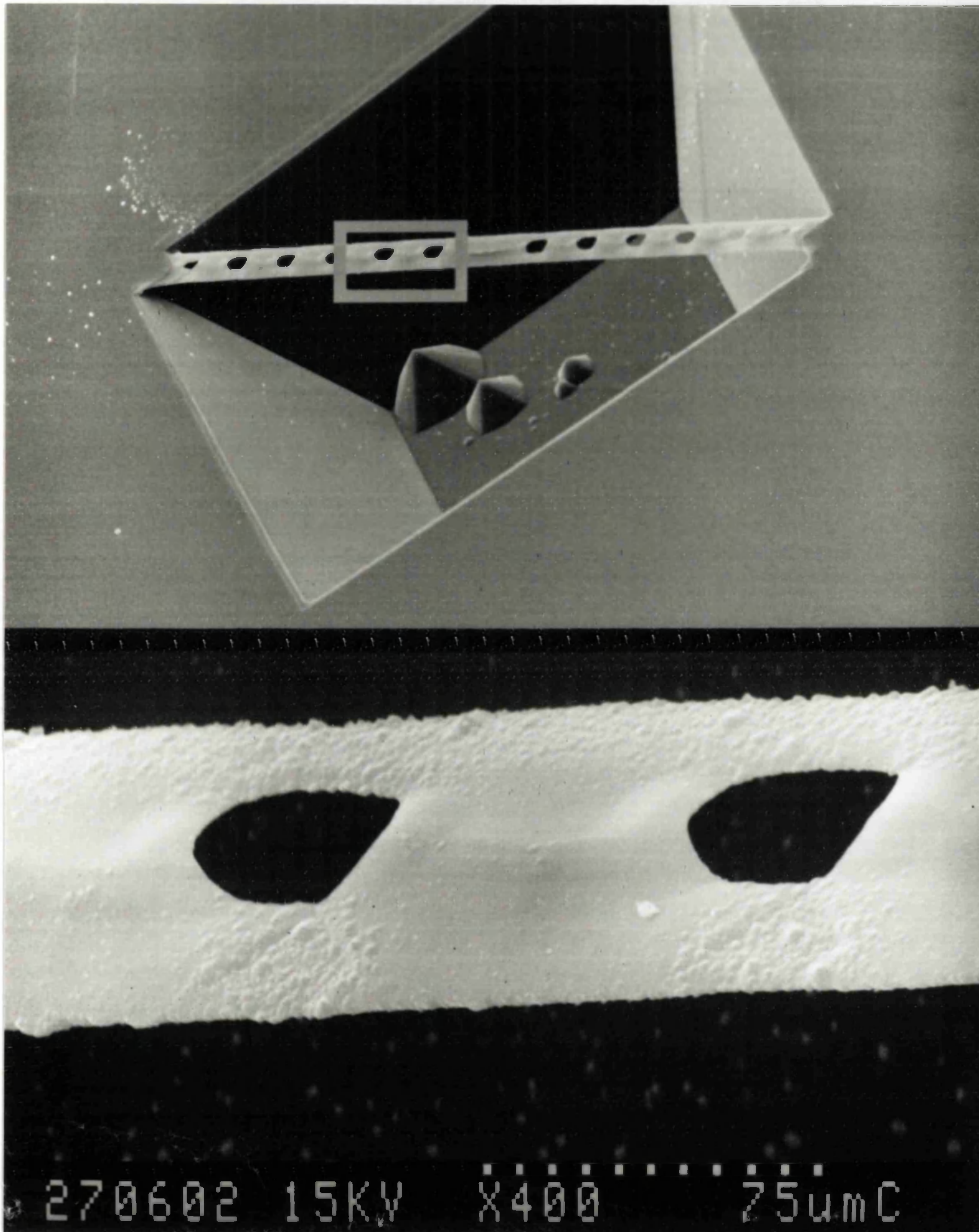

Fig 4.44: An SEM of an apertured beam.

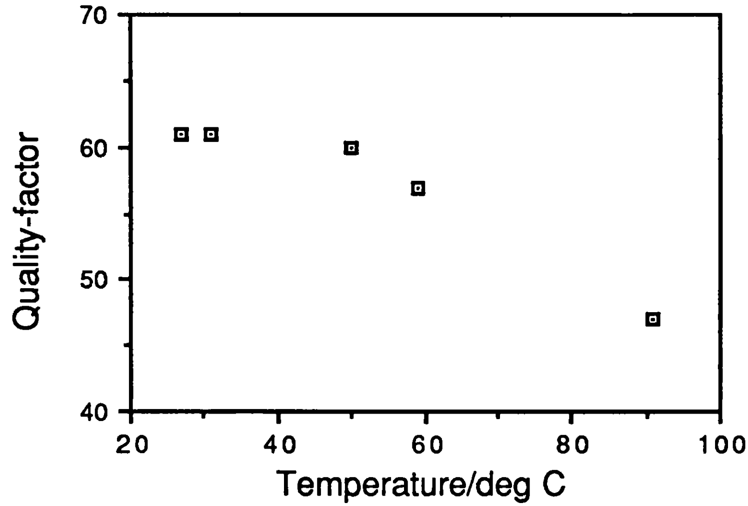

Fig 4.45: The dependence of the quality-factor of a silicon dioxide resonator upon the temperature. The resonator is a paddle beam (Fig 4.6) with dimensions of L=175μm, w=4μm, L_p=21μm, w_p=8μm and 0.5μm thick. It is evaporation-coated with 200nm of aluminium.

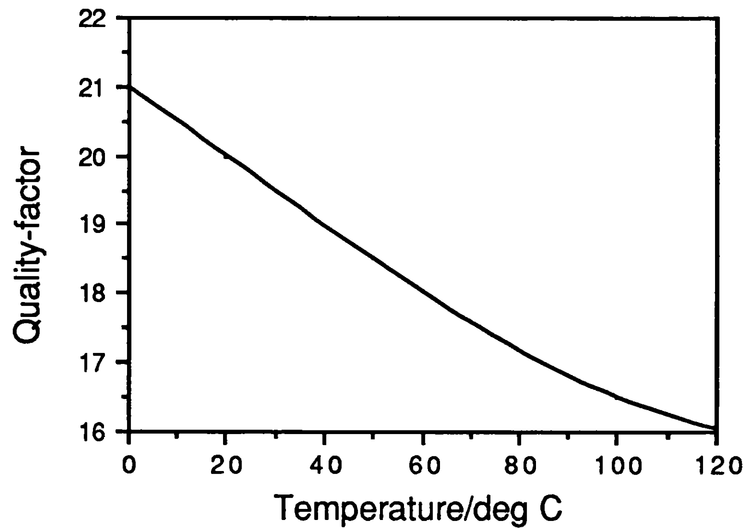

Fig 4.46: The dependance of the quality-factor on the temperature. The device is assumed to be silicon and to be 170μm long, 2μm wide and 0.5μm thick.

ii.b) Viscous damping:

Newell's theory indicates that the quality-factor of a microresonator is mainly dominated by air damping. Therefore, a vacuum encapsulation of the resonator should increase the quality-factor dramatically. In vacuum, the quality-factor is determined by the inner friction of the material which arise from two mechanisms [5]. The first is called the Akhieser mechanism and is caused by phonon interaction. The second is the thermoplastic mechanism by which energy flows from compressed regions of the beam to regions of rarefaction.

Damping such as viscous air damping affects the quality-factor and the resonant frequency of the resonator. A vacuum encapsulation cell has been designed to characterise the vacuum behaviour of the resonators (Fig 4.47). A vacuum of about $7x10^{-2}$ mbar (3 torr) was achieved. However, no drastic increase in the quality-factor of silicon dioxide beams was observed. The quality-factor while decreasing the pressure in the cell rose by a factor of 3.

The resonant frequency also changes with a decrease in the air pressure in which the resonator vibrates. The finite damping causes the observed resonant frequency to vary from that given by the resonant equation. The resonant frequency of the devices shifted from 90KHz to 95KHz and for another one it shifted from 31KHz to 37KHz when the pressure around the devices was decreased to 10^{-3} torr. This is the principle by which these devices can be used to measure the vacuum level.

4.8.4. Conclusions:

The quality-factor of a microresonator is important for the creation of accurate devices that are economical in power. The higher the quality-factor, the higher the precision of the device and also the lower the energy required for activation. Predicting the quality-factor is important for calculating the device's accuracy and the power efficiency. There has been no simple formula to calculate the quality-factor of these devices because of the complexity of the fabrication process which gives undefinable end conditions and also because of the

doping and oxidation of single crystal silicon to form silicon and silicon dioxide resonators. However the Newman [30] formula has been modified in the light of the intensive experimental results.

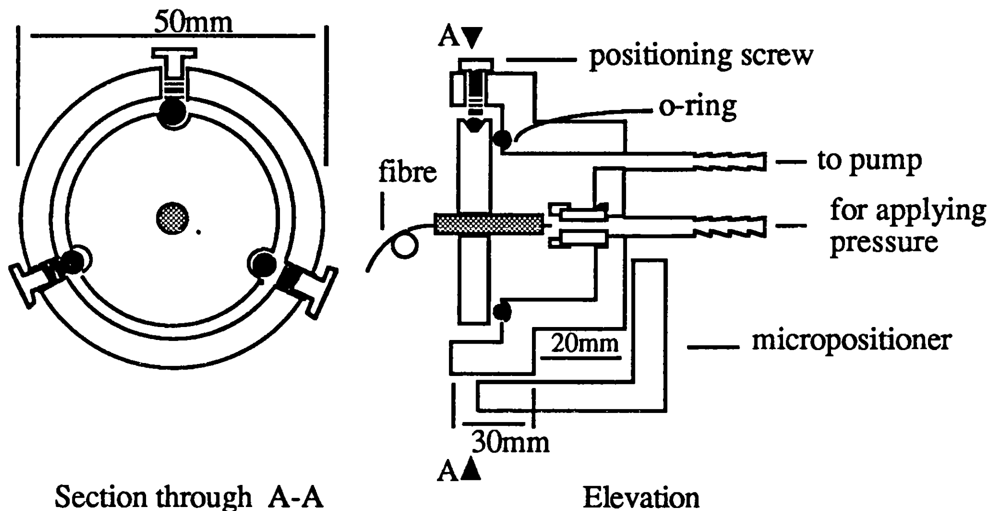

Fig 4.47: The pressure cell that was designed for vacuum measurements and differential pressure applications.

The effect of several parameters has been studied. It is realised that a higher quality-factor can be obtained by encapsulation of the device in the vacuum and by modifying the end conditions. In studying different materials, namely silicon, silicon dioxide and silicon nitride, it is realised that silicon has the highest quality-factor.

The metal coating introduces compression stress in the resonator and this in turn increases damping and hence the quality-factor.

4.9. Overall conclusions

The following points have been studied in this chapter:

1 . The fabrication criteria can produce ill-defined end conditions which in turn can modify the vibration characteristic of the resonators, and hence the resonant equation.

2 . Silicon beams are under tensile stress. The stress is due to lattice mismatch between silicon atoms and doped baron atoms. This stress is quantified to be in the order of 601×10^6 Nm^{-2}. This is still lower than the tensile strength of silicon which is calculated to be 19×10^9 Nm^{-2}. Therefore, we are still operating in the 'safe zone'.

3 . Silicon dioxide beams are under compression stress which is a result of thermal expansion mismatch between silicon and its oxide. This compression stress has been studied by the workers [20-29] in this field and is about 3×10^9 Nm^{-2}. However, the stress is relieved after undercutting the oxide resonator; as a result the beam deflects upwards or downwards by about 4μm. Furthermore, this compression stress shapes the oxide beam fabricated on silicon. These shapes termed 'static modes' were studied. The effect of this deflection of the device as a sensor will be studied in chapter 7.

4 . The metal coating puts the resonator beam under compression owing to the thermal expansion mismatch between the metal and the resonator materials. The coefficient of the stress induced by the metal coating for silicon dioxide beams has been measured to be - 0.2nm KHz^{-1} . This phenomenon is important in using the device as a sensor.

5 . The quality-factor of these devices has been studied. Methods of improving this factor are to be studied.

4.10. References

1. Greenwood J C: 'Etched silicon vibrating sensor' J Phys E: Sci Instrum, Vol 17, 1984, pp 650-652.

2. Uttamchandani D, Thornton K E B and Culshaw B: 'Optically excited resonant beam pressure sensor', Electron Lett, 3 Dec 1987, Vol 23, No 25, pp 1333-1334.

3. Thornton K E B, Uttamchandani D and Culshaw B: 'Novel optically excited resonant pressure sensor', Electron Lett, 12 May 1988, Vol 24, No 10, pp 573-579.

4. Petersen, K E: 'Young's modulus measurements of thin films using micromechanics', J Appl Phys, Vol 50, 1970, pp 6761-6766

5. Hok, B and Gustafsson, K: 'Vibration analysis of micromechanical elements', Sensors and actuators, Vol 8, 1985, pp 235-243.

6. Culshaw B, Nixon J, Thornton K E B, Uttamchandani D and Wright A: 'Optically excited resonator sensor', IOP short meetings series 3: (Silicon based sensors), London, Dec 1986, pp 59-68.

7. Othman M B and Brunnschweiler: 'Electrothermally excited silicon beam mechanical resonators', Electron Lett, 2 July 1987, Vol 23 No 14, pp728-30.

8. Petersen, K E: 'Dynamic micromechanics on silicon: techniques and devices', IEEE Trans on Elec Devices, Vol ED-25, No 10, 10 Oct 1978, pp 1241-1250.

9. Wolfelschneider H, Kist R, Knoll G, Ramakrishnan S, Hofflin H: 'Optically exited and interrogated micromechanical silicon cantilever structure', Procs of SPIE, Vol 798 Fibre Optic Sensor II, 1987, pp 61-66.

10. Andres M V, Foulds K W H and Tudor M J: 'Optical activation of silicon vibrating sensor', Electron Lett, Vol 21, 1985, pp 1097-1099.

11. Fatah R M A , Stokes N A D and Venkatesh S: 'Activation of silicon micromechanical resonators in fibre optic systems', Procs EFCO 89, Amsterdam, June 1989, pp 418-422.

12. Fatah R M A and Stokes N A D: 'Optical activation of silicon micromechanical resonators: end-conditions', Procs of Frontiers in electro optics, UK, March 1990, PP .

13. Fatah, R M A: 'Electrostatic activation of micromechanical resonators', Electron Lett, Vol 27, No 2, 1991, pp 166-168.

14. Venkatesh S and Culshaw B: 'Optically activated vibrations in a micromachined silica structure', Electron Lett, Vol 21, 1985, pp 315-317

15. Venkatesh S and Culshaw B: 'Optically activated resonator sensors', SPIE Vol 566 Fibre Optic and Laser sensors III, 1985, pp110-12.

16. Blevins R D: 'Formulas for natural frequency and mode shape' (Van Nostrand Reinhold Company, New York, 1979)

17. Petersen K: 'Silicon as a mechanical material', Procs of IEEE, Vol 70, No, 5, May 1982, p 420-457.

18. Albert W C: 'Vibrating quartz crystal accelerometer', Procs 28th Int Instrum Symp Las Vegas USA, 1982, pp 33-44

19. Cottell A H: 'The mechanical properties of matter', (John Wiley & Sons, Inc,1964)

20. Kobeda E and Irene E A: 'SiO_2 film stress distribution during thermal oxidation of Si', J Vac Sci Technol, Vol B6 (2), Mar/Apr 1988, pp 574-578.

21. Gaskell P H: 'Thermal properties of silica', pp 1055

22. Jaccodine R J and Schlegel W A: 'Measurement of strain at Si-SiO interface', J Appl Phys, Vol 37, No 6, May 1966, pp 2429-2434.

23. Weland M W and Goemans A H: 'Residual stress at an oxide-silicon interface', Appl Phys Lett, Vol 10, May 1967, pp 262-264,

24. Alexandrova S, Szekfres A and Christova K: 'Stress in silicon dioxide films', Phil Magazine Lett, Vol 58, No 1, 1988, pp 33-36.

25. Wilmsen C W, Thompson E G and Meissner H G: 'Buckling of thermally-grown SiO_2 thin films', IEEE Trans on Electron Devices, ED-19, Jan 1972, pp 122.

26. Jolly D R and Muller R S: 'Miniature cantilever beams fabricated by anisotropic etching of silicon', J Electrochem Soc: Solid-state science and Technology, Vol 127, Dec 1980, pp 2750-2754.

27. Lin S C H and Pugacz-Muraszkiewicz I: 'Local stress measurement in thin thermal SiO_2 films on Si substrates', J Appl Phys, Vol 43, No 1, Jan 1972, pp 119-125.

28. Conru H M: 'Measuring small-area Si/SiO_2 interface stress with SEM', J Appl Phys, Vol 47, No 5, May 1976, pp 2079-2081

29. Pugacz-Muraszkiewicz I: 'Methods for determination of silicon-silicon dioxide interface stress in thermally grown extra thin films', USA IBM Tec Disclosure Bull, Vol 27, No 7B, 1984, pp 4457-4460.

30. Newell W E: 'Miniaturisation of tuning forks', Science, Vol 161, 1968, pp1320-1326.

31. Newell, W E: 'Ultrasonics in integrated electronics'; Procs IEEE, Vol 53, 1965, pp1305-1309.
32. Kate G W and Laby T H: 'Tables of physical and chemical constants', (Longman, London, 15th ed, 1968)

Appendix: material parameters

materials	Young's modulus/10^{10} Pa	density/10^3 kgm^{-3}	expansivity/10^{-5} °C
SiO_2 (fused silica)	7.0	2.2	0.04
Si	19	2.3	0.2
Al	7.0	2.7	2.4
Au	8.0	19.3	1.4
Ag	7.9	10.5	1.9
Cr	2.5	7.1	0.85

CHAPTER FIVE

Electrical Activation of Micromechanical Resonators

5.1. Electrostatic Activation of Micromechanical Resonators

5.1.1. Introduction

So far we have discussed the optical activation of micromechanical resonators. Here we report on a novel method of activating these devices. The devices were driven into mechanical resonant vibration by the application of a time-dependent potential difference and a laser beam guided via a fibre optic coupler used for the detection of mechanical vibration.

The electrostatic activation of these devices is a complementary technique to the optical activation because of two reasons. Firstly, it has been observed that not every device can be

optically activated [1], and secondly, this technique will open up a new field of applications. For example where current or magnetic sensing is involved, electrical activation is more reliable because of the interaction between these parameters and the charges flowing into the beam resonator. Additionally, by using this technique an electrical modulation can be converted into an optical modulation and optical filtering can be achieved.

A resonant structure sustained at resonance produces a stable output for two reasons. Firstly, a resonator at resonance requires enough power to recover its losses which is only a few nanowatts for the structure described in this chapter. Secondly, the resonant frequency is determined by the dimensions and mechanical properties of the beam resonator and not the activation and detection sources. In this device an electrical input is converted into mechanical vibration which is then converted into an optical output signal ready to be interfaced with digital signal processing.

5.1.2. Device construction

Silicon oxide or nitride beams can be formed on silicon wafers using silicon technology. These beams are mechanical devices suspended on the silicon wafer with built-in ends to the silicon oxide or nitride formed on the wafer. Fig 5.1 shows a scanning electron micrograph of an oxide beam etched on silicon and Fig 5.2 shows a schematic diagram of the device formed. Let us assume a silicon oxide or nitride beam formed on a silicon wafer. Metalising both sides of the wafer forms a parallel plate capacitor having dielectric mediums sandwiched between two electrodes. The dielectric materials in question will be air in the cavity under the beam, the oxide or nitride layer and the silicon substrate. The dynamic part of the capacitor which is of interest is the surface area of the beam.

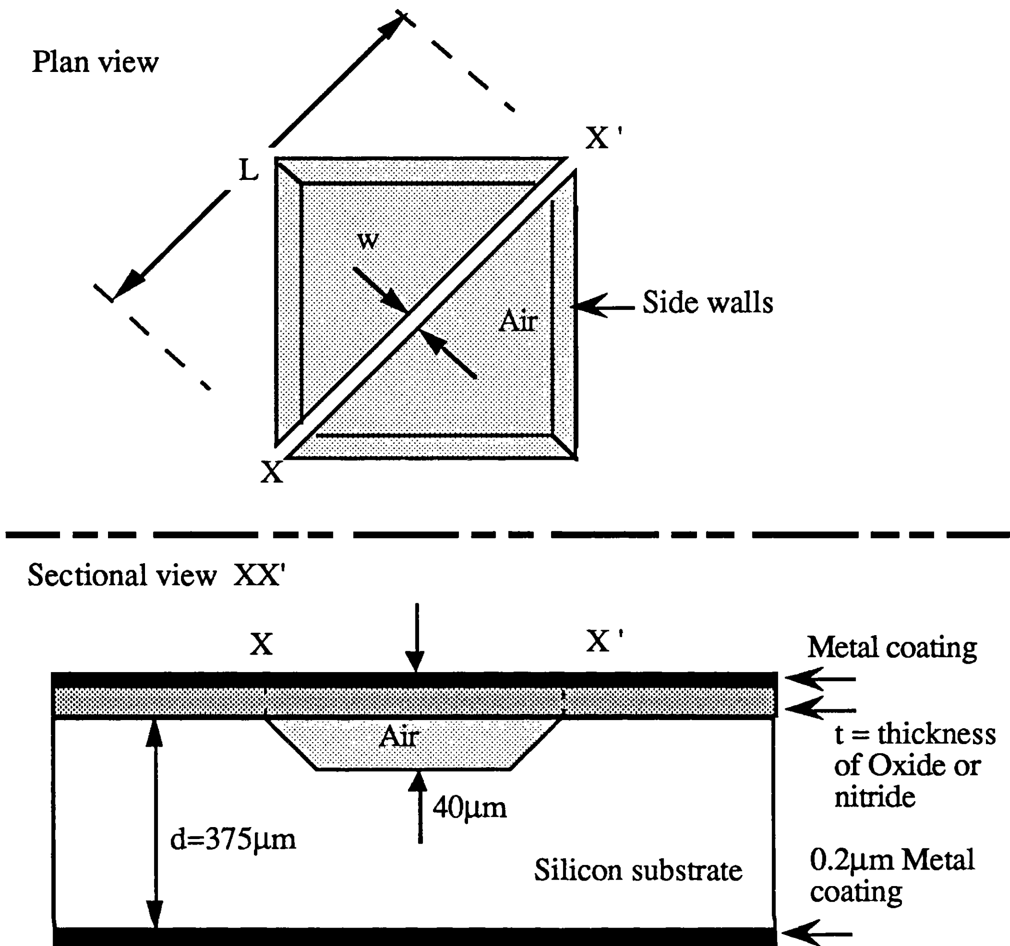

Fig 5.2: Schematic diagram of a beam microresonator.

5.1.3. Principle of activation

It is possible to sustain a micromechanical resonator at resonance by utilising the Coulombic attraction between the metal coatings on each side of the silicon sample.

Coulomb attraction between the parallel-plates may be produced as opposite charges are introduced to them, Fig 5.3. One of the plates, the beam resonator, is free to move. The attraction can displace the beam from its position of equilibrium towards the substrate and hence decrease the separation between the two electrodes.

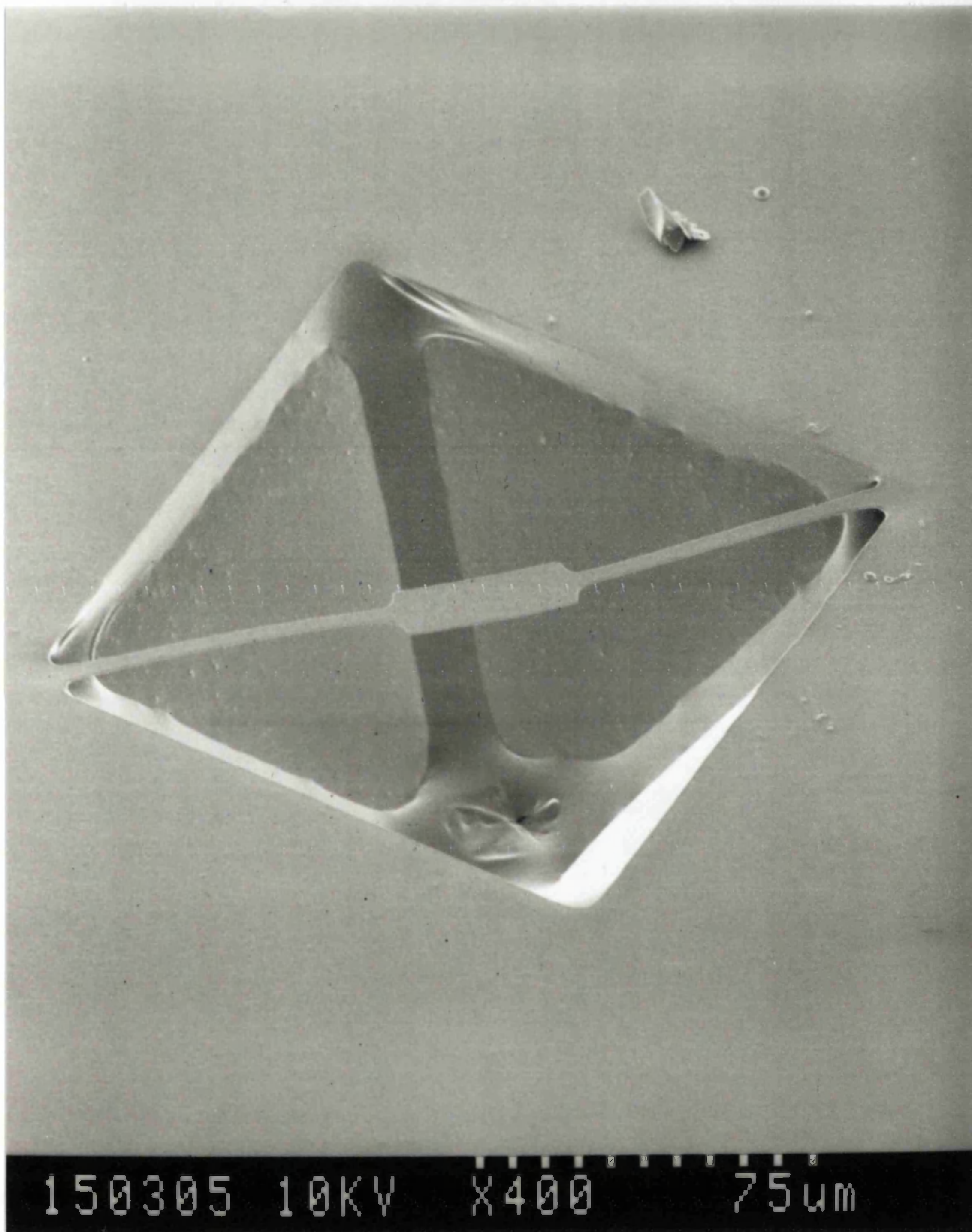

Fig 5.1: An SEM of a silicon dioxide beam resonator.

By varying the charge introduced to the electrodes, the magnitude of the Coulomb force is changed, hence the separation between the electrodes changes, too. If the charges are varied periodically the displacement of the beam resonator will vary periodically. If the periodic displacement of the beam is equal to one of the natural frequencies of the beam, it will then be sustained at resonance. Practically, this may be achieved by applying a time-dependent potential difference. The vibration of the resonator is sensed optically using a fibre optic coupler as shown in Fig 5.4. The mechanism of detection is discussed in section 3.7.

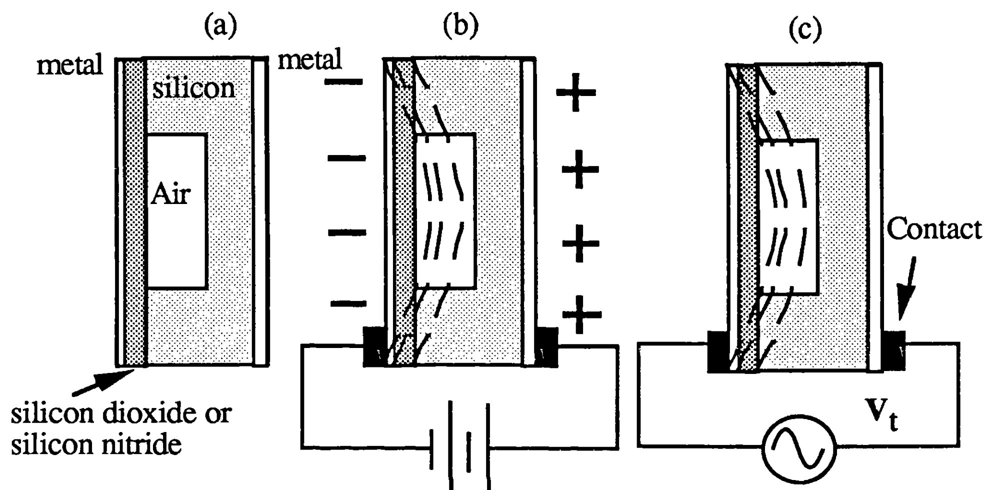

Fig 5.3: Electrostatic activation of beam resonators.

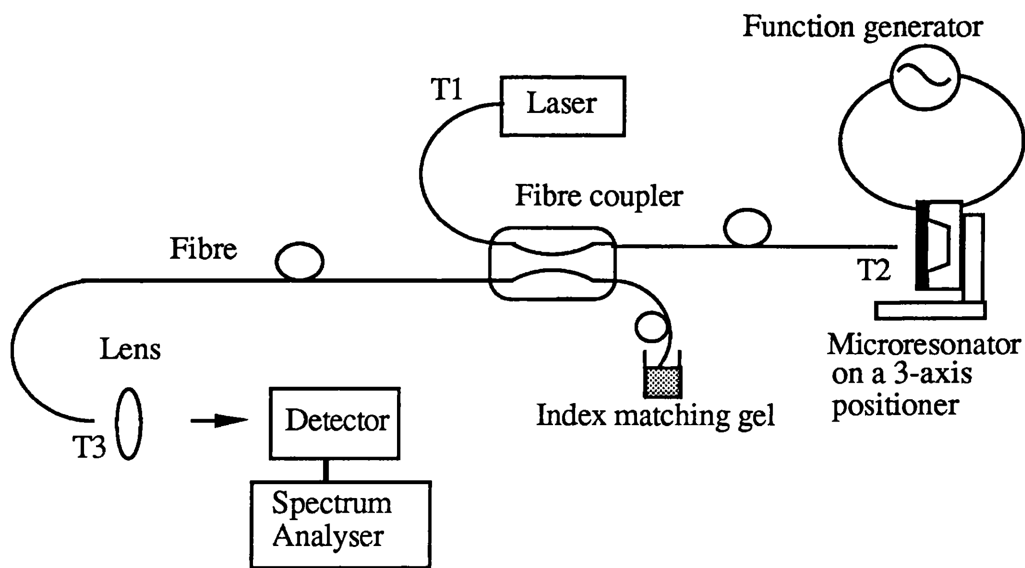

Fig 5.4: Optoelectric system for activation and detection of resonators.

5.1.4. Electromechanical analysis

Following the analyses by Nathanson et al [2], the simplified model of electrostatic activation of microresonators is shown in Fig 5.5. The equation for the electrostatic force on the vibrating mass is given by:

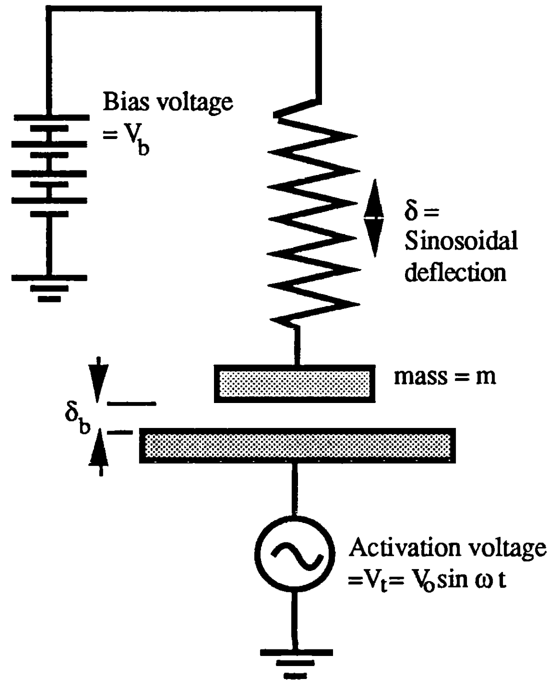

Fig 5.5: A mass-on-a-spring model to simplify the electrostatic activation of beam resonators. After Nathanson [2].

$$\text{Electrostatic force} = \frac{1}{2}\left[V_b+V_t\right]^2\frac{\partial C_t}{\partial \delta_b}$$
$$= \frac{1}{2}\left[V_b^2+2V_bV_o\sin\omega t+\frac{V_o^2}{2}\{1-\cos 2\omega t\}\right]\frac{\varepsilon A}{\delta_t^2} \quad (5.1)$$

where V_b is the bias voltage and V_t (= V_o sin ωt) is the sinusoidal input with angular frequency ω; C is the capacitance associated with the area of the beam resonator; δ_b the equilibrium spacing between the beam resonator and the silicon substrate when a bias voltage is applied and δ_0 when it is zero; δ is the sinusoidal resonator deflection under V_t and ε is the permittivity of the media i.e. the silicon substrate and the air under the beam.

The silicon nitride and oxide layers have been ignored in these calculations.

The first term in the bracket in (1) represents the time-independent component of the force caused by the bias voltage which leads to the dependence of δ_b on V_b. The third term is ignored in linear operations. The second term is the time-dependent component of the force:

$$F(t) = F_o \sin \omega t = \frac{2V_b \varepsilon V_o}{\delta_t^2} \sin \omega t \qquad (5.2)$$

In the presence of bias, the net force on the spring is zero, i.e. the electrostatic force is equal to the mechanical force. Mathematically:

$$\text{Net force} = \frac{\varepsilon A V_b^2}{2\delta_t^2} - k_o(\delta_o - \delta_t) = 0 \qquad (5.3)$$

which gives δ_t as a function of V_b.

Another result of the interaction between the electrostatic and the mechanical force is that the spring 'constant' is not constant, but varies with V_b. Differentiating (5.3) with respect to δ_t gives:

$$k_b = k_o(3 - 2\frac{\delta_o}{\delta_t}) \qquad (5.4)$$

The variation in k also sets a new resonant condition. The new resonant frequency ω_b is related to the 'true' one ω_i by:

$$\frac{\omega_b}{\omega_i} = \frac{\sqrt{\frac{k_b}{m}}}{\sqrt{\frac{k_o}{m}}} = (3 - 2\frac{\delta_o}{\delta_t})^{\frac{1}{2}} \qquad (5.5)$$

However, for the bias level that we have applied and the quality-factor obtained, the deviation from ω_i has been negligible.

5.5.5. Experimental work

i) Frequency response of the resonators:

Two materials have been studied, namely silicon dioxide and silicon nitride. A typical paddle type silicon dioxide resonator studied is shown in Fig 5.6. The device was activated at two resonant modes: 60 and 157KHz.

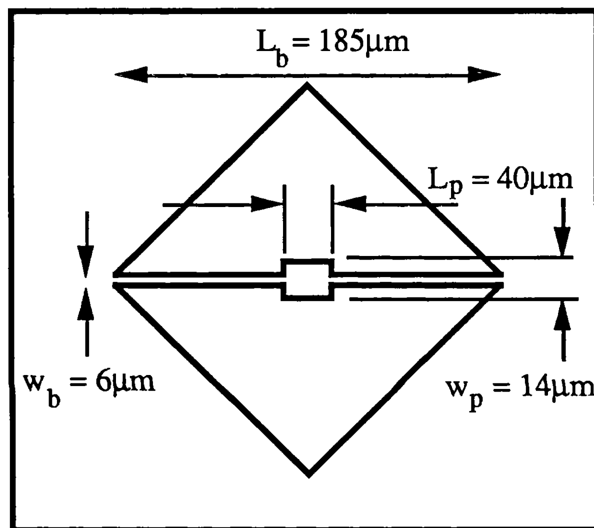

Fig 5.6: A plan view of the silicon dioxide resonators.

The first batch of silicon nitride beams formed on silicon was similar to the device shown in Fig 5.2 with dimensions of L = 200μm, t = 20μm, w = 0.2μm. They were coated with 20nm of chromium using the evaporation technique. When the devices were biased at 10V and a time-dependent potential difference of 5V peak-to-peak was applied responses at 48, 91, 184, 294, 392 and 591KHz were observed. The corresponding quality-factors 10, 17, 20, 26, 28 and 41 respectively were measured. The measured values of resonant frequency and their predicted values against mode number are plotted in Fig 5.7. The device has clamped end-conditions [3].

The quality-factor is measured by taking the ratio of the resonant frequency to the bandwidth of the resonant peak at its half amplitude. The measured and predicted values of the quality-factor are plotted in Fig 5.8.

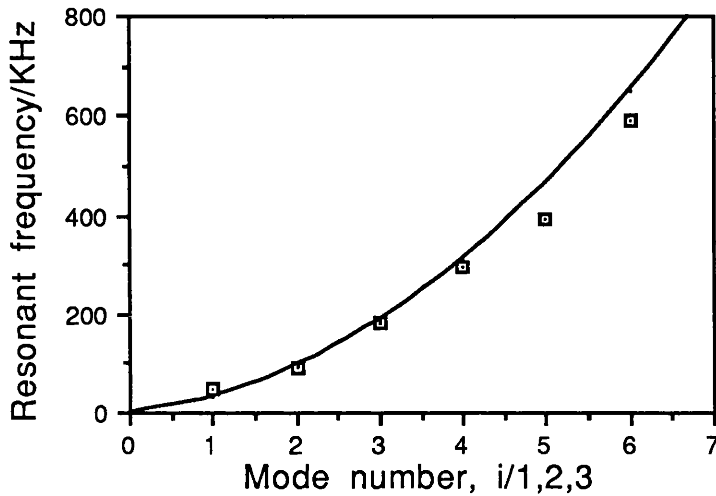

Fig 5.7: The resonant frequency of the silicon nitride resonator against mode number. Clamped end-conditions considered.

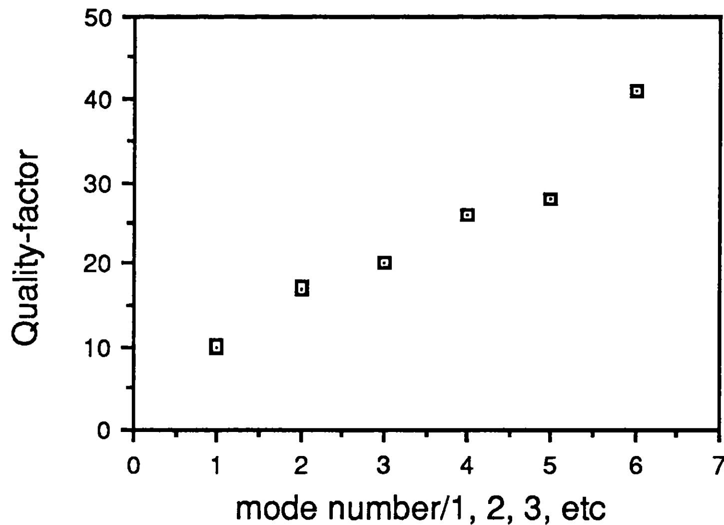

Fig 5.8: The relationship between the quality-factor and the mode number for the silicon nitride resonators.

ii) Dependence of signal amplitude on applied voltage level:

The nitride samples were studied at constant bias voltages as shown in Fig 5.9. The characteristic of the oxide samples at zero bias are shown in Fig 5.10. The resonant amplitude increases with increasing time-dependent voltage as predicted by (3).

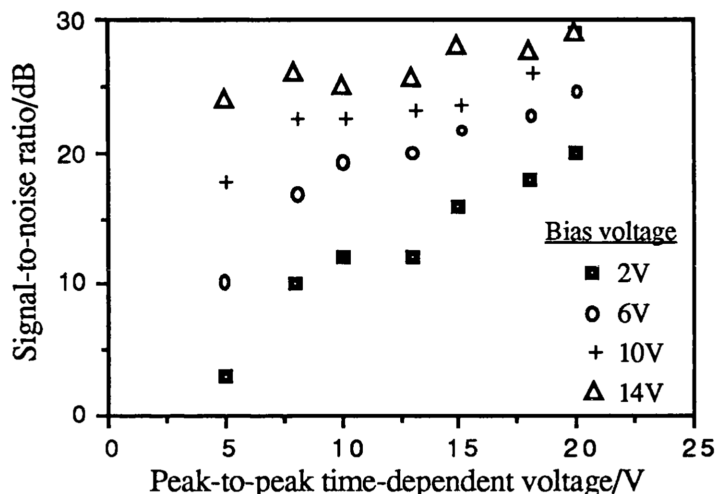

Fig 5.9: The dependence of the amplitude of resonance for silicon nitride upon the time-dependent potential difference across the wafer at constant bias voltage.

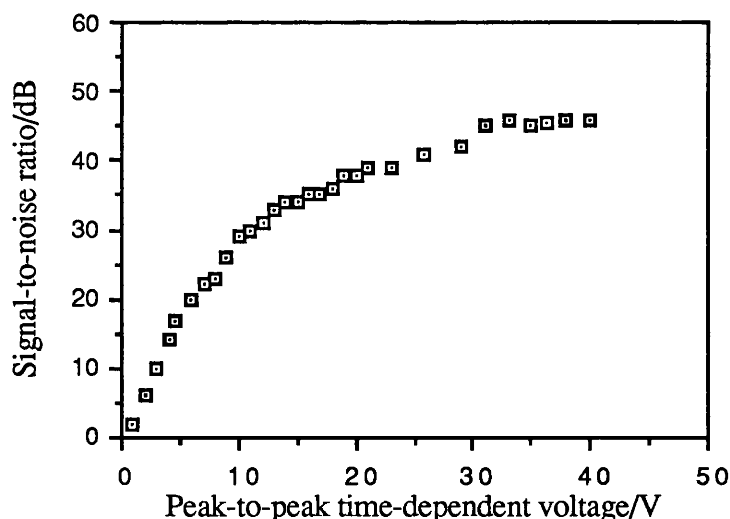

Fig 5.10: The dependence of the amplitude of resonance for silicon dioxide resonators upon the time-dependent potential difference across the wafer at zero bias voltage.

The amplitude of resonance also increases with increasing bias voltage at a constant time-dependent voltage as is predicted by (3). Fig 5.11 shows the characteristic of the silicon nitride devices.

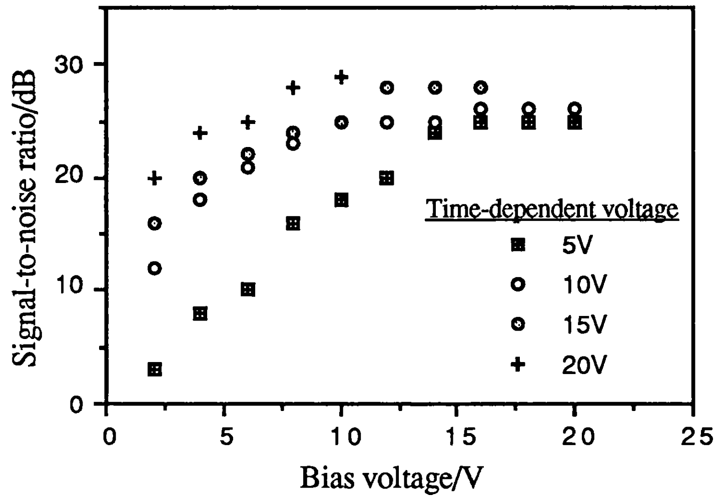

Fig 5.11: The dependence of the amplitude of resonance for the silicon nitride resonators upon the biased potential difference across the wafer at constant time-dependent voltage.

iii) Comparison between electrical and optical activation:

The experimental set-up used to study microresonators optically in fibre optic systems is given in Fig 3.2. None of the nitride devices were driven into vibration by optical energy. One explanation of this is that the thickness, 0.2μm, is not sufficient to establish a temperature gradient along the length of the beam which is the cause of the activation.

Nevertheless, smaller silicon nitride devices similar in shape to the oxide ones were possible to activate optically. The dimensions of these devices were L_b = 175μm, L_p = 38μm t = 0.5μm, w_b = 5μm and w_p = 13μm. They were evaporation coated with 200nm of aluminium. Only two modes of resonance were activated, 297KHz and 745KHz, the corresponding measured quality-factors being 28 and 55.

The silicon dioxide devices were also studied using optical activation techniques. It was observed that the fundamental resonant frequency of the device was still 60KHz. The only other frequency at which the device responded was 270KHz. This mode was not observed during electrical activation. Furthermore, the response at 157KHz which was detected by electrical activation was not observed in the optical technique.

However, other silicon dioxide devices with a triple paddle, shown in Fig 5.12, were not driven into resonance optically. When driven electrically only two resonant frequencies were observed, at 697 KHz and 911KHz with a quality-factor of 75. Short beams have higher flexure rigidity[1] than longer ones, so a higher bending force is required to activate the shorter beams. This may be the reason for not activating the shorter beams using the optical technique since the electrical activation has a higher bending force.

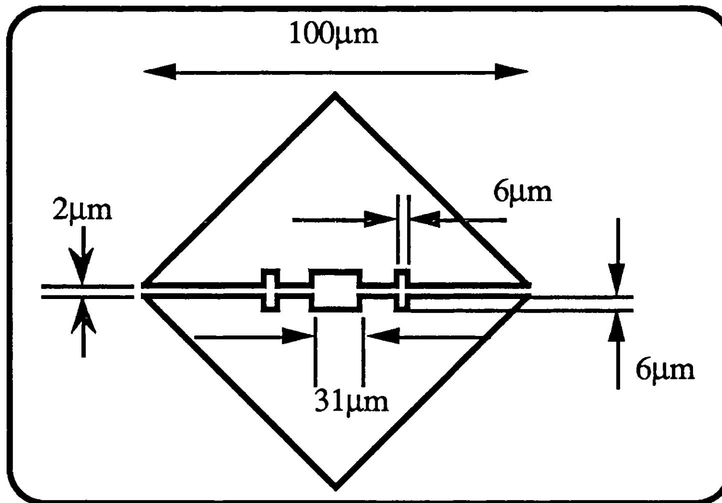

Fig 5.12: A plan view of a triple paddle microresonator.

[1] See section 3.4.3.

5.5.6. Discussion and conclusions:

While all the devices mentioned, with lengths from 100μm to 200μm, have been activated electrically, only some of them have been activated optically. The optical activation is determined by the heat distribution along the beam resonator while the electrostatic activation is determined by the Coulombic force. The response of the charged particles is faster than the thermal response, but both processes are ultimately determined by the inertia of the beam material. So while the Coulombic force may be sufficient to deflect the beam the temperature gradient may not be sufficient to do this.

Optical activation is an ideal sensing system in medical and engine monitoring when the use of electrical current is to be avoided. However, the electrical activation expands the applications of these devices. Such applications may be involved in magnetic and current sensing. In addition, optical filtering and optical modulation can be achieved without any circuitry complications since the device produces a stable intensity modulation.

Multiplexing more than one device can be achieved by connecting the required number of devices in a parallel scheme and ramping the frequency of the drive in time to cover the mechanical resonant frequency of all the devices. For multiplexing, the devices have to have differing mechanical resonant frequencies since the individual devices have to be recognised.

These devices have been used to calculate the Young's modulus and density of silicon dioxide and silicon nitride [4]. From the equation of resonance the geometry of the resonator beam can be found. In these cases the metal coatings must be kept no thicker than, say, 50nm as the metal coating makes it difficult to measure the resonant frequency accurately. It has been shown that silicon nitride and silicon dioxide beams etched on a silicon wafer can be driven into mechanical resonance electrostatically. These devices have the capability to be used as sensors, and to measure Young's modulus, density and geometry of the beam materials. Furthermore, they can be used as optoelectronic components such as modulators and filters.

5.2. Electrothermal Activation of Resonator Sensors

5.2.1. Introduction:

Electrical power can be delivered and partially dissipated in the form of heat in a resonator. This resonator may be in the form of a beam, diaphragm or more complicated structure, using some form of resistor (heater). As the electrical energy transfers to the resonator, the heating (Joule) effect deflects the resonator from its initial position by introducing a tensile stress. When the beam cools down the stress relaxes and the beam returns to its initial position. So a periodic electric current input causes the resonator to displace in an oscillatory motion. Resonance occurs whenever the periodic current is equal to that of the natural resonant frequencies of the resonator. The mechanical oscillation lags the input signal by some phase angle which is due to the inertia of the system. This is the principle of electrothermal activation.

Wilfinger et al 1968 [5] first investigated this effect by the activation of a silicon cantilever which dissipated heat in its suspended end. Resistors were diffused in the suspended end to dissipate the periodic electric power. This in turn generated periodic contraction and expansion in the skin near the surface of the cantilever. Dieulesaint et al 1986 [6] activated a sapphire (Al_2O_3) beam (40 x 3 x 3 mm) which was suspended at two points away from the ends to form a free ended beam. A 100nm thickness of chromium provided the resistor. An alternating current was applied to the suspension wires which produced a periodic heating and hence mechanical vibrations. Air resistivity was high enough to damp the mechanical resonance, due to the size of the device, so vacuum encapsulation was required to achieve the resonant condition. Othman and Brunnschweiler 1987 [7] mounted a U-shaped polysilicon resistor in a cantilever. This resistor dissipated periodic heat in the cantilever and as a result resonance occurred. This resonator also only operate in a vacuum.

We shall now report a simple method to activate and detect the resonant frequency of resonators. Fig 5.13 shows our silicon beam resonator through which a current was passed. A metal coating was evaporated on the beam resonator to form a resistor which

converted part of a periodic electrical current into mechanical vibration via an intermediate thermal stage. This simplified the activation and the method can be used for any type of beam. In addition, the resonance was detected optically via optical fibres.

5.2.2. Theory:

One of the electrical properties of thin metal films, namely high resistivity, is utilised in heating the strip. The magnitude of the rate of heat energy produced is given by:

$$H = I^2 R \qquad (5.6)$$

where I is the current passed through the strip and R is the resistance of the metal coating on the beam. Thus, a time-dependent current produces a periodic expansion and contraction of the strip. If the time-dependent current can be given by $I_0 \cos(\omega t)$, where ω is the angular frequency of the current, then (1) can be re-written as:

$$H = R\, I_0^2 \langle \cos(\omega t) \rangle^2 = \frac{R\, I_0^2}{2} \langle 1 + \cos(\omega t) \rangle \qquad (5.7)$$

where I_0 is the amplitude of the current. The significance of the above equation is that the rate of heating produced is double the frequency of activation.

The resistance of the metal coating is given by:

$$R(T) = \frac{\rho(T)\, L}{S} \qquad (5.8)$$

where ρ is the resistivity of the metal coating, S and L are the surface area and the length of the resonator, respectively. However the resistance is temperature dependent and can be given by:

$$R(T) = R_0 \left(1 + \alpha T + \beta T^2 + \cdots \right) \qquad (5.9)$$

The temperature resistivity of bulk chromium on temperature is $5 \times 10^{-9}\ \Omega\, m\, K^{-1}$ [8]. The temperature is time-dependent because the current is time-dependent, and it may be given

by:

$$T(t) = T_o \cos(\omega t + \psi) \qquad (5.10)$$

where T_o is the amplitude of the time-dependent temperature introduced by the current in the resonator, ψ is some phase difference between the current flowing in the metal coating and the temperature induced. Substituting the relations (4) and (5) in (2) after neglecting the higher terms we have:

$$H = \frac{R_o I_o^2}{2} \Big[1 + T_o \, \alpha \cos(\omega t + \psi) + \cos(2\omega t) + \alpha T_o \cos(\omega t + \psi) \cos(2\omega t) \Big] \qquad (5.11)$$

The first term in the brackets is the time independent component of the heat which does not contribute to the amplitude of vibration. The second term contains ωt and the third term $2\omega t$ whilst the last term contains both ωt and $2\omega t$. This implies that for each mechanical resonant frequency, the device can be activated at the frequency of the electrical drive and double that frequency. However, for normal linear operations the last two terms will be neglected and the mechanical frequency will be equal to the electrical frequency.

When the period equals one of the natural resonant frequencies of the beam, resonance will occur, i. e. electrical frequency = mechanical resonant frequency. The resonant frequencies, $f_i = \omega_i / 2\pi$, of flexural vibrations of a homogeneous prismatic beam are given by (3.21).

The metal coating provides the surface for electro-thermo-mechanical conversion, which allows the beam to be set into vibration. Moreover, silicon is transparent for wavelengths higher than 1.1μm, so a metal coating is essential to act as a mirror reflecting the incident laser beam which is used in the detection scheme. The metal coating changes the resonant frequency of the beam, and the equivalent value for EI is given by (3.26).

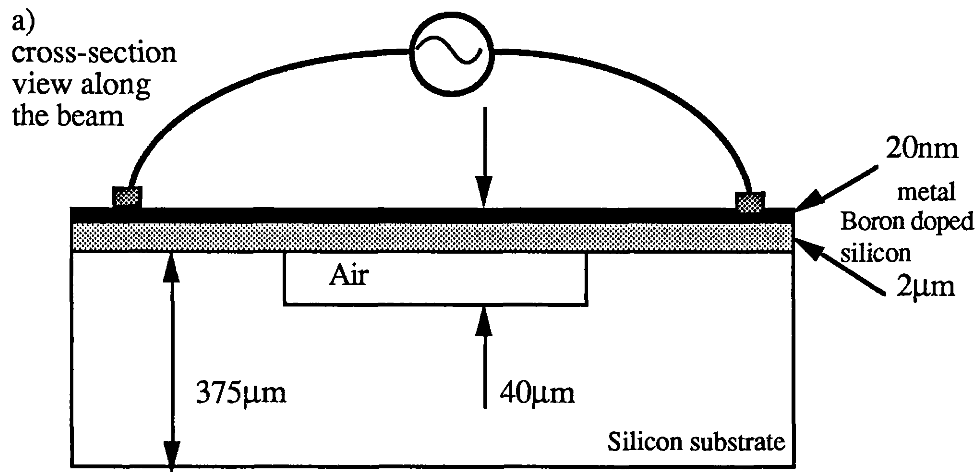

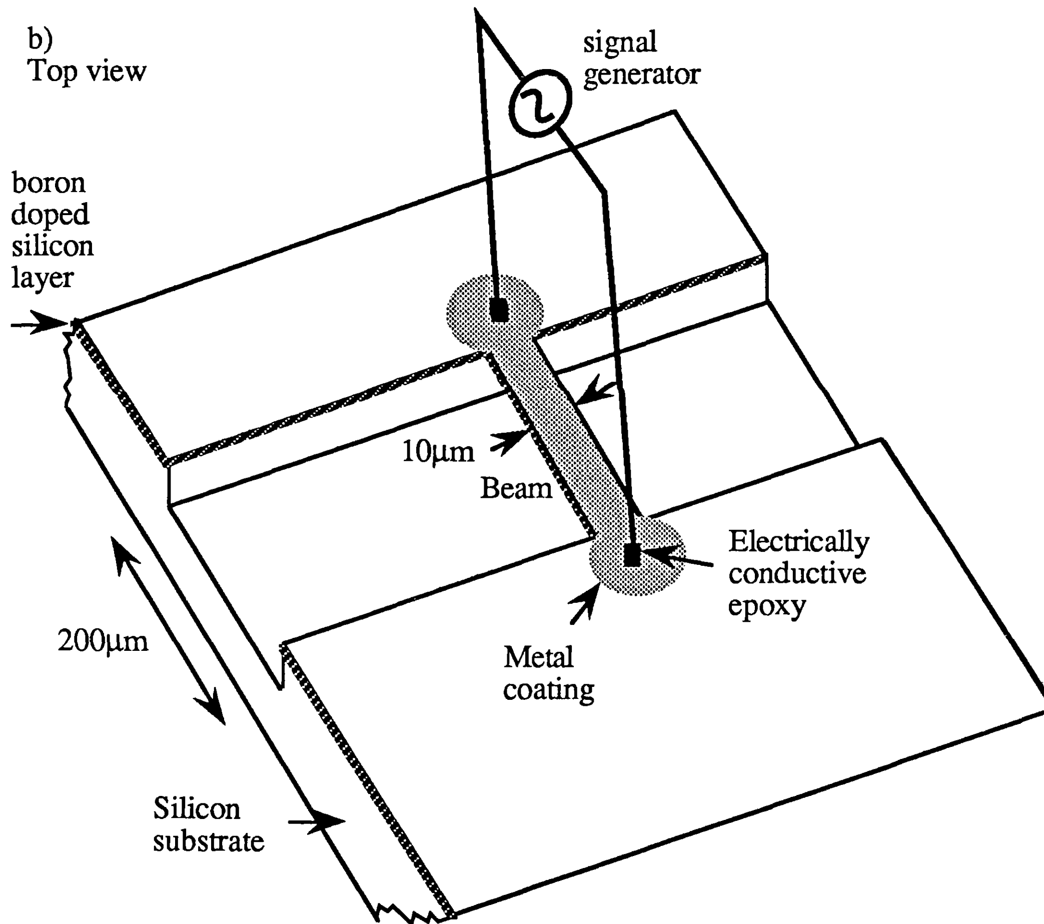

Fig 5.13: Electrothermal activation of a micromechanical resonator.

5.2.3. Experiments:

Micromechanical resonators, in the form of boron-doped silicon strips, have been fabricated using anisotropic etching techniques and evaporation coated with 20nm of chromium. Their dimensions are 200μm long, 10μm wide and 2μm thick. Two copper wires were connected to each side of the beam (Fig 5.13) away from the suspensions at each end. Electrical connections were made between the copper wires and the metal coating of the resonator. The only connection between the two wires was via the beam resonator surface and not the wafer.

The vibration of the resonator was sensed optically using a fibre optic coupler as shown in Fig 5.14. The mechanism of detection is discussed in section 3.7.

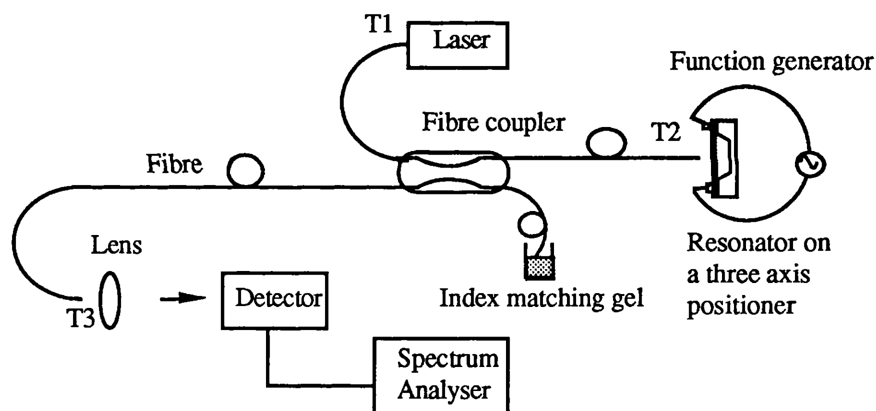

Fig 5.14: Electrothermally activated and optically detected micromechanical resonators in fibre-optic systems.

Two optical fibre systems were successfully used: firstly, a monomode system operating at 1.3μm wavelength and secondly a multimode system operating at 850nm wavelength. A set of devices was characterised. A resonant peak of 35dB above the noise floor for these devices was observed at 258kHz, for an electrical drive at half that natural resonant frequency. Fig 5.15 shows the display of the spectrum analyser. The same response was also observed when the device was activated at 258KHz. As predicted from (6), the

mechanical resonance of the beam can be activated at two electrical frequencies which are equal to or half the mechanical resonance frequency. The quality-factor of the device was 60.

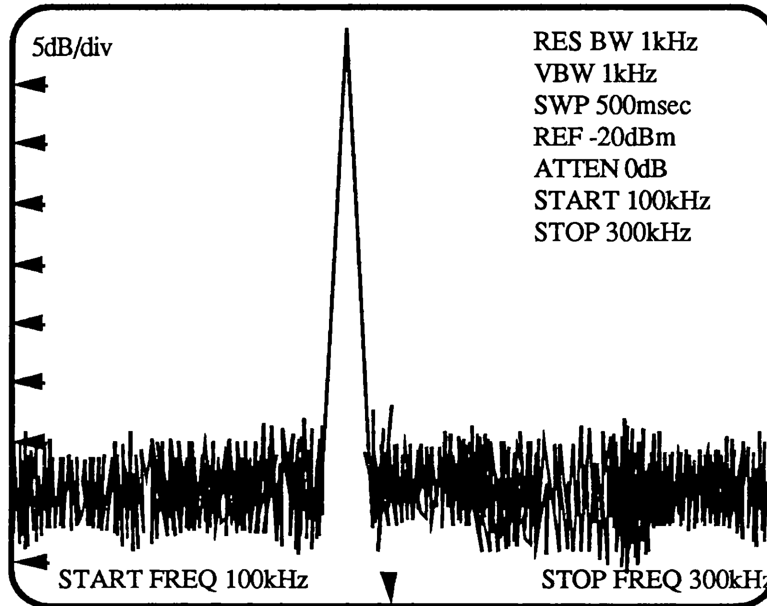

Fig 5.15: A spectrum analyser display of the resonant frequency.

5.2.4. Discussion and conclusions:

It is possible to use a metal coating evaporated (or deposited) on a beam resonator as a resistor to convert electrical current into mechanical vibration via an intermediate heating stage. This mechanical vibration is detected by directing a laser beam guided through an optical fibre on to the surface of the resonator, and monitoring the reflected signal.

The predicted resonant frequency calculated from (7) and (8) is 466KHz which is higher than that measured. This may be caused by thermal mismatch between the metal coating and the silicon. At room temperature the silicon beam is under compression stress which is

primarily caused by the tension in the metal coating. After the evaporation process the metal and the silicon both cool to room temperature and contract. However, silicon has a lower thermal expansion (2.6×10^{-6} ^{o}C) than that of chromium (4.6×10^{-6} ^{o}C). As a result the silicon will be under compression whilst the metal will be under tension. The compression stress reduces the resonant frequency of the resonator.

The electrothermal activation of these devices is a complementary technique to the optical activation for two reasons. Firstly, it has been observed that not every device can be optically activated [1], and secondly, this technique will open a new field of applications in telecommunications and sensing. For example where current or magnetic sensing is involved, electrothermal activation is more reliable because of the interaction between these parameters and the electric current flowing into the beam resonator. Additionally, by using this technique an electrical modulation can be converted into an optical modulation and optical filtering can be achieved.

5.3. References

1 . Langdon R M and Dowe D L: 'Photoacoustic oscillator sensors', Procs SPIE Conf on Fibre Optic Sensors II, The Hague, 1987, pp 86-93.

2 . Newell H C, Wickstrom W E and Davis J R: 'The resonant gate transistor', IEE Trans of Electron Devices, Vol ED-14, No 3, March 1967, pp117-133.

3 . Fatah R M A and Stokes N A D: 'Optical activation of silicon micromechanical resonators: end-conditions', Procs of Frontiers in Electro Optics, Birmingham, 1990, pp 118-125.

4 . Petersen, K E: 'Young's modulus measurements of thin films using micromechanics', J Appl Phys, Vol 50, 1970, pp 6761-6766.

5 . Wilfinger R J, Bardell P H and Chhabra D S: 'The resonator: a frequency selective device utilizing the mechanical resonance of silicon substrate', IBM J Res and Dev, Vol 12, 1968, pp 113-118.

6 . Dieulesaint E, Royer D and Servajan X: 'Sapphire resonator', Electron Lett, 1986, 22, pp 266-268.

7 . Othman, M B, and Brunnschweiler A: 'Electrothermally excited silicon beam mechanical resonators', Electron Lett, 1987, 23, pp 728-30.

8 . Kay G W and Laby T H: 'Tables of physical and chemical constants', (Longman, London, 15th ed, 1968)

CHAPTER SIX

Self-Excitation of Micromechanical Resonators

6.1. Introduction

The two source system as it stands is not reliable for multiplexing a number of resonator sensors. This is because each sensor has to have a different resonance frequency and it has to be modulated at its resonance frequency. So n resonators require n sources of activations. However, the solution for this problem is self-excitation. In this system only one laser source is used for both activation and detection. Therefore, no optical and electrical drive is used to set the activation as shown in Fig 6.1. This would be achieved by the Fabry-Perot intensity variation which is set between the partially reflected surfaces of the resonator and the fibre end cross-section, as shown in Fig 6.2.

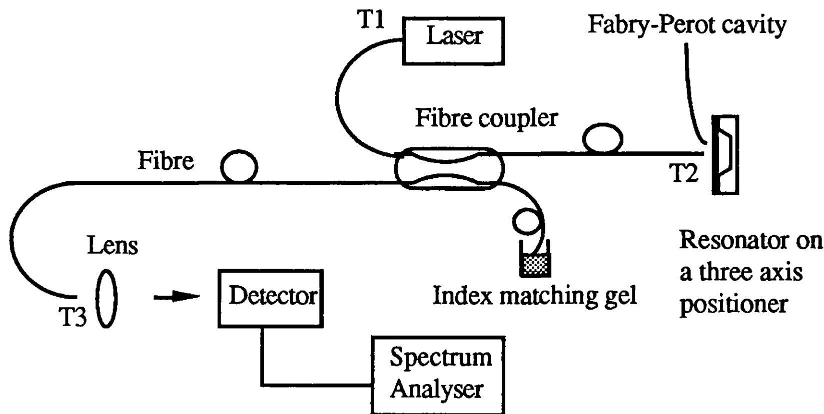

Fig 6.1: Self-excitation of microresonators in fibre-optic systems.

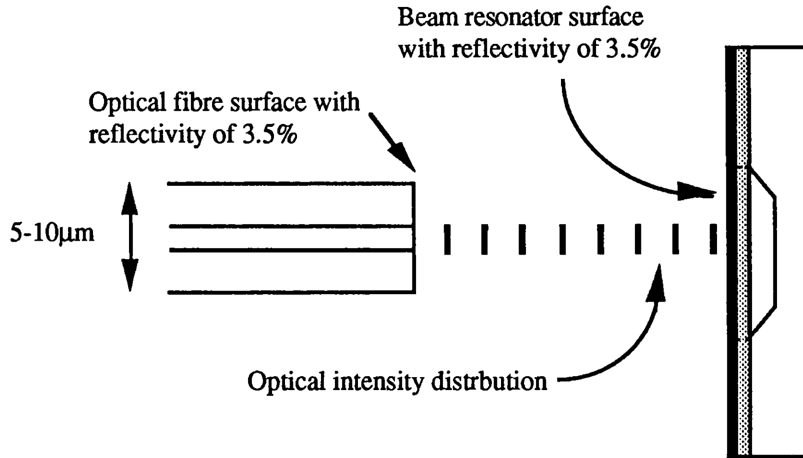

Fig 6.2: The Fabry-Perot intensity variation between the partially reflected surfaces of the resonator and the fibre end cross-section

We have analysed the Fabry-Perot intensity variation in the cavity in chapter 3. We may recall the equation (3.43) which gives the intensity in the cavity.

$$I = \frac{I_o T_f T_b}{(1-\sqrt{R_b R_f})^2} \left[1 + \frac{4\sqrt{R_b R_f}}{(1-\sqrt{R_b R_f})^2} \sin^2\left(\frac{\Delta}{2}\right) \right]^{-1} \qquad (9.1)$$

All the symbols are defined in section 3.8. Fig 3.42 shows the Fabry-Perot intensity for two wavelengths 633nm and 1.3μm. Fig 6.3 represents the Fabry-Perot intensity field distribution in the cavity. Let us consider that the beam is initially at point a. As a result of absorbing light from this point, it is expanding and deflecting either towards point b or c. The amount that the beam moves depends on its geometry, mechanical and optical properties. Let us say that the beam moves to point b. This position is cooler than point a, so the beam cools down and consequently returns back, under its restoring force, to its initial position point a. The same analogy can be used if the beam moves to point c. Therefore, the beam absorbs light, i.e. restores (potential) energy and as a result it deflects. As the beam gets into a cooler position in the Fabry-Perot intensity distribution, it cools down and as a result contracts and returns to its initial position. The potential energy changes to kinetic energy and deflects to the other extreme, and so on. In this fashion the

vibration continues. According to the law of the conservation of energy the vibration continues with the lowest energy possible. By definition the lowest energy level of vibration is the natural resonant frequency. Hence resonance occurs.

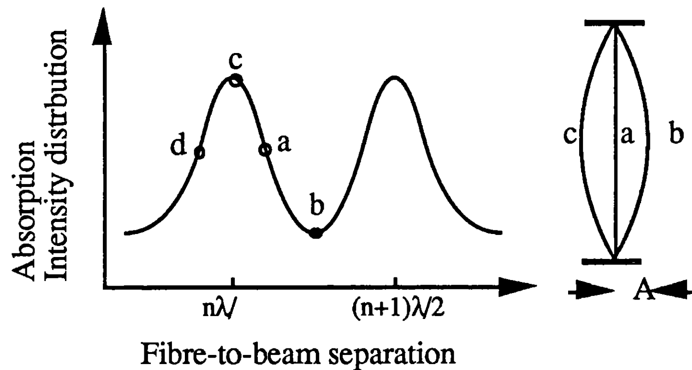

Fig 6.3: Absorption and intensity distribution in the cavity between the fibre end and the resonator. The beam is also shown.

Going back to (6.1), it can be seen that the Fabry-Perot intensity depends on the intensity of the source, the reflectivity of the surfaces (fibre/resonator) and the wavelength of light.

Several suggestions can be made. Firstly the end of the fibre can be coated with a thin metal film to make the reflectivity higher. Secondly, with reference to Fig 3.42 (a and b), starting the vibration may be easer with longer wavelengths since they are less critical in keeping the beam in the linear portion of the intensity distribution (around point a). Thirdly, the surfaces must be flat and parallel and they should be as close as possible (~few μm) since both coupling and intensity drops with angular misalignment and distance (see section 3.7).

The condition of self-excitation can be satisfied if the force induced in the resonator beam owing to absorption is either equal to or larger than the summation of damping, inertia and spring force of the beam. Therefore, softer materials like metals may help self-excitations.

This method was proposed first by Langdon and Dowe for micromechanical resonators and was achieved by them for bulk optics. However, the first time this was achieved for

micromechanical resonators is reported in [2,3]. Since then there have been other reports on self-excitations [3-5].

The advantage of self-excitation is in the multiplexing scheme. Fig 6.4 shows a number of self-excited sensors multiplexed using a stare coupler.

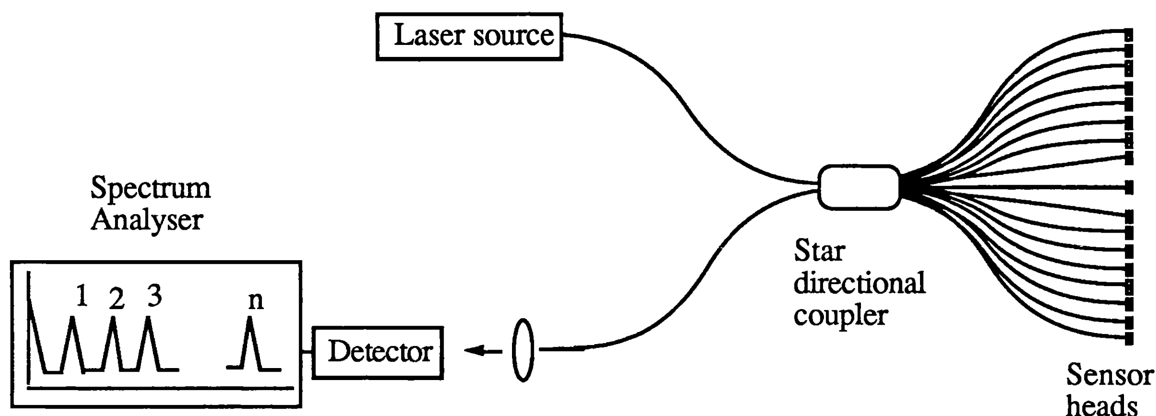

Fig 6.4: Multiplexing self-excited microresonators in fibre-optic systems.

6.2. Experimental work

6.2.1. Observation of self-excitation:

The self-excited devices studied were silicon dioxide beams. The oxide thickness of all these devices was about 0.15μm and spattered with approximately 0.2μm of gold. The beams examined were approximately 190μm long and 2.5μm wide, with a paddle of length 20μm and width 14μm. Using the experimental setup of Fig 6.1 with an unmodulated He-Ne laser. The end of the fibre was held approximately 5μm away from the surface of the resonator. The spectrum of the reflected light signal for an intensity of 600μW is shown in Fig 6.5. A number of peaks can be seen at integer multiples of the resonant frequency. The quality-factor was 50. The resonant frequency was sustained with an SNR of 40dB over a period of several hours.

The second source was a 1.3μm which was used for the self-excitation experiment. A resonant frequency for another device similar to the previous one is shown in Fig 6.6 which has an SNR of 60. The power used was 250μW.

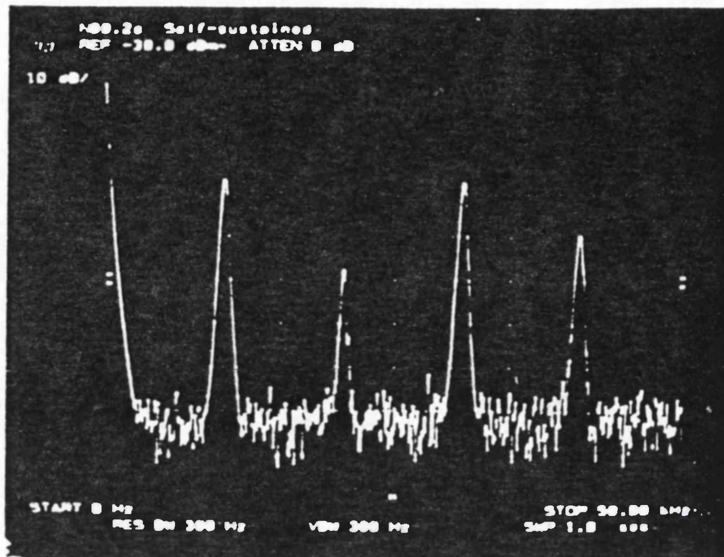

Fig 6.5: Spectrum of a reflected signal from a self-excited microresonator, frequency range 0 to 50KHz, amplitude 10dB/division.

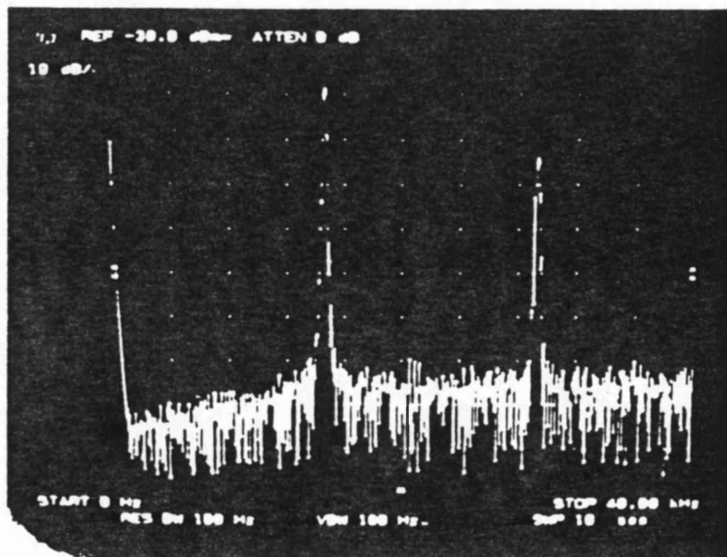

Fig 6.6: Spectrum of a reflected signal from a self-excited microresonator, frequency range 0 to 40KHz, amplitude 10dB/division.

The position of the resonator surface on the absorption peak (Fig 6.3) affects the resonance signal. Fig 6.7 is the time-domain response of a resonator vibrating in the linear region (around point a) of the absorption peak while Fig 6.8 is at one of the peaks of the absorption peak.

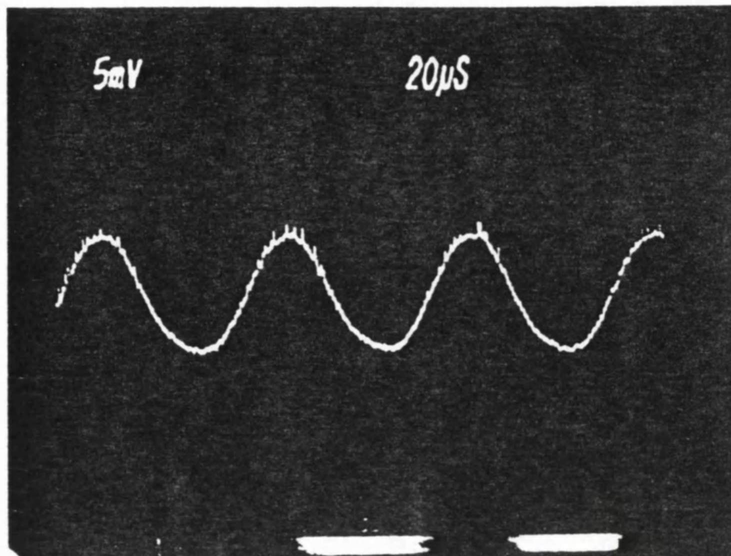

Fig 6.7: Reflected signal from a self-excited microresonator at a position of maximum response, timebase 20μs/division.

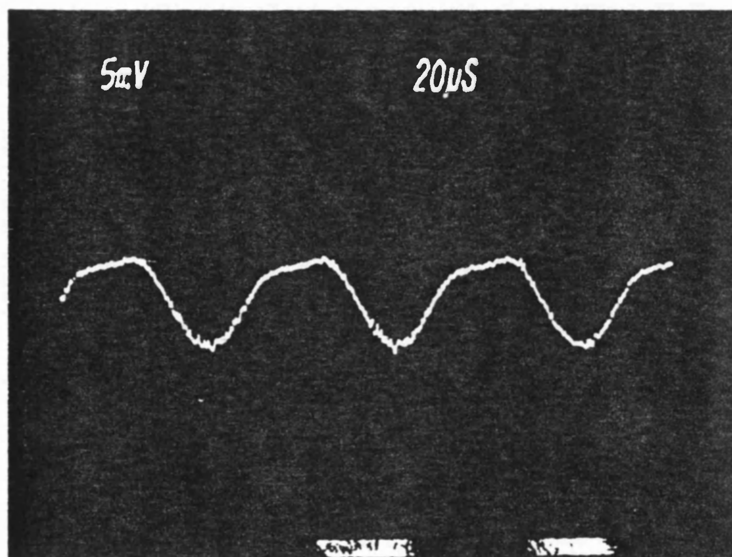

Fig 6.8: Reflected signal from a self-excited microresonator near a position of maximum response, timebase 20μs/division.

Fig 6.9 shows the amplitude of resonance as a function of the absorbed power. It is clear that the higher the power the higher the amplitude.

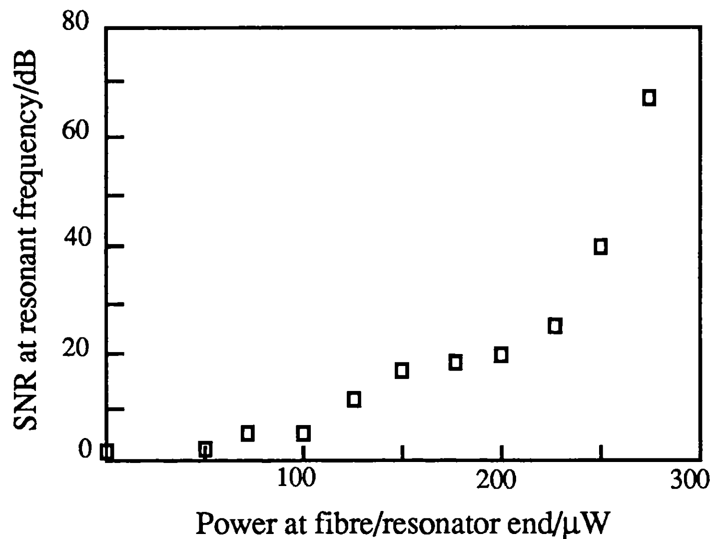

Fig 6.9: Dependence of the resonator amplitude upon (unmodulated) optical power for a self-excited resonator.

6.2.2. Sensitivity and multiplexing self-excited resonators:

A temperature sensitivity for a resonator was examined in the way described in chapter 7. From Fig 6.10 it was found that the temperature coefficient of the resonant frequency is 0.2KHz ± 0.01KHz/deg C. The SNR was maintained over the temperature range of 20 °C to 80 °C.

Using the experimental setup of Fig 6.11 two microresonators were self-excited. The spectrum analyser output of these devices is shown in Fig 6.12.

6.3. Conclusions

There is still a considerable amount of work to be done before self-excitations become a practical sensor system. However, we have shown that the system has the potential for sensing and multiplexing. This system makes an optical fibre based microresonator simple to assemble and low-cost.

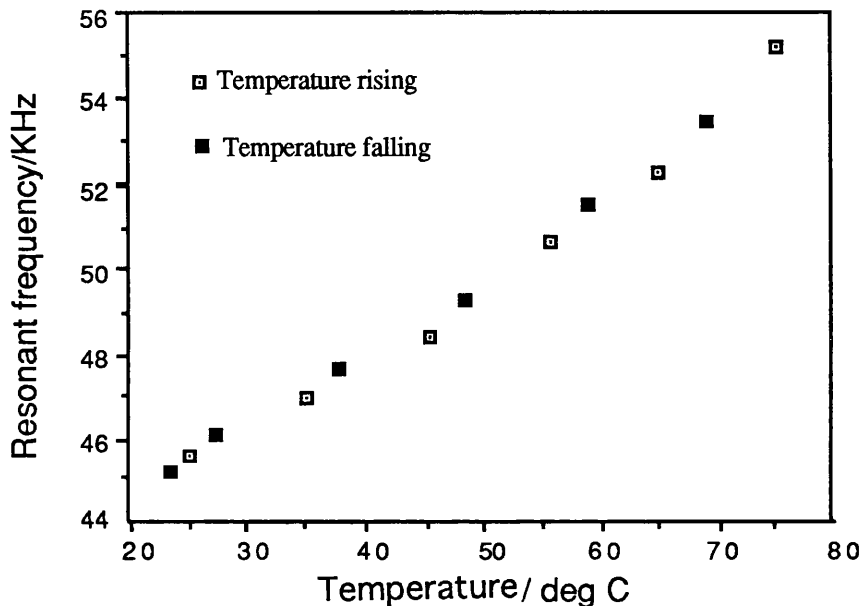

Fig 6.10: Temperature sensitivity of a self-excited microresonator.

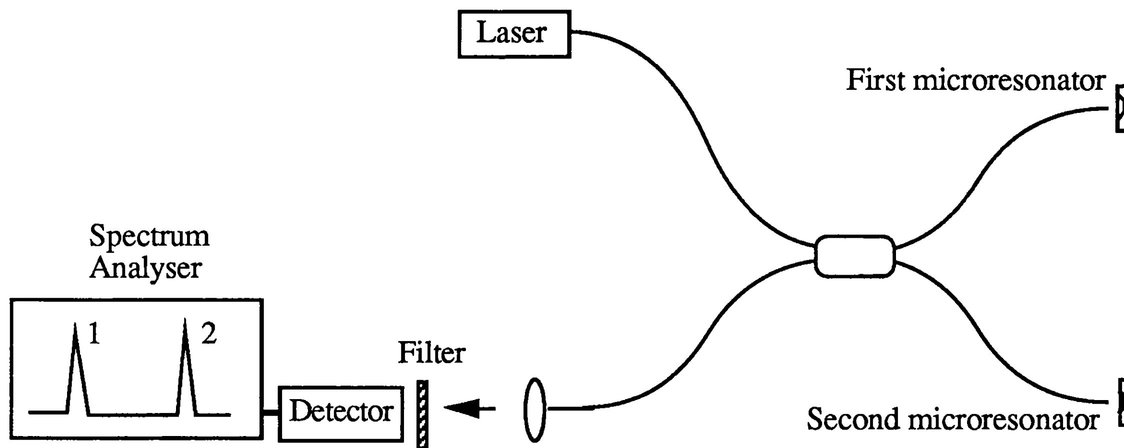

Fig 6.11: Multiplexing two self-excited resonators.

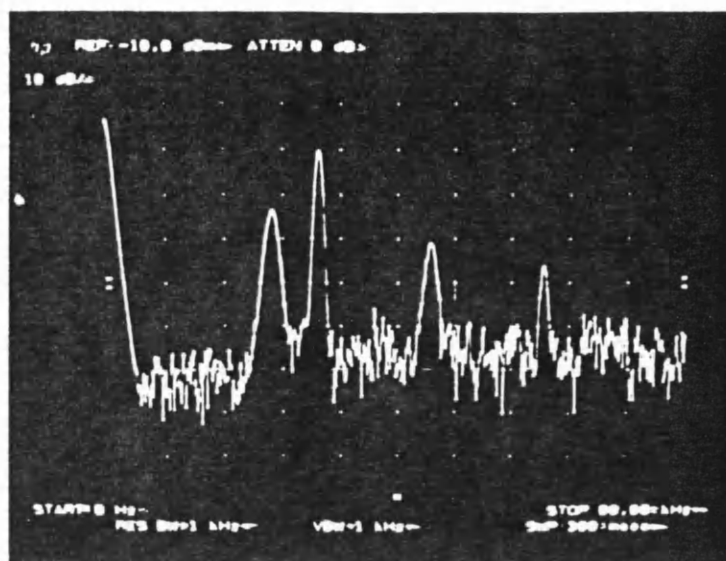

Fig 6.12: A spectrum analyser display of a detected optical output of two multiplexed self-excited microresonator.

6.4. References

1. Langdon R M and Dowe D L: 'Photoacoustic oscillator sensors', Procs SPIE Conference on Fibre Optic Sensors II, The Hague, 1987, pp 86-93.

2. Stokes N A D, Fatah R M A and Venkatesh S: 'Self-excited vibrations of optical microresonators', Electron Lett, Vol 24,1988, pp 777-778.

3. Stokes N A D, Fatah R M A and Venkatesh S: 'Self-excitation in fibre-optic microresonator sensors', Conf on solid-state sensors and actuators (Transducers 89 Procs of, Montreux, June 1989)

4. Stokes N A D, Fatah R M A and Venkatesh S: 'Self-excitation in fibre-optic microresonator sensors', Sensors and Actuators, A21-A23, 1990, pp 369-372.

5. Zhang L M, Uttamchandani D and Culshaw B: 'Optically powered silicon microresonator pressure sensor', Spring procs in physics, Vol 44, 1989, pp 470-477.

6. Zhang L M, Uttamchandani D and Culshaw B: 'Stabilisation of optically excited self-oscillation', Electron Lett, Vol 25, 1989, pp 1235-1236.

CHAPTER SEVEN

All Fibre-Optic Micromechanical Resonator Sensor System

7.1. Introduction

The sensing principle of microresonators is based upon the interaction of an environmental parameter with the resonant frequency. In most applications the measured parameter introduces stress in the resonator beam which in turn changes the resonant frequency. If a resonant structure is sustained at resonance, external environmental parameters, such as temperature and pressure, can affect the mechanical state of the beam, and change the frequencies at which resonance occurs. In the case of using the sensor as a gas detector the beam should be coated with a film of a substance that absorbs the gas to be detected. As the film absorbs the gas the mass of the resonator changes and as a result the resonant frequency shifts. The shift in resonant frequency with some parameter of interest can be calibrated. Monitoring the resonant frequency allows the device to be used as a sensor for that parameter.

The induced stress can be due to a variety of parameters which interact with the resonant frequency. These parameters can be intrinsic, such as doping and dislocations, or can be extrinsic factors, such as pressure, temperature, humidity, vacuum level, density, viscosity and flow. The pressure sensitivity of these devices is the main area of interest of this work. The resonant frequency of the silicon beam shifts with both an applied differential pressure across the wafer and a change of the ambient temperature. A comparison has been made between the different materials.

Microfabricated silicon resonators are compatible in size to the cross-sectional area of the fibre optic. This makes them particularly attractive for applications where fibre can replace electric cables. For instance, blood pressure can be directly monitored by putting the fibre in the patients' blood vessels. In telecommunication applications, the microresonator sensor system would allow for continuous pressure readings along the cables. This technique is particularly attractive since no electrical signals are associated with the sensor head as the device is optically activated and monitored.

These devices are driven into resonant vibration by using the technique described in chapter 3. An intensity-modulated laser source and a cw laser at a different wavelength is used to monitor the mechanical vibration. Both laser beams are guided through the same monomode optical-fibre and directed on to the resonator beam surface. In this chapter the pressure and temperature sensitivity of these devices are studied.

Pressure and temperature sensitivities of microresonators using bulk optic systems have been reported by Uttamchandani et al [1] and by Thornton et al [2]. For devices with more complicated shapes fibre optic systems with two fibres have been used, one for activation and the other for detection, as reported by Andres et al [3]. The sensitivities of these devices were first measured in a fibre-optic system by Fatah et al [4,5]. In the latter system two laser beams, activation and detection, were guided through the same optical fibre and positioned on the resonator. Furthermore, the latter group reported that silicon dioxide

resonators sense only temperature and not pressure. Thus silicon dioxide beams 'naturally' compensate for pressure changes in the environment.

7.2. Theoretical analyses

With reference to Fig 7.1 let us assume that the beam is on a circular wafer area clamped or pinned at the edges, and this area is exposed to a uniform differential pressure, ΔP, then two components of the stress can be considered, a radial one, σ_r, and a tangential one, σ_t. While these components are equal in the centre they are different near the edges. The equations relating stress to radial distance for clamped edge condition are [6][1] :

$$\sigma_r = \frac{3}{8}\left(\frac{\Delta P}{d^2}\right)\left[R^2 (1+\nu) - r^2 (3+\nu)\right] \quad (7.1.a)$$

$$\sigma_t = \frac{3}{8}\left(\frac{\Delta P}{d^2}\right)\left[R^2 (1+\nu) - r^2 (1+3\nu)\right] \quad (7.1.b)$$

and for pinned edge condition

$$\sigma_r = \frac{3}{8}\left(\frac{\Delta P}{d^2}\right)\left[(3+\nu) - r^2 (R^2 + r^2)\right] \quad (7.2.a)$$

$$\sigma_t = \frac{3}{8}\left(\frac{\Delta P}{d^2}\right)\left[R^2 (3+\nu) - r^2 (1+3\nu)\right] \quad (7.2.b)$$

where R is the sample radius exposed to pressure, d is the wafer thickness, r is the distance from the centre of the wafer to the point where the stress is measured. ν is Poisson's ratio which will vary with crystallographic direction in single crystal silicon. However, since its

[1] For further discussion see [7-9]

variation is small a value of 0.3 will be considered for all crystallographic directions. Thus the orientation of the resonator beam on the wafer affects the magnitude of the applied stress. The edge-conditions are similar to what we discuss in context of resonator beam end-conditions in chapter 3. Fig 7.2 shows both components of the stress induced in the surface of the silicon wafer under test.

The effect of the edge conditions can be seen from Fig 7.2. The wafer with pinned edge condition has one type of stress in each of its faces. While the face with lower pressure is under compression, the other is under tension. This is not the case for a wafer clamped at the edge, in which both types of stress exist in each face. The centre of the face with lower pressure is under compression while close to the edges it is under tension. The reverse is the case for the face with higher pressure. The consequence of this is that, in a wafer clamped at the edge, there is a circular region with zero stress. In this area, despite presence of differential pressure across the wafer, there is no stress induced, hence no pressure sensitivity.

To understand these stress regions in the presence of differential pressure, let us consider the wafer at the microscopic scale. Fig 7.3 shows the mechanical field distribution of clamped edge condition.

Fig 7.2 shows that the maximum pressure sensitivity in the centre of the wafer. For practical applications it is necessary to ensure that the beam is in the middle of the wafer to get maximum sensitivity. Neglecting the effect of the etch pit under the beam, the stress at the centre, σ_c, of the sample is given by:

$$\sigma_c = \left(\frac{3\,R^2}{8\,d^2}\right)(1+\nu)\,\Delta P \qquad (7.3)$$

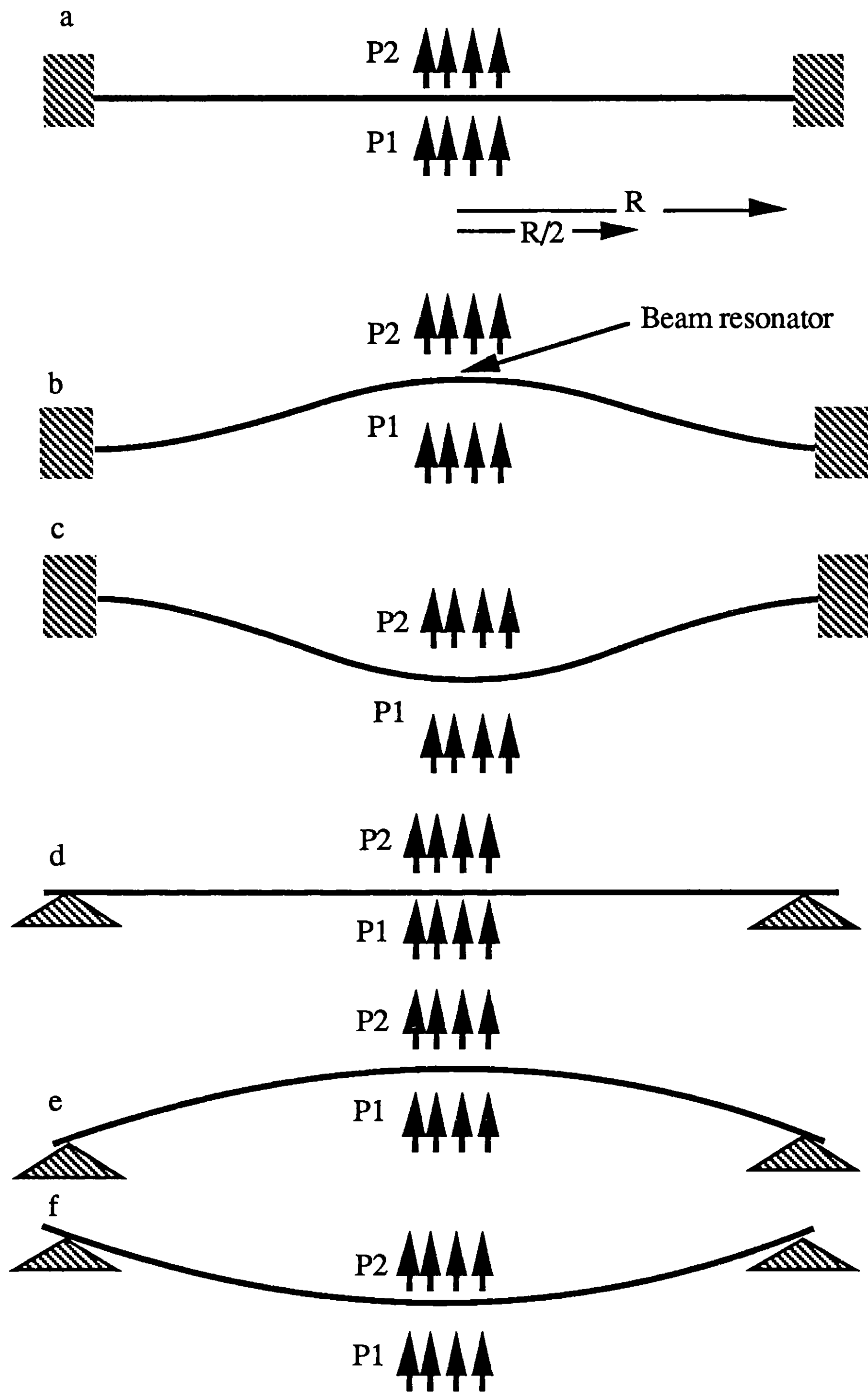

Fig 7.1: The mode shape of the wafer with application of differential pressure. Two edge conditions are shown. In a (clamped edge) and d (pinned edge) the wafers are shown with application of no differential pressure, i.e. P1 = P2. In b and e P1 > P2 while in c and f P1 > P2.

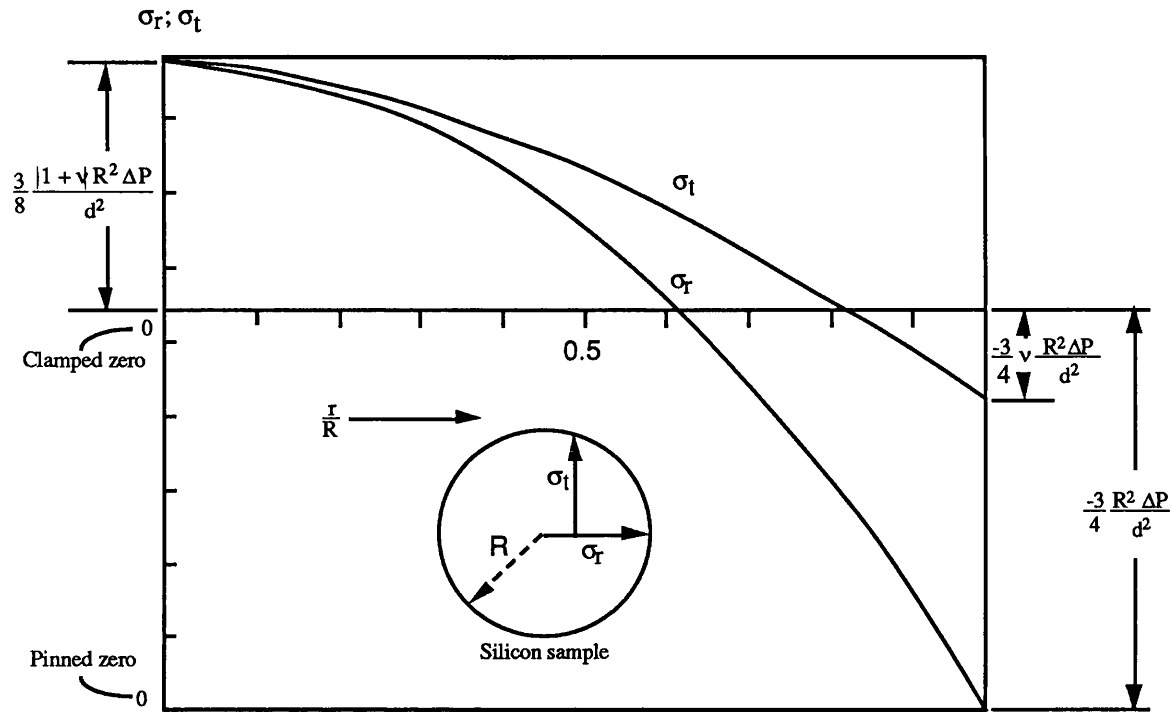

Fig 7.2: Theoretical stress pattern induced in a diaphragm [6].

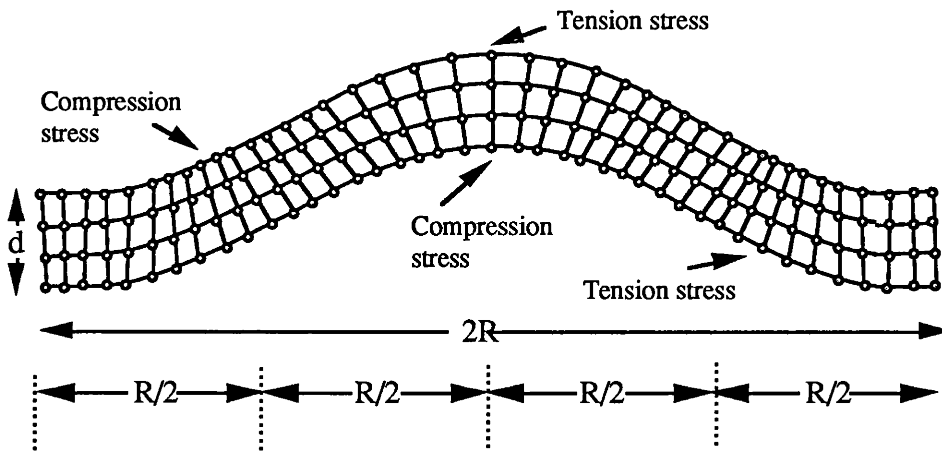

Fig 7.3: A clamped edge wafer being considered as four layers. The wafer can be considered as a four quarter-length beam. The points of inflexion occur half-way between the ends and the centre. The regions of stress are shown and can be related to Fig 7.1.

Whatever the edge condition, the centre of the wafer ($r < R/2$) still experiences the same stress state (Figs 7.1-7.3). Let us consider a resonator beam in the centre of the wafer. If the applied pressure at the back of the wafer is higher than atmospheric, i.e. positive ΔP applied, the front of the wafer assumes a convex shape, Fig 7.4(b), introducing a tensile stress where the beam is, at the centre of the outer surface. By contrast, if the pressure at the back of the wafer is lower than that of atmospheric Fig 7.4(c), i.e. a negative applied pressure, the front of the wafer then assumes a concave shape introducing a compressive stress at the centre of the outer surface.

It is not just the edge condition of the wafer that affects the magnitude of the stress induced in the beam but the end conditions of the beam resonator also affect it. Determining mode shape of the resonator is important in calculating stress induced in the beam due to its interaction with the measured parameter. The stress induced in the beam depends upon the its end-condition and hence the mode shape. The shift in resonant frequency, f_F, for a beam of rectangular cross-section with pinned [10] and clamped [11] end-conditions subjected to an axial stress σ is given by:

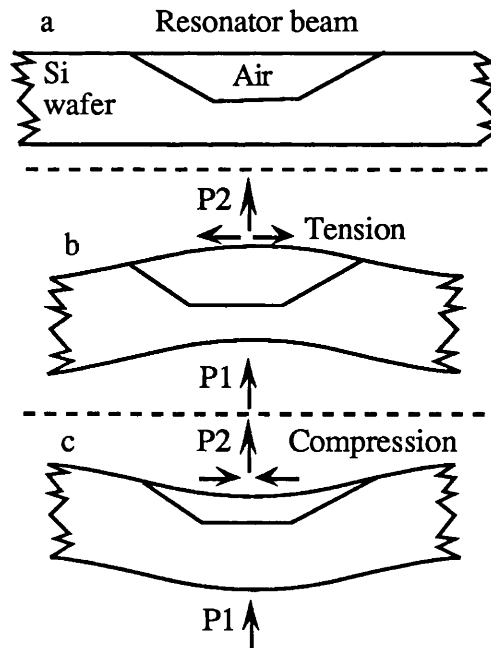

Fig 7.4: The beam resonator is shown under application of no pressure in (a), positive differential pressure in (b) and negative differential pressure in (c).

$$\left(\frac{f_F}{f_o}\right)_{Pinned} = \left[1 \pm \frac{12L^2\sigma}{\pi^2 Et^2}\right]^{0.5} \qquad (7.4)$$

$$\left(\frac{f_F}{f_o}\right)_{Clamed} = \pm\frac{0.147L^2\sigma}{Et^2} \qquad (7.5)$$

where f_0 is the resonance frequency of the relaxed beam given by (3.22), L and t are the length and the thickness of the beam respectively, and E is the Young's Modulus. The positive and the negative signs are, respectively, applied to the applications of tensile and compressive forces. The positive and the negative signs are applied to the applications of tensile and compressive forces, respectively.

Therefore, both the silicon wafer edge-condition (7.1 and 7.2) and the beam resonator end-conditions (3.24 and 3.25) affect the magnitude of the stress induced in the beam. Fig 7.5 shows the stress induced in a beam resonator while Fig 7.6 shows the pressure sensitivity of the resonant frequency. The sensitivity also depends on the geometry of the beam resonator as shown in Fig 7.7. Thin resonators have high pressure sensitivity because the top atomic layer of the wafer is under greater stress (Fig 7.1-7.4). Longer resonators also experience higher sensitivity as they cover a wider area, hence they experience higher stress.

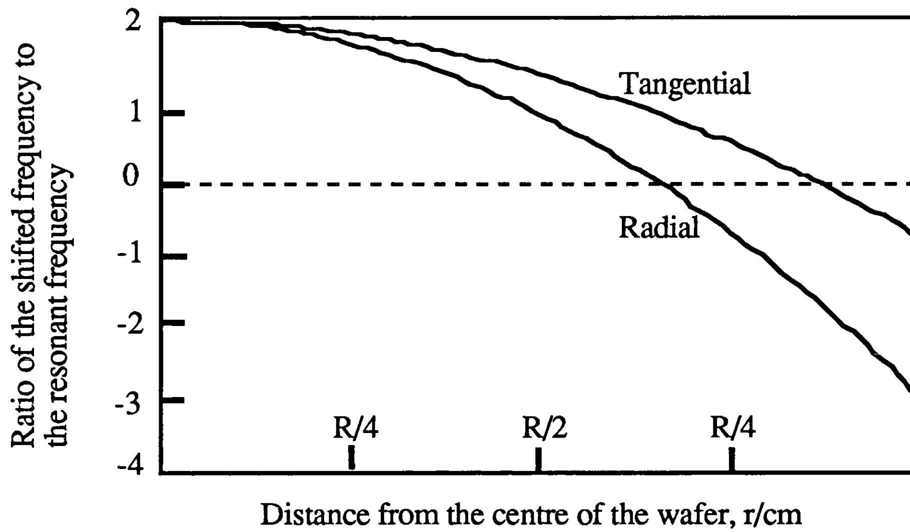

Fig 7.5: The dependence of the pressure sensitivity of the resonant frequency upon its position and orientation, radial and tangential, on the wafer. The relevant parameters are d=100μm, L=180μm, t=0.5μm and $\Delta P = 10^5 Nm^{-2}$.

If the beam is in the centre of the wafer to which pressure is to be applied, then 7.3 may be substituted in 7.5. Then, putting F = σ w t we have:

$$\frac{f_F}{f_0} = \pm \frac{aL^2}{Et^2} \frac{3R^2}{8d^2} (1+\nu)\Delta P \qquad (7.6)$$

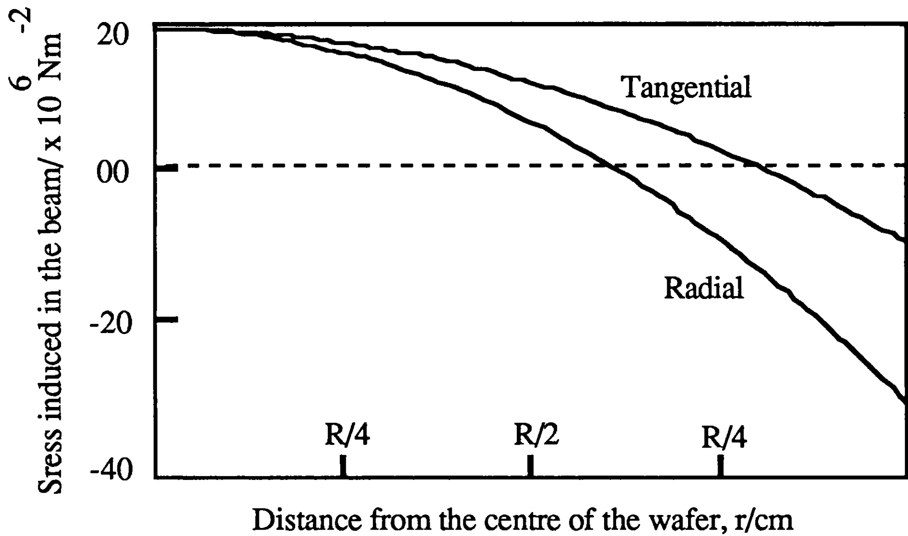

Fig 7.6: The stress induced in a resonator by differential pressure dependent on its position and orientation, both radial and tangential. The relevant parameters are d=100μm, L=180μm, t=0.5μm and $\Delta P=10^5 Nm^{-2}$.

Here, we have considered the clamp-edge condition for the wafer. Application of differential pressure deflects the wafer and the deflection w_o is maximum in the centre and can be calculated [12]:

$$w_o = \frac{0.221\pi R^4}{Ed^3}\Delta P \qquad (7.7)$$

Therefore the deflection depends upon the area in which the pressure is applied, the thickness of the wafer and the differential pressure (Fig 7.10).

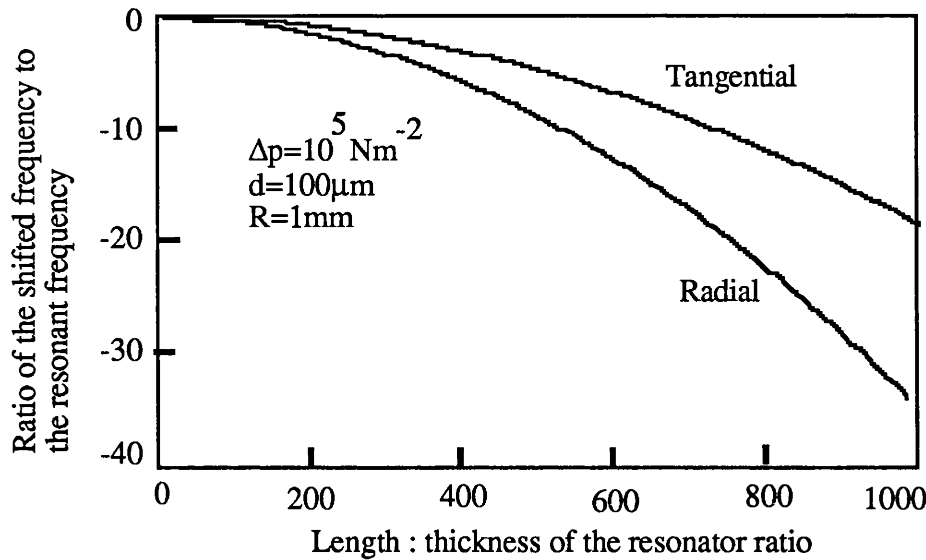

Fig 7.7: The resonant frequency dependence upon the geometry of the resonator in the presence of differential pressure. The relevant parameters are R=1mm, d=100μm, L=180μm, t=0.5μm and $\Delta P=10^5 Nm^{-2}$.

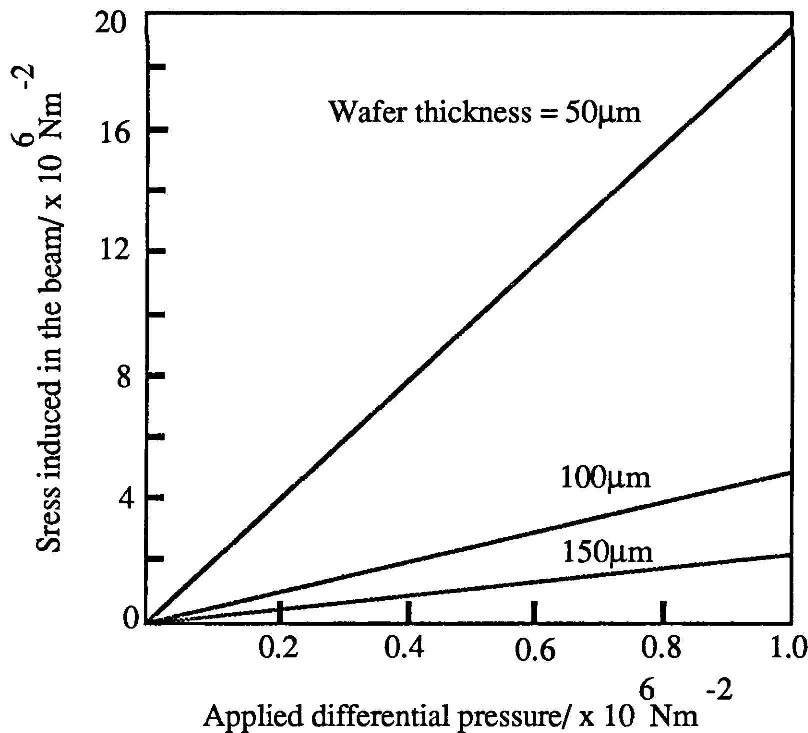

Fig 7.8: The stress induced in a beam positioned in the centre of the wafer. Both end- and edge-conditions are considered to be clamped for the resonator and the wafer. The relevant parameters are R=1mm, L=180μm, t=0.5μm and $\Delta P=10^5 Nm^{-2}$.

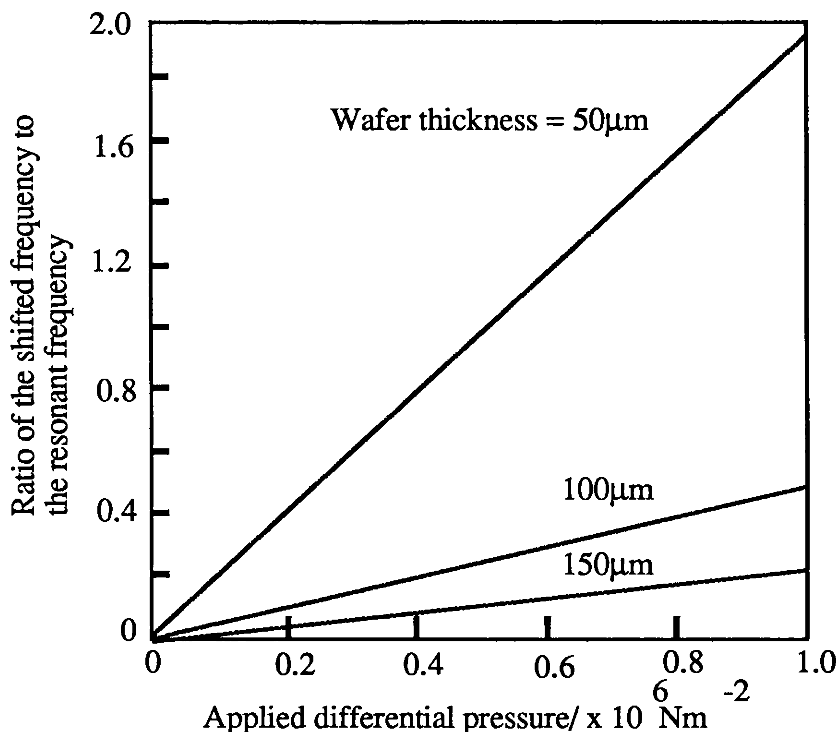

Fig 7.9: The resonant frequency dependence upon the applied differential pressure for a beam positioned in the centre of the wafer. Both end- and edge-conditions are considered to be clamped for the resonator and the wafer. The relevant parameters are R=1mm, L=180μm, t=0.5μm and $\Delta P=10^5 Nm^{-2}$.

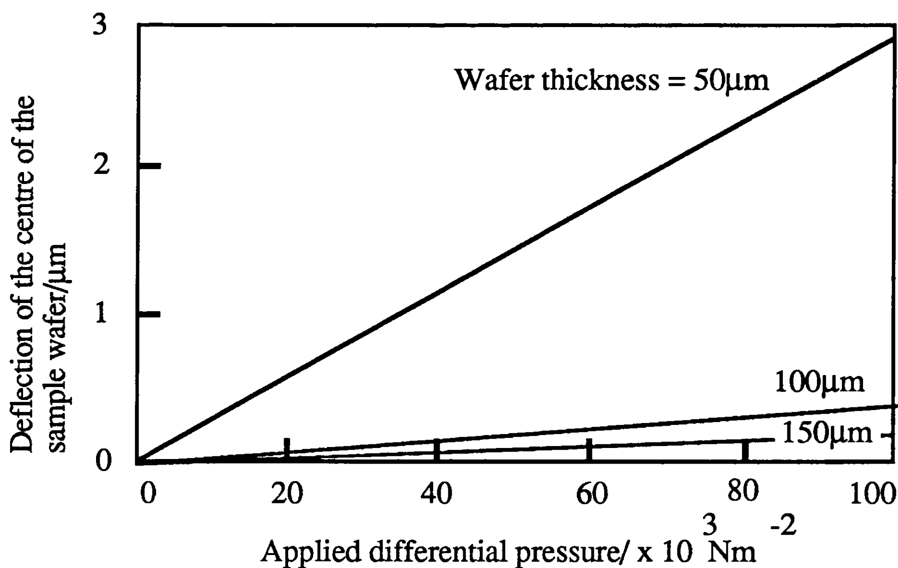

Fig 7.10: The displacement of a wafer as a function of the applied pressure. The wafer is assumed to have dimensions of 1mm in radius and 100μm thickness. The relevant parameters are R=1mm, L=180μm, t=0.5μm and $\Delta P=10^5 Nm^{-2}$.

7.3. Experimental work

7.3.1. Pressure sensitivity of resonance frequency:

The sample was mounted on a metal ring with a circular cross-section using a commercial epoxy; the metal ring was then connected to a nitrogen cylinder via a tube. The set-up to test the pressure sensitivity of the beam resonance is shown in Fig 7.11. In preparing the samples for pressure application the resonator could not be positioned accurately at the centre of the wafer and this affected the pressure sensitivity.

The silicon device (sample A) shown in Fig 7.12(a) was examined using this set-up. The silicon beam thickness was 0.5μm and the device was spatter-coated with 65nm of gold. The measured resonance frequency was 225 KHz, the quality-factor was 40 and signal-to-noise ratio 20dB. This frequency shifted to 247KHz when the sample was glued to the pressure ring. The resonant frequency then shifted with the application of 4-bar differential pressure across the full wafer thickness (380μm) and over a circular area of 2mm diameter from 247KHz to 250KHz. It was not possible to make an accurate measurement of the position and orientation of the beams on the wafer. The calculated shifted resonant frequency for such a beam positioned at the wafer centre (from 7.6) is approximately 2.4% per bar. The experimental value of the resonant shift is 0.3% per bar.

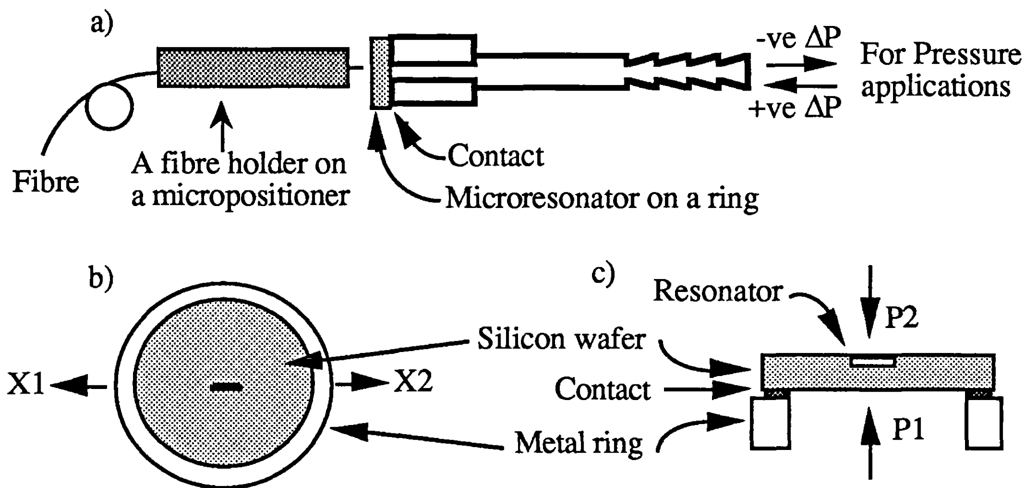

Fig 7.11: The experimental set-up for pressure sensitivity measurements shown in (a). The plan view of the silicon wafer is shown in (b) and section alone X1-X2 is shown in (c). P1 is atmospheric pressure and P2 is the applied pressure.

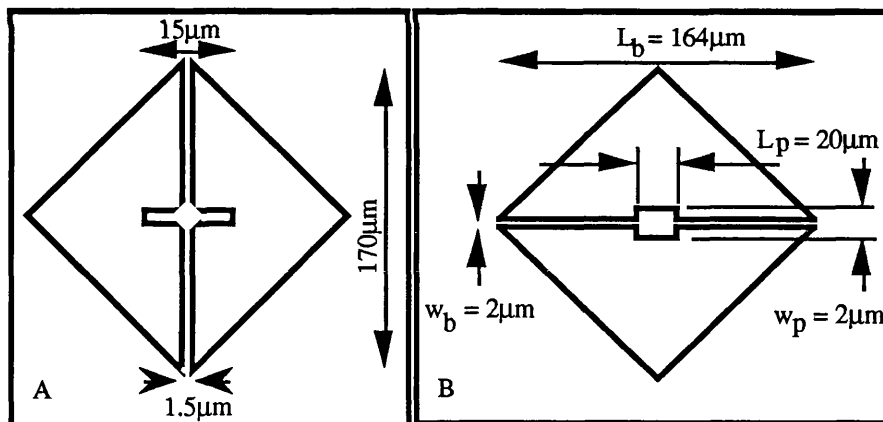

Fig 7.12: The plan views of micro-resonators examined. (Samples A and B)

Considering 7.6 we note that the pressure sensitivity of a resonator increases with decreasing wafer thickness. The back of a wafer with a beam fabricated on it (sample B) was chemically thinned from 380µm to 180µm and then mounted on a metal ring with area

of 1.8mm in diameter. In this case, the beam was 0.5μm thick and was coated with 200nm of aluminium. The first measured resonant frequency was 179 KHz, the quality-factor 33 and the signal-to-noise-ratio 35dB. The experimental results have shown that the sensitivity of the resonance frequency is 4.1% per bar. Fig 7.13 shows frequency plotted against applied pressure. The calculated shifted resonant frequency, from 2, is approximately 5.2% per bar.

Another resonator beam close to the edge of a wafer shows a negative pressure sensitivity. The resonant frequency shifted from 391KHz to 367KHz with the application of 2-bar differential pressure. Fig 15 shows the pressure sensitivity of this resonator which is 0.012 KHz per mbar or 0.0061% per a mbar. It can be calculated that this device is about 600μm away from the centre of the wafer. This device is in the region of compression mentioned in context of Fig 7.2 and 7.3.

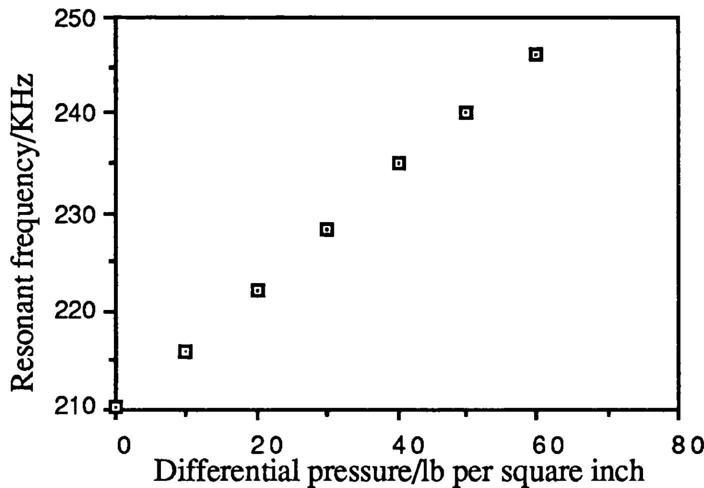

Fig 7.13: The pressure sensitivity of the first resonant frequency of the beam resonator shown in sample B.

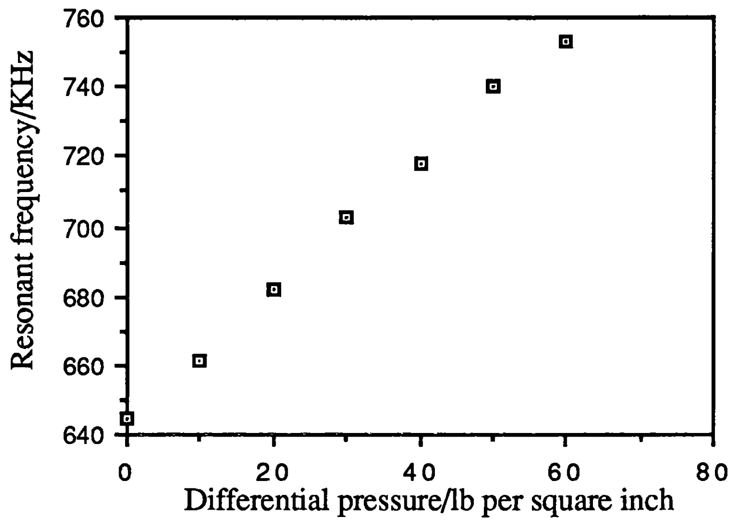

Fig 7.14: Pressure sensitivity of the second resonant frequency of a single crystal beam resonator shown in sample B.

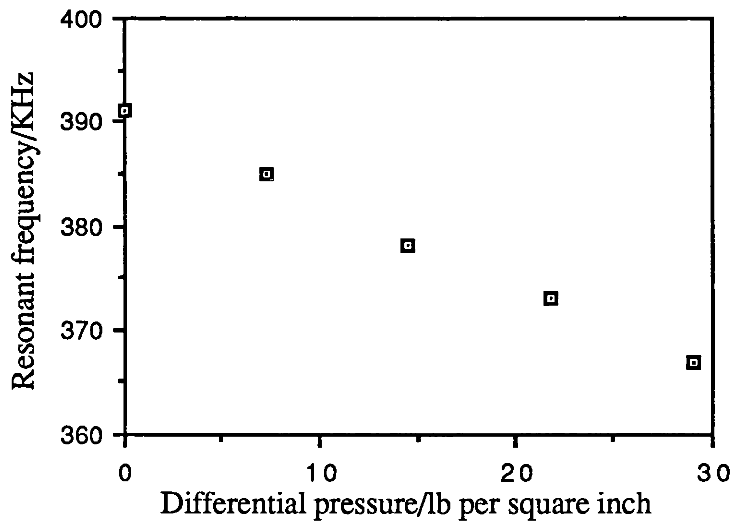

Fig 7.15: Pressure sensitivity of the first resonant frequency of a single crystal beam resonator similar to that shown in sample B.

The pressure sensitivity of a beam resonator fabricated from silicon dioxide thermally grown on a silicon wafer was also studied. In order to predict the pressure sensitivity the wafer is considered to be single-material and the interface between the silicon and the silicon dioxide is ignored. The direct application of (2) predicts a greater sensitivity for a silicon dioxide than for an equivalent silicon beam because of the lower value of Young's modulus.

A series of samples of silicon dioxide beams were examined using the set-up described for examining silicon devices. These beams were of similar dimensions to sample B, of thickness 0.5μm and coated with a thin layer of evaporated aluminium or spattered gold. Differential pressures (of up to 4-bars) across circular samples of up to 5.0mm in diameter were applied across the full wafer thickness. However no shift in the resonant frequency was observed above the resolution bandwidth of 1KHz. The fundamental resonant frequency of these devices was 230KHz.

In order to increase the sensitivity of the devices, the wafer was thinned to 150μm from 380μm and bounded to a metal ring with internal diameter of 5mm. In this case a shift in the resonant frequency was observed when the applied pressure was 4 bars. The pressure sensitivity of a resonator located in the centre of the wafer was 1.7% of resonant frequency per bar over 0-4 bars. This shift is much lower that that predicted by application of (7.6) which does not account for fabrication-induced stresses.

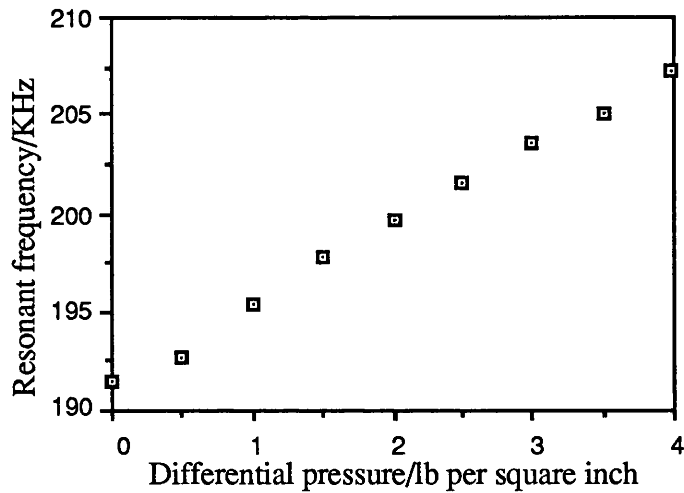

Fig 7.16: The pressure sensitivity of the first resonant frequency of a silicon dioxide beam thermally grown on silicon with dimensions similar to that of in sample B.

Discussion:

The results obtained for the pressure sensitivities of the resonant frequencies of the silicon beams are of the order predicted. A higher sensitivity is obtained by using a thinned wafer. The position and orientation of the microresonator beams on the wafer is clearly significant. Thus in order to reliably optimise the pressure sensitivity it is desirable to position the beam in the centre of the wafer. The beam stress is also affected by any dislocations or defects which may be introduced during the process of fabrication, and by the surface roughness resulting from the chemical thinning process. Further, the epoxy used to bond the sample to the pressure ring introduced significant stress to the beam. This was indicated by the 6% resonant frequency shift of the beam of sample A on bonding to the metal ring. For the implementation of a practical sensor it will be necessary to consider these factors.

When silicon is thermally oxidised, the silicon dioxide resulting is in a state of compression, hence when a silicon dioxide beam is defined by etching the silicon beneath

an oxide strip it deflects either upward or downward. This compression is a combination of intrinsic stress and thermal stress. The intrinsic stress is attributed to the volume expansion resulting from the conversion of silicon to its oxide [13][2] . The thermal stress is induced when the wafer, oxidised at around 1000°C, is cooled to room temperature. When the beam is undercut and allowed to deflect, nearly all the stress is relieved. The scanning electron micrographs of chapter 4 show that a thermally grown silicon dioxide beam on silicon is deflecting either downwards or upwards.

The deflection of the oxide microbridge can be measured using a scanning electron microscope to be around 5μm. The displacement of the wafer (from 7.7) is not significant, and we conclude from this that when the differential pressure is applied the bend shape of the beam will change so that the stress remains relieved. Any change in the resonant frequency must then result from a change in the residual stress remaining in the bent beam. This residual stress is thought to be about two orders of magnitude lower than the relieved compressive stress [14][3] and the change in resonant frequency is expected to be almost negligible. This conclusion is supported by the above results, which indicate a frequency shift of less than 0.2% per bar.

These results indicate that silicon rather than silicon dioxide will be a more suitable material for pressure-sensitive microresonator beams. However for other sensor applications the pressure-insensitivity of the silicon dioxide microbeams may prove to be a useful property.

7.4. Temperature sensitivity of the resonant frequency

The temperature sensitivity of the resonant frequency was measured by mounting the samples on a Peltier heating block. To attach the wafer a thin layer of heat-sinking compound was used. To monitor the temperature, a thermocouple was fixed to the metal-coated surface of the wafer within 6mm of the resonator. Good thermal contact was ensured

[2] For further information see chapter 4.

[3] For further information see chapter 4.

by fixing the thermocouple tip with thermally conductive epoxy.

A silicon device similar to sample A was examined. The dimensions of the beam were as follows: L_b = 175μm, L_p = 21μm, w_b = 3.5μm, w_p = 8μm and silicon thickness 1.0μm. It was evaporation coated with 200nm of aluminium. The experimentally measured resonant frequency was 353KHz with a quality-factor of 62. The resonant frequency is plotted against temperature in Fig 7.17. It can be seen that the dependence is not linear; however the temperature coefficient of the resonant frequency between 5 and 60°C is of the order of -0.17% /^{o}C.

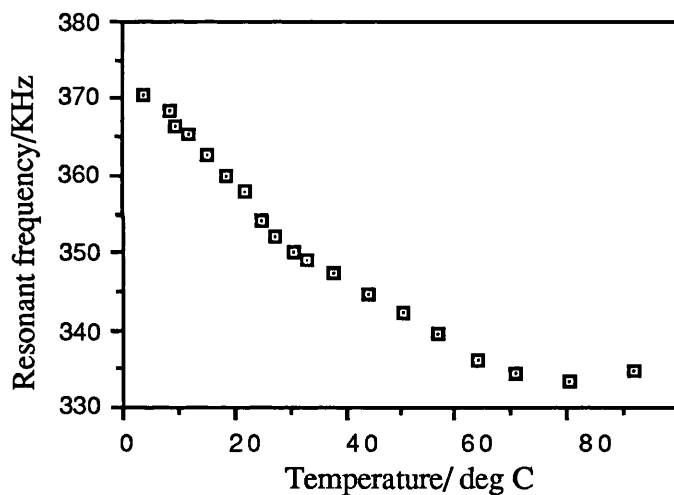

Fig 7.17: Dependence of the resonant frequency on temperature for a silicon beam.

A silicon dioxide device similar to sample B was also examined. The silicon dioxide thickness was 0.5μm, and the device was evaporation coated with 200nm of aluminium. The experimentally measured resonant frequency was 333KHz with a quality-factor of 40. The resonant frequency is plotted against temperature in Fig 7.18. The temperature coefficient of the resonant frequency between 25° and 60°C is of the order of -0.13% / ^{o}C.

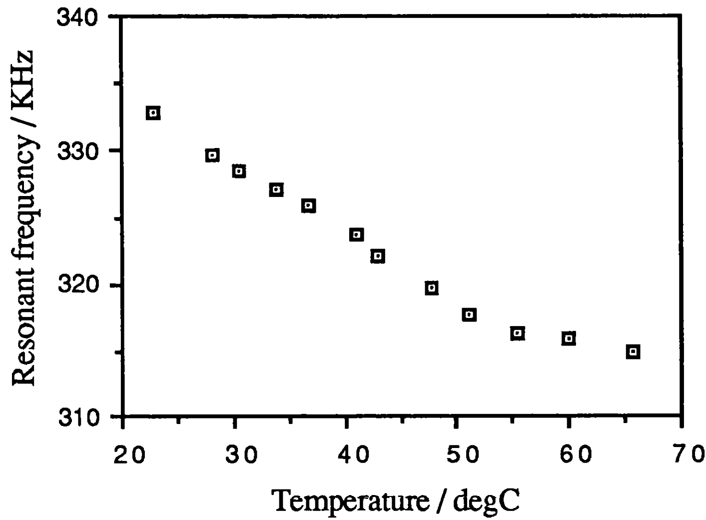

Fig 7.18: Dependence of the resonant frequency on temperature for a silicon dioxide beam.

Discussion:

The variation of the resonant frequency with temperature is due to a combination of the thermal dependence of material parameters: Young's modulus and density, as shown in Table 7.1.

The temperature coefficient of the metal coated silicon dioxide beams is dependent on the relative thickness of the oxide and the metal because of the opposite polarities of the temperature coefficient of the Young's modulus of these materials. Because of the observed negative shift, this indicates that the dominant factor is the change in beam stress. The calculated temperature coefficient of material parameters for the silicon dioxide beams under study is not greater than +0.02% / ^{o}C, and for the silicon beams the coefficient is negative (Table 7.1).

However, the experimental observations of the thermal coefficient for both silicon and

silicon dioxide beams cannot be justified by the calculated values. Therefore, the stress of the beams must depend on the thermal variations for both silicon and silicon dioxide.

Table 7.1: Linear expansivity and thermal dependence of Young's modulus for some resonator materials [15-17].

Material	Linear expansivity/ $ppmK^{-1}$	Thermal variation of Young's Modulus/ $ppmK^{-1}$
Silicon	2.3	-52
Silicon dioxide	0.4	192
Aluminium	14	-480
Gold	24	-480

At room temperature the silicon beam is under stress, which is primarily due to two causes. The metal is under tension thermally induced in the evaporation process and the silicon is under tension as it is highly doped with boron as part of the fabrication process. (The tension is caused by the lattice mismatch between silicon atoms and the doped boron (chapter 4)). The tension in both materials, principally in the metal, is reduced as the temperature of the beam is raised, since the expansivity of the metal is higher than that of the silicon. This in turn will reduce the resonant frequency (7.5), as the experimental results confirm. A reduction in metal thickness is expected to significantly reduce the temperature sensitivity of the beams since this reduces the compression stress induced by expanding the metal.

The mechanism is more complicated for the silicon dioxide beams. Again the observed negative coefficient indicates that the dominant factor is the change in beam stress. At room temperature the metal is under thermally-induced tension, but this keeps the oxide under

compression (see Fig 7.19). An increase in temperature will reduce both the tension and the compression so that the polarity of the temperature coefficient of the resonant frequency will depend on the relative thickness of the metal and the oxide. It should thus be possible to compensate for the effect of temperature by a suitable choice of thickness.

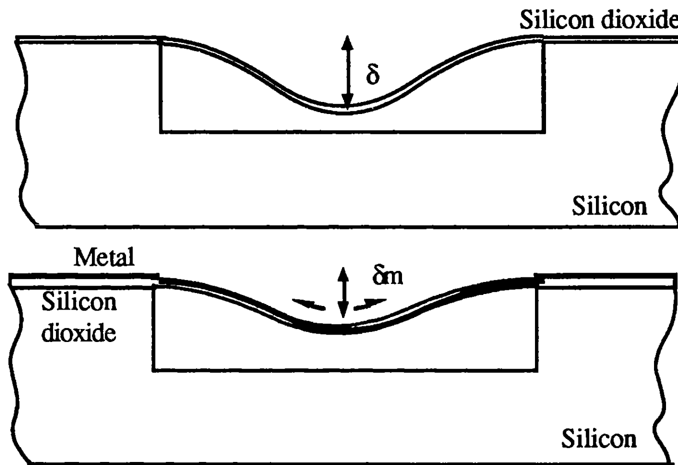

Fig 7.19: Stress in a silicon dioxide beam is relieved after undercutting; the metal coating puts the oxide back under compression ($\delta > \delta_m$).

It has been suggested [18] that because of the difference of polarity of the thermal dependence of the Young's modulus for silicon and silicon dioxide, composite structures can be arranged with zero net thermal dependence. However this cannot be achieved for a metal coated silicon resonator unless account is taken of the beam stress.

It may be possible to reduce the temperature sensitivity by coating only the middle part of the resonator. In this way the expansion of the metal does not put the beam under compression; hence a lower temperature coefficient will result.

A further method of temperature compensation involves the excitation of a beam and a cantilever using a single multimode fibre. Such a structure is shown in Fig 7.20. The

resonant frequency of the cantilever is independent of the differential pressure across the wafer, and it is therefore straightforward to process the signals received from the two vibrating elements to achieve a temperature-compensated pressure measurement. A multimode optical fibre system similar to that used for the previous work has been assembled. This system was successfully used for activating resonators, including cantilevers such as that characterised in Fig 7.21. The experimentally measured resonant frequency is 74KHz with a quality-factor of 15.

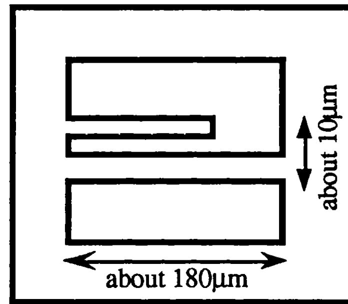

Fig 7.20: Microresonator beam pressure sensor with cantilever for temperature compensation.

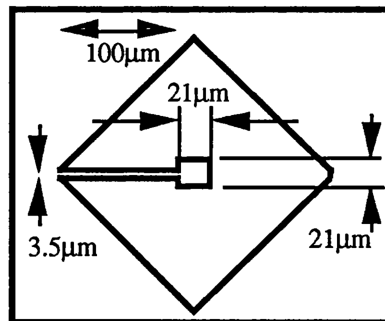

Fig 7.21: Silicon cantilever beam resonator which is evaporated with 200nm of aluminium.

7.5. Assembly of the sensor head to the systems fibre

Some of the devices are assembled by mounting a fabricated silicon device on another silicon device or on a different material, usually glass. In some other cases, the full head is fabricated on a silicon wafer and assembly is not required. What is required is electronic connections. In the case of an optically powered and detected sensor head the essential task is to attach the head to the optical fibre. This has not yet been achieved. A proposed method is to use a standard fibre assembly system used for pigtailing optical fibres to laser chips. The experience with fibre alignment to the active region of lasers provides all the necessary means of dealing with this. The second method may be fabricating the device on the optical fibre itself which may be achieved by using an eximer laser [19-20]. However this method may be more appropriate for plastic fibres rather than silica because of the absorption coefficient of glass at UV wavelengths, and its application is limited to miniature beams and diaphragms in which some examples are shown in Fig 7.22 and Fig 7.23.

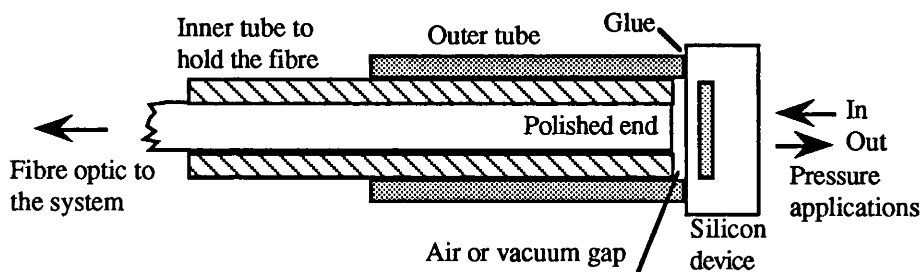

Fig 7.22: Assembling the sensor head to the fibre optic end using available fibre assembly system developed for pigtailing laser sources.

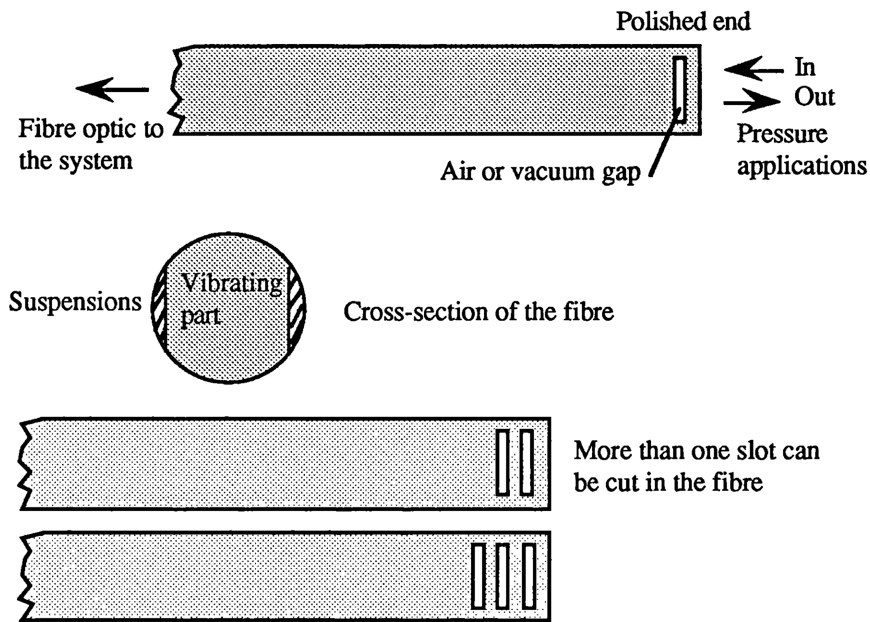

Fig 7.23: Fabricating diaphragm using eximer laser on optical fibres.

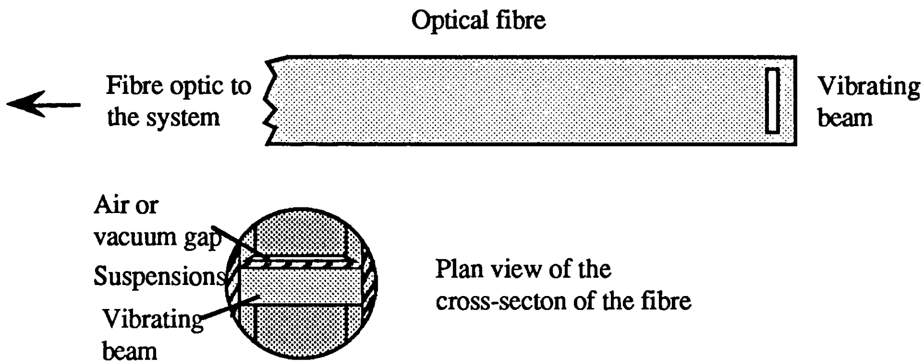

Fig 7.24: Fabrication of beams using eximer laser on optical fibres.

7.5. Conclusions

The change in the resonance frequency of a metal-coated silicon beam with applied differential pressure is found to be in agreement with theoretical predictions. The sensitivity may be increased by thinning the wafer on which the device is fabricated. The metal-coated silicon dioxide beam resonant frequency has a very low pressure sensitivity (less than 0.2% per bar). This is thought to be a result of the beam deformation induced during fabrication.

For optical cable monitoring 30psi is required. A pressure range up to 70psi here was studied. Therefore, the devices satisfy the conditions required for cable monitoring.

The temperature coefficients of the resonant frequency measured are of the same order for the silicon and silicon dioxide beams. The polarity of the temperature coefficient of the resonant frequency for a metal-coated oxide beam is thought to depend on the relative thickness of the metal and oxide. A compensation scheme has been proposed.

A novel method was proposed to assemble the sensor head and to fabricate the sensor head on the optical fibre itself which makes the sensor easy to fabricate without need for assembly.

7.6. References

1. Uttamchandani D, Thornton K E B and Culshaw B: 'Optical excited resonant beam pressure sensor', Electron Lett, Vol 23, No 25, 1987, pp 1333-4.

2. Thornton K E B, Uttamchandani D and Culshaw B: 'Novel optically excited resonant pressure sensor', Electron Lett, 12 May 1988, Vol 24, No 10, pp 573-579.

3. Andres M V, Foulds K W H and Tudor M J: 'Optical activation of silicon vibrating sensor', Electron Lett, Vol 21, 1985, pp 1097-1099.

4. Fatah, R M A, Stokes, N A D and Venkatesh S : 'All fibre-optic microresonator sensor system', presented in Sensors and Their Applications-S+AIV, University of Kent, 25-27 September 1989.

5. Fatah R M A and Stokes N A D: 'All fibre-optic microresonator sensor system', New Materials and their applications 1990 (IOP conference series No. 111, Norfolk, 1990).

6. Timoshenko S: 'Theory of plates and shells', (McGraw-Hill Book Company, New York, 1940) pp 59,62.

7. Tufte O N and Long D: 'Recent developments in semiconductor piezoresistive devices', Solid State Electronics, Vol 6, 1963 pp 323-38.

8. Tufte O N, Chapman P W and Long D: 'Silicon diffused-element piezoresistive diaphragm', J Appl Phys, Vol 33, No 11, 1962 , pp 3322-3327.

9. Gieles, A C M and Somers G H J: 'Miniature pressure transducers with silicon diaphragm', Philips Tech Rev, Vol 33, 1973, pp 14-20.

10. Timoshenko S: 'Vibration problems in engineering', (John Wiley and Sons, 4th ed, 1974)

11. Albert W C: 'Vibrating quartz crystal accelerometer', Procs 28th Int Instrum Symp Las Vegas USA, 1982, pp 33-44

12. Oberg E, Jones F D and Horton H: 'Machinery's handbook' 23rd Edition (New York 1989)

13. Alexandrova S, Szekfres A and Christova K: 'Stress in silicon dioxide films', Phil Magazine Lett 58, 1988, pp 33-36.

14. Lin S C H and Pugacz-Muraszkiewiz I: 'Local stress measurement in thin thermal SiO_2 films on Si substrates', J Appl Phys 43, 1972, pp 119-125.

15. Kate G W and Laby T H: 'Tables of physical and chemical constants', (Longman, London, 15th ed, 1968)

16. Fowle F E: 'Smithsonian physical tables', (Longmans Green & Co, London, 12 ed, 1959)

17. McSkimin H J: 'Measurements of elastic constants at low temperature by means of ultrasonic waves - data for silicon and germanium single crystals and for fused silicon' J Appl Phys, Vo 24, 1953, pp 988-997.

18. Othman M B and Brunnschweiler A: 'Electrothermally excited silicon beam mechanical resonators', Electron Lett, 1987, 23, pp. 728-30.

19. Tonshoff H K and Butje R: 'Material processing with excimer laser' Lasers in manufacturing: Procs of the 5th international conference, W Germany, May 1988, pp 35-46.

20. Poulin D, Eisele P and Znotins T: 'Excimer lasers in manufacturing', Lasers in manufacturing: Procs of the 6th international conference, May 1989, UK, pp 41-50.

CHAPTER EIGHT

Multiplexed Microresonator Sensors for Optical Fibre Cable Surveillance[1]

8.1. Introduction

So far we have treated these devices as sensors at only one location. However it is possible to multiplex a number of sensors to monitor different parameters along a line, or to monitor the same parameter at different places. One of the applications for telecommunications is to monitor pressurised optical cables.

At present conditions on optical cables are generally monitored by the use of additional metal carriers. The move towards cables with no metal bearers indicates the need for an optically based monitoring system. To date, the major parameter which has been continuously monitored has been the pressure of joint housings in the cable. These are normally measured by using simple contact pressure sensors which at a certain pressure put a loop on to the monitor pair and signal an alarm at the repeater station. A subsequent bridge measurement identifies the sensor which has been triggered. The microresonant sensor would allow for continuous pressure readings along the cable to be made and also other environmental parameters such as tension and temperature could be monitored if required. One possible novel application of this type of sensor could be in the monitoring of the build up of explosive gas in the duct route by means of mounting the sensor head on the external joint housing wall. This technique is particularly attractive since no electrical signals are associated with the sensor head as the device is optically activated and monitored.

[1] Patent pending.

8.2. System Architecture

So far we have shown that the optical power used for activation of sensors with a gold coating is just a few tens of μW. The lowest reported sustaining energy for a gold coated sensor is <10μW.

For practical applications of these sensors for cable monitoring the energy required to activate and monitor the sensors needs to be as low as possible. The British Telecom trunk network in general has section lengths of <40 Km, with nearly all of these having losses of less than 20dB/ section at 1300nm and <15dB/ section at 1550nm. Ideally the route would be monitored at each joint housing separated by about 1Km. Fig 8.1 shows a schematic diagram of a proposed cable monitoring system based on the use of a single monomode fibre for both activating and monitoring the sensors. Each sensor is connected to the fibre via one arm of a Y coupler. It should be stressed that there the fibres used to carry sensing information are not the fibres carrying communication information.

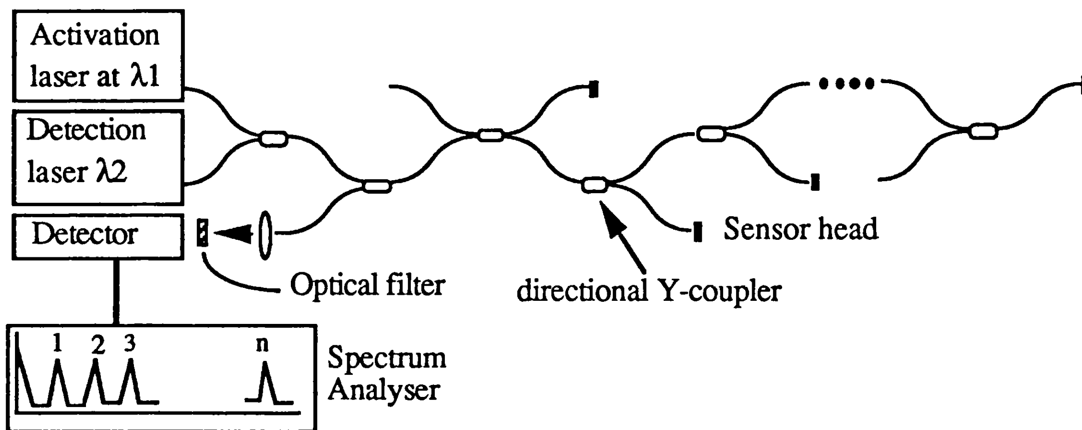

Fig 8.1: Multiplexing of micromechanical resonator sensors.

The optical activation power at the Nth sensor, P_{SNa} is given by:

$$P_{SNa} = \left[\frac{C_a \alpha_a L_a^N}{(1+\frac{1}{R})^{N-1} (1+R)} \right] P_{in} \qquad (8.1)$$

where L is the fractional fibre loss between sensors at the activation wavelength (assumed to be ~0.89 at 1.3μm); R is the coupling ratio in the coupler; N is the sensor number; "a" denotes the activation wavelength; P_{in} is the input power to the fibre; C is the coupling efficiency between the fibre and the sensor; and α_a is the absorption coefficient of the sensor at the activation wavelength. Fig 8.2 shows the optical power distribution in the fibre bus and at the sensors for a coupler splitting ratio of 100:1, and an input power of 10mW.

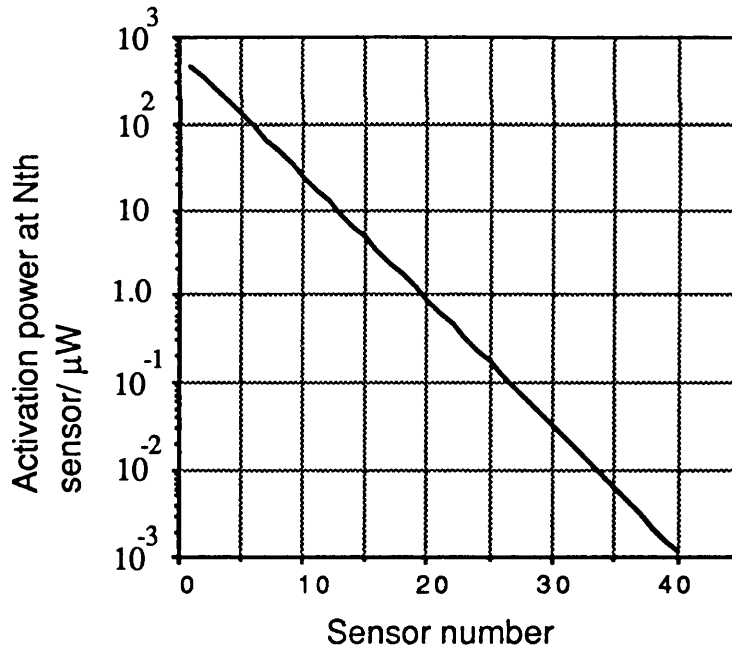

Fig 8.2: The distribution of the activation power to the sensors.

The detection wavelength needs to be different from the activation wavelength in order to discriminate at the detector. As the detection light has to travel both to and from the sensor

and be reflected from its surface, it will be attenuated more than the activation light. To optimise the system performance its wavelength is therefore chosen to correspond to the fibre loss minimum of ~1.55μm.

The optical detection power at the detector from the Nth sensor, P_{SNd} is given by:

$$P_{SNd} = \left[\frac{C_d R_s L_d^{2N}}{(1+\frac{1}{R})^{N-1} (1+R)} \right] P_{in} \qquad (8.2)$$

where C_d is the coupling efficiency of the reflected light from the sensor coupled into the fibre; R_s is the reflectivity of the beam resonator at the detection wavelength; L_d is the total fractional fibre loss between the sensor and the detector at the detection wavelength. Here, L has a power of 2N since the detection beam travels from the source to the sensor and back to the detector. The absorption coefficient for the activation power at the sensor in (3), is replaced in (4) by the reflection coefficient for the detection power. Fig 8.3 shows the power budget for the monitoring wavelength.

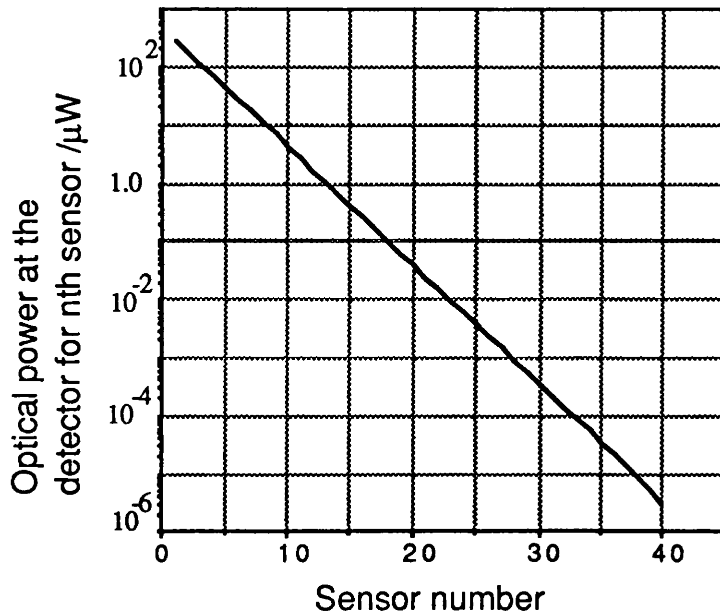

Fig 8.3: The detection power from the sensors to the detector.

8.3. Multiplexing of Sensors on a Single Fibre

Fig 4 shows how the sensors are differentiated from each other by using long pulse optical time domain reflectometry (LPOTDR). The activating laser is amplitude modulated at a frequency which corresponds to the natural frequency of oscillation of the sensors (f_S= ~1MHz). The detection laser beam is pulsed at a pulse width corresponding to $100f_S$ to $1000f_S$ (i.e. 0.1-1ms). At each sensor it is amplitude modulated and the reflected signal sent back to the detector .

If the sensors are monitored at (L)m apart (Fig 8.4) then there are (N x L)m to the Nth sensor. The signal from the Nth sensor has to travel (2N x L)m to be detected (Fig 8.5), and the time it takes is given by:

$$\tau_N = \frac{2NL\,n}{c} \qquad (8.3)$$

(where n is refractive index of the fibre ≈ 1.5; L is the distance between the monitoring laser and the first sensor, or the distance between each sensor; and c is speed of light). If L is 1Km then t_1 will be equal to about 10μs and for a 40Km route t_{39} will be equal to 390μs. The separation of the pulses from the detection laser has to be greater than this time and in practice could be as long as 10ms to allow for secondary reflection effects to die away before the next pulse is applied. This > 10: 1 pulse mode should allow the detection laser to be overdriven without seriously effecting its reliability.

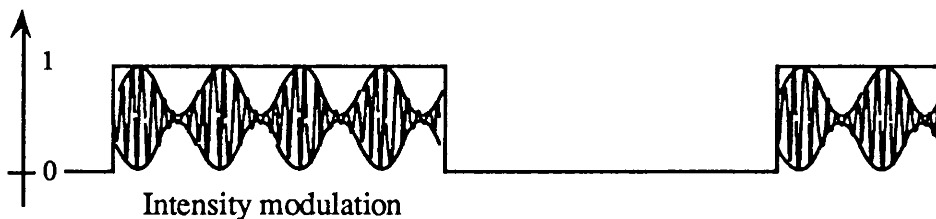

Fig 8.4: Reflected signal from a resonator sensor.

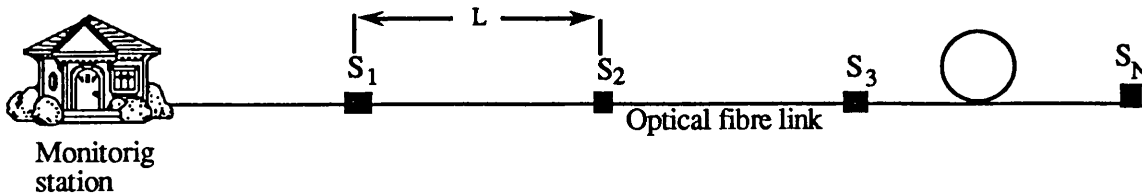

Fig 5: Monitoring the state of a telecommunication cables.

The detected signal will consist of a series of returning pulses with each pulse having been modulated by the resonating sensor. The frequency of the modulation will give information on the state of the particular sensor, and the distance between each pulse giving its location.

8.4. Improvement in LPOTDR System Performance

Although the present research sensor system has been demonstrated as having reasonable performance characteristics, additional research and development is required in a number of areas in order to make use of it in a LPOTDR system for cable condition monitoring.

8.3.1. The Sensor:

The performance of the monitoring system could be significantly improved if the activation and/or the monitoring power of the sensors could be reduced. This may be possible by:

1. Selective wavelength coatings on the surface of the sensor in order to improve the absorption of the activation laser (increasing α_a) and the reflection of the detection beam (increasing R_s).

2 . Improved coupling between the monomode fibre and the sensor. This could be achieved by redesign of the coupling optics (increasing the coupling coefficients C_a and C_d). Present designs use a simple butt-ended fibre which is positioned up to 10μm away from the sensor, this can cause coupling losses for both the activation and monitoring signals.

3 . Redesign of the sensors to increase their natural resonant frequencies. This would then reduce the pulse widths of the lasers and it may be possible to increase the peak laser power with a lower duty cycle (increasing P_{in}). (It also offers the possibility of using the sensor as part of a maintenance telephone system).

In addition the sensor needs to be designed to be more rugged for field deployment, and versions need to be designed for monitoring different physical parameters.

8.3.2. The System:

1 . Improved electronics at the detector could be used to increase the detection sensitivity of the system.

2 . Development of a narrow bandwidth receiver with a suitable wide dynamic range would improve the sensitivity of the system. This could possibly be a modified optical feedback receiver.

3 . The use of other detection wavelengths would make possible the monitoring of more than one parameter at each monitoring point.

4 . The use of pulsed output for the activation laser could achieve higher peak powers.

In conclusion, we have proposed a sensor system that can be optically activated and monitored remotely with no electronics involved in the sensor heads. The system consists of a single monomode fibre to which sensors are attached via Y couplers. Present designs of the sensors could allow semi-continuous monitoring of selected parameters along a cable route, with the state of the sensors being monitored using a novel LPOTDR technique

which allows the sensors to be multiplexed. Further work is required on the design of both the sensors and the system in order to optimise their performances.

The feasibility of a multiplexed sensor system has been studied. Every laser with 10mW output power is capable of providing 40 sensors with optical powers. This would require a sensor to be placed at every km of a BT network section (which is less than 40km). One activation laser and one detection laser would be sufficient to provide this section with optical power.

CHAPTER NINE

Summary, Discussion and Conclusions

9.1. Introduction:

To achieve an optimum multiplexed sensor system suitable for optical fibre cable surveillance, three technologies were merged together, namely:

i) silicon ,
ii) laser and fibre optics and
iii) optical time domain reflectometry (OTDR).

We have demonstrated that a silicon based sensor can be combined to fibre optic cable without involvement of any electronics in the sensor head. This has been achieved without any significant changes to the above technologies. Silicon has been developed for IC technology. Optical fibre cables and optical time domain reflectometers have been developed for telecommunication. The advantage of such a system can be summarised as follows:

9.2. The sensor head:

1 . The stability of silicon as a resonator material with virtually no hysteresis can be exploited. We have seen in chapter one that most of the sensors after fabrication have to go through a number of assembling steps which can be operationally time-consuming and hence expensive. This is not the case here. The sensor head is mass produced and does not require any electrical connections.

2 . The frequency is determined by the material properties and the beam geometry which is independent of the optical drive and only affected by the environmental changes. The signal is stable and compatible with digital signal processing. Calibration of the sensor simply consists of the measurand-resonant frequency curve. Hence it does not require any complicated electronics; all that is required is a frequency meter.

3 . Silicon as a material is well understood and the technology is established. This makes the devices capable of mass production at a low cost. The micrometer size of these devices make them very attractive and comparable to the cross-section of optical fibres.

4 . Changing the pressure sensitivity of the device is possible. There are four parameters that determine the sensitivity of the device. The pressure sensitivity of the samples can be increased either by increasing the area which is exposed to pressure and the length of the resonator or by decreasing the thickness of the wafer and the beam. We recommend thickness of about 50μm, area up to 3mm in diameter and resonator thickness and length of the device up to 0.1μm and up to 200μm, respectively. It is important to fabricate the resonator beam in the centre of the sample since there are regions on the wafer where the stress induced due to the differential application is zero or negative.

Analysing the pressure sensitivity of the resonator gives information about where on the wafer is the 'safe zone' to fabricate the device. It is shown that if the radius of the circular sample in which the pressure is applied is R, areas larger than 0.6R for radial 0.8R for tangential components for the stress have either zero or negative stress. This is in the concave side of a clamped-edge sample (see Fig 7.4). In short it is shown that the

orientation of the resonator on the sample, the location relative to the centre of the sample, the end-condition of the resonator and the edge-condition of the sample affect the sensitivity of the beam resonator.

5. The low sensitivity of the silicon dioxide beams fabricated on silicon is related to the fabrication criteria. The thermal mismatch between silicon and its oxide is responsible for deflecting the oxide beam upwards or downwards. The undercut silicon dioxide beam resonator is effectively longer than the straight line joining its both ends. Therefore despite the existence of a differential pressure across the sample, the beam does not take any significant stress. Equation (7.7) predicts that the displacement at the surface of the sample for $10^6 Nm^{-2}$ is about 4μm, however the displacement of the beam due to the thermal mismatch is of the same order, so very low pressure sensitivity has been observed for silicon dioxide.

The low pressure sensitivity of silicon dioxide resonators make them suitable as temperature sensors without any further precaution for pressure compensation being needed. There is a considerable demand for temperature sensors to operate in hostile environments. This increases the implementation field for these devices. The devices are capable of sensing temperatures from -40°C to 400°C. They need to have air encapsulation for sub zero temperature sensing since the condensation dampens the vibration of the resonator.

Perhaps a silicon dioxide device can be used with a silicon device to give the temperature compensation. This can be arranged by exploiting the system shown in Fig 9.1. The coupler delivers equal power to both devices: the silicon device which registers temperature and pressure simultaneously and the silicon dioxide device which reads only temperature. By using electronic circuitry, any shift in the frequency of the silicon dioxide device can be taken out from the shift in the silicon resonator frequency. In this way temperature compensation can be achieved. Furthermore, pressure and temperature can be read at the same time without any cross-sensitivity.

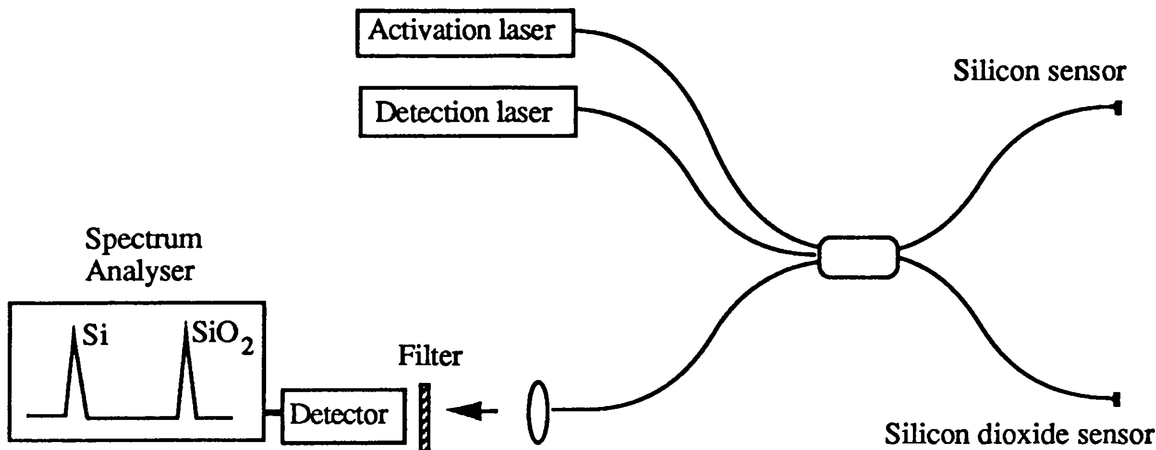

Fig 9.1: Temperature compensated optical fibre resonator pressure sensor system.

9.3. The optical fibre system

1. The only electronics involved in the system is in the monitoring station and this makes the system immune to EMI, hence it can be used in explosive environments.

2. The signal processing can be performed remote from the sensor head and the only link between the sensor and the processing station is the optical cables. The optical links are flexible tubes with very low losses (>0.2dBmkm^{-1}) between the source and the sensor head. Their function is to deliver power from the source to the sensor and from the latter to the receiver. The output signal is determined by the shift in the resonant frequency via change in the measurand and is independent of the length of the optical fibre and consequently is unaffected by the environmental parameters affecting the cable.

3. The amount of optical power (minimum: 10µW) used for activation and detection makes the system not just safe to use but practical for multiplexing. Potentially up to 40 sensors can be used from the same source with an output power of 10mW. The device at resonance requires enough energy to recover its losses which is mainly determined by the internal friction and air viscosity. These loss mechanisms can be reduced, which helps to

increase the quality-factor of the device and increase the number of multiplexed sensors from the same source. Encapsulation of the (silicon) device will eliminate the air viscosity. The internal loses can also be reduced by improving the device. The end conditions can be improved by taking up the design of Fig 4.39.a. Reducing the length (~100μm) and increasing the thickness (~5μm) as predicted by (4.10) will increase the quality-factor, i.e. reduce losses.

4 . The future work should be focused on self-excitation because of simplicity, cost and its potential for multiplexing sensors. In this system, only one laser source is used for both activation and detection. The potential of this system has already been shown [1-3]. The improvement of this system means improving both the sensor head and the system. It is encouraging to see that workers in this field are already focusing their effort on the self-excitation system [4,5].

9.4. Electo-optic systems

One of the advantages of these devices is that they can be activated using both optical and electrical techniques. We have shown their potential in electrostatic and electrothermal activations. In the first technique, the coulombic attraction force between the electrodes (the resonator is part of one of them) is used to activate the device. In the second technique a time-dependent current is passed through the resonator and the resultant periodic heating makes the device resonate. In both cases a fibre optic system is used for detection.

Optical activation is an ideal sensing system when the use of electrical current is to be avoided. However, the electrical activation expands the range of applications of these devices. Such applications may involve magnetic and current sensing. In addition, optical filtering and optical modulation can be achieved without any circuitry complications since the device produces a stable intensity modulation. Table 9.1 shows a comparison between optical and electrical activation.

Table 9.1: Comparison between optical and electrical activation:

Categories:	Electrical system	Optical fibre systems
1) Amenity to EMI	No	Yes
2) Single cable can be used for both activation and detection	No	Yes
3) Electronic contact with the sensor head	Yes	No
4) Can be used in explosive environment	No	Yes
5) Relative price to produce the sensor head	Cheap	Cheaper
6) Small size	Yes	Yes
7) Easy to assemble the head	Yes	Yes
8) Can be used for current and magnetic sensing	Yes	No
9) Can the sensor head be disposable as required in some applications such as blood monitoring?	Yes	Yes
10) Can be multiplexed	Not easily	Yes

9.5. Theoretical work

Understanding the physics of the optical resonator sensor system is the key for developing both the sensor head and the sensor system. One dimensional theory is used to analyse the mechanisms by which the optical power transfers into mechanical vibration in the beam. One conclusion of this work is that silicon dioxide is a good insulator when used as a layer on a silicon beam since it establishes a good temperature gradient along the beam. Therefore, if thicker devices are required ($>1\mu m$) a multilayer structure is recommended.

A simple universal relationship for all the materials has been found. According to this relationship resonance frequencies and material properties of all the materials are related together in a simple mathematical formula, viz:

$$\left(\frac{f_i}{\sqrt{\frac{E}{\rho}}}\right)_{\text{any materials}} = \text{constant} \qquad (9.1)$$

This relationship enables us to choose different materials for change in the resonance frequency and predict (E/ρ) values from the measured resonance frequencies.

The end-conditions determine the resonant frequency and its mode shape. Furthermore this parameter determines the sensitivity of the device as a sensor. Analysing the complex end-conditions and relating them to the fabrication criteria enables us to improve both the device and the fabrication process. The new end-conditions (called webbed) in the form of a simple mathematical formula (4.2) enable us to predict the resonant frequency, their mode shape and most importantly their sensitivity.

Study of the resonant frequency behaviour and of the methods of activating a resonant mode (e.g. torsional) shows that transverse resonance frequencies are preferable for sensing applications. However, other modes (such as torsional) can be used for the same purpose but the enhancement of this mode should be built into the design. For example the dominant resonant frequency mode of a beam clamped at both ends is transverse.

The effect of four metal coatings on silicon and silicon dioxide resonators has been studied. It has been concluded that all the metals except aluminium behave similarly in effecting the resonance frequency.

It is shown that the detection mechanism is interferometric. The amplitude of the detected signal drops to half its value if the fibre is misaligned by 2 degrees. This signal can be improved by forming a partially transmitting mirror at the end of the fibre and keeping the two surfaces (fibre and resonator) parallel.

The detection signal can be improved by splicing a GRIN lens to the end of the fibre. This provides a collimated beam without increasing the fibre cross-section since the radius of the

lens is comparable to that of the fibre. A collimated beam decreases the walk-off light in two ways. Firstly it decreases the spot size of the laser beam; in this way most of the laser beam is incident to the resonator surface. Secondly it increases the reflected signal to the fibre. Furthermore, a collimated beam is more efficient for activation since decreasing the spot size of the incident beam increases the intensity of the light; this in turn establishes a higher temperature gradient along the beam resonator. Hence a lower energy is required to activate the device.

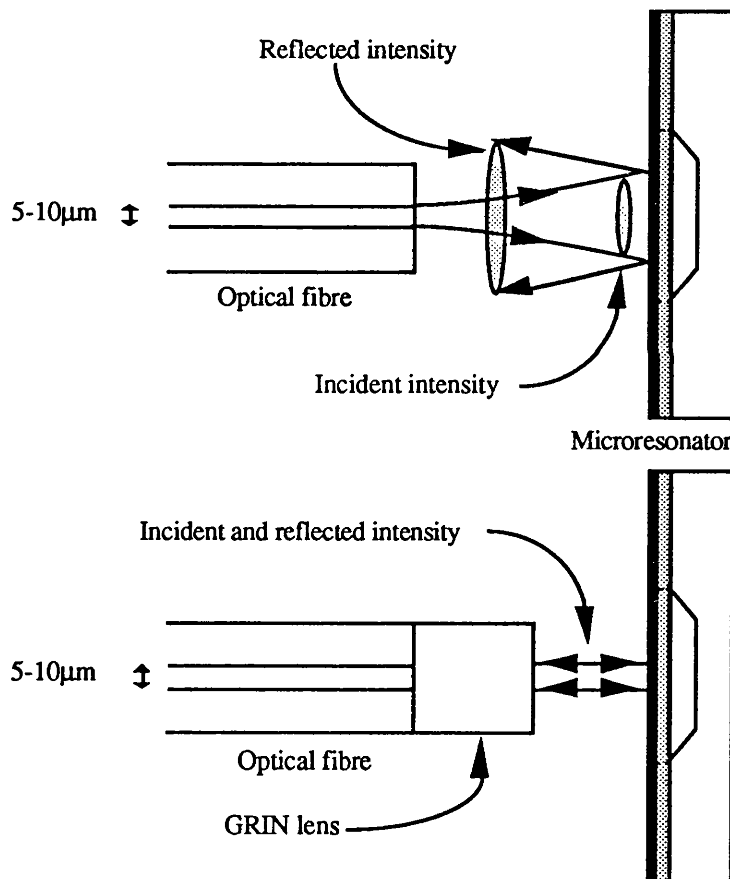

Fig 9.2: Increasing the efficiency of the optical system by splicing a GRIN lens to the end of the systems fibre.

9.6. Long pulse optical time domain reflectometry: a technique for multiplexing resonator sensors

One criticism of these devices is that in multiplexing each device requires a different resonant frequency. This makes the multiplexing sensors of these kinds complicated for two reasons. Firstly, a range of devices has to be fabricated each with different resonant frequencies since the information from different locations or different environmental parameters has to be distinguished at the monitoring station. Secondly, and probably more importantly, each device has to be driven with an optical modulation equal to its mechanical resonant frequency. Therefore the number of activation lasers required has to be equal to the number of sensors. It may be possible to use the same laser for activating different sensors but this needs special circuitry and can be complex. However, sensors with the same resonant frequency are differentiated from each other by use of long pulse optical time domain reflectometry (LPOTDR), since they are located at different distances along the cables from the monitoring station, so the signals from various sensors arrive at the station at different times. The time when the pulse arrives at the station gives information about the location of the sensor while the resonant frequency gives information about the measurand. In this way, only one activation laser can be used to activate a number of sensors.

Installing such a sensor system is cheap and easy since there are already extra optical fibres in the cables.

In summary, we have developed a reliable multiplexed sensor system based on silicon, fibre optic and LPOTRDR technology for optical fibre surveillance monitoring.

9.7. References

1. Stokes N A D, Fatah R M A and Venkatesh S: 'Self-excited vibrations of optical microresonators', Electro Lett, Vol.24, 1988, pp 777-778.

2. Stokes N A D, Fatah R M A and Venkatesh S: 'Self-Excitation in fibre-optic microresonator sensors', Conf on solid-state sensors and actuators (Procs of Transducers 89, Montreux, June 1989.

3. Stokes N A D, Fatah R M A and Venkatesh S: 'Self-excitation in fibre-optic microresonator sensors', Sensors and Actuators, A21-A23, 1990, pp 369-372.

4. Zhang L M, Uttamchandani D and Culshaw B: 'Optically powered silicon microresonator pressure sensor', Spring procs in physics, Vol 44, 1989, pp 470-477.

5. Zhang L M, Uttamchandani D and Culshaw B: 'Stabilisation of optically excited self-oscillation', Electro Lett, Vol.25, 1989, pp 1235-1236.

9.6. Long pulse optical time domain reflectometry: a technique for multiplexing resonator sensors

One criticism of these devices is that in multiplexing each device requires a different resonant frequency. This makes the multiplexing sensors of these kinds complicated for two reasons. Firstly, a range of devices has to be fabricated each with different resonant frequencies since the information from different locations or different environmental parameters has to be distinguished at the monitoring station. Secondly, and probably more importantly, each device has to be driven with an optical modulation equal to its mechanical resonant frequency. Therefore the number of activation lasers required has to be equal to the number of sensors. It may be possible to use the same laser for activating different sensors but this needs special circuitry and can be complex. However, sensors with the same resonant frequency are differentiated from each other by use of long pulse optical time domain reflectometry (LPOTDR), since they are located at different distances along the cables from the monitoring station, so the signals from various sensors arrive at the station at different times. The time when the pulse arrives at the station gives information about the location of the sensor while the resonant frequency gives information about the measurand. In this way, only one activation laser can be used to activate a number of sensors.

Installing such a sensor system is cheap and easy since there are already extra optical fibres in the cables.

In summary, we have developed a reliable multiplexed sensor system based on silicon, fibre optic and LPOTRDR technology for optical fibre surveillance monitoring.

9.7. References

1. Stokes N A D, Fatah R M A and Venkatesh S: 'Self-excited vibrations of optical microresonators', Electro Lett, Vol.24, 1988, pp 777-778.

2. Stokes N A D, Fatah R M A and Venkatesh S: 'Self-Excitation in fibre-optic microresonator sensors', Conf on solid-state sensors and actuators (Procs of Transducers 89, Montreux, June 1989.

3. Stokes N A D, Fatah R M A and Venkatesh S: 'Self-excitation in fibre-optic microresonator sensors', Sensors and Actuators, A21-A23, 1990, pp 369-372.

4. Zhang L M, Uttamchandani D and Culshaw B: 'Optically powered silicon microresonator pressure sensor', Spring procs in physics, Vol 44, 1989, pp 470-477.

5. Zhang L M, Uttamchandani D and Culshaw B: 'Stabilisation of optically excited self-oscillation', Electro Lett, Vol.25, 1989, pp 1235-1236.